

ROLE OF FERROELECTRIC DOMAIN CONFIGURATIONS ON THE INDENTATION BEHAVIOUR OF PIEZOCERAMICS

Ph.D. Thesis

By

VAIBHAV SANJAY KATHAVATE



**DEPARTMENT OF METALLURGY ENGINEERING AND
MATERIALS SCIENCE
INDIAN INSTITUTE OF TECHNOLOGY INDORE
MAY 2021**

ROLE OF FERROELECTRIC DOMAIN CONFIGURATIONS ON THE INDENTATION BEHAVIOUR OF PIEZOCERAMICS

A THESIS

*Submitted in partial fulfillment of the
requirements for the award of the degree
of*

DOCTOR OF PHILOSOPHY

By

VAIBHAV SANJAY KATHAVATE



**DEPARTMENT OF METALLURGY ENGINEERING AND
MATERIALS SCIENCE
INDIAN INSTITUTE OF TECHNOLOGY INDORE
MAY 2021**



INDIAN INSTITUTE OF TECHNOLOGY INDORE

CANDIDATE'S DECLARATION

I hereby certify that the work which is being presented in the thesis entitled “**Role of Ferroelectric Domain Configurations on the Indentation Behaviour of Piezoceramics**” in the partial fulfillment of the requirements for the award of the degree of **DOCTOR OF PHILOSOPHY** and submitted in the **Department of Metallurgy Engineering and Materials Science, Indian Institute of Technology Indore**, is an authentic record of my own work carried out during the time period from December 2017 to May 2021 under the supervision of **Dr. Eswara Prasad Korimilli, Asst. Prof., IIT Indore** and **Dr. Indrasen Singh, Asst. Prof., IIT Indore**.

The matter presented in this thesis has not been submitted by me for the award of any other degree of this or any other institute.

24/08/2021

**Signature of the student with date
(VAIBHAV SANJAY KATHAVATE)**

This is to certify that the above statement made by the candidate is correct to the best of my/our knowledge.

24/08/2021

Signature of Thesis Supervisor #1 with date
(Dr. ESWARA PRASAD KORIMILLI)

24/08/2021

Signature of Thesis Supervisor #2 with date
(Dr. INDRASEN SINGH)

VAIBHAV SANJAY KATHAVATE has successfully given his Ph.D. Oral Examination held on **August 24, 2021**.

24/08/2021

Signature of Thesis Supervisor #1 with date
(Dr. ESWARA PRASAD KORIMILLI)

24/08/2021

Signature of Thesis Supervisor #2 with date
(Dr. INDRASEN SINGH)

FIRST and FOREMOST.....

Dedicated

To

***All the Soldiers and Farmers of
the Country.....***

***(Being an Integral Part of Our
Life)***

***To The Four Pillars of my
Life.....***

Prof. A.S. Adkine (Since 2012)

Dr. P.P. Deshpande (Since 2014)

Cdr. K. Gopakumar (Since 2016)

Dr. Eswara Prasad Korimilli and

Dr. Indrasen Singh (Since 2017)

(I really don't know, where I would have been.....

If I wouldn't have met these folks)

Dedicated

To

Mr. Narayan Pawar

(A selfless person I ever met)

And his son

Mr. Dhananjay Pawar alias Dan

*(A true friend and his brotherly
concern)*

ACKNOWLEDGEMENTS

Forget the help which you do it to others and never ever mention about it.....

.....**My Mother**

If you can't repair the home appliances like TV, Grinder and Fridge, then your gold medal, doctorate, mechanical or metrology (he pronounces metallurgy as metrology) is of no use..... Country doesn't need doctors and engineers; it needs good characters.....

.....**My Father**

Here I am.... at my final journey towards Doctorate. Achieving this dream was never ever easy right from the two and half years of struggle to get the admission for Ph.D. in IIT (yes... I was very particular about IIT... since I dreamt it in 2007 and it took me 2017 to step in... 10 years of suicide) to write the last word of the chapter 5 and many people contributed to this journey directly and indirectly. Acknowledging them is only the small thing that I can do in return to their help.

"The persons like you may opt for Ph.D." this was the statement made by Prof. A.S. Adkine (my Gary Kirsten), when I was in the 3rd year of my graduation and writing the draft of the paper on *"Computational Fluid Dynamics"*. I am still wondering why he said that? This made my nights sleepless since 2012. Sir, thank you very much (I know "thank you" is not enough). Neither you would have encouraged me nor I would have achieved this mile stone (on a lighter note, still believing in the mentality that after B.E. I am going to join Varroc-Plant 5 or Endurance). Thank you once again for your continuous support, guidance and encouragements. The second step towards this mile stone was when I met Dr. P.P. Deshpande (my Duncan Fletcher) at College of Engineering Pune in 2014 during my Master's. This made me the man with simplicity and sincerity (which is still in process) and helped me a lot during my professional career. I still remember his words *"don't waste your time in clapping for others instead do such a work worth remembering it"* that changed my attitude and I was the first person to be present every day in COEP library at 0400 hours in the morning (even if in 8 °C during winter). Sir thank you very much, your lessons helped me maintaining that sincerity to the present date and I hope it will continue throughout my professional life.

In 2016, I met Cdr. K. Gopkumar at National Institute of Ocean Technology Chennai, a third step towards this journey. His way of winning arguments in group meetings in Naval

style, convincing the people (of course that include both higher authorities and subordinates), taking responsibility on own shoulders and presenting the technical stuff is marvelous and fascinating. His friendly attitude always allowed me to work freely and put forth my ideas in the group meetings. “*Don’t lose your hope, we Navy person never ever give up and still there is lot more potential in you to do something better for the country*” I took this personally and continued to work in similar fashion. Thank you, Commander for the words of encouragements and letting me dive deeper inside the ocean.

Ahhh !!!... and the most beautiful thing happened in my life in September 2017 is when I met Dr. Eswara Prasad Korimilli (of course this was not planned and I met him accidentally and all the beautiful things happen unexpectedly). His cool attitude of “*winning the experiments*” is admirable. I still remember his comment during our Ceramics International paper, “*Vaibhav, we have to be very critical about our own work before anyone could do it*”. His way of simplifying the things and being crisp (yes... this is his one of the favourite words) in representing the data (of course, as a student we always look to present the entire 4 years data/work in 45 min) feels us happy to work with him. His ethics and integrity to achieve the perfectionism are really appreciable (there are two incidents which make me to think about this). Sir, thank you very much for availing me the opportunity to work with you. I am fortunate to work with you and hope that I met your expectations. I am also indebted to Dr. Indrasen Singh for his continuous inputs and suggestions during the course of work. The kind of training which he gave it to me will be remembered till the last breath of my life. I could remember his disagreement over benchmarking the $P-h$ curves even if we were following a little short.

I take this opportunity to thank past and present Directors of IIT Indore Profs. Pradeep Mathur and Neelesh Kumar Jain for availing the experimental and other facilities. I further extend this opportunity to thank past and present Head of the Department, MEMS Profs. I.A. Palani and P.M. Shirage, and Dr. Vinod Kumar for availing the departmental facilities and administrative help. My sincere gratitude to past and present Departmental Post Graduate Conveners (DPGC), Profs. P.M. Shirage and Rupesh S. Devan and Dr. Mrigendra Dubey for their timely help regarding Ph.D. related administrative activities. I am also thankful to other faculties from the MEMS department, especially Prof. Santosh S. Hosmani for his profound and knowledgeable lectures on “*Concepts in Materials Science*” in COEP (I was his student during my Master’s at COEP), which were really helpful for the deep understanding of the subject. I (rather we, a batch of 36) really enjoyed his lectures even if they were scheduled

between 1400 to 1600 hours after a lunch break. I am also very grateful to Ph.D. seminar progress committee (PSPC) members Dr. Jayaprakash Murugesan and Dr. Satyajit Chatterjee for their constructive comments and suggestions for improving the quality of the work.

My sincere gratitude to all the technical and administrative staff of the department of MEMS and Sophisticated Instrument Center (SIC). The helping nature of Mayur sir on professional and personal front is appreciable. I am thankful to him for giving the training on SEM and other departmental facilities and help in conducting practical for MM:251 course. I am also grateful to Shubham sir for his help in conducting the tension test on the samples from the other departments. I am thankful to Kinny sir and Dr. Radhe Shyam Ji for allowing me the unlimited access to AFM/PFM facility. I am also indebted to the MEMS office staff Brijesh sir and Mukesh sir for being the needful for administrative activities.

I also would like to extend my gratitude to Dr. B. Praveen Kumar, Scientist-F, ARDE, DRDO, Pune for providing us with the materials to perform the experiments and his helpful attitude for providing the technical information about the same. In February 2021, we were successful in fetching the CSIR-SRF grant and thankful to the CSIR-HRDG unit. Thanks are also due to Dr. Sunil Kumar, Department of MEMS, IIT Indore for providing the access to d_{33} measurements, helpful discussions and generous suggestions on the XRD studies. I also would like to extend my heartfelt gratitude to Prof. U. Ramamurty, NTU Singapore for initially helping us with the nanoindentation facility. Still, I used to read his publications (even if not related to indentation mechanics) and try to sense something meaningful from them. His research attitude and passion inspire me every time. I am also indebted to Dr. Abhishek Chaturvedi, IISc Bangalore, for providing the access to the nanoindentation facility and making my IISc stay pleasant. Thanks are due to Dr. Rajesh Korla and Sairam, IIT Hyderabad for helping me to perform the nanoindentation experiments at IIT Hyderabad. Visiting IITH is always an ennobling experience. I am also thankful to Prof. Ajit R. Kulkarni and Dr. N. Shara Sowmya, IIT Bombay and Prof. Rajiv Ranjan, IISc Bangalore for the helpful discussions on the ferroelectric domains during ISMANAM 2019 at Chennai. The friendly attitude of Prof. Kulkarni always allowed me to eat out his brain on the discussions related to kinetics of ferroelectric domains.

Without the healthy atmosphere in research lab/group, someone's aim of achieving the doctorate is merely impossible. I thank all my Mechanics of Materials lab members (I call them MoMies including me) who made my stay pleasant in the lab. The discussion both technical and non-technical with Tulika and Abhinav were helpful for the improving the

understanding. Particularly the discussion related to high strain rate experiments with Tulika helped me for preparing for the postdoc interviews. I also thank Abhinav for discussing his work on BMG and NG (though not related my area except the indentation mechanics). What can I say about Raineesh...? I must admit, still I am learning and acquiring some presentation skills from him. The discussion related to dislocations and twins were really helpful. Discussing the culture and beauty of Kerala with him and gossips about the superstars Mohanlal and Mammooty helped to recharge my mind whenever I was feeling exhausted. Meanwhile, he was surprised and shocked to hear that I know all the Malayalam actors and actresses and watched almost all their movies (this is true). Chaitanya, Yashwant and Vartika are among the sincere juniors. I would also like to thank the past MoMies Harshal, Chetan, Janmejai and Mohit for their help.

I am thankful to the seniors Dr. Prateek (Pat) Bhojane, Dr. Maniprabhu, and Dr. Ashish Shukla for their unconditional advice. I also would like to thank contemporaries Sheetal Ji, Digvijay, Aditya, Reliance, Sandeep, Achyuth, Mahesh, Sangram, Nagaraju, Siddhartha, Sushmita, Yeeshu, Mahendar, Vishesh, Narasimha, Sarathkumar, Subhash, Sidram, Kishor, Vaibhav, Palash Ji, Gupta Ji, Jaychandran and Manikandan, while Vikesh, Ankush, Hitesh, Ramanand, Prathamesh and Manish are among the helpful juniors. The discussion with Manish on Pb-free piezoceramics helped in profound understanding of the subject. The discussions with Sheetal Ji on high entropy alloys and postdoc opportunities on every morning walk were amazing. Special thanks to Manoj and his wife and her sisterly affection and unconditional support. They treated me and my wife as their own. Especially, the time spent with kutty (little) Vallabh (Golya) will last long forever.

I am also grateful to Dr. G.A. Ramadass, Director NIOT Chennai (then group head DST) for his support. My sincere gratitude to Mr. N.R. Ramesh, Mr. P. Muthuvel and Mr. Muthukrishna Babu for their encouraging words. I also extend my warm regards to Mr. A.A. Gnanaraj, Mr. S. Rajesh and Mrs. K. Amudha (they were my immediate superior officers cum colleagues cum mentors). Especially the heartfelt support and help from Mr. Gnanaraj was commendable. The discussion both technical (mining) and non-technical with Amudha and Rajesh over a cup of soup at IIT colony and a plate of chilly idly at Aarya Bhavan was amazing. Mr. Rajesh is an encyclopedia and I explored most of the Chennai with him after office hours. Especially, I enjoyed the street food hot idly and rawa dosai with him and feels me the real South Indian test (as I am a great foodie). I recall that time as “KCT” (King of Chennai times). I also take the opportunity to thank my contemporaries at NIOT Sriram

(Annayya), Nitin, Shyam, Hema, Survindar (Paaji) and Dinesh sir. I still remember the words of Sriram *“If you work hard that doesn’t mean, you will get it and if somebody doesn’t work that doesn’t mean he/she will not get it”*. Shyam is a car/automobile astrologer. Spending quality time with Nitin was a cherish experience. We four me, Nitin, Rajesh and Amudha were the default companions at movies, Domino’s, Sub Way and Sarvana Bhavan. My warm regards to Mr. Janarthanan and Mr. Pranesh, and entire crew of Deep Sea Mining department.

I am also thankful to Profs. R.S. Pawar, R.S. Khaparde, D.D. Pawar and P.R. Cheke (my B.E. project advisor), P.B. Lagdive, A.S. Gadgaj and Mr. Amar Babar for their help and guidance during my B.E. On a lighter note, the friendly career guidance by Prof. D.D. Pawar, particularly about Varroc plant-5 and Endurance (yes... these two are his favourite industries) was admirable. The discussion with Prof. Khaparde (both technical and non-technical) were amazing. I am fortunate to have my B.E. friends, Badal (his funny jokes), Rajesh (I am still missing his abusive words), Sachin, Tushar, Dattatray, Prashant, Girijram, Vikas, Pranav, Abhilash, Mohit, Nandan, Shekhar, Ashish, Anil, and Krishna.

The following quote by C.S. Lewis is dedicated to all my school and childhood friends: *“Friendship is unnecessary, like philosophy, like art.... It has no survival value; rather it is one of those things which give value to survival”*. First and foremost, I would like to thank school friends Narendra, Satyabhushan and Kuldeep (we are the four musketeers) for their support and wishes. We have closely seen each other’s struggle. Kuldeep was the companion for movies, particularly at Amba-Apsara, breakfast at Gulabrao hotel and anna dosa centre, lunch and dinner, for four years in Aurangabad. While the discussion related to jobs, vacancies and politics with Narendra, particularly at Deccan bridge was an ennobling experience. Satyabhushan is a sincere UPSC aspirant as well and discussion on Indian polity, current affairs and geography enriched my existing knowledge. My deepest regards to Nilesh as well. We two were among the back-benchers. I also extend my gratitude to Sohan, Drs. Sushil and Ashish, Sachin, Rohan, Shrikant, Prakash (Balu), Abhijit, Mahesh, Amar, Rishikesh, Pramod, Mukesh, Prathamesh, Aditya, Jayant (salute to you Assistant Collector and the way you have achieved it in difficult circumstances) and our entire Champavati 2007 batch (in case I left with anybody). Following this, the next quote by Scott Hayden is dedicated to all the school teachers; *“Teachers have 3 loves: love of learning, love of learners and the love of bringing first two loves together”*. I am grateful to Ghadge sir, Chausalkar sir, Deshpande sir, Varape sir, Pawar sir, Pimpalkar sir, Mahajan sir, Chaunde sir, Dhakane sir (particularly his style of asking question), Jadhav madam, Kulkarni madam and among others

for their school level training that they gave me which makes me what I am. Especially, the English language and grammar from Chausalkar sir, learning Sanskrit from Ghadge sir was an amazing experience (I am still his favourite student), mathematics and geometry from Pimpalkar sir and Chemistry from Chaunde sir enriched my knowledge.

I would also like to thank Shivakant, Ganesh, Ranjit, Gaurav, Ajay, Sachin Chopade and Sandip (all are Pune friends). Particularly, Shivkant's help in difficult time and discussing different stuffs with him was dignifying. The timely help from Sachin Chopade is also appreciated. Ranjit's advice on investing in stock market and his profound knowledge about the stocks is helping me now a days to survive, as I am enjoying easy and profitable returns on it.

"Life is what happens, when you are busy in making other plans" by John Lennon. This quote fits here to describe one's Ph.D. life (boring, frustrating and even depressing) when all the bad/worst things happen together. My case is not different by any means. In my initial days, we struggled a lot to get even a single microstructure of PMN-PT or PZT. My heartfelt thanks to Indian Cinema. It (only a good movie) worked like Yoga or meditation for me in my critical time. Every day I used to watch at least one good movie (even if it is late night at 0200 hours to complete the work, I watched a movie). I am also thankful to actors Dr. Shahrukh, Amitabh Ji, Amir, Salman, Irfan, K.K. Menon, Nasiruddin Shah, Dilip Kumar, Rajesh Khanna, Vinod Khanna, Raj Kumar, Nana Patekar and Saurabh Shukla for their contribution to Bollywood. I also extend my gratitude to Mohanlal and Mammooty (I often discuss about these two with Raineesh) for their contribution to Malayalam cinema, while Dr. Chiyan Vikram, Rajani sir, Thalapathy Vijay, Thala Ajith Kumar, Makkal Selvan Vijay Sethupathi, Suriya and Vishal are among Tamil entertainers. Thank you Akkineni Nagarjuna gaaru, Mega star Chiranjeevi gaaru, Power star Pawan Kalyan gaaru, Stylish star Allu Arjun, Natural star Nani, Young Tiger Jr. NTR, Prince Mahesh babu, Ram Charan, Rebel star Prabhas and Bramhanandam gaaru (for his expression, because comedy is the difficult part) for their nice contribution to Telugu cinema. Thanks are due to Kiccha Sudeep, Arjun Sarja, Puneeth Rajkumar and Yash for entertaining with the Kannada films.

Its family time now.... I would like to thank my mother for her care and prayers, which makes me to achieve this mile stone. My deepest gratitude to the man behind all these silences, my father. I thank my grandpa for his guidance, his funny jokes and for training me in Carrom (I lost to him every time), whom I lost in 2018. With deepest gratitude, I thank my in-laws for believing in me and their heartfelt wishes. I also would like to thank my caring

sister Dr. Anjali and brother-in-law Dr. Suraj and their family. Especially, little Spruha (Bholu) for coming in our life and making us happy through childish activities on video call. I thank Nagnath too for his brotherly affections. My heartfelt gratitude to all my family members for their affection and lovingly nature. Last but not least, my deepest and heartfelt gratitude to Nisha (Selfie) for taking care of me, my diet and her understanding. I also would like to acknowledge her arranging the references and making efforts for type setting and format related issues for the timely completion of this thesis in short span of time.

SYNOPSIS

The technology at the driving seat of the 21st century is, of course, “*the nanotechnology*”, and the design of nanostructured materials with novel microstructural features for micro-electro-mechanical systems (MEMS) and nano-electro-mechanical systems (NEMS) is going to play a decisive role in the progress of this century. Of the several materials used in MEMS and NEMS, piezoelectric materials are arguably gaining wide attention in applications such as actuators, sensors and energy harvesting due to their inherent polarization and electro-mechanical coupling characteristics. The word “*piezo*” in Greek means “*to press*”, and “*electric*” has a Latin root “*electrum*” implies the flow of electrons. Therefore, piezoelectric materials are a class of materials that exhibit electricity upon external mechanical pressure (or vice versa), which further intermingles the electric and elastic fields. This piezoelectric behaviour is often seen in 20 non-centrosymmetric crystals (out of 32 crystal classes) whose centre of positive and negative charges are spaced apart, thereby creating a dipole effect to exhibit piezoelectricity. However, of the 20 piezoelectric crystals, 10 crystals show reorientation of dipoles upon an external electric field, known as “*ferroelectric crystals/materials*”, while the orientation of dipoles in the remaining 10 crystals can be changed upon an external thermal gradient, often known as “*pyroelectric crystals/materials*”. Therefore, essentially all the ferroelectric and pyroelectric crystals are piezoelectric. However, the converse is not true.

The piezoelectric materials used in actuators mainly contain ceramics of various compounds and exhibit ABO_3 type perovskite structure, with “*A*” atoms occupying the corners of the unit cell, “*O*” atoms at the centre of six faces and “*B*” atoms at the centre of the unit cell. These perovskites exhibit rhombohedral, monoclinic, and tetragonal crystal structure below the Curie temperature (T_c) based on their stoichiometric composition with respect to morphotropic phase boundary (MPB), thereby exhibiting the piezoelectric phase, while they possess a cubic symmetry above the T_c indicating the paraelectric behaviour of the material, shown in Fig.1. Conventional piezoceramics such as lead zirconate titanate (PZT) and barium titanate (BT) have a limited operating temperature range (i.e., 130 to 200 °C). Therefore, self-heating during service due to high frequency electrical and mechanical stresses may induce microstructural incompatibilities in the materials, which further deteriorates the electro-mechanical properties. However, the high-temperature applications of these piezoceramics in fuel injection systems, military impact fuzes, and structural health monitoring demand thermal and electro-mechanical stability. One way to mitigate this

problem is to alter the intrinsic microstructural features that span across μm sized grains to nm sized ferroelectric domains, presented in Fig. 2. Further, the addition of aliovalent acceptor/donor cations are reported to enhance the thermal stability (i.e., increase in T_c) of Pb-based and Pb-free piezoceramics.

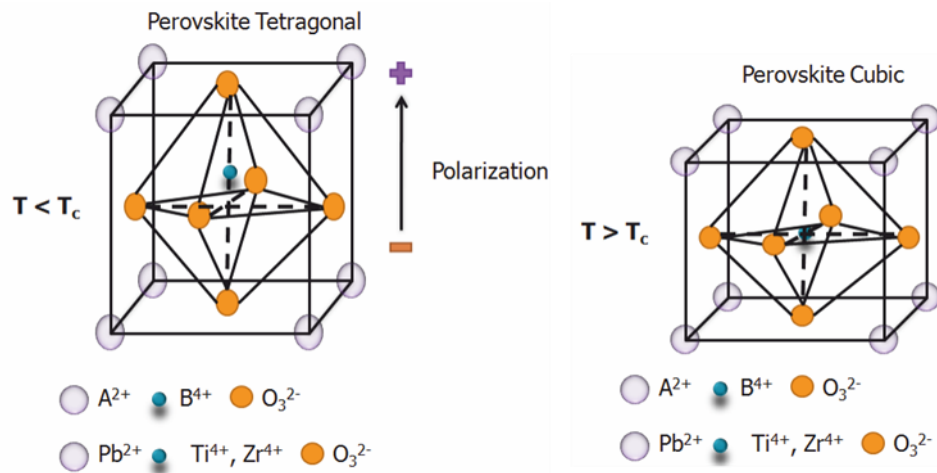


Fig. 1 Schematic representation of ABO_3 type perovskite unit cell of PZT piezoceramics.

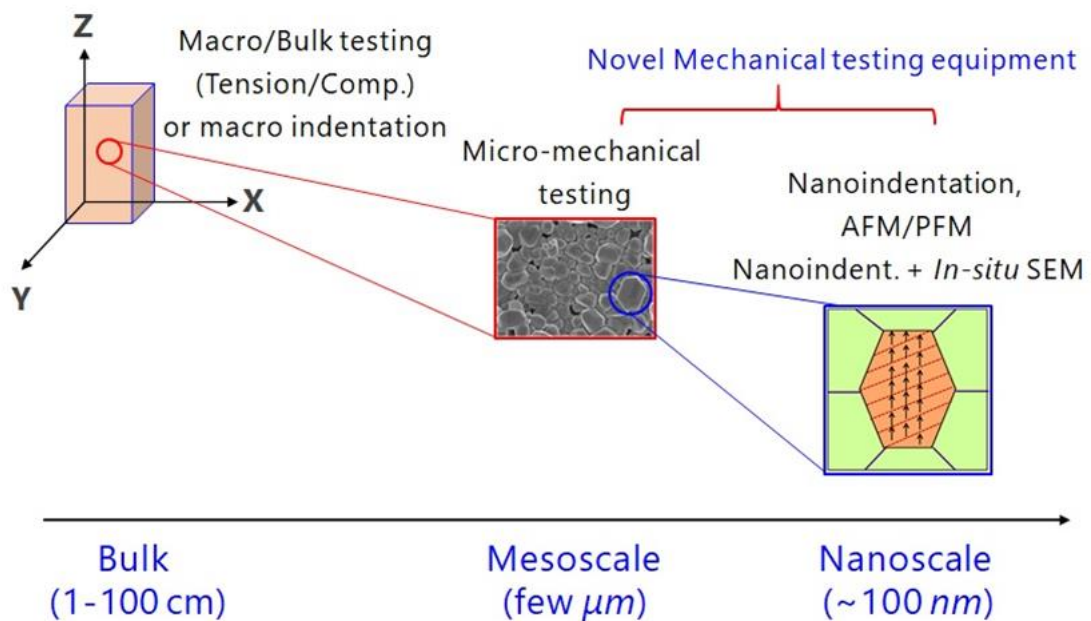


Fig. 2 Representation of microstructural length scales in piezoceramics.

Keeping this in view, polycrystalline systems of $(\text{PbZr}_{0.52}\text{Ti}_{0.48}\text{O}_3)$ (PZT undoped), $\text{Pb}_{0.98}\text{K}_{0.02}(\text{Zr}_{0.47}\text{Ti}_{0.51}\text{Al}_{0.02})\text{O}_3$ (hard-doped PZT, abbreviated as PZT-H) and $\text{Pb}_{0.98}\text{La}_{0.02}(\text{Zr}_{0.47}\text{Ti}_{0.51}\text{Nb}_{0.02})\text{O}_3$ (soft-doped PZT, abbreviated as PZT-S), $0.90(\text{PbMg}_{0.33}\text{Nb}_{0.66}\text{O}_3) - 0.10(\text{PbTiO}_3)$ (PMN-PT), and $0.94(\text{NaK}_{0.5}\text{Nb}_{0.5}\text{O}_3) - 0.06(\text{NaTaO}_3)$ (NKN-NT- Pb-free) have been systematically investigated to understand the role of intrinsic microstructural length scales on their mechanical and piezoelectric behaviour.

In piezoceramics, the region of directionally aligned dipoles along distinct polarization directions is known as “*ferroelectric domains*”. The previous and recent studies [Mehta and Virkar, 1990, Haertling, 1999 and Wang et al., 2021] have indicated that the ferroelastic effects such as the orientation of the ferroelectric domains and domain wall (DW) motion have a pronounced influence on the piezoelectric and mechanical response of the piezoceramics.

Domain engineering (DE) is a technique used to enhance the electro-mechanical properties of piezoceramics by altering the ferroelectric domain configuration i.e., size, orientation, and interdomain spacing. Several ways of implementing DE technique in piezoceramics are as follows; (i) modifying the crystal structure *via* aliovalent cation doping, (ii) controlling the grain size, (iii) growing the nano-patterns of semiconductor thin films, (iv) altering remnant polarization, (v) imposing mechanical stresses during poling and (vi) controlled thermal annealing. Of all these techniques obtaining the different ferroelectric domain configurations *via* thermal annealing is quite economical and less tedious. However, one of the downsides of thermal annealing is the temperature-induced depolarization in the material. Therefore its use as a DE is limited, despite the applications of piezoceramics at elevated temperatures. Several studies have been highlighted the importance of DE, particularly on single-crystal piezoceramics, as the use of single-crystals rule out the complex interaction between ferroelectric domains and grain boundaries. However, most of the practical applications of piezoelectric materials are based on ceramic polycrystals. Therefore, one of the objectives of the present thesis is to investigate the effects of below- and above- T_c thermal annealing on the ferroelectric domain configurations in polycrystalline piezoceramics. The piezoresponse force microscopy (PFM) is used to probe the differences in local ferroelectric domain configurations in PZT-H, PZT-S and PMN-PT, while piezoelectric charge coefficient, d_{33} studies are performed to probe the bulk response in other piezoceramics. The implementation of DE technique *via* selective annealing revealed the following observations; (i) distinct peak splitting is observed in X-ray diffraction (XRD) patterns of annealed samples, indicating the change in the ferroelectric domain structure (ii) annealed samples showed a transgranular cracking within the grains, (iii) degree of crystalline disorderness of ferroelectric domains increases with respect to annealing temperature and (iv) the d_{33} , converse piezoelectric charge coefficient, d_{33}^* and remanent strain, ε_r decreases with an increase in annealing temperature.

Though there have been several studies on understanding the role of domain configurations on electro-mechanical coupling characteristics, limited attention is given to investigate their influence on mechanical properties. During service, piezoceramics often experience variable mechanical loading conditions, particularly at high frequency, and it is important to understand the role of ferroelectric domain configurations on the mechanical behaviour of piezoceramics. Of the several mechanical properties, indentation hardness, H , a quick estimate of material's resistance to the plastic deformation, is the widely preferred technique due to the following advantages; (i) it requires a small volume of the test specimen and (ii) it is non-destructive (at small indentation loads, as the indentation impressions are confined to the smaller areas). Recent developments in instrumented indentation techniques (IIT) such as nanoindentation allows to obtain indentation load, P vs. displacement, h data from which it is possible to determine H and elastic modulus, E . During nanoindentation, the fully plastic regime in the material can be achieved even at low P (from several μN to few mN). However, there is no comprehensive understanding of role of microstructural features on the H of piezoceramics despite the few studies which were focused towards understanding the fracture response (R-curve behaviour) [Mehta and Virkar, 1990 and Webber et al., 2009].

The limited bulk indentation experiments (mostly with the spherical indenters on PZT and BT samples) and nanoindentation simulations have observed that indentation response in piezoceramics is dependent on nature of the material (i.e., poled vs. unpoled), and type of indenter (i.e., electrically conducting vs. insulating) [Ramamurty and co-workers, 1999, 2009 and Cheng and Venkatesh, 2012]. However, these experiments are mostly used for validating the continuum level simulations and ignores the role of microstructural parameters (e.g., ferroelectric domain configurations and DW motion) on H . It is difficult to probe the mechanical properties with bulk indentation tests as the high indentation loads, often leads to cracking of materials. Therefore, it would be interesting to examine the effect of different ferroelectric domain configurations on H of the polycrystalline piezoceramics both at micro and nanoscale. The ferroelectric domain configurations are systematically varied by annealing the as poled (AP) piezoceramics at below and above the T_c , referred to as STD and ATD, respectively. The different ferroelectric domain configurations are characterized directly using piezoresponse force microscopy (PFM), which is also reflected in their d_{33}^* values. Following this, nano and micro indentation experiments are performed on AP, STD and ATD samples and the nanohardness is determined using Oliver and Pharr method while the microhardness is obtained from Meyer's approach. In PZT (undoped), PZT-H, PZT-S, and NKN-NT samples, H follows the following trend, $H_{ATD} > H_{STD} > H_{AP}$, while in PMN-

PT, it follows the trend as; $H_{STD} > H_{ATD} > H_{AP}$. In all the samples, the H decreases with increasing P , often known as indentation size effects (ISE). The underlying mechanisms responsible for the enhancement and anomalies in H and the occurrence of ISE are discussed in detail.

ISE in crystalline materials is attributed to indenter geometry, presence of high plastic strain gradients, nucleation of discrete deformation bands underneath the indenter, the surface free energy of the material, and high dislocation nucleation stresses. However, limited nanoindentation experiments on piezoceramics [Gharbi et al., 2009] have indicated that the presence of ISE in contact stiffness is mainly due to the strain gradient polarization (i.e., flexoelectricity). The ISE is analyzed with the help of analytical, empirical or semi-empirical models which enables to determine the load (or size) dependent and independent H from the indentation data. The critical analysis of nanoindentation data using classical Meyer's law, Hays-Kendall (H-K) approach, elastic recovery (ER) model, proportion specimen resistance (PSR) model, and modified PSR (MPSR) model lead to the following observations; (i) ISE in H of all the samples are sensitive to the differences in ferroelectric domain configurations, (ii) all the models show good agreement with the nanoindentation data, and (iii) true (or load independent) H values obtained from the ER, PSR and MPSR models are comparable to those obtained from nanoindentation experiments (i.e., machine H values).

During indentation, the material in the vicinity of the impression undergoes a significant amount of deformation, which may alter the ferroelectric domain configurations [Schneider et al., 2005, Park et al., 2007 and Wang et al., 2021]. Further, beyond a critical load, indentation causes cracking at the imprint corners, altering the texture of ferroelectric domains and is expected to influence the crack growth characteristics. To date, there is no clear experimental evidence on the ferroelectric domain configurations in the vicinity of the indentation imprint and near the advancing crack. In the present thesis, ferroelectric domain orientation maps and butterfly curves (remnant strain, ϵ_r vs. electric field, E) (Fig. 3) are generated in the vicinity of the indentation zone and crack front leads to the following observations; (i) The ferroelectric domains change their texture in the vicinity of the indentation zone, thereby exhibiting indentation-induced domain switching (IIDS), (ii) The ferroelectric domains ahead of the crack tip undergo a considerable change in domain configurations and some of which, based on the location, re-orient back to the initial configurations while some remain inelastic, (iii) The indentation fracture toughness, K_{IC}^i

determined from the indentation imprints showed distinct dependence, albeit small, on the ferroelectric domain configurations.

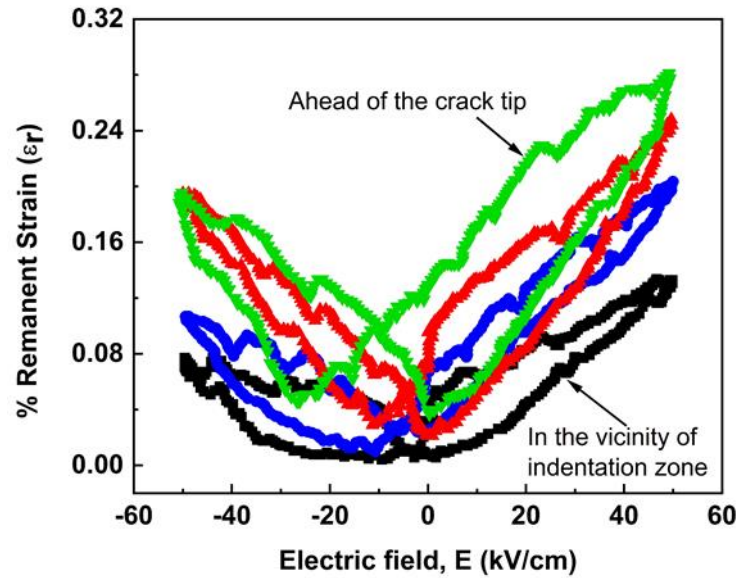


Fig. 3 The butterfly loops collected in the vicinity of the indentation zone and crack front.

In summary, the present thesis essentially centered on two parts; (a) altering the intrinsic microstructural features (e.g., ferroelectric domain configurations) of piezoceramics *via* selective annealing and (b) investigating the role of ferroelectric domain configurations on the mechanical and piezoelectric properties at micro and nanoscale.

The organization of the present thesis is as follows;

CHAPTER 1 presents the introduction of piezoelectric materials, their crystal structure, and related fundamentals responsible for piezoelectric properties. Role of the complex interaction between the intrinsic microstructural features, particularly at lower length scales in the deformation behaviour of piezoelectric materials is difficult to understand and explained as the motivation for the present work. Keeping this in view, all the possible prior literature is presented with a focus on the theories that tailor the piezoelectric and dielectric properties in general and mechanical properties in particular, while specifically emphasizing the mechanical response of the piezoceramics under different structural states. Further, a brief overview of the nanoscale characterization techniques such as nanoindentation and PFM is presented. Finally, possible gaps in previous literature are identified to define the objectives for the present thesis.

CHAPTER 2 describes the effect of selective annealing (DE technique) on the mechanical properties of PMN-PT and NKN-NT piezoceramics with different ferroelectric domain configurations. The underlying mechanisms of enhancement in mechanical properties in light of crystal structure and ferroelectric behaviour are discussed in detail.

CHAPTER 3 presents the important results regarding the role of different ferroelectric domain configurations and aliovalent dopants on the mechanical behaviour of PZT (undoped), PZT-H and PZT-S. The toughening mechanisms such as IIDS and domain rearrangement in the vicinity of the indentation site are explained with the help of ferroelectric domain orientation maps. Butterfly curves (remnant strain, ϵ_r vs. electric field, E) are used to rationalize the results.

CHAPTER 4 deals with the description of observed ISE in nanoindentation H of PMN-PT, PZT-H and PZT-S using the mechanistic models. The outcomes of the mechanistic modelling and origins of ISE in H are further explained in light of the differences in ferroelectric domain configurations.

CHAPTER 5 presents the conclusions from the present work. The last part of this chapter gives certain directions for the future work from the mechanisms proposed in this study.

List of Publications and Conferences

Publications in refereed journals

[1] **V.S. Kathavate**, H. Sonagara, B. Praveen Kumar, I. Singh, K. Eswar Prasad, Direct observations of changes in ferroelectric domain configurations around the indentation and ahead of the crack front in soft-doped PZT, **Materialia**, 19 (2021) 101191.

<https://doi.org/10.1016/j.mtla.2021.101191>

[2] **V.S. Kathavate**, H. Sonagara, B. Praveen Kumar, I. Singh, K. Eswar Prasad, Tailoring the nanomechanical properties of hard and soft PZT via domain engineering by selective annealing, **Materials Today Communications**, 28 (2021) 102495 (I.F.- 3.38).

<https://doi.org/10.1016/j.mtcomm.2021.102495>

[3] **V.S. Kathavate**, B. Praveen Kumar, I. Singh, K. Eswar Prasad, Analysis of indentation size effects in nanoindentation hardness in polycrystalline PMN-PT piezoceramics with different domain configurations, **Ceramics International**, 47 (09) (2021) 11870-11877 (I.F.- 4.52). <https://doi.org/10.1016/j.ceramint.2021.01.027>

[4] **V.S. Kathavate**, H. Sonagara, B. Praveen Kumar, I. Singh, K. Eswar Prasad, Role of domain configurations on the mechanistic modelling of indentation size effects (ISEs) in nanohardness of Hard and Soft PZT piezoceramics, **International Journal of Advances Engineering Science and Applied Mathematics**, 13(01) (2021) 63-78.

<https://doi.org/10.1007/s12572-020-00279-1>

[5] **V.S. Kathavate**, B. Praveen Kumar, I. Singh, K. Eswar Prasad, Effect of sub and above Curie temperature annealing on the nanomechanical properties of PMN-PT piezoceramics, **Ceramics International** 46(08) (2020) 12876-12883 (I.F.- 4.52).

<https://doi.org/10.1016/j.ceramint.2020.01.155>

[6] **V.S. Kathavate**, B. Praveen Kumar, I. Singh, Palash Roy Chaudhary, K. Eswar Prasad, Nanoindentation response of PZT and NKN-NT piezoceramics, **Journal of Coupled Systems and Multiscale Dynamics**, 6(04) (2018) 291-299.

<https://doi.org/10.1166/jcsmd.2018.1175>

Conferences

[1] **V.S. Kathavate**, H. Sonagara, B. Praveen Kumar, I. Singh, K. Eswar Prasad, Role of domain configurations on the nanomechanical properties of PZT piezoceramics, **58th National Metallurgist Day-Annual Technical Meet (NMD-ATM 2020)** held at Indian Institute of Technology Bombay (IIT Bombay) (India) (23-26 February, 2021). **(Best oral presentation awards in the category of Advances in Materials Science and Engineering)**

Session Chair: Prof. Indradev Samajdar, IIT Bombay

[2] **V.S. Kathavate**, B. Praveen Kumar, I. Singh, K. Eswar Prasad, Description of indentation size effects (ISEs) in piezoceramics: Analysis of nanoindentation hardness, **83rd Annual Session of Indian Ceramics Society**, CSIR-NIIST, Thiruvananthapuram (India) (11-12 December, 2019).

Session Chair: Prof. Ajit R. Kulkarni, IIT Bombay and Retd. Prof. K.G.K. Warrior, CSIR-NIIST, Thiruvananthapuram

Significant Awards, Honors and Achievements

[1] **Best Oral Presentation Award**

This award is presented for the best oral presentation in the category **“Advances in Materials Science and Engineering”** at 58th National Metallurgist Day Conference held at IIT-Bombay during 23-26 February, 2021.

[2] **CSIR-SRF Award**

This fellowship is awarded by Council of Scientific and Industrial Research (CSIR), a premier R&D institute of Government of India to bright men and women for training in methods of research. The award was conferred on 08 February, 2021.

TABLE OF CONTENTS

DEDICATION AND ACKNOWLEDGEMENTS	iv
SYNOPSIS	xiv
LIST OF FIGURES	xxvii
LIST OF TABLES	xxxiv
NOMENCLATURE	xxxvi
ACRONYMS (if any)	xxxix
CHAPTER 1: Introduction	1-32
1.1. Piezoelectricity: Fundamentals, Applications and Advances	1
1.1.1. Pb vs. Pb-free piezoceramics	4
1.2 Microstructural length scales in piezoelectric materials	6
1.2.1. Ferroelectric activities: Role of ferroelectric domains and domain walls	8
1.3. Domain engineering	11
1.4. Mechanisms of enhanced electro-mechanical response in piezoceramics	18
1.5. Small scale characterization techniques	21
1.5.1. Nanoindentation studies on piezoceramics	22
1.5.2. Nanoindentation	23
1.5.3. Piezoresponse force microscopy (PFM)	28
1.6. Scope and objectives of the present Thesis	30
1.7. Organization of the Thesis	31

CHAPTER 2: Effect of sub and above Curie temperature annealing on the mechanical properties of PMN-PT and NKN-NT piezoceramics	33-54
2.1. Introduction	33
2.2. Materials and Experiments	35
2.2.1. Materials	35
2.2.2. X-Ray Diffraction: Phase and crystal structure analysis	36
2.2.3. Indentation experiments	36
2.2.4. Microstructure and ferroelectric domain characterization	37
2.3. Results and Discussion	37
2.3.1. Characterization of crystal structure	37
2.3.2. Characterization of microstructure: Composition, grain size and porosity	40
2.3.3. Analysis of indentation load, P vs. displacement, h curves	42
2.3.4. Variation of H with respect to P_{max} : Indentation size effects (ISE)	46
2.3.5. Role of crystal structure and crystal orientation on the mechanical properties	49
2.3.6 Role of ferroelectric domain configurations on mechanical properties	49
2.4. Summary	54
CHAPTER 3: Mechanisms of enhanced mechanical response of polycrystalline hard and soft- doped PZT via domain engineering technique	55-95
3.1. Introduction	55
3.2. Materials and Experiments	58

3.2.1. Materials and sample preparation	58
3.2.2. X-ray Diffraction (XRD) and Microstructural Characterization	60
3.2.3. Mechanical characterization: Nano and microindentation experiments	60
3.2.4. Domain visualization - Piezoresponse Force Microscopy (PFM)	61
3.3. Results and Discussion	62
3.3.1. Effect of DE on crystal structure and microstructures of PZT-U, PZT-H and PZT-S	62
3.3.2. Effect of annealing on the ferroelectric domain configurations	70
3.3.3. Analysis of indentation load, P vs. displacement, h curves	73
3.3.4. Indentation size effect (ISE) in H	78
3.3.5. Effect of microstructural features on H of PZT-H and PZT-S	80
3.3.6. Effect of ferroelectric domain configurations on H and indentation fracture toughness, K_{IC}^i	81
3.3.7. Direct observations of ferroelastic activities in indentation vicinity	85
3.3.8. Role of characteristics behaviour (<i>hard and soft vs. undoped</i>) on H	92
3.4. Summary	95
CHAPTER 4: Analysis of indentation size effects (ISE) in nanoindentation hardness of polycrystalline piezoceramics with different ferroelectric domain configurations	96-128
4.1. Introduction	96
4.2. Experimental Procedure	98
4.2.1. Materials and Ferroelectric Domain Configurations	98

4.2.2. Nanoindentation experiments	98
4.3. Results and Discussion	99
4.3.1. Analysis of P vs. h curves and H of different ferroelectric domain configurations	99
4.3.2. Assessment of nanoindentation data: Mechanistic modelling of ISE	103
4.3.2.1. Meyer's Law and Hays-Kendall (H-K) model	103
4.3.2.2. Elastic Recovery (ER) model	109
4.3.2.3. Proportion specimen resistance (PSR) model	114
4.3.2.4. Modified proportion specimen resistance (MPSR) model	122
4.4. Summary	127
CHAPTER 5: Conclusions and Future Scope	129-132
5.1. Summary and Conclusions	129
5.2. Directions for Future work	132
APPENDIX 1	133-140
BIBLIOGRAPHY	141-165

LIST OF FIGURES

Fig. 1.1	Schematic representing piezoelectric effect (a) direct (sensor) effect and (b) converse (actuator) effect.....02	02
Fig. 1.2	Schematic representation of ABO ₃ type perovskite unit cell with illustration for BT piezoceramics (a) cubic perovskite (when $T > T_c$) and (b) tetragonal perovskite ($T < T_c$).....04	04
Fig. 1.3	Schematic representation of intrinsic microstructural length scales present in the piezoceramics.....07	07
Fig. 1.4	(a) Schematic representing the ferroelectric domains in a ferroelectric crystal and (b) representation of 180° and 90° DW (the deformation due to formation of 90° DW is shown by δ).....09	09
Fig. 1.5	(a) TEM micrograph of $a - a$ ferroelectric domains with a period of 1 μm [Adopted from Chou et al. 2009], (b) high resolution TEM (HRTEM) image of ferroelectric domain patterns with a period of ~ 17 nm in 3% La doped BiFeO ₃ -PbTiO ₃ thin film [Adopted from Freitas et al., 2014], (c) ferroelectric domain activities probed <i>via</i> CGM during local poling in single-crystals LN (\otimes and \odot represents the downward and upward polarization, respectively) [Adopted from Esfahani et al. 2017] and (d) conductivity map showing interaction between different ferroelectric domains and DW obtained from X-PEEK in ErMnO ₃ [Adopted from Schaab et al. 2014].....10	10
Fig. 1.6	(a) Cross-hatched ferroelectric domain structure in Pb ₅ Ge ₃ O ₁₁ produced by a copper mesh electrode (first attempt of DE) [Adopted from Newnham, 1975] and (b) Periodic ferroelectric domain structure in LN crystals with a period ~ 20 μm [Adopted from Ming et al., 1982].....11	11
Fig. 1.7	(a) Optical microscope image of spherical ferroelectric domain patterns with size down to ~ 200 nm with a period ranging from 0.5-2 μm in LN crystals [Adopted from Grilli et al., 2005] and (b) Ferroelectric domain patterns on as polished (001) PZN-PT wafer showing [110] strip and [100] braided patterns [Adopted from Ranjan et al., 2004].....14	14

Fig. 1.8	A strip-like ferroelectric domain structures observed on the surface of $[001]_c$ PZN-6%PT single crystal with a period of $\sim 10 \mu\text{m}$ at four different poling conditions (a) $T=160 \text{ }^\circ\text{C}$, $E_p= 18 \text{ kV/cm}$, (b) $T=170 \text{ }^\circ\text{C}$, $E_p= 9 \text{ kV/cm}$, (c) $T=168 \text{ }^\circ\text{C}$, $E_p= 11 \text{ kV/cm}$ and (d) $T=166 \text{ }^\circ\text{C}$, $E_p= 10 \text{ kV/cm}$ [Adopted from Xiang et al., 2010].....	15
Fig. 1.9	Variation in d_{33} and k_{33} values with respect to ferroelectric domain size [Adopted and reproduced from Xiang et al., 2010].....	16
Fig. 1.10	(a) Patterned nanodomain structure [Adopted from Chang et al., 2018] and (b) microdomain structure [Adopted from Luo et al., 2020] obtained after grating nanoelectrodes of (Ti/Au-MnO _x) on PMN-PT single crystals.....	16
Fig. 1.11	Typical phase diagram for PZT clearly showing the MPB (subscript C, R, M, and T represents the cubic, rhombohedral, monoclinic and tetragonal phase of PZT, respectively) [Adopted from Noheda et al., 2000].....	18
Fig. 1.12	MPB phase diagram of KNN based BNT-BKT ternary system [Adopted from Fan et al., 2007].....	19
Fig. 1.13	Direct observations of ferroelectric domains beneath the indentation zone (a) topographic image with contour plots, (b) ferroelectric "a" domains in x-direction and (c) ferroelectric "a" domains in y-direction in the indentation zone [Adopted from Schneider et al. 2005].....	23
Fig. 1.14	Schematic representing the geometry and shape of the (a) Berkovich [Adpoted from Bharat Bhushan, 2017], (b) conical [Adpoted from Wang, 2016] and (c) cube-corner indenter [Adpoted from Wang, 2016].....	24
Fig. 1.15	(a) Graphical representation of the quantities used in the nanoindentation data analysis on P vs. h curve and (b) Schematic representation of the section of indentation surface profile [Adopted and Redrawn from Oliver and Pharr (1992)].....	26
Fig. 1.16	Representative P vs. h curves indicating the (a) <i>pop-in</i> events shown by arrows in (100) face of Form I aspirin and (b) <i>pop-out</i> event shown by arrows in (100) face of single-crystal Si during nanoindentation [Adopted from Ramamurty and Jang, 2014].....	28

Fig. 1.17	Schematic representing the working principle of PFM [Courtesy: National Institute of Standards and Technology, Gaithersburg, USA] URL: https://www.nist.gov/image/afmschematic	28
Fig. 1.18	Schematic representation of (a) in-plane deformation, (b) in-plane piezoresponse, (c) out-of-plane deformation and (d) out-of-plane piezoresponse of a ferroelectric material [Adopted from PFM Wikipedia] URL: https://en.wikipedia.org/wiki/Piezoresponse_force_microscopy].....	29
Fig. 1.19	Predictive capabilities of PFM (a) ferroelectric domain imaging (50 nm thick PbTiO ₃ thin films) [Adopted from Gruverman et al., 2019] and (b) property manipulation via ferroelectric domain switching and probing the electro-mechanical response [Adopted from Kalinin et al., 2010].....	30
Fig. 2.1	XRD patterns of AP, STD and ATD samples of (a) PMN-PT and (b) NKN-NT. The subscript “p-c” and “T” represents the pseudo-cubic and tetragonal phase, respectively.....	38
Fig. 2.2	Representative SEM images indicating the microstructures of (a) AP, (b) STD (0.6T _c), (c) STD (0.8T _c) and (d) ATD samples of PMN-PT piezoceramics.....	40-41
Fig. 2.3	Representative SEM images indicating the microstructures of (a) AP and (b) ATD samples of NKN-NT piezoceramics.....	42
Fig. 2.4	Representative <i>P vs. h</i> curves for (a) AP, (b) STD (0.6T _c), (c) STD (0.8T _c) and (d) ATD samples of PMN-PT piezoceramics.....	43-44
Fig. 2.5	Representative <i>P vs. h</i> curves for (a) AP and (b) ATD samples of NKN-NT piezoceramics.....	45
Fig. 2.6	Variation of micro and nanoindentation <i>H</i> with respect to <i>P_{max}</i> for all the samples of (a) PMN-PT and (b) NKN-NT piezoceramics.....	47
Fig. 2.7	Representative SEM images demonstrating the self-assembled ferroelectric domains after wet etching of (a) AP, (b) STD (0.8T _c) and (c) ATD samples of PMN-PT (magnified view of the ferroelectric domains is shown in inset).....	50-51

Fig. 2.8	Representative PFM (PR signal) topographic images of self-assembled nanodomains in (a) AP, (b) STD (0.8T _c) and (d) ATD samples of PMN-PT piezoceramics. Piezoelectrically active region (high contrast region) is shown in in dotted rectangle	51
Fig. 2.9	Summary of variation in H and d_{33} values with respect to the different structural states for (a) PMN-PT and (b) NKN-NT piezoceramics.....	52
Fig. 2.10	Schematic representing the ferroelectric domain configurations in AP, STD and ATD samples of piezoceramics as a result of thermal treatment.....	52
Fig. 3.1	Schematic showing the doping, sintering, and annealing procedure for obtaining different domain configurations in PZT-H and PZT-S.....	60
Fig. 3.2	Representative XRD patterns of AP, STD and ATD samples of (a) PZT-U, (b) PZT-H and (c) PZT-S. Evaluation of symmetric/asymmetric peak splitting is shown in Appendix 1 (Fig. A1a-b). The subscript “R” and “T” represents the rhombohedral and tetragonal phase, respectively.....	64-65
Fig. 3.3	Representative SEM images indicating the microstructures of (a) AP, (b) STD and (c) ATD samples of PZT-U.....	67
Fig. 3.4	Representative SEM images indicating the microstructures of (a) AP, (b) STD and (c) ATD samples of PZT-H.....	68
Fig. 3.5	Representative SEM images indicating the microstructures of (a) AP, (b) STD and (c) ATD samples of PZT-S.....	69
Fig. 3.6	Representative PFM phase images, domain quantification plots, and butterfly and hysteresis curves of (a-c) AP, (d-f) STD and (g-i) ATD samples of PZT-H, respectively.....	71
Fig. 3.7	Representative PFM phase images, domain quantification plots, and butterfly and hysteresis curves of (a-c) AP, (d-f) STD and (g-i) ATD samples of PZT-S, respectively.....	72
Fig. 3.8	Representative P vs. h curves for (a) AP, (b) STD and (c) ATD samples of PZT-U.....	73-74

Fig. 3.9	Representative P vs. h curves for (a) AP, (b) STD and (c) ATD samples of PZT-H.....	75-76
Fig. 3.10	Representative P vs. h curves for (a) AP, (b) STD and (c) ATD samples of PZT-S.....	76-77
Fig. 3.11	Variation of H with respect to P_{max} in AP, STD and ATD samples of (a) PZT-U, (b) PZT-H and (b) PZT-S indicating the indentation size effect (ISE). The schematics shown in the circles represent the differences in domain density, interdomain spacing, and domain mobility of AP, STD and ATD samples of PZT-H and PZT-S.....	78-79
Fig. 3.12	Variation of K_{IC}^i with respect to different structural states in (a) PZT-H and (b) PZT-S (values within $\pm 5\%$ error limit).....	83
Fig. 3.13	Representative optical microscope image of Vickers indentation imprint (at $P_{max} = 20$ N) on AP sample of PZT-S.....	86
Fig. 3.14	(a) Schematic representing the plan of domain imaging around and ahead of the indentation crack, (b) representative PFM phase images at various locations as per the scheme shown in (a).....	86-87
Fig. 3.15	Variation in ϵ_r with respect to E_p at various locations around and ahead of the indentation crack (a) A to D, (b) E-H and (c) I to K as per the plan shown in Fig. 3.14(a).....	88-89
Fig. 3.16	Variation of H (from nanoindentation) with different structural states in PZT-U, PZT-H and PZT-S.....	92
Fig. 3.17	Schematic representing the orientation and arrangement of defect dipoles and oxygen vacancies in (a) AP, (b) STD and (c) ATD samples of PZT-H, PZT-S and undoped PZT. The size, interdomain spacing, defect dipoles and oxygen vacancies increases with increase in annealing temperature.....	94
Fig. 4.1	Variation of nanoindentation H with respect to h_c for AP, STD and ATD samples of (a) PMN-PT, (b) PZT-H and (c) PZT-S piezoceramics. All the materials exhibit typical ISE in H	100-101

Fig. 4.2	Representative plots of $\ln P_{max}$ vs. $\ln h_c$ data according to the Meyer's model for AP, STD and ATD domain configurations of (a) PMN-PT, (b) PZT-H and (c) PZT-S, (d) Variation in Meyer's index, "n" with respect to different structural states of PMN-PT, PZT-H and PZT-S.....	104-105
Fig. 4.3	Representation of the Hays-Kendall model on the plots of P_{max} vs. h_c^2 for AP, STD and ATD samples of (a) PMN-PT (b) PZT-H and (c) PZT-S.....	108-109
Fig. 4.4	Dependency of indentation size, h_c on $P_{max}^{1/2}$ according to the ER model for AP, STD and ATD samples of (a) PMN-PT, (b) PZT-H and (c) PZT-S piezoceramics	110-111
Fig. 4.5	Representation of typical ISE in true hardness values for AP, STD and ATD samples of (a) PMN-PT, (b) PZT-H and (c) PZT-S piezoceramics according to the ER model. (H_1)- Load-dependent hardness, (H_2)- Load-independent hardness).....	112-113
Fig. 4.6	Representation of the nanoindentation data on P_{max}/h_c vs. h_c scale to the PSR model for AP, STD and ATD samples of (a) PMN-PT, (b) PZT-H and (c) PZT-S piezoceramics.....	115-116
Fig. 4.7	Representation of typical ISE in true hardness values for AP, STD and ATD samples of (a) PMN-PT, (b) PZT-H and (c) PZT-S piezoceramics according to the PSR model. (H_1)- Load-dependent hardness, (H_2)- Load-independent hardness).....	118-119
Fig. 4.8	(a-c) Representation of ISE on size effect curve according to the PSR model for AP, STD and ATD samples of PMN-PT, PZT-H and PZT-S, respectively clearly showing the ISE boundary and (d) schematic representation of the PSR effective zone and h_{crit} beyond which these ISE are ineffective.....	120-121
Fig. 4.9	Representation of the nanoindentation data on P_{max} vs. h_c scale to the MPSR model for AP, STD and ATD samples of (a) PMN-PT, (b) PZT-H and (c) PZT-S piezoceramics.....	122-123

Fig. 4.10 Representation of typical ISE in true hardness values for AP, STD and ATD samples of (a) PMN-PT, (b) PZT-H and (c) PZT-S piezoceramics according to the MPSR model. (H_1)- Load-dependent hardness, (H_2)- Load-independent hardness).....125-126

APPENDIX 1

Fig. A1 (a) Vector representation of ferroelectric domains in PbTiO₃ thin film visualized using PFM phase images [Adpoted from Kalinin et al., 2006] (b) schematic representing the contributions of cantilever deflection.....133

Fig. A2 Representative XRD pattern showing the peak splitting in (a) PZT-H and (b) PZT-S134

Fig. A3 Representative mapping of the elemental constituents present in PZT-H obtained through EDS (scanned area is shown in inset) as well as stoichiometric %wt proportions are presented in the pie chart.....135

Fig. A4 Representative mapping of the elemental constituents present in PZT-S obtained through EDS (scanned area is shown in inset) as well as stoichiometric %wt proportions are presented in the pie chart.....136

Fig. A5 Variation in A_m with respect to V_B at various locations around and ahead of the indentation crack (a) A to D, (b) E-H and (c) I to K as per the plan shown in Fig. 3.14(a)137-138

Fig. A6 Representative area function calibration curve obtained before performing nanoindentation experiments on piezoceramics. The polynomial fit ($R^2 \sim 1$) indicates the zero deviation from of the ideal geometry of the Berkovich indenter.....139

Fig. A7 Representation of Meyer's index, "n" values on size effect curve.....140

LIST OF TABLES

Table 1.1	Summary of crystal symmetry, d_{33} and k_{33} values of various Pb and Pb-free piezoceramics and relaxor ferroelectrics.....	06
Table 1.2	Summary of compositions at MPB, d_{33} and T_c values of various Pb and Pb-free piezoceramics.....	20
Table 2.1	Summary of XRD results, d_{33} values and d_{avg} values for all the samples of PMN-PT and NKN-NT piezoceramics.....	39
Table 2.2	Summary of H and elastic recovery (H/E), χ values obtained from micro and nanoindentation experiments for all the samples of PMN-PT and NKN-NT piezoceramics.....	48
Table 3.1	Summary of the XRD results, d_{33} and d_{33}^* values obtained for AP, STD and ATD samples of PZT-U, PZT-H and PZT-S.....	66
Table 3.2	Summary of d_{avg} and H values obtained for AP, STD and ATD samples of PZT-U, PZT-H and PZT-S.....	66
Table 3.3	Summary of c , E , H and K_{IC}^i values for AP, STD and ATD samples of PZT-H and PZT-S.....	82
Table 3.4	Comparison of the K_{IC} values (with ± 5 % error) of PZT-H and PZT-S and other Pb-based and Pb-free piezoceramics (from the literature) to those obtained in the present work. (PZT-S: Soft-PZT, PZT-H: Hard-PZT (doping element)).....	84
Table 3.5	Summary of the d_{33}^* and ε_r values around and ahead of the indentation crack for AP samples of PZT-S as per the scheme shown in Fig. 3.14a.....	89
Table 4.1	Summary of the descriptive parameters obtained from Meyer's law and Hays-Kendall model for all the samples of PMN-PT, PZT-H and PZT-S piezoceramics.....	107

Table 4.2	Summary of the descriptive parameters and true hardness values obtained from the ER model for all the samples of PMN-PT, PZT-H and PZT-S piezoceramics. (H_1)- Load-dependent hardness, (H_2)- Load-independent hardness).....	112
Table 4.3	Summary of the descriptive parameters and true hardness values obtained from the PSR model for all the samples of PMN-PT, PZT-H and PZT-S piezoceramics. (H_1)- Load-dependent hardness, (H_2)- Load-independent hardness).....	115
Table 4.4	Summary of the descriptive parameters and true hardness values obtained from the MPSR model for all the samples of PMN-PT, PZT-H and PZT-S piezoceramics. (H_1)- Load-dependent hardness, (H_2)- Load-independent hardness).....	124

NOMENCLATURE

ABBREVIATIONS AND SYMBOLS (UNITS)

1-D	One dimensional
2-D	Two dimensional
3-D	Three dimensional
A	Power-law coefficient (Oliver and Pharr method) (mN/nm^m)
a	Contact radius (nm)
ABO_3	Perovskite structure
A_c	Contact area (nm^2)
$A(h_c)$	Area function in nanoindentation experiments
A_m	Piezoelectric amplitude (in Amplitude vs. bias response) (pm)
A_p	Projected area of elastic contact (nm^2)
B	Descriptive parameter from Hays-Kendall model (mN/nm^2)
Ba^{2+}	Barium ions
C	Coulomb
cm	Centimeter (cm)
D_i	Output electric displacement vector (C/m^2)
d_{ijk}	Third order piezoelectric charge coefficient tensor- Strain based (C/N)
d_{kij}	Third order piezoelectric charge coefficient tensor- Stress based (C/m^2)
d_{33}	Piezoelectric charge coefficient in (3-3 mode) (pC/N)
d_{15}/d_{24}	Piezoelectric charge coefficient in (1-3 mode) (pC/N)
E	Elastic modulus (GPa)
E_c	Coercive field (kV/cm)
E_{ac}	Activation electric field (kV/cm)
E_d	Depolarization field (kV/cm)
E_k	External applied electric field (V/m)
E_p	Applied external electric field during poling (kV/cm)
E_{red}	Reduced elastic modulus (GPa)
G	Shear modulus (GPa)
H	Hardness (GPa)
H_m	Meyer's hardness (GPa)
H_1	True hardness (load-dependent) (GPa)

H_2	True hardness (load-independent) (GPa)
h	Indentation depth (nm)
h_c	Contact depth/indentation size (nm)
h_c^*	Corrected indentation size (nm)
h_{crit}	Critical indentation size (nm)
h_f	Final indentation depth (nm)
h_i	Instantaneous indentation depth (nm)
h_{max}	Maximum indentation/penetration depth (nm)
K_{IC}^i	Indentation fracture toughness ($\text{MPa}\cdot\text{m}^{1/2}$)
k_{33}	Electro-mechanical coupling coefficient in (3-3 mode)
k_{31}	Electro-mechanical coupling coefficient in (1-3 mode)
m	Power-law index/exponent from the loading curve (Oliver and Pharr method)
mN	Millinewton (mN)
N	Newton (N)
n	Power-law index/exponent from the unloading curve (Oliver and Pharr method)
“n”	Meyer’s index/exponent
nm	Nanometer (nm)
O^{2-}	Oxygen ions
P	Indentation load
P-h	Indentation load vs. displacement curve
P_{max}	Maximum indentation load (mN or N)
P_{min}	Minimum test load from Hays-Kendall model (mN)
P_r	Remanent polarization (C/m^2)
P_s	Saturation polarization (C/m^2)
Pb^{2+}	Lead ions
Q_m	Mechanical quality factor
R^2	Correlation coefficient / goodness of curve fit / regression coefficient
R_A	Ionic radius of A-site atom in ABO_3 perovskite
R_B	Ionic radius of B-site atom in ABO_3 perovskite
R_O	Ionic radius of O-site atom in ABO_3 perovskite
S	Unloading stiffness (mN/nm)
s	Second (s)
S_{ij}	Output mechanical strain tensor

T_c	Curie temperature
Ti^{4+}	Titanium ions
T_{jk}	External applied mechanical stresses (MPa)
Zr^{2+}	Zirconium ions

GREEK SYMBOLS

α	Descriptive or proportionality constant in Meyer's law (mN/nm^n)
α_0	Descriptive parameter from the modified proportion specimen resistance model (mN)
α_1	Descriptive parameter from the proportion specimen resistance model (mN/nm)
α_2	Descriptive parameter from the proportion specimen resistance model (mN/nm^2)
β	Constant depends on indenter geometry (empirical value- 0.75 for Berkovich indenter)
γ	Descriptive parameter from the elastic recovery model (mN/nm^2)
η	Power law coefficient from Oliver and Pharr equation
ε	Constant related to geometry of the indenter in the elastic recovery model
ε_d	Dielectric constant
ε_p	Piezoelectric strain (%)
ε_r	Remanent strain (%)
ε_s	Spontaneous strain (%)
σ_a	Applied stress (MPa)
σ_c	Coercive stress (MPa)
ρ_r	Relative density (%)
ν	Poisson's ratio
θ	PFM Phase angle ($^\circ$)
2θ	Diffraction angle in XRD experiments ($^\circ$)

ACRONYMS

A.C.	Alternating current (A)
AFM	Atomic force microscope
AP	As-Poled samples
ATD	Above- T_c depoled samples
BCT	Barium calcium titanate
BT/BaTiO ₃	Barium titanate
CD	Completely depoled (same as ATD) samples
CGM	Charge gradient microscopy
D.C.	Direct current (A)
DE	Domain engineering
ER	Elastic recovery model
FIPR	Electric field induced polarization rotation
GND	Geometrically necessary dislocations
G.T.	Goldschmidt Tolerance factor
H-K	Hays Kendall model
HV	Vickers Hardness (GPa)
KNN	Potassium sodium niobate
LN/LiNbO ₃	Lithium niobate
LT/LiTaO ₃	Lithium tantalate
MEMS	Micro-electro-mechanical system/device
MgO	Magnesium oxide
MPB	Morphotropic phase boundary
MPSR	Modified proportion specimen resistance model
NEMS	Nano-electro-mechanical system/device
O&P	Oliver and Pharr method
PD	Partially depoled (same as STD) samples
PDZ	Plastically deformed zone
PFM	Piezoresponse force microscope
PLM	Polarized light microscopy
PMN-PT	Lead magnesium niobate-lead titanate
PRT	Polarization rotation technique

PSR	Proportion specimen resistance model
PZT	Lead zirconate titanate
PZT-H	Hard doped-Lead zirconate titanate
PZT-S	Soft doped-Lead zirconate titanate
PZT-U	Undoped lead zirconate titanate
SEM	Scanning electron microscope
SONAR	Sound Navigation and Ranging
SSD	Statistically stored dislocations
SS-PFM	Piezoresponse force spectroscopy
STD	Sub- T_c depoled samples
STEM	Scanning transmission electron microscopy
TEM	Transmission electron microscope
V-PFM	Vector piezoresponse force microscopy
X-PEEK	X-ray photoemission electron microscopy
XRD	X-ray diffraction
ZnO	Zinc oxide

CHAPTER 1

INTRODUCTION

Abstract: In this chapter, a brief overview of the theory of piezoelectricity, piezoelectric materials, and related fundamentals are presented with a focus on applications of piezoelectric materials in miniaturized devices. The microstructural length scales in piezoelectric materials are described. The prior literature on the mechanisms of enhancement in the electro-mechanical properties of various Pb and Pb-free piezoceramics is briefly discussed. Various small-scale characterization techniques used in this thesis are explained. The last part of the chapter presents the significant research gaps from the previous literature and states the scope of the present thesis.

1.1. Piezoelectricity: Fundamentals, Applications and Advances

Piezoelectricity was first discovered in the year 1880 by the French physicists Profs. Jacques Curie and Pierre Curie (Curie brothers) who found that certain class of crystals exhibit electricity upon external mechanical pressure [Curie and Curie, 1880]. The Greek route “*piezo*” means “*to press*”, and the Latin route “*electrum*” has the meaning “*flow of electrons*”. The Curie brothers thought that this rise of piezoelectricity would be a “*direct effect*” because of the electric potential generated due to a change in mechanical strain. In the following year, 1881, Gabriel Lippmann [Lippmann, 1881] made a twist in the piezoelectricity saga by stating that the same crystals can also exhibit mechanical strain in response to an applied external electric field, known as the “*converse effect*”, thereby confirming that piezoelectricity can indeed work in either direction. The direct and converse piezoelectric effects are schematically represented in Fig. 1.1. However, not necessarily that all the crystals exhibit piezoelectricity. Only those who have their centre of positive and negative charges/ions spaced apart (i.e., non-centrosymmetric) exhibit piezoelectric behaviour. There are 20 non-centrosymmetric classes of natural crystals (For ex., quartz, tourmaline, and Rochelle salt) that possess piezoelectric properties [Neumann, 1885]. Soon after the initial discovery, the excitement about piezoelectricity has disappeared in the materials community for nearly the next 20 years due to the complexities associated with the mathematical formulation of piezoelectricity theory. In 1910, Voigt proposed the electro-mechanical coupling constitutive equations for direct and converse piezoelectric effect, presented in eq. 1 and 2, respectively with 18 macroscopic piezoelectric coefficients [Voigt, 1910];

$$D_i = d_{ijk}T_{jk} \quad (1)$$

$$s_{ij} = d_{kij}E_k \quad (2)$$

where, D_i and s_{ij} represent output electric displacement vector and mechanical strain, respectively, while T_{jk} and E_k are externally applied mechanical stress and electric field, respectively. The terms d_{ijk} and d_{kij} specifies the 3rd order direct and converse piezoelectric charge coefficient tensor, respectively.

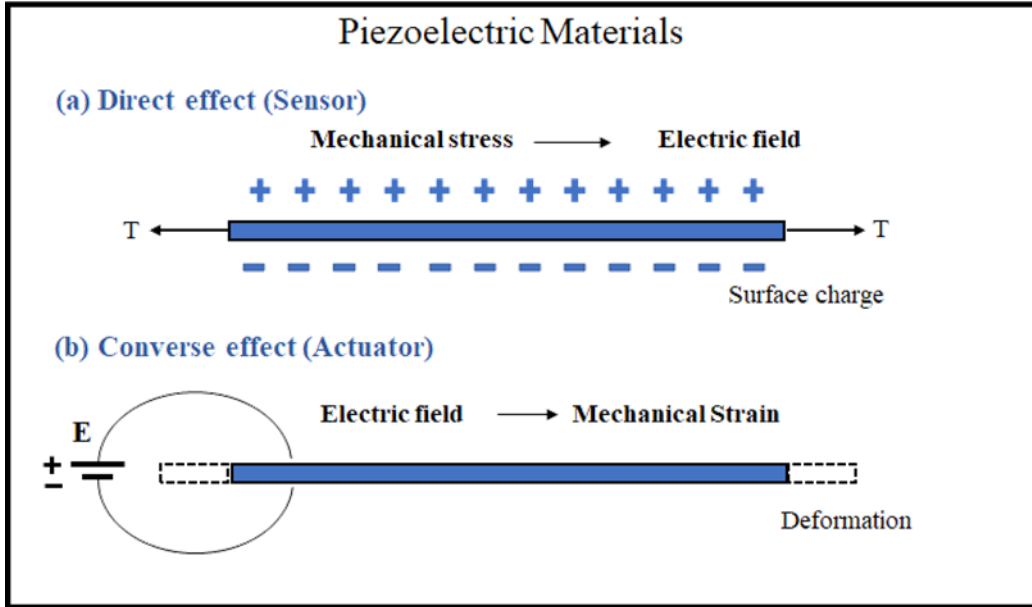


Fig. 1.1 Schematic representing piezoelectric effect (a) direct (sensor) effect and (b) converse (actuator) effect.

Of the 20 non-centrosymmetric piezoelectric crystals, 10 crystals possess a unique polar axis whose spontaneous polarization change with a temperature gradient, known as “*pyroelectric crystals*”. While spontaneous polarization of other 10 crystals can be changed/reoriented under the influence of an external electric field, known as “*ferroelectric crystals*”. Therefore, all the pyroelectric and ferroelectric crystals exhibit piezoelectricity, while the converse is not true. These piezoelectric crystals are thought to be used for commercial applications in the late 1910s, wherein Paul Langevin introduced thin quartz film in SONAR for submarine applications. Since then, there is a great deal of interest among the materials community to bring these piezo crystals in various industrial applications such as sensors, transducers, energy harvesting, electric controllers, thermostats, and the defence and security sectors. Over the last two decades, there is a significant increase in the usage of piezo crystals in micro-electro-mechanical systems (MEMS) and nano-electro-mechanical systems

(NEMS). These piezo-based MEMS and NEMS devices are extensively used in communication, underwater acoustics, naval hydrophones, and medical diagnosis devices.

Natural piezoelectric crystal such as quartz does not exhibit high piezoelectric properties, and hence the piezoelectric materials used in commercial applications are centred on using a ceramic compound that has ABO_3 type perovskite crystal structure (as shown in Fig. 1.2). These piezoelectric ceramics (hereafter referred to as piezoceramics) are the ferroelectric materials in which the ferroelectric effect disappears (i.e., paraelectric state) above the Curie temperature, T_c . However, below the T_c , the transition from paraelectric to ferroelectric state occurs, thereby inducing a polar axis with spontaneous polarization. Barium titanate-BT ($BaTiO_3$) is the first ferroelectric material used as piezoceramics which exhibit cubic crystal structure above T_c with Ba^{2+} , and Ti^{4+} ions are in equilibrium with O^{2-} ions (Fig. 1.2), while below T_c , Ba^{2+} and Ti^{4+} ions are displaced relative to O^{2-} ions, thereby creating a dipole (i.e., elongated c -axis) as shown in Fig. 1.2. In the late 1950s, the discovery of lead zirconate titanate (PZT), a solid solution of $PbZrO_3$ - $PbTiO_3$, bypassed the inherent disadvantages such as low T_c (~ 120 °C) associated with BT, thereby exhibiting superior and stable piezoelectric properties [Jaffe, 1971]. After 1960, significant efforts are directed to enhance the thermal stability of BT and PZT *via* compositional modifications, which also resulted in an improved piezoelectric response. This ultimately reflected in introducing new aliovalent cation (acceptor/donor) doped PZTs (i.e., hard-doped and soft-doped), particularly for the high-temperature applications in military impact fuzes and fuel injection systems.

Meanwhile, generous progress has been made to develop the other Pb-based relaxor ferroelectrics such as $PbMgO_3$ - $PbTiO_3$ (PMN-PT), PZN-PT, $BiScO_3$ - $PbTiO_3$ (PBST), and $Pb(Yb-Nb)O_3$ - $PbTiO_3$ (PYB-PT) with enhanced piezoelectric and dielectric properties to suit them for automotive and aerospace sensors applications. Relaxor ferroelectric materials are a special class of ferroelectrics that possess high dielectric constant, ϵ_d and large electrostriction (the elastic deformation in dielectrics due to small displacement in ions under electric field) than normal ferroelectrics. Compared to normal ferroelectrics, relaxor ferroelectrics has the following distinct characteristics; (a) diffused phase transition and (b) frequency dispersion [Yang et al., 2003]. The former is an indication of gradual ferroelectric to paraelectric phase transformation (in normal ferroelectrics, this transformation is rapid/sharp), while the latter one represents the shift in dielectric peak at high temperature with the increase in frequency. Unlike normal ferroelectrics, a well-defined T_c does not exist in relaxor ferroelectrics. The experiments of Park and Shrout (1997) indicated that the ultra-high piezocharge coefficient, d_{33} (~ 2500

pC/N), electro-mechanical coupling coefficient, k_{33} (~ 90%), and large piezoelectric strain, ϵ_p (~ 1.7%) with dielectric loss < 1% in (001) relaxor PZN-PT single-crystals. The d_{33} values of (001) crystallographically oriented PZN-PT were five times higher than the undoped/pristine PZT. The ferroelectric domain switching though 71° is expected in (001) rhombohedral PZN-PT crystal at the higher coercive field, E_c (> 30 kV/cm), which results in hysteresis free behaviour and consequently stable ferroelectric domain structure. Therefore, the superior piezoresponse of relaxor PZN-PT could be attributed to the ferroelectric domain stability along the (001) rhombohedral phase. However, one of the downsides of Pb-based piezoceramics is the involvement of toxic Pb, which is hazardous from an environmental standpoint and hence, the focus is in the discovery and development of Pb-free piezoceramics as an alternative.

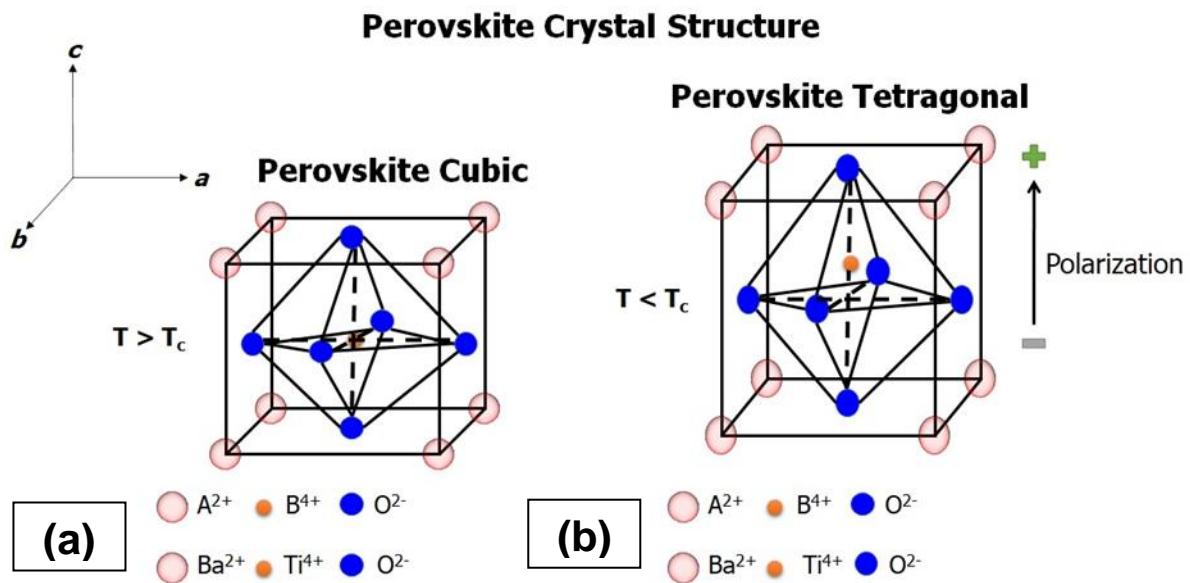


Fig. 1.2 Schematic representation of ABO_3 type perovskite unit cell with illustration for BT piezoceramics (a) cubic perovskite (when $T > T_c$) and (b) tetragonal perovskite ($T < T_c$).

1.1.1. Pb vs. Pb-free piezoceramics

The development of Pb-free piezoceramics started in the late 1960s, just one decade after the invention of PZT. However, initially because of their poor piezoelectric properties, the focus of researchers never shifted from the contemporary PZT. After groundbreaking research at Toyota R&D Laboratories, Japan, [Saito et al. \(2004\)](#) showed that La, Ta, and Sb modified potassium-sodium-niobate (KNN), a Pb-free solid solution, exhibits electro-mechanical properties comparable to PZT. The Pb-free piezoceramics can be classified into three distinct categories: (i) perovskite BT, BiNaTiO_3 (BNT), BiKTiO_3 (BKT) and KNaNbO_3 (KNN), (ii) non-perovskite Bi layered structured ferroelectric (BLSF) and (iii) non-perovskite tungsten

bronze type ferroelectrics. Thus far, several studies demonstrated the ability of KNN and BCT based Pb-free piezoceramics to replace PZT or other Pb-based piezoceramics in high-temperature applications due to their high T_c (~ 400 to 460 °C) [Birol et al., 2006, Du et al., 2006, Minhong et al., 2011, Yang et al., 2011, Tan et al., 2020, Redhu et al., 2021; among others]. The comparison of d_{33} , crystal symmetry, and k_{33} values of typical Pb and Pb-free piezoceramics and relaxor ferroelectrics is shown in Table 1.1.

Pristine or undoped Pb-free piezoceramics do not exhibit piezoelectric properties comparable to PZT. Hence, chemical modifications and stoichiometric control are necessary to make them competitive to PZT or other Pb-based piezoceramics [Rödel et al., 2009 and Shibata et al., 2018]. For instance, comparatively lower density, ρ (~ 4.51 g/cm³, i.e., $\sim 45\%$ of PZT), moderate piezoelectric properties (mechanical quality factor, $Q_m \sim 500$ to 800 , $k_{33} \sim 0.41$ - 0.52 and $d_{33} \sim 110$ - 135 pC/N) and good temperature stability ($T_c \sim 250$ to 650 °C) make KNN based piezoceramics suitable for high-frequency imaging applications [Rödel et al., 2009 and Levassort et al., 2011]. Further, NBT based/modified piezoceramics showed a giant piezoelectric strain ε_p upto $\sim 0.45\%$ (at 80 kV/cm) and potential candidates for actuator applications where the high electric field-induced giant strain is required [Jo et al., 2012, Liu and Tan, 2016]. Another Pb-free piezoceramic of particular interest in high-temperature applications is the multiferroic BiFeO₃ in either bulk or thin-film form [Rojac et al., 2016 and Wang et al., 2018].

However, the three decisive factors in the discovery and understanding of the piezoelectric effect in ceramics are (i) high dielectric constant, (ii) a ferroelectric effect, and (iii) poling process. During the poling process, dielectric materials show a linear polarization in response to an applied electric field, E_p . However, piezoelectric materials are the class of dielectrics that generate the spontaneous strain, ε_s in addition to the polarization by the application E_p . The generation of ε_s is mainly due to the relative displacement of cation and anion in ABO₃ lattice, which further forms the dipoles in crystals, a ferroelectric effect (as explained earlier in Fig. 1.2). Therefore, it would be appropriate to state that the above three factors govern the electro-mechanical behaviour of piezoceramics at the macroscopic level. Besides this, several microstructural aspects, particularly at lower length scales, control the electro-mechanical response in piezoceramics and are explained in the below section.

Table 1.1 Summary of crystal symmetry, d_{33} and k_{33} values of various Pb and Pb-free piezoceramics and relaxor ferroelectrics

Material	Point group/ crystal symmetry	d_{33} (pC/N)	k_{33} (%)	Reference
α -Quartz crystal	32	2.31	10	Bechmann (1958)
BT	$6mm$	191	50	Bechmann (1956)
BT (hydrotherm. synth.)	$6mm$	460	42	Karaki et al. (2007)
BT Single crystal	$4mm$	90	55	Zgonik et al. (1994)
LN Single crystal	$3m$	6	17	Smith and Welsh (1971)
LT Single crystal	$3m$	5.7	14	Smith and Welsh (1971)
PZT	$6mm$	223	67	Jaffe (1971)
(001) poled PMN-PT	$4mm$	2820	94	Zhang et al. (2001)
(001) poled PZN-PT	$4mm$	2890	94	Zhang et al. (2002)
KNN (pure)	$Amm2$	279	46	Li et al. (2011)
KNN (LT doped)	$Amm2$	300-416	62	Gao et al. (2011)
$(Bi_{1/2}Na_{1/2})TiO_3$	$R3c$	98	48	Nagata et al. (2004)
$(Na_{1-x}K_x)_{0.5}Bi_{0.5}TiO_3$	$R3m$	192	32	Zhang et al. (2008)
BNT-BKT-BT	$P4mm$	158	25	Hu et al. (2009)
BZT-BCT	$P4mm$	620	56	Liu and Ren (2009)

1.2. Microstructural length scales in piezoelectric materials

The structural and functional properties of engineering materials strongly depend on the intrinsic microstructure, which can be controlled either during the manufacturing or post-fabrication treatment. The microstructure spans across several length scales, starting from individual atoms in the size of angstroms Å to few micron-sized grains. The mechanical properties (e.g., strength) of metals can be tailored by altering the microstructure through various strengthening mechanisms such as grain boundary strengthening, work hardening, precipitation, dispersion strengthening, etc. In piezoceramics, the characteristic length scales of the microstructure consist of grain size and morphology, ferroelectric domain orientation, domain width, and interdomain spacing, as shown in Fig. 1.3. Of all these, ferroelectric domains have a pronounced influence on the piezoelectric and mechanical response of piezoceramics. Under the application of electrical and/or mechanical loading, changes occur in

ferroelectric domain configurations leading to the alteration of their orientation and interdomain spacing, thereby causing significant hysteresis and nonlinearity in the electro-mechanical properties.

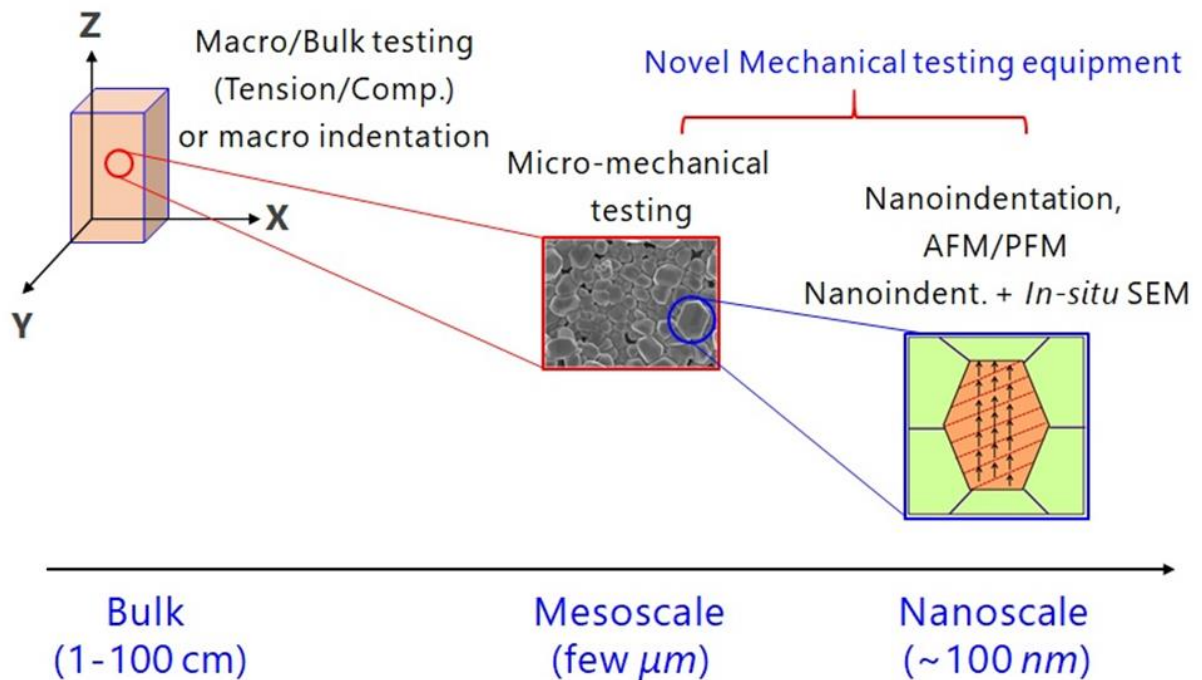


Fig. 1.3 Schematic representation of intrinsic microstructural length scales present in the piezoceramics.

Over the last three decades, a considerable number of efforts have been made to investigate the mechanical behaviour of single and polycrystalline piezoceramics using uniaxial compression, fracture, and fatigue experiments on bulk samples. Furthermore, there are focused studies to understand the effect of grain size and morphology on the electro-mechanical response of piezoceramics (discussed in detail in section 1.4). However, there are limited studies in understanding the deformation behaviour of piezoceramics of small sample volumes primarily due to the lack of experimental facilities which can apply loads in the range of few nano-Newtons (nN) and measure displacements in the order of few nm to μm as well as provide comprehensive information about the deformation events (e.g., changes in ferroelectric domain configurations) taking place at μm or sub- μm length scales. The advent of experimental techniques like nanoindentation and micro-compression combined with the piezoresponse force microscope (PFM) will enable to characterize the role of ferroelectric domain configurations on the mechanical properties of piezoceramics at small length scales. So, this

work presents a comprehensive discussion on the role of intrinsic microstructural length scales, particularly ferroelectric domain configurations, on the mechanical behaviour of piezoceramics.

1.2.1. Ferroelectric activities: Role of ferroelectric domains and domain walls

The spontaneous polarization is usually not uniformly oriented in ferroelectric crystals. For example, the spontaneous polarization in BaTiO₃ (Fig. 1.1) is oriented along the tetragonal *c*-axis, and lattice distortion is generally described as a shift in O²⁻ and Ti⁴⁺ ions with respect to Ba²⁺ ions. The lattice distortion in the ferroelectric phase induces spontaneous strain in the crystal [Damjanovic, 1998]. However, while cooling the cubic crystal through ferroelectric transition temperature, spontaneous polarization vector may orient along six possible directions (i.e., positive and negative orientations along three cubic axes) with equal probability. During this process, the electrical and mechanical boundary conditions imposed on the material are thought to control the pattern of spontaneous polarization vectors, while crystal symmetry regulates the polarization directions. The homogeneous region of crystal with the unidirectionally aligned spontaneous polarization vectors is known as ferroelectric domains in piezoceramics, shown in Fig. 1.4a. The complex interaction between the electric and mechanical fields at each grain tends to split the ferroelectric crystal into many ferroelectric domains. However, the process of switching and aligning the distinct polarization vectors in a particular direction (i.e., the direction of an applied electric field) upon an external applied electric field, E_p is known as “poling”. Note that the E_p required during poling must be higher than the coercive electric field, E_c (generally 2 times the E_c in case of piezoceramics and 1.5 times for relaxor ferroelectrics).

The ferroelectric domains can be classified into two types; (i) 180° domains and (ii) non-180° domains. The former has the polarization vectors of adjacent domains antiparallel, while the latter has polarization vectors of adjacent domains oriented at an angle other than 180° (random orientation). Randomly distributed polarization vectors induce “zero” net polarization in the material. The boundary which separates the two adjacent ferroelectric domains is known as the ferroelectric domain wall (DW). The ferroelectric DW that separate two antiparallel polarization vectors are 180° DW (also known as “ferroelectric DW”), and those which separate mutually perpendicular polarization are 90° DW (ferroelastic DW). The schematic representation of 180° DW and 90° DW is presented in Fig. 1.4b. In addition to the separation

in orientations of polarization vectors, the 90° DW also separates the strain tensor among two adjacent ferroelectric domains (hence they are ferroelastic), which is shown by the small deformation, δ in Fig. 1.4b.

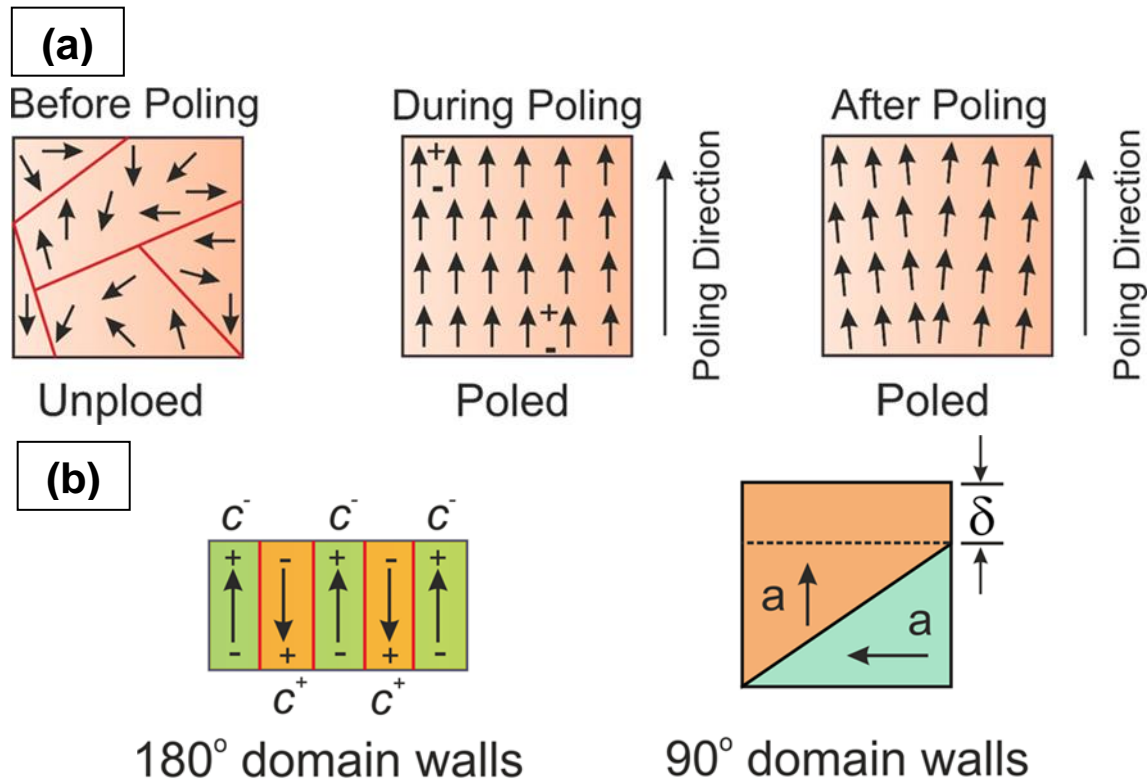


Fig. 1.4 (a) Schematic representing the ferroelectric domains in a ferroelectric crystal and (b) representation of 180° and 90° DW (the deformation due to formation of 90° DW is shown by δ).

Although piezoresponse force microscopy (PFM) and X-ray diffraction (XRD) tools are frequently used to characterize the nano-sized ferroelectric domain activities, other techniques such as transmission electron microscopy (TEM), scanning TEM (STEM) and photoemission electron microscopy (PEM) are also preferred in many instances. For instance, the TEM observations of [Line and Glass \(1979\)](#), [Stemmer et al. \(1995\)](#) and [Chou et al. \(2009\)](#) have shown that the DW size in the ferroelectric crystal may vary between 1-20 nm, as shown in Fig. 1.5a. The symmetry of the paraelectric and ferroelectric phases controls the formation of 90° DW (~ 17 nm size) in ferroelectric crystals, which further controls the ferroelectric behaviour in $\text{BiFeO}_3\text{-PbTiO}_3$ thin films (Fig. 1.5b) [[Freitas et al., 2014](#)]. Furthermore, the fast formation of screening/surface charges and ferroelectric domain kinetics during local poling is demonstrated by [Esfahani et al. \(2017\)](#) in single-crystals LN *via* charge gradient microscopy (CGM). The two adjacent ferroelectric domains with opposite polarity can be seen in Fig. 1.5c

with a period of $\sim 10 \mu\text{m}$. In another study, [Schaab et al. \(2014\)](#) illustrated the formation of 90° and 180° DW in polycrystalline ErMnO_3 ferroelectric system using X-ray photoemission electron microscopy (X-PEEM). The X-PEEM technique is found to be effective for probing the photo-induced charging effects and local variations in electronic conductance (Fig. 1.5d) which cannot be probed using PFM and XRD experiments. From the above observations, we note that the morphology and stability of ferroelectric domains and DW control the electro-mechanical behaviour in piezoceramics, and in the below section, we shed light on these aspects.

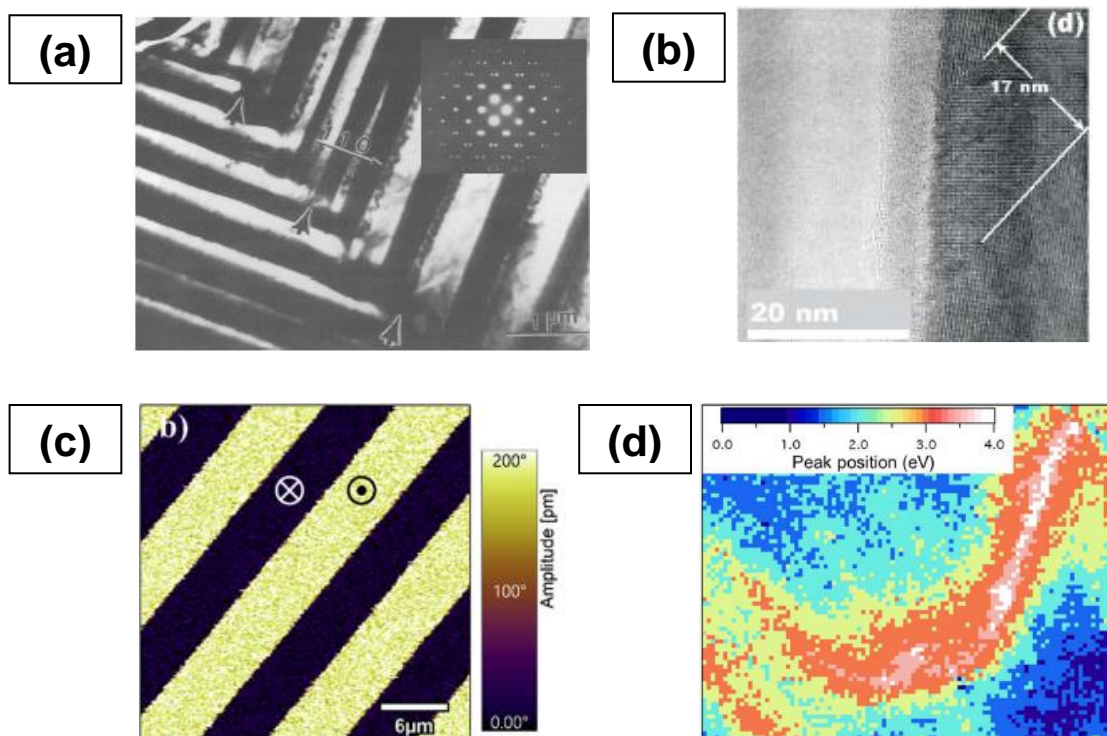


Fig. 1.5 (a) TEM micrograph of $a - a$ ferroelectric domains with a period of $1 \mu\text{m}$ [[Adopted from Chou et al. 2009](#)], (b) high resolution TEM (HRTEM) image of ferroelectric domain patterns with a period of $\sim 17 \text{ nm}$ in 3% La doped $\text{BiFeO}_3\text{-PbTiO}_3$ thin film [[Adopted from Freitas et al., 2014](#)], (c) ferroelectric domain activities probed *via* CGM during local poling in single-crystals LN (\otimes and \odot represents the downward and upward polarization, respectively) [[Adopted from Esfahani et al. 2017](#)] and (d) conductivity map showing interaction between different ferroelectric domains and DW obtained from X-PEEM in ErMnO_3 [[Adopted from Schaab et al. 2014](#)].

1.3. Domain engineering (DE)

Ferroelectric domain engineering (DE) is a branch of technology directed to the creation of stable tailored ferroelectric domain structures with periodic and/or quasi-periodic arrangement to enhance the electro-mechanical performance of commercially available piezoceramics. The idea of DE was first proposed by Robert Newnham and co-workers [Newnham, 1975], where intricate micron-sized cross-hatched ferroelectric domain structures (~ 10 to $70 \mu\text{m}$) were obtained in lead germanate ($\text{Pb}_5\text{Ge}_3\text{O}_{11}$) by controlled application of external mechanical stresses and electric field, shown in Fig. 1.6a. Subsequently, Feng, Ming and co-workers (1982, (1988) have grown periodic patterns of ferroelectric domains with an interdomain spacing of ~ 20 - $50 \mu\text{m}$ (Fig. 1.6b) on lithium niobate (LN) crystals *via* polarization rotation technique (PRT). The PRT can be achieved via slightly displacing and then rotating the rotational axis of the growing crystal from the axis of symmetry. This DE technique yields very good electro-mechanical properties of LN and thus enabling them suitable for optoelectronic, photorefractive and piezoelectric applications. Yamada et al. (1993) and Byer (1997) reported the periodic wave-like ferroelectric domain structure with a period of ~ 2 - $3 \mu\text{m}$ obtained by photolithography followed by poling at the high E_p ($> 210 \text{ kV/cm}$). The DE in single domain LN crystal resulted in higher T_c ($> \sim 1200 \text{ }^\circ\text{C}$) and thus suit them for nonlinear second harmonic generation (SHG) applications such as laser printers, display and data storage devices.

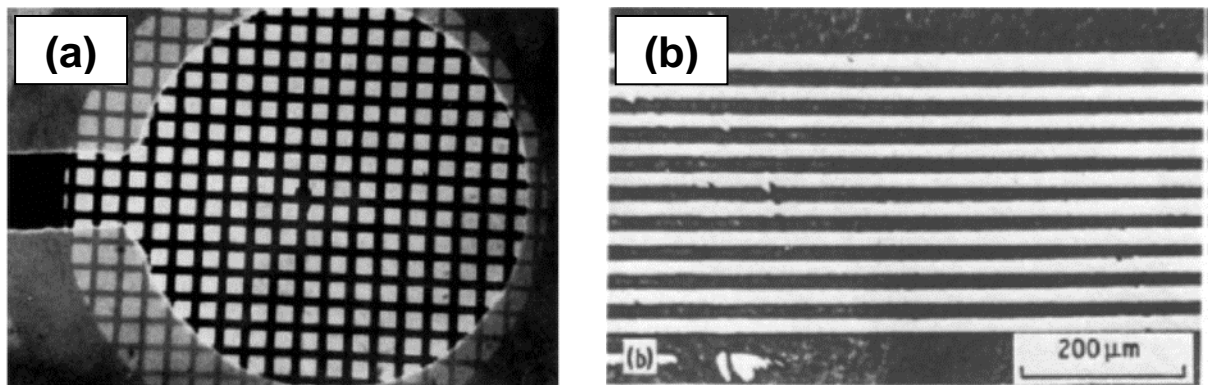


Fig. 1.6 (a) Cross-hatched ferroelectric domain structure in $\text{Pb}_5\text{Ge}_3\text{O}_{11}$ produced by a copper mesh electrode (first attempt of DE) [Adopted from Newnham, 1975] and (b) Periodic ferroelectric domain structure in LN crystals with a period $\sim 20 \mu\text{m}$ [Adopted from Ming et al., 1982].

The addition of relaxor dopants such as MgO and ZnO also found to be an effective ferroelectric DE technique in LN and LT crystals. Gopalan et al. (1999) obtained spherical ferroelectric domain patterns in conventional and MgO doped LN crystals, which showed

merging of 180° DW with respect to poling time, indicating the DW motion and ferroelectric domain switching/reorientation depends on the time. The electric field during poling, E_p required for the reversal of ferroelectric domains in MgO doped LN crystals is $\sim 1/5^{\text{th}}$ of the conventional LN crystals highlighting the role of dopants on DE. In another study, [Gopalan and Mitchell \(1999\)](#) demonstrated that, in conventional lithium tantalate (LT) crystals, the nucleation and growth of ferroelectric domain structure occurs by pinning-depinning type of growth mechanism. The *in-situ* monitoring of the ferroelectric domains during poling (at E_p as high as ~ 212 kV/cm) showed hexagonal growth of ferroelectric domain patterns with side-ways wall growth velocity ~ 100 $\mu\text{m/s}$ for a switch time ~ 1 s. Following this, [Kitamura et al. \(2001\)](#) obtained different ferroelectric domain patterns and compared E_p values for undoped and MgO doped (> 0.78 % mol.) LN and LT crystals and observed that doping of MgO resulted in the respective decrease of E_p by $\sim 88\%$ and $\sim 90\%$ in LN and LT crystals, which leads to $\sim 50\%$ decrease in infrared absorption, a clear indication of DE *via* doping of relaxor dopants.

Shur [[Shur, 2006 and Shur, 2006](#)], proposed four important steps for implementing DE on LN crystals *via* bipolar electric field technique: First, the formation of ferroelectric domain structure takes place on the surface of the crystal by “*nucleation of new domains*” followed by “*forward growth*”. The former one is an outcome of activation electric field, E_{ac} , which depends on the intrinsic material properties and operating temperature, while the latter one represents the expansion of ferroelectric domains along the polar axis. The third stage of the formation of ferroelectric domain structure involves “*side-ways growth*” of domains, indicating the expansion of ferroelectric domains transverse to the polar axis. The last stage is “*domain coalescence*”, in which DW merge and leading to a complete switching process.

The implementation of DE technique in piezoceramics requires a comprehensive understanding of ferroelectric domain kinetics. Systematic investigations of Shur [[Shur, 1996, Shur, 2006 and Shur, 2006](#)] on ferroelectric domain kinetics using experimental and simulation approach revealed that the formation of ferroelectric domain patterns depend on variety of kinetics. For instance, the range of applied electrical field and ferroelectric domain switching rate may differ from one ferroelectric domain to another under different experimental conditions. The external and bulk screening of depolarization field, E_d upon the redistribution of surface charges in the electrode also plays a vital role in stabilizing poled ferroelectric domain structure. The magnitude of E_d can vary according to the size and shape of the ferroelectric domains. For ex., the magnitude of E_d required to form a single narrow

ferroelectric domain with a needle-like shape is around 10^3 - 10^4 kV/cm, while the formation of triangular and spherical ferroelectric domains require E_d around $\sim 10^1$ - 10^2 kV/cm [Shur, 2006].

The reversal ferroelectric domain patterning *via* electric field over poling (EFOP) and subsequent wet etching was effectively employed by Grilli et al. (2005) to obtain the 1 and 2-D periodic spherical domain patterns down to ~ 200 nm with a period ranging from 0.5-2 μ m in LN crystals, shown in Fig. 1.7a. The fabricated spherical ferroelectric domain patterns found effective for nonlinear optics and short wave-length conversion applications. Over the years, considerable efforts have been directed to enhance the piezoelectric performance of LN, LT and KTiOPO₄ crystals due to their ease in implementation of the DE technique compared to other conventional piezoceramics (unfortunately, undoped/pristine PZT cannot be grown into a large single crystal, which prevents their enhanced structural and functional performance using DE technique). These studies adopted simple DE techniques such as stoichiometric control, growing single crystal in a confined glass, and infrared femtosecond pulse method for obtaining stable and periodic domain patterns [Kao et al., 2004, Dogheche et al., 2005, Bo et al., 2012, Chen et al., 2015, Veenhuizen et al., 2019].

In the last two decades, DE has triggered the revolution in enhancing piezoelectric properties and electro-mechanical coupling factors in other Pb and Pb-free piezoceramics. This typically contains charged DW, co-existence of multiphase systems, and ferroelectric domain pattern symmetries [Sun and Cao, 2014]. For instance, Ranjan et al. (2004) have obtained [110] oriented strip patterns, and [100] oriented braided patterns in PZN-PT single crystals, shown in Fig. 1.7b and achieved extremely high electro-mechanical coupling coefficient (in 3-1 mode), k_{31} and piezocharge coefficient (in 3-1 mode) d_{31} . The observed high k_{31} (~ 0.88) and d_{31} (~ -1850 pC/N) values are attributed to the electric field-induced polarization and phase change in the single crystal. Yao et al. (2011) obtained strip-like ferroelectric domain patterns in (21 $\bar{1}$) single crystal PMN-PT with varying E_p (from 0.5 kV/cm to 1 kV/cm). Direct observations through polarized light microscopy (PLM) and TEM revealed that the DW tend to retract (or merge) with an increase in E_p .

Several studies in the open literature also indicated that the macroscopic symmetry in the ferroelectric domain configurations is the key factor for implementing DE in various single crystals. In single-crystal rhombohedral PMN-PT and PZN-PT, poling along $[001]_c$ induces $4mm$ symmetry in ferroelectric domains while poling along $[111]_c$ direction induces $3m$ symmetry, which is further expected to tailor stable ferroelectric domain patterns. In view of

this, the observations of [Zhang and Li and co-workers \(2002\) \(2011\)](#) revealed an extremely high piezoelectric coefficient in shear mode, d_{15} around 3000 pC/N and 9200 pC/N for single crystals of PMN-PT (macroscopic symmetry $3m$) and PZN-PT (with macroscopic symmetry $4mm$), respectively. In consensus to this, [Wada et al. \(2004\)](#) implemented the DE technique on single-crystal BT *via* controlling the crystal structure and observed the $\sim 200\%$ increase in d_{33} values.

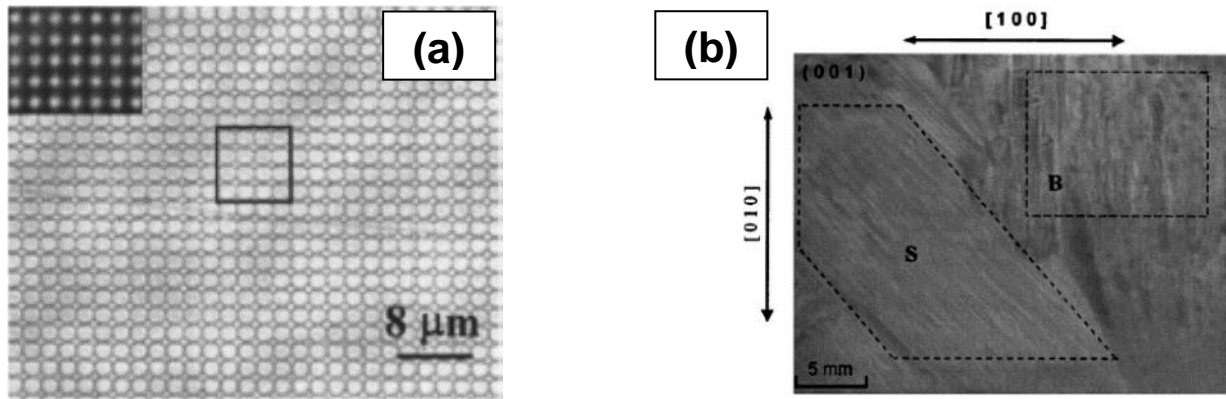


Fig. 1.7 (a) Optical microscope image of spherical ferroelectric domain patterns with size down to ~ 200 nm with a period ranging from $0.5\text{-}2\ \mu\text{m}$ in LN crystals [[Adopted from Grilli et al., 2005](#)] and (b) Ferroelectric domain patterns on as polished (001) PZN-PT wafer showing [110] strip and [100] braided patterns [[Adopted from Ranjan et al., 2004](#)].

Besides the above studies, several reports have mentioned that DE could also be achieved *via* altering the grain size and morphology, the addition of aliovalent dopants (particularly in PZT), imposing the mechanical stresses during electric poling, nano metal (di)oxide patterning or grating on the electrode-fired surface of piezoceramics, and reduction in ferroelectric domain size *via* electric poling. [Pramanick et al. \(2011\)](#) have shown that polarization and d_{33} increases by 166% and 4 times, respectively with the decrease in grain size ($\sim 50\%$) due to the addition of dopants in soft-doped PZT. The enhanced polarization and d_{33} values are attributed to the increased contributions of non- 180° DW motions (at nanoscale) and lattice strain incompatibilities. The phase-field simulations of [Wong et al. \(2013\)](#) and experimental observations of [Pramanick et al. \(2019\)](#) also showed that the electro-mechanical response in PMN-PT and other polycrystalline piezoceramics could be enhanced by reducing the grain size ($\sim 55\%$).

[Njiwa et al. \(2006\)](#) have shown that the mechanical stress-induced electrical poling increases the fracture response (R-curve behaviour) of PZT and found the net decrease in E_p .

The tailored ferroelectric domain patterns due to DE appears to be a primary reason for the enhanced R-curve response. Zhang et al. (2005) showed that the ferroelectric domain structure could be tailored in BSPT piezoceramics *via* the addition of Mn dopant, thus suiting them for high-temperature shear mode sensor applications (upto ~ 440 °C). The giant unipolar ϵ_p (upto $\sim 0.16\%$) and improved temperature stability upto ~ 175 °C was achieved *via* the addition of 2 % wt. MnO₂ in KNN based- CaZrO₃ Pb-free piezoceramics [Wang et al., 2013]. Besides this, previous studies have also shown that doping of aliovalent cations (both acceptor and donor) improves electro-mechanical properties in several piezoceramics [Ding et al., 2013, Xu et al., 2014, Zhou et al., 2014, Feng et al., 2015, Song et al., 2019; references therein].

Several studies in the past have also indicated that altering the interdomain spacing, domain size, and crystallographic orientation elicits the piezoelectric performance of electro-mechanical devices. For instance, the mathematical framework developed using the Ginzburg-Landau model by Ahluwalia and co-workers (2001) (2004) demonstrated that the decrease in ferroelectric domain size from 22 μm to 6.5 μm enhanced the d_{33} values by a factor of 3. They used parameters related to BT to demonstrate the single and multiple ferroelectric domain behaviour.

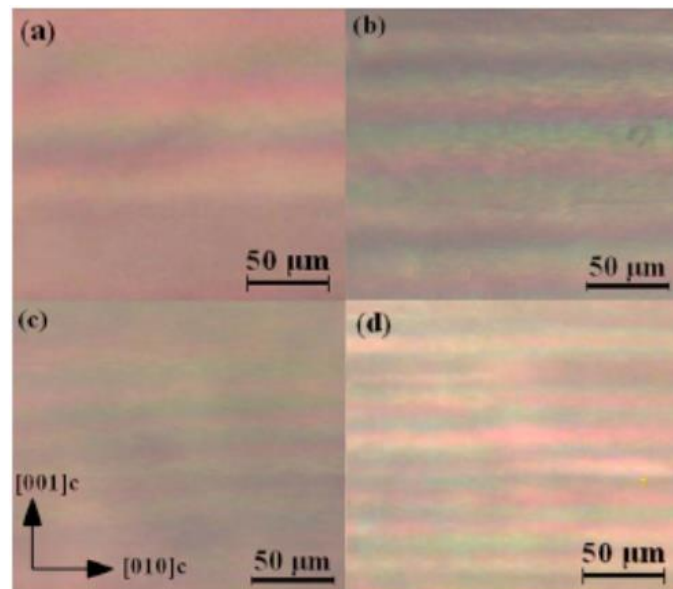


Fig. 1.8 A strip-like ferroelectric domain structures observed on the surface of $[001]_c$ PZN-6%PT single crystal with a period of ~ 10 μm at four different poling conditions (a) $T=160$ °C, $E_p= 18$ kV/cm, (b) $T=170$ °C, $E_p= 9$ kV/cm, (c) $T=168$ °C, $E_p= 11$ kV/cm and (d) $T=166$ °C, $E_p= 10$ kV/cm [Adopted from Xiang et al., 2010].

Furthermore, [Xiang et al. \(2010\)](#) demonstrated an enhancement in piezoelectric properties by controlling the strip-like ferroelectric domain structure in $[001]_c$ PZN-6%PT (Fig. 1.8) *via* electric poling at different temperatures and E_p . The decrease in ferroelectric domain size from 20 μm to 8 μm resulted in a $\sim 58\%$ increase in d_{33} values with a marginal increase in k_{33} values, a clear indication of regulating the piezoelectric properties by controlling the domain size (Fig. 1.9). Very recently, [Chang and Luo and co-workers \(2018\)](#) (2019) have shown the respective increase in d_{33} and ϵ_d by $\sim 36\%$ and $\sim 38\%$, respectively with the help of micro or nanoelectrode patterning of some metal oxide films on the poled surface of single-crystal PMN-PT, shown in Fig. 1.10.

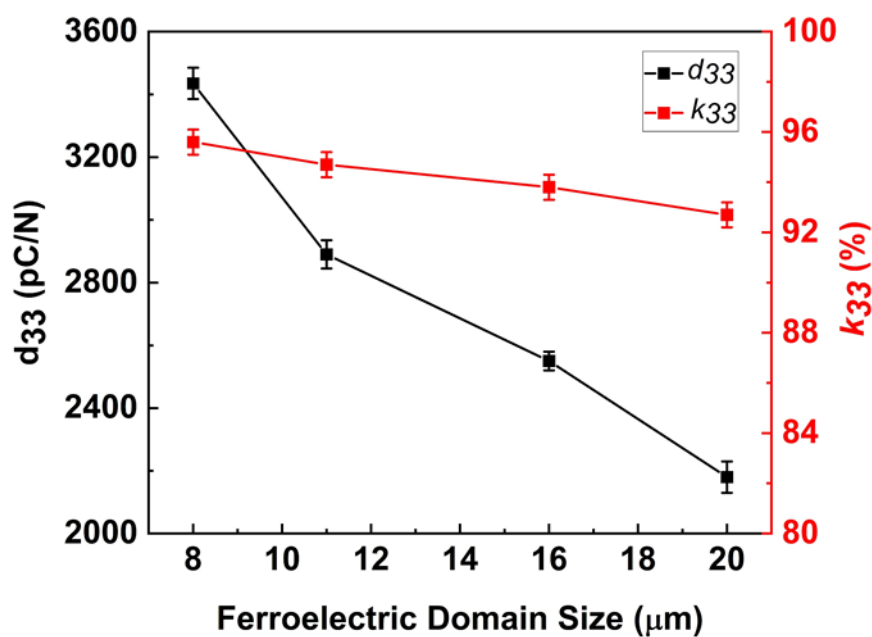


Fig. 1.9 Variation in d_{33} and k_{33} values with respect to ferroelectric domain size [[Adopted and reproduced from Xiang et al., 2010](#)].

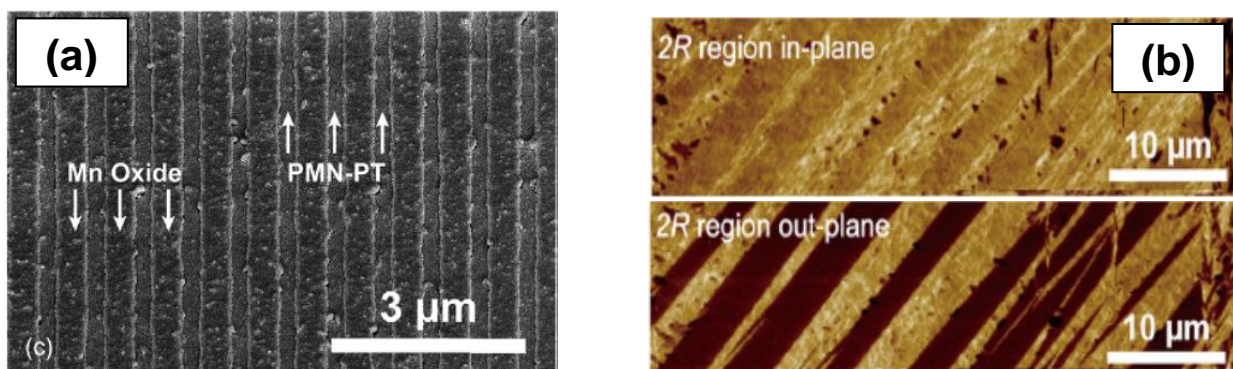


Fig. 1.10 (a) Patterned nanodomain structure [[Adopted from Chang et al., 2018](#)] and (b) microdomain structure [[Adopted from Luo et al., 2020](#)] obtained after grating nanoelectrodes of (Ti/Au-MnO_x) on PMN-PT single crystals.

In addition to the experiments, a good number of theoretical or modelling studies have been performed in understanding the influence of DE on the electro-mechanical response of piezoelectric materials. Sai et al. (2002) performed first-principles calculations using density perturbation functional theory (DPFT) on BT and PZT and demonstrated that compositionally broken inversion symmetry and structural phase transition due to electric and mechanical field leads to lattice distortion and influences ϵ_d values in piezoceramics. Bell and Li and co-workers (2001) (2004) implemented continuum Landau theory to investigate the effect of temperature and electric field directions on the electro-mechanical response of BT and relaxor PMN-PT and illustrated that DW density along the direction of applied electric field strongly influences the piezoelectric properties in the material. The origins of domain size dependence of piezoelectric properties can be systematically investigated using time-dependent Ginzburg Landau (TDGL) by Ahluwalia et al. (2004).

Of the several DE techniques mentioned thus far, controlling the ferroelectric domain orientations, interdomain spacing and domain size *via* thermal annealing is quite economical and efficient. Different ferroelectric domain configurations in as-poled (AP) piezoceramics (where ferroelectric domains are highly ordered) can be obtained by annealing them at selective temperatures below and above the T_c . The sub- T_c annealing is expected to cause partial perturbations in ferroelectric domain structures, while above- T_c annealing likely to induce complete disorderness in ferroelectric domains. However, one of the downsides of thermal annealing as a DE is the temperature-induced depolarization due to the reorientation of ferroelectric domains. Therefore, its use is limited despite the application of piezoceramics at high-temperature¹.

In summary, the ferroelectric domain structure can be tailored by using an appropriate DE technique, thereby enhancing the electro-mechanical response of piezoceramics. Most of the studies focus on investigating the effect of DE on the electrical, dielectric, and piezoelectric properties of piezoceramics, particularly at ambient/room temperature, while little attention has been given to understand the role of ferroelectric domain structure on the mechanical properties of piezoceramics. During service, electro-mechanical devices are often experience variable high frequency electrical, mechanical, and thermal environments, and the stresses arising from these loading conditions may induce significant nonlinearity and deterioration in mechanical

¹ Note that, unlike other metals and alloys, the term high temperature in case of piezoceramics is limited to their applications upto Curie temperature, T_c which may vary from material to material.

properties and thus affecting the reliability of these devices. The reorientation of ferroelectric domains appears to be a primary reason for such nonlinear behaviour. Further, most of the above studies highlight the importance of DE, particularly on single-crystal piezoceramics, as the use of single crystals eliminates the possibility of a complex interaction between ferroelectric domains, DW with the grain boundaries. However, several practical applications of piezoceramics are centred on using the polycrystals of various oxides. Therefore, it would be interesting to examine how the local changes in ferroelectric domain configurations (i.e., highly aligned, partially disturbed and fully disturbed) affects the mechanical behaviour in polycrystalline Pb and Pb-free piezoceramics.

1.4. Mechanisms of enhanced electro-mechanical response in piezoceramics

The enhanced electro-mechanical response of piezoceramics is observed for the compositions close to the morphotropic phase boundary (MPB). The previous studies have reported that MPB is a compositional line in the phase diagram of piezoceramics which separates two different structural phases, while recent studies have indicated that MPB should be a region according to varying contents of dopants/constituents. The most commonly investigated material so far is PZT, where rhombohedral (Zr rich) and tetragonal (Ti rich) phase co-exists at MPB, shown in Fig. 1.11 [Jaffe, 1971, Noheda et al., 2000, Mishra et al., 2001, Schmitt et al., 2007, Schönau et al., 2007, 2009, Singh et al., 2008, Theissmann et al., 2009, Schierholz et al., 2012, Liu et al., 2018, Gao et al., 2020; references therein].

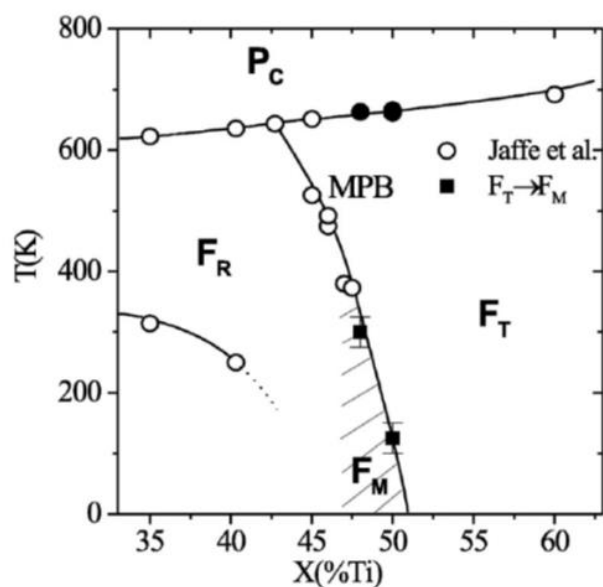


Fig. 1.11 Typical phase diagram for PZT clearly showing the MPB (subscript C, R, M, and T represents the cubic, rhombohedral, monoclinic and tetragonal phase of PZT, respectively) [Adopted from Noheda et al., 2000].

In the tetragonal phase, the spontaneous polarization is orientated along six possible [001] directions (along 3 negatives and 3 positive directions), while the rhombohedral phase has spontaneous polarization oriented along the eight [111] directions (along 4 negatives and 4 positive directions). Therefore, the compositions close to MPB are relatively less stable due to the fourteen energetic orientation of spontaneous polarization (coexistence of two phases due to slight local compositional fluctuations) and exhibits a larger response to applied stimuli under electric, thermal, and mechanical environment. Consequently, higher d_{33} , ϵ_d and coercive stress, σ_c values can be observed. Few studies showed a relatively high piezoelectric response and k_{33} values in PZT ($\text{PbZr}_x\text{Ti}_{(1-x)}\text{O}_3$) near MPB at composition $x \approx 0.48$ [Jaffe, 1971 and Sun and Cao, 2014]. The *ab initio* calculations performed by Bellaiche et al. (2001) on PZT ($\text{PbZr}_x\text{Ti}_{(1-x)}\text{O}_3$) have shown maximum d_{33} values for the composition close to MPB, which are directly related to the polarization rotation phenomenon. Kuwata et al. (1981) observed extremely high d_{33} (upto ~ 1500 pC/N) and saturation polarization, P_s (~ 0.45 C/m²) values for relaxor PZN-PT $x(\text{PbZr}_x\text{Nb}_{(1-x)}\text{O}_3) - (1-x)\text{PbTiO}_3$ with $x \approx 0.09$ composition at MPB. Similarly, enhancement in piezoelectric and dielectric properties in other ferroelectric relaxors such as PMN-PT with composition $x \approx 0.33$ to $x \approx 0.38$ is also reported by Chao et al. (1989) and Noheda et al. (2002).

Fan and co-workers (2007) reported a 55% increase in d_{33} values in case of KNN based BNT-BKT Pb-free piezoceramics at composition ($x \approx 0.20$) close to MPB on ternary phase diagram (Fig. 1.12) with a marginal increase in k_{33} .

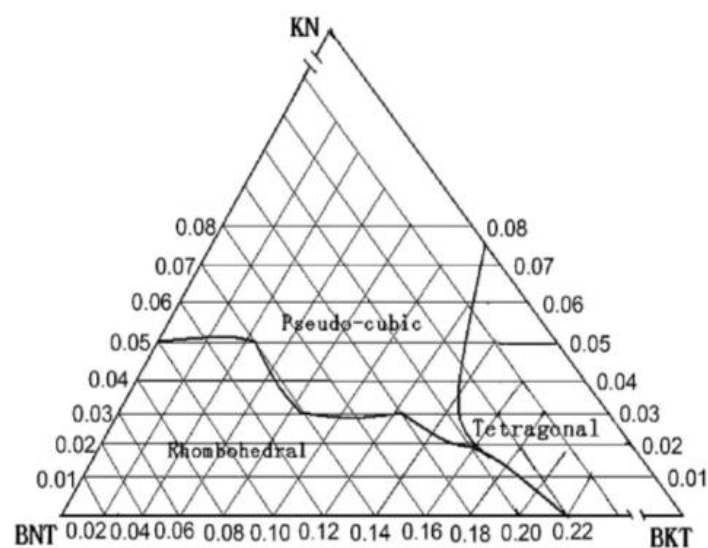


Fig. 1.12 MPB phase diagram of KNN based BNT-BKT ternary system [Adopted from Fan et al., 2007].

A notable review by [Wang and Li \(2012\)](#) addressed the enhancement in temperature stability, particularly in KNN based Pb-free piezoceramics *via* controlling the composition close to MPB in the range of $x \approx 0.20 - 0.22$. Few more recent studies, [Yuan et al. \(2017\)](#) and [Habib et al. \(2019\)](#) demonstrated enhanced piezoelectric performance of some Pb-free piezoceramics at $x \approx 0.20$, a composition close to MPB of Pb-free piezoceramics. Table 1.2 below summarizes the MPB compositions and respective d_{33} and T_c values for various Pb and Pb-free piezoceramics.

Table 1.2 Summary of compositions at MPB, d_{33} and T_c values of various Pb and Pb-free piezoceramics

Material	x content	d_{33} (pC/N)	T_c ($^{\circ}$ C)	Reference
PZT	~ 0.48	223	~ 360	Jaffe (1971)
PMN-PT	~ 0.33	2000-2500	~ 150	Noheda et al. (2002)
PZN-PT	~ 0.09	2500-3000	~ 180	Kuwata et al. (1981)
PNN-PT	~ 0.40	~ 600	~ 170	Banno et al. (1975)
92KNN-6BZ-2BNT	~ 0.06	348	~ 243	Wang et al. (2015)
KNN-BZ-BNZ	~ 0.04	345	~ 260	Tang et al. (2016)
KNN-BLT-BNKLZ	~ 0.06	310	~ 338	Cheng et al. (2014)

The giant piezoelectric response of Pb and Pb-free piezoceramics at a composition close to MPB can also be attributed to the external electric field-induced polarization rotation (FIPR) mechanism. In fact, the phase transformation taking place across MPB is also an outcome of FIPR. Further, the Ti and Zr atoms influence the polarization differently. The polarizations associated with Zr atoms rotate more quickly and grow in magnitude, while polarizations associated with Ti atoms lag significantly, and their magnitude also decreases. Therefore, this may be the acceptable mechanism for the enhanced piezoelectric response close to MPB. A similar effect was also observed by [García and Vanderbilt \(1998\)](#) in BT, wherein FIPR along certain paths creates the polarization-strain coupling. Further, the giant ϵ_p values (upto ~ 0.3 to 1.5%) are also observed in some relaxor ferroelectrics due to rhombohedral to tetragonal phase transformation, which is an outcome of FIPR [[Liu et al., 1999](#) and [Paik et al., 1999](#)].

Another acceptable mechanism responsible for the enhanced electro-mechanical response of piezoceramics at MPB is the ‘‘Adaptive phase theory (APT)’’, which is indicative of the influence of ferroelectric domain structure (particularly of nanometric size) on the crystal

symmetry [Jin et al., 2003 and Wang, 2006, 2007]. The morphology of nanoassembled ferroelectric domains changes markedly even with the small changes in composition, temperature, E_p and σ_c values resulting in a change in lattice parameter, spontaneous strain, ε_s and polarization [Jin et al., 2003]. The nanoassembled ferroelectric domains are expected to exhibit a more piezoelectric effect than micron-sized ferroelectric domains due to the high density of DW. Therefore, the strain component arising from DW motions in nanoassembled ferroelectric domains contributes to the higher macroscopic strain, resulting in enhanced piezoelectric response at MPB.

Bouzid et al. (2005) tried to construct the phase diagram for PZT by measuring elastic, E and shear, G moduli. The phase transitions are identified from the changes in E and G , which was validated concomitantly by XRD analysis, revealed the following; (i) Curie transition causes a change in crystal symmetry from cubic to tetragonal and (ii) rhombohedral to tetragonal transformation occurs at MPB. Recently, Ramajo et al. (2017), in the case of $(K_{0.44}Na_{0.52}Li_{0.04})[(Nb_{0.86}Ta_{0.1}Sb_{0.04}) - xZr_{5x/4}]O_3$ Pb-free piezoceramics demonstrated an increase in H (by $\sim 50\%$), E (by $\sim 27\%$), and indentation fracture toughness, K_{IC}^I (by $\sim 55\%$) at composition close to MPB ($x \approx 0.05$) as compared to the faraway compositions to MPB ($x \approx 0.00, 0.005, 0.01$ and 0.03). Doping of Zr^{4+} ions stabilize the microstructure with uniform sub- μm grain size appears to be an important reason for enhancing mechanical properties. However, the role of composition close to MPB and ferroelectric domain configurations on the mechanical response of piezoceramics needs to be investigated in detail. In order to probe the local mechanical behaviour, small scale characterization techniques such as nano- and microindentation and PFM are employed, which are explained in detail in the below section.

1.5. Small-scale characterization Techniques

Conventional mechanical testing experiments fails to probe the local deformation characteristics and hence provide limited information about the mechanisms prevalent at sub- μm length scales. In crystalline materials, it has been observed that miniature samples exhibit higher strength as compared to bulk samples giving a belief to the saying “*smaller the stronger*”. It is possible to measure the mechanical response of an individual or few ferroelectric domains using *in-situ* or *ex-situ* nanoindentation, which will help in designing the piezoceramics with a good combination of piezoelectric and mechanical properties. In the present work, we explore the local mechanical and piezoelectric response of Pb and Pb free

piezoceramics with the help of micro and nanoindentation along with (PFM) and details about these techniques with some studies in piezoceramics are given in the below section.

1.5.1. Indentation studies on piezoceramics

Indentation hardness, H , a quick estimate of material's resistance to the plastic deformation, is one of the most convenient and commonly used experimental techniques to probe the plastic deformation in materials due to the following advantages; (i) It requires a small volume of the test specimen, and (ii) it is non-destructive (particularly at small indentation loads, as the indentation impressions are confined to the smaller areas) (iii) The specimen preparation is quite simple and test is easy to perform. The electro-mechanical devices made of piezoceramics often experience variable contact loading conditions in high frequency electrical and mechanical environments. Therefore, they must exhibit resistance against the indentation or wear so that their electro-mechanical properties are less affected. Conventional macro-indentation experiments (because of the high loads) often lead to cracking of these materials and hence may not be the right choice to obtain hardness and study the influence of ferroelectric domains on the mechanical properties. For instance, [Ramamurty and co-workers \(1999\) \(1999\) \(2009\)](#) performed macro indentation experiments (with spherical indenter) on conventional PZT and BT piezoceramics and observed that the indentation response of piezoceramics is mainly dependent on the electro-mechanical boundary conditions (i.e., electrically conducting vs. insulating indenter and poled vs. unpoled material and their combinations). The fracture in PZT also changes from Hertzian cracking in case of unpoled PZT to subsurface damage in poled PZT though no direct correlation with microstructural aspects (i.e., concomitant changes in ferroelectric domain structure in subsurface deformation zone) was proposed.

Previous nanoindentation experiments performed mostly on single-crystal BT and PZT indicated rearrangement of ferroelectric domains and domain switching underneath the indenter (Fig. 1.13) [[Schneider et al., 2005](#), [Park et al., 2007](#), [Wong and Zheng, 2008, 2010](#)], the occurrence of distinct pop-in events in the loading curves [[Macias et al., 2008](#)], dislocation mediated slip [[Scholz et al., 2007](#) and [Mathews et al., 2020](#)], and the existence of flexoelectric effect [[Gharbi et al., 2009](#)] as the important features of deformation. Furthermore, the nanoindentation simulations performed by [Cheng and Venkatesh \(2012\) \(2013\) \(2014\)](#) and [Liu and Yang \(2012\)](#) on PZT, PMN-PT, and LN single-crystals showed that the deformation behaviour of these piezoceramics is influenced by the geometry of the indenter (spherical vs. conical vs. flat), electro-mechanical boundary conditions, and poling directions. In fact, the P

vs. h curves obtained from nanoindentation can be helpful in identifying the poling directions in piezoceramics [Cheng and Venkatesh, 2013].

There have been few Vickers indentation experiments in understanding the hardness and indentation fracture toughness, K_{IC}^i , in single crystal PZT and some Pb-free piezoceramics. The crack growth characteristics may influence the ferroelectric domain configurations ahead of the crack tip, thereby effecting the K_{IC}^i [Mehta and Virkar, 1990, Sun and Park, 2000, Fu and Zhang, 2000, Wang et al., 2021; references therein]. Despite these studies, there is no clear visualization of how the ferroelectric domains effects the crack growth characteristics and toughening mechanisms.

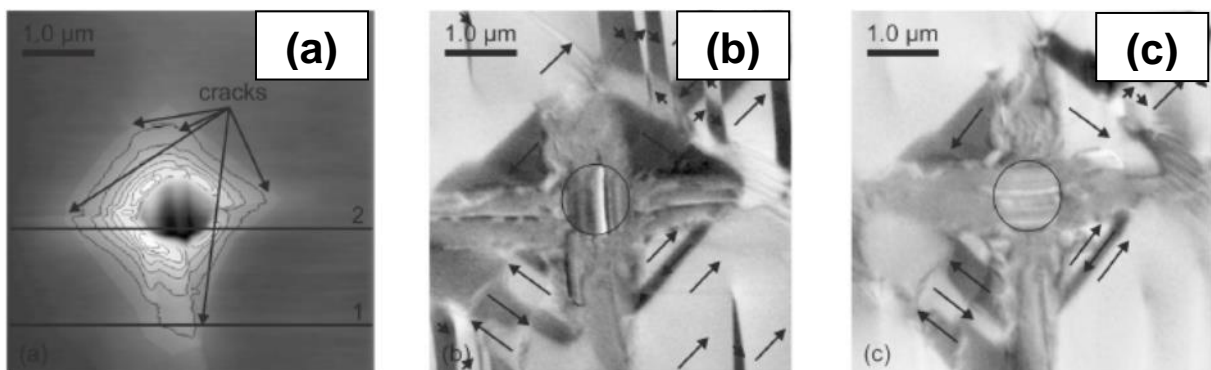


Fig. 1.13 Direct observations of ferroelectric domains beneath the indentation zone (a) topographic image with contour plots, (b) ferroelectric "a" domains in x-direction and (c) ferroelectric "a" domains in y-direction in the indentation zone [Adopted from Schneider et al. 2005].

All the above indentation studies are performed on poled piezoceramics where the ferroelectric domains are highly ordered and the variation of H and E with on partially poled (i.e., intermediately ordered ferroelectric domain configurations is largely unexplored. Therefore, it would be interesting to examine the mechanical response of polycrystalline piezoceramics having different ferroelectric domain configurations. In view of the above, the present work attempts to ascertain the indentation behaviour of ferroelectric domain configurations and toughening behaviour of polycrystalline piezoceramics. The ferroelectric domain configuration before and after the indentation is analyzed using PFM.

1.5.2. Nanoindentation

Recent developments in instrumented indentation techniques (IIT) such as micro and nanoindentation offer *in-situ* characterization of mechanical properties of materials at small

length scales. These IIT were first invented in Russia during late 1970s and recognized as a load (vis-à-vis depth) sensing indentation instruments [Bulychev et al., 1975 and Ramamurty and Jang, 2014]. In 1980s, the IIT made it possible to estimate the elastic properties (elastic modulus, E) of materials in addition to indentation H [Ramamurty and Jang, 2014]. Further advent in IIT led the discovery of the indentation technique which can probe the response of individual micron or sub-micron sized grains and capable of measuring the P vs. h response with high precision, popularly known as “*nanoindentation technique*”. In last two decades, nanoindentation has gained tremendous attention of materials community who are interested not only in probing the nanomechanical properties (with high precision) of crystalline and amorphous materials but also correlating the measured properties with underlying microstructural aspects, particularly at lower length scales.

The nanoindentation technique can generate P - h curves with high load (upto few nN) and displacement (~ 5 nm) resolutions. The fully plastic regime in an elastic-plastic material can be achieved even at small indentation loads ($\sim nN$) due to the usage of three-sided pyramidal Berkovich indenter having much sharper tip than the Vickers indenter. A schematic of Berkovich indenter is presented in Fig. 1.14a.

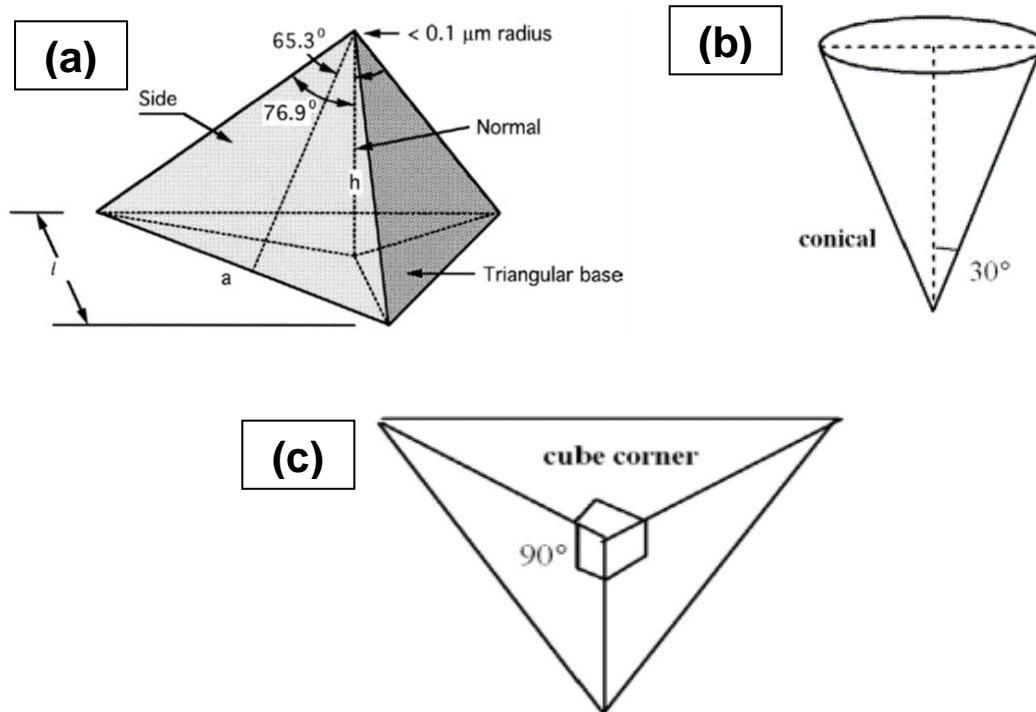


Fig. 1.14 Schematic representing the geometry and shape of the (a) Berkovich [Adpoted from Bharat Bhushan, 2017], (b) conical [Adpoted from Wang, 2016] and (c) cube-corner indenter [Adpoted from Wang, 2016].

Another unique advantage of nanoindentation, in contrast to the conventional indentation technique, is its ability to obtain both H and E without directly measuring the indentation impression of the material. Though Berkovich indenter (tip radius ranging from ~ 50 to 200 nm) is the most commonly used, experiments are also performed using conical and cube-corner indenters as shown in Fig. 1.14b and c, respectively [Wang, 2016]. The main difference between Berkovich, conical and cube-corner indenters reflect in geometry and shape of the indenter. The centreline-to-face angle for Berkovich indenter is typically $\sim 65.3^\circ$, while it is $\sim 90^\circ$ for cube-corner indenters, as shown in Fig. 1.14. It is also worth to mention that the nanoindentation response of the material is different with all the three geometries. For instance, Jang and Pharr (2008) systematically investigated the nanoindentation response of single-crystal (001) Si and (001) Ge with pyramidal and cub-corner indenters with a centreline-to-face angle (in the range 35° to 85°) and demonstrated that crack propagation during indentation is greatly influenced by indenter angle. On the other hand, indent size and hardness remain independent of indenter geometry. For the small volume of materials (e.g., thin films, coatings and small crystals of few μm size), nanoindentation technique has been beneficial for probing the nanomechanical properties. The sample preparation techniques, surface conditions (allowable roughness) and standard methods for conducting the nanoindentation tests on different materials are very well documented in International Standards Organization (ISO-14577 part 1-4) and American Society of Testing of Materials (ASTM E2540).

The detailed procedure for the analysis of nanoindentation data is proposed by Oliver and Pharr (1992) (2004), known as Oliver-Pharr (O-P) method. The O-P method estimates the H and E of the materials during one complete loading and unloading cycle, schematically shown in Fig. 1.15a. The analysis of nanoindentation data (i.e., P - h curves) begins with the fitting of unloading curve according to power law (eq. 3) proposed by Oliver and Pharr (1992);

$$P = \eta(h - h_f)^m \quad (3)$$

Here, P represents the indentation load, while h and h_f specifies the instantaneous and final penetration depth (Fig. 1.15a). The power law coefficient, η and power index, m can be obtained by fitting the eq. 3 according to power law. The typical m values for various materials reported in the literature are; (i) $m = 1$ for flat punch/indenter and (ii) $m \sim 1.20 - 2$ for Berkovich indenter [Oliver and Pharr, 1992]. The P - h curves represents three important quantities; (i) maximum indentation load, P_{max} , (ii) maximum displacement, h_{max} and (iii)

unloading stiffness, $S \left(\frac{dP}{dh} \right)$, slope of the initial part (elastic) of unloading curve required to estimate the H and reduced or effective elastic modulus, E_r values according to following equations 4 and 5 given below and details of which are mentioned in [Oliver and Pharr \(1992\) \(2004\)](#);

$$\text{Hardness, } H = \frac{P_{max}}{24.5h_c^2} \quad (4)$$

$$\text{Effective Elastic modulus, } E_r = \frac{1}{\beta} \frac{\sqrt{\pi}}{2} \frac{S}{\sqrt{A_c}} \quad (5)$$

where, A_c represents the projected contact area. Most of the strain-hardened and strain-softened materials exhibit pile-up and sink-in effects, respectively during nanoindentation.

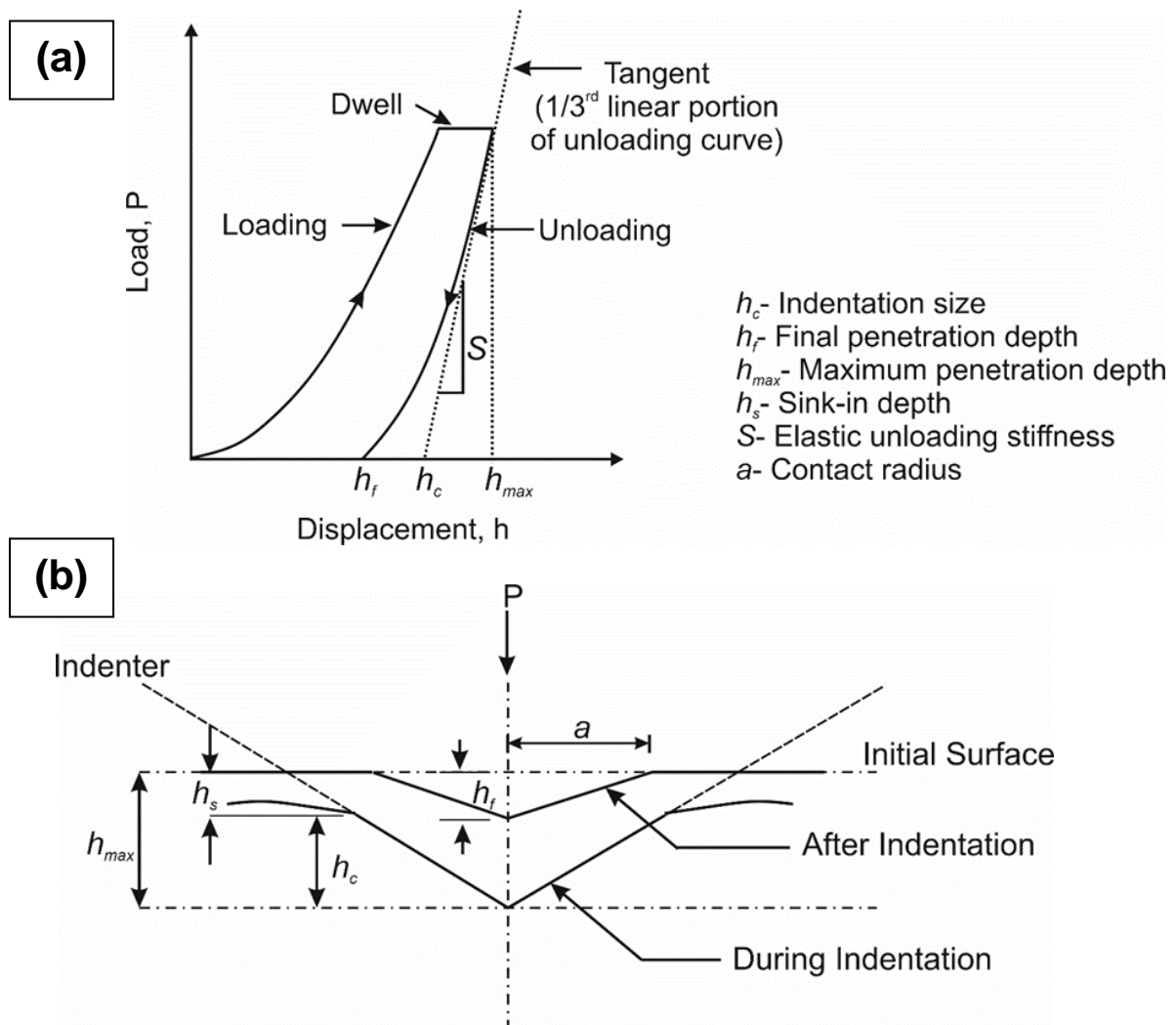


Fig. 1.15 (a) Graphical representation of the quantities used in the nanoindentation data analysis on P vs. h curve and (b) Schematic representation of the section of indentation surface profile [[Adopted and Redrawn from Oliver and Pharr \(1992\)](#)].

The O-P method does not correct the pile-up effects (this is one of the limitations), while contact depth, h_c shown in Fig. 1.15b can be estimated after eliminating the sink-in effect according to eq. 6 proposed by [Oliver and Pharr \(1992\)](#);

$$h_c = h_{max} - \beta \frac{P_{max}}{S} \quad (6)$$

Here, β is the constant that depends on indenter geometry. The typical value of β for conical indenter is 0.72, 0.75 for rounded tip and Berkovich indenter and 1 for flat punch/indenter. The elastic modulus of specimen, E_s that has been subjected to nanoindentation can be given according to following eq. 7 [[Oliver and Pharr, 1992](#)];

$$\frac{1}{E_r} = \frac{(1-\nu_s^2)}{E_s} + \frac{(1-\nu_i^2)}{E_i} \quad (7)$$

where, ν represents the Poisson's ratio and subscripts i and s specifies the indenter and specimen, respectively. The values of E and ν for diamond indenter are ~ 1170 GPa and ~ 0.07 , respectively [[Simmons and Wang, 1971](#)].

Unlike other conventional indentation techniques, the fracture during the nanoindentation (i.e., during both loading and unloading) and pressure-induced phase transformation in the material can be identified from the displacement bursts (i.e., *pop-in* during loading and *pop-out* during unloading) on $P-h$ curves, as shown in Fig. 1.16a. This alleviates the tedious indentation impression imaging process, as the indentation impressions sometimes are confined to very small area (around sub-micron zone) and difficult to locate. The occurrence of first *pop-in* indicates the elastic to plastic transition of the materials, while afterwards the occurrence of distinct *pop-in* events suggests the fracture (or cracking), particularly in brittle materials around and beneath the indentation. On the other hand, the *pop-out* event during the relaxation of indentation stresses (i.e., unloading) occurs mostly due to the sudden change in the volume of the material being indented and indicates the pressure (indentation)-induced phase transformation in the material, as shown in Fig. 1.16b.

In summary, nanoindentation is a versatile tool capable of characterizing the mechanical properties of materials, particularly small in volume/size and useful for correlating the structure-mechanical property relationship. All the piezoceramics that are investigated in the present work contain nano-sized ferroelectric domains (~ 20 to 80 nm) within the few microns sized grains (~ 1 to 2 μm) and therefore, nanoindentation technique will be helpful to probe the local mechanical response of individual or clusters of ferroelectric domains and DW.

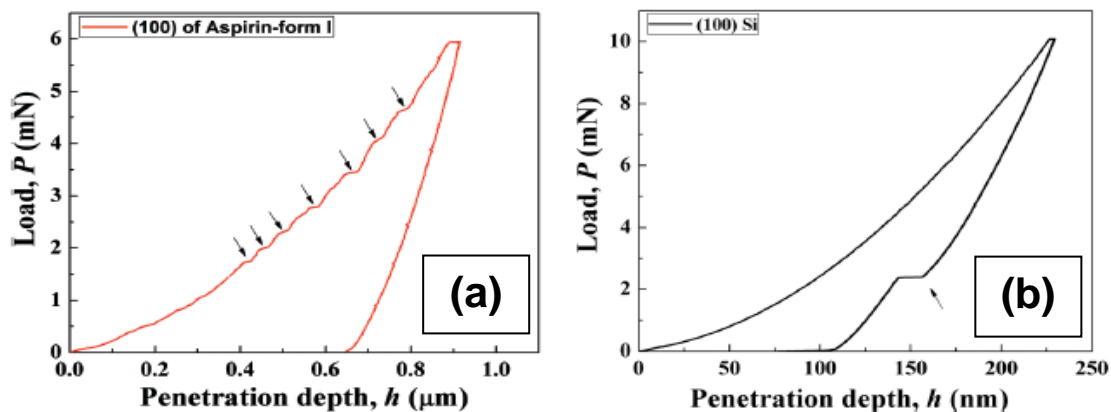


Fig. 1.16 Representative P vs. h curves indicating the (a) *pop-in* events shown by arrows in (100) face of Form I aspirin and (b) *pop-out* event shown by arrows in (100) face of single-crystal Si during nanoindentation [Adopted from Ramamurty and Jang, 2014].

1.5.3. Piezoresponse Force Microscopy (PFM)

Piezoresponse force microscopy (PFM) is a channel equipped with a functional atomic force microscope (AFM), which allows the characterization of electro-mechanical properties of ferroelectric materials, semiconductors and even some biological materials. The PFM was first invented by Güthner and Dransfeld (1992) and became a mainstream technique in the field of nano ferric materials in recent years due to its attractive features such as identification and imaging of ferroelectric domains over a large scale (as high as $100 \times 100 \mu\text{m}^2$) down to few nanometers with an additional advantage of surface topography imaging. The working principle of PFM is schematically shown in Fig. 1.17.

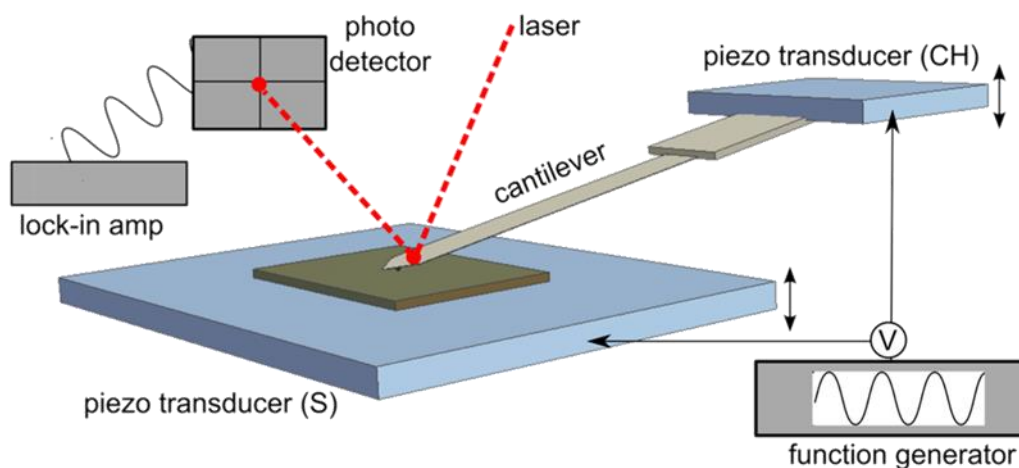


Fig. 1.17 Schematic representing the working principle of PFM [Courtesy: National Institute of Standards and Technology, Gaithersburg, USA]

URL: <https://www.nist.gov/image/afmschematic>

PFM technique allows ferroelectric domain imaging with the help of a conductive cantilever (curvature ~ 20 to 30 nm), coated with dense, hard and lustrous metal thin film (possibly of titanium and iridium) being gradually pressed into the scan surface (of few μm^2). The local ϵ_p values are monitored by the application of small A.C. electric field. The role of the conductive cantilever is of two fold; (i) actuation strains can be collected in the nanoscale contact regime of bulk or thin film sample upon small electric excitation, an actuation effect and (ii) probe electro-mechanical response of the material by controlling the mechanical motion of cantilever, a sensor effect [Gruverman et al., 2019]. The PFM technique allows to capture *in-plane* and *out-of-plane* response of material, shown in Fig. 1.18. The *in-plane* response can be captured when cantilever applies the A.C. electric field in the direction same as the polarization/poling direction of the specimen, indicating the *in-phase* response of drive voltage and piezoelectric properties. On the other hand, the application of A.C. electric field in the counter direction of polarization leads to the *out-of-phase* response of drive voltage and piezoelectric properties.

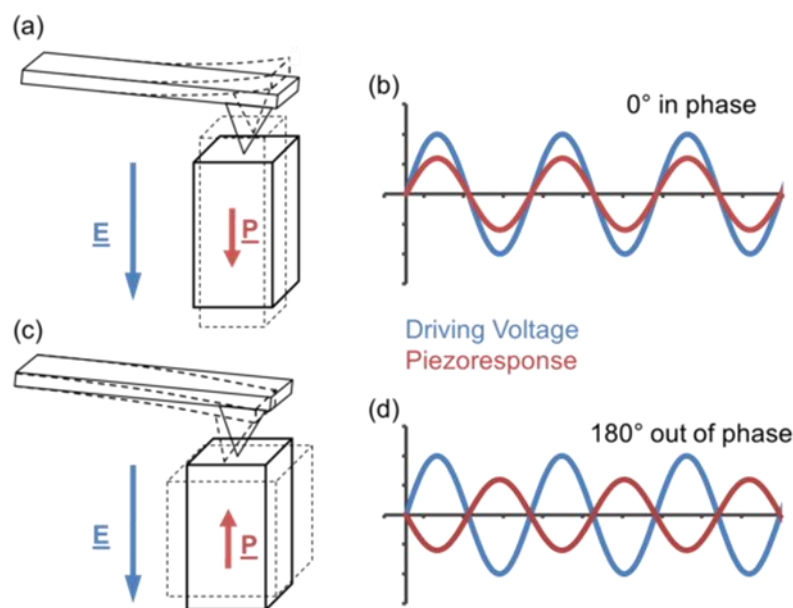


Fig. 1.18 Schematic representation of (a) in-plane deformation, (b) in-plane piezoresponse, (c) out-of-plane deformation and (d) out-of-plane piezoresponse of a ferroelectric material [Adopted from PFM Wikipedia].

URL: https://en.wikipedia.org/wiki/Piezoresponse_force_microscopy

PFM, within its predictive capabilities in the field of nano ferric materials, can perform the following main functions; (i) high-resolution imaging of ferroelectric domains (Fig. 1.19a), (ii) electro-mechanical property manipulation at the nanoscale (Fig. 1.19b) and (iii) probes the

local electro-mechanical properties (Fig. 1.19b). In recent years, the advances in the PFM technique has led to the determination of the following properties in addition to the ones mentioned above are: (a) switching spectroscopy PFM (SS-PFM), a technique used to acquire local PFM butterfly (amplitude, A_m vs. bias voltage, V_B) and hysteresis (phase, θ vs. bias voltage, V_B) loop, (b) vector PFM (V-PFM), typically used for probing the orientation dependence of electro-mechanical response with respect to polarization, piezoelectric constants and crystallographic orientations of the specimen, as shown in Fig. A1 of the Appendix 1 and (c) resonance enhanced PFM (RE-PFM), a technique facilitates the local electro-mechanical response and piezoelectric measurements in samples having weaker piezoelectric properties and low E_c .

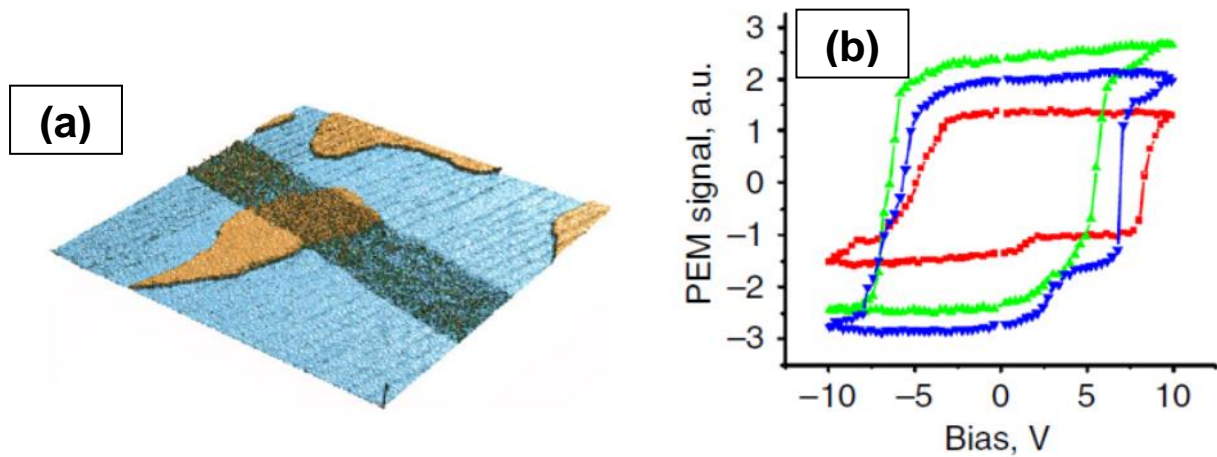


Fig. 1.19 Predictive capabilities of PFM (a) ferroelectric domain imaging (50 nm thick PbTiO₃ thin films) [Adopted from Gruverman et al., 2019] and (b) property manipulation via ferroelectric domain switching and probing the electro-mechanical response [Adopted from Kalinin et al., 2010].

1.6. Scope and objectives of the Thesis

In summary, the literature review mentioned above reveals that the intrinsic microstructural length scales (i.e., from several μm sized grains to few nm size ferroelectric domains) have a pronounced influence on the electro-mechanical response of piezoceramics. Therefore, the attractive properties of piezoceramics can be exploited by altering such microstructural features though their role in mechanical behaviour is not very well understood. Most of the previous studies in the open literature were focused on investigating the mechanical response of bulk piezoceramics at the macro scale, and less attention is given to understand their mechanics at lower length scales (i.e., micro and nanoscale). Furthermore, the effect of local changes in

ferroelectric domain configurations on the mechanical properties of polycrystalline piezoceramics needs a detailed investigation. Besides this, there is no comprehensive understanding of the addition of aliovalent dopants on the mechanical response of polycrystalline piezoceramics. We explore the above open issues using indentation (both micro and nano) and PFM techniques in the present work.

Further, there are no direct microstructural observations in the open literature (except for the work of [Schneider et al., 2005](#)), which indicate the ferroelectric domain activities in the vicinity of the indentation zone. A comprehensive understanding of such domain-dependent indentation behaviour will be helpful for the accurate estimation of mechanical properties in piezoceramics. Towards this front, the present work attempts to accomplish the following objectives:

- To obtain different ferroelectric domain configurations in PZT (undoped), PZT-H, PZT-S, PMN-PT and NKN-NT piezoceramics *via* DE technique (i.e., annealing at selective temperatures).
- To characterize the ferroelectric domain configurations of sub- and above- T_c annealed samples using PFM.
- To obtain nanomechanical properties of these samples by performing nanoindentation experiments.
- To develop a comprehensive understanding of the role of ferroelectric domains, DW activities and addition of dopants on the nanomechanical properties of piezoceramics.
- To characterize the changes taking place in the ferroelectric domain configurations in the deformation zone and in the vicinity of crack front.
- To examine the origins of ISE in nanoindentation H of polycrystalline piezoceramics having different domain configurations.

1.7. Organization of the Thesis

Following the above objectives, the present thesis is organized in the following manner; **CHAPTER 2** describes the effect of annealing (DE technique) on the mechanical properties of PMN-PT and NKN-NT piezoceramics having different ferroelectric domain configurations. The underlying mechanisms of enhancement in mechanical properties in light of crystal structure and ferroelectric behaviour are discussed in detail.

CHAPTER 3 presents the important results regarding the role of different ferroelectric domain configurations and aliovalent dopants on the mechanical behaviour of PZT (undoped), PZT-H and PZT-S. The toughening mechanisms such as indentation induced domain switching (IIDS) and domain rearrangement in the vicinity of the indentation are explained with the help of ferroelectric domain orientation maps. Butterfly curves (ϵ_r vs. E_p) are used to rationalize the results.

CHAPTER 4 deals with the description of observed ISE in nanoindentation H of PMN-PT, PZT-H, and PZT-S using the mechanistic models. The outcomes of the mechanistic modelling and origins of ISE in H are further explained in light of the differences in ferroelectric domain configurations.

CHAPTER 5 presents the conclusions from the present work. The last part of this chapter gives certain directions for future work from the mechanisms proposed in this study.

CHAPTER 2

Effect of sub and above Curie temperature annealing on the mechanical properties of PMN-PT and NKN-NT piezoceramics

Abstract: In this chapter, the role of different ferroelectric domain configurations on the mechanical properties of the polycrystalline PMN-PT and NKN-NT (Pb-free) piezoceramics is investigated. Annealing treatment is used at selective temperatures (i.e., below and above the T_c) to obtain the different ferroelectric domain configurations in both materials. Nanoindentation experiments are performed in the load range of 1 to 5 mN, followed by micro-Vickers indentation experiments to probe the mechanical properties. The effects of crystal structure and differences in ferroelectric domain configurations on enhancing mechanical properties are explored¹.

2.1. Introduction

Among the several classes of piezoelectric materials, solid solution of $x(\text{PbMgNbO}_3)-(1-x)\text{PbTiO}_3$ (abbreviated as PMN-PT) is quite popular for their high electro-mechanical coupling coefficients, dielectric constants, and low dielectric losses and hence attractive choice for sensitive sensors, more efficient transducers, and actuators [Newnham and Ruschau, 1991, Haertling, 1999, Zhang et al., 2001, Dahiya and Valley, 2013]. Although Pb-based piezoceramics exhibit a higher electro-mechanical response, many countries have enacted their use due to toxic Pb, which further creates hazardous impacts on the entire ecological system, particularly in young children. Therefore, the piezo community is continuously trying to develop an alternative Pb-free ceramic that can replace Pb-based ceramics. Some commonly used Pb-free piezoceramics on this front are BT, BNT, BKT and KNN perovskites. Among all of them, KNN-based Pb free piezoceramics can replace PZT and PMN-PT, particularly in high-temperature applications due to their relatively high T_c (250-460 °C) [Cheng et al., 2014 and Tang et al., 2016].

¹The work presented in this chapter is based on the following publications:

[1] V.S. Kathavate, B. Praveen Kumar, I. Singh, Palash Roy Chaudhary, K. Eswar Prasad (2018), Nanoindentation response of PZT and NKN-NT piezoceramics, *J. Coupled Syst. Multiscale Dyn.*, 06(04) 291-299.

[2] V.S. Kathavate, B. Praveen Kumar, I. Singh, K. Eswar Prasad (2020), Effect of sub and above curie temperature annealing on the nanomechanical properties of PMN-PT piezoceramics, *Ceram. Int.*, 46(8) 12876-12883.

During their service, components made of these materials often experience variable mechanical and electrical loading conditions, which sometimes may deteriorate their electro-mechanical properties defeating the specific application for which they are designed. A comprehensive understanding of the role of microstructural parameters on the mechanical, electrical and electro-mechanical properties is beneficial in designing piezoceramics with improved mechanical and electrical durability [Pramanick et al., 2011]. Ferroelectric domains, regions of directionally aligned dipoles under an applied external electric field, are the most prominent microstructural features which control the electro-mechanical properties of piezoceramics [Ye and Dong, 2000].

Several studies have been, in the past, reported the influence of ferroelectric domain configuration on the piezoelectric properties of various piezoceramics [Zhang et al., 1994, Ye et al., 2001, Wada et al., 2004, Shur, 2006, Wada, 2006, Choudhury et al., 2007, Fancher et al., 2017, Chang et al., 2018, Li et al., 2018; references therein]. All these studies indicate that the nature of the piezoelectric behaviour (linear vs. nonlinear), ferroelectric, and dielectric properties can be controlled by altering the size and orientation of ferroelectric domains, often referred to as domain engineering (DE) [Cady et al., 1946, Nelson et al., 2011, Wang et al., 2013; references therein]. DE is typically achieved by tailoring the grain size (or domain size) [Karaki et al., 2007, Gupta and Venkatesh, 2008, Zheng et al., 2012, Huan et al., 2014, Wu et al., 2016, Bai et al., 2017, Pramanik et al., 2019], addition of dopants [Shur, 2013], controlling the crystallographic texture, micro, or nano-metal electrode patterning, and superimposition of radial stresses on the applied electric field [Bai et al., 2018].

Most of the studies conducted on piezoceramics are primarily focused on investigating the role of DW motion and ferroelectric domain orientations on the electrical, dielectric, and piezoelectric properties, while less attention has been given to understand their influence on mechanical properties. Ramamurty and co-workers (1999) (1999) (2009) have studied the spherical macro-indentation response of conventional PZT and BT piezoceramics and demonstrated that the combination of material state (poled vs. unpoled) and nature of the indenter (conducting vs. insulating) influence the charge distribution around the indenter and affects both the indentation stiffness and H though they did not report any structural or microstructural characterization. The previous nanoindentation studies performed on various single-crystal piezoceramics revealed the complex events such as ferroelectric domain switching and reordering beneath the indenter [Kim et al., 1993, Muñoz-Saldaña et al., 2001, Schneider et al., 2005], presence of strong strain gradient polarization (flexoelectric effect)

[Maranganti and Sharma, 2007, Zubko et al., 2007, Gharbi et al., 2009], and dislocation mediated plasticity [Scholz et al., 2007, Hurtado-Macias et al., 2008]. Though these studies highlight the importance of several important events taking place during the indentation, a detailed understanding of the role of different ferroelectric domain configurations on the indentation behaviour of piezoelectric materials is still far from complete. In view of this, we have conducted micro and nanoindentation experiments on polycrystalline PMN-PT and sodium-potassium-niobate-sodium-tantalate (NKN-NT) piezoceramics having different ferroelectric domain configurations that are obtained by systematically annealing the as-poled (AP) samples below and slightly above the T_c .

2.2. Materials and Experiments

2.2.1. Materials

PMN-PT and NKN-NT piezoceramics prepared *via* solid-state reaction route are used in the current experiments. A high purity raw oxides MgO (Sigma Aldrich, 71%) and Nb₂O₅ (Sigma Aldrich, 98.9%) (for PMN-PT) and Na₂CO₃, K₂CO₃, Nb₂O₅ and Ta₂O₅ (for NKN-NT) are uniformly mixed in a stoichiometric ratio $0.90(\text{PbMg}_{0.33}\text{Nb}_{0.66}\text{O}_3) - 0.10(\text{PbTiO}_3)$ (for PMN-PT) and $0.94(\text{NaK}_{0.5}\text{Nb}_{0.5}\text{O}_3) - 0.06(\text{NaTaO}_3)$ (for NKN-NT) with ethanol as a medium in a mill for 24 hours. The prepared magnesium niobate oxide (Columbite-MgNb₂O₆) (for PMN-PT) is again synthesized with PbO (Qualigens, 98%) and TiO₂ (TTK products, 98.5%) for 24 hours. The ball-milled mixtures are calcinated at 1100 °C (for PMN-PT) and 900 °C (for NKN-NT) for 2 h followed by ball milling for another 24 h to ensure the homogeneous mixing of powders. The calcinated powders are then hot-pressed into discs of 10 mm diameter and thickness of 1 mm followed by sintering at 1200 °C (for PMN-PT) and 1150 °C (for NKN-NT). The as-cast discs are poled along the thickness in the temperature range of 60 to 80 °C in a silicon oil bath at E_p 40 kV/cm around 45 min (for PMN-PT) and 20 kV/cm around 30 min (for NKN-NT). The surfaces of the discs are coated with a conductive silver paste to make them conductive to enable to poling process and to be able to determine the d_{33} values. The T_c for PMN-PT and NKN-NT is determined to be ~ 200 °C and ~ 300 °C, respectively. As the objective of the current study is to investigate the role of ferroelectric domains configurations on the mechanical properties, the as-poled (AP) samples are subjected to an annealing treatment at $0.6T_c$, $0.8T_c$, and $1.2T_c$ (for PMN-PT) and $1.2T_c$ (for NKN-NT) for 2 h. The d_{33} values along the thickness direction of all the samples are measured at room temperature using SINOCERA (Model- YE2730A) d_{33} meter. The sub and

above- T_c annealed samples are hereafter referred to as sub- T_c depoled (STD) and above- T_c depoled (ATD) samples.

2.2.2. X-Ray Diffraction (XRD): Phase and crystal structure analysis

The nature of phases and crystal structure of all the samples is determined using a high-resolution Rigaku RINT (SmartLab 2000) X-ray diffractometer. The XRD experiments are performed in the diffraction angle range of 20-80° using Cu/ K_α radiation ($\lambda = 1.54 \text{ \AA}$). A step size of 10 s and a scan speed of 0.01° is employed to obtain a high number of counts and clearly distinguish the closely spaced peaks. Indexing of the peaks and corresponding identification of the phases are done with the help of the Joint Commission on Powder Diffraction (JCPDS) database. The lattice parameters are determined from the high-intensity peaks.

2.2.3. Indentation experiments

Quasi-static nanoindentation experiments are conducted using Bruker Hysitron TI nanoindenter to obtain the nanomechanical properties. A Berkovich three-sided pyramidal indenter is used, and the area function of the indenter is calibrated using a standard quartz sample. Indentations are performed in a load-controlled mode in the peak load range of 1 mN to 5mN with an interval of 1 mN. All the indentations are performed at a constant loading/unloading rate of 0.1 mN/s with a dwell time of 5 s at peak load. To obtain representative data, 20 indentations are performed at each loading case. The spacing between the successive indentations maintained about 10 times the maximum penetration depth to avoid the interaction of strain fields. The hardness, H values are determined by following Oliver and Pharr method [Oliver and Pharr, 1992] using equations 1, respectively.

$$\text{Hardness, } H = \frac{P_{max}}{A_c} \quad (1)$$

Here, P_{max} refers to maximum indentation load, A_c is the contact area obtained from the area function calibration. The micro-Vickers indentation experiments are performed on the AP, STD and ATD samples of both the materials using a microhardness tester (Micro-Mach Technologies Ltd., Pune) equipped with the Vickers tip in the load range of 0.25 to 2 N with a nominal velocity of Vickers indenter 60 $\mu\text{m/s}$ and a dwell time 10 s at P_{max} . The Meyer's hardness (HV) values are then obtained by dividing the P_{max} with the projected area of the impression [Meyer, 1908].

2.2.4. Microstructure and ferroelectric domain characterization

Pristine samples do not exhibit a good contrast under SEM, and hence the metallographically polished samples are ultrasonically cleaned around 10 min followed by chemical etching in steps for about 5-8 min in DI H₂O + 48% wt HF solution and 3 min in DI H₂O + 37% wt HNO₃. The microstructural analysis of all the samples (i.e., grain size distribution, domain size, and porosity) is carried out using a scanning electron microscope (SEM) (model JEOL JSM-7610FPlus). Further, the domain visualization is performed both under SEM and piezoresponse force microscopy (PFM) (Park-NX Wafer, model-NX20). PFM employs Ti/Ir coated cantilever tip with a radius of 20 nm as specified by the manufacturer. The spring constant and resonant frequency of the cantilever is ~ 2 N/m and 60 kHz, respectively. AC modulated voltage at an amplitude of 5 V and scan frequency 1 Hz are used to detect the PFM signal.

2.3. Results and Discussion

2.3.1. Characterization of crystal structure

X-ray diffraction patterns of all the samples of PMN-PT and NKN-NT are shown in Fig. 2.1(a) and 2.1(b), respectively. It has been reported in the literature that one of the common problems during the synthesis of PMN-PT piezoceramics is the formation of unwanted pyrochlore phase [Mylnikova and Bokov, 1959, Setter and Cross, 1980, Swartz and Shrout, 1982, Garg et al., 2013]. However, the XRD patterns of the current samples do not indicate the presence of the pyrochlore phase but only show the diffractions peaks corresponding to the perovskite phase, indicating the good quality of ceramics. The differences in diffraction patterns among all samples of PMN-PT and NKN-NT are obvious from Fig. 2.1. The AP sample of PMN-PT shows strong and sharp peaks of (111), (200) followed by (220) planes, while AP samples of NKN-NT exhibit the preferential orientation of the grains along (101), (201) and (200) directions. In contrast to this, the annealed samples of both the materials show a sharper and intense peak of (110) planes indicating that annealing has caused slight changes in the crystal structure. Further, the identification of peaks from the JCPDS file confirms the transformation of crystal structure from pseudo-cubic to nearly-cubic phase for PMN-PT and tetragonal to near-cubic for NKN-NT piezoceramics.

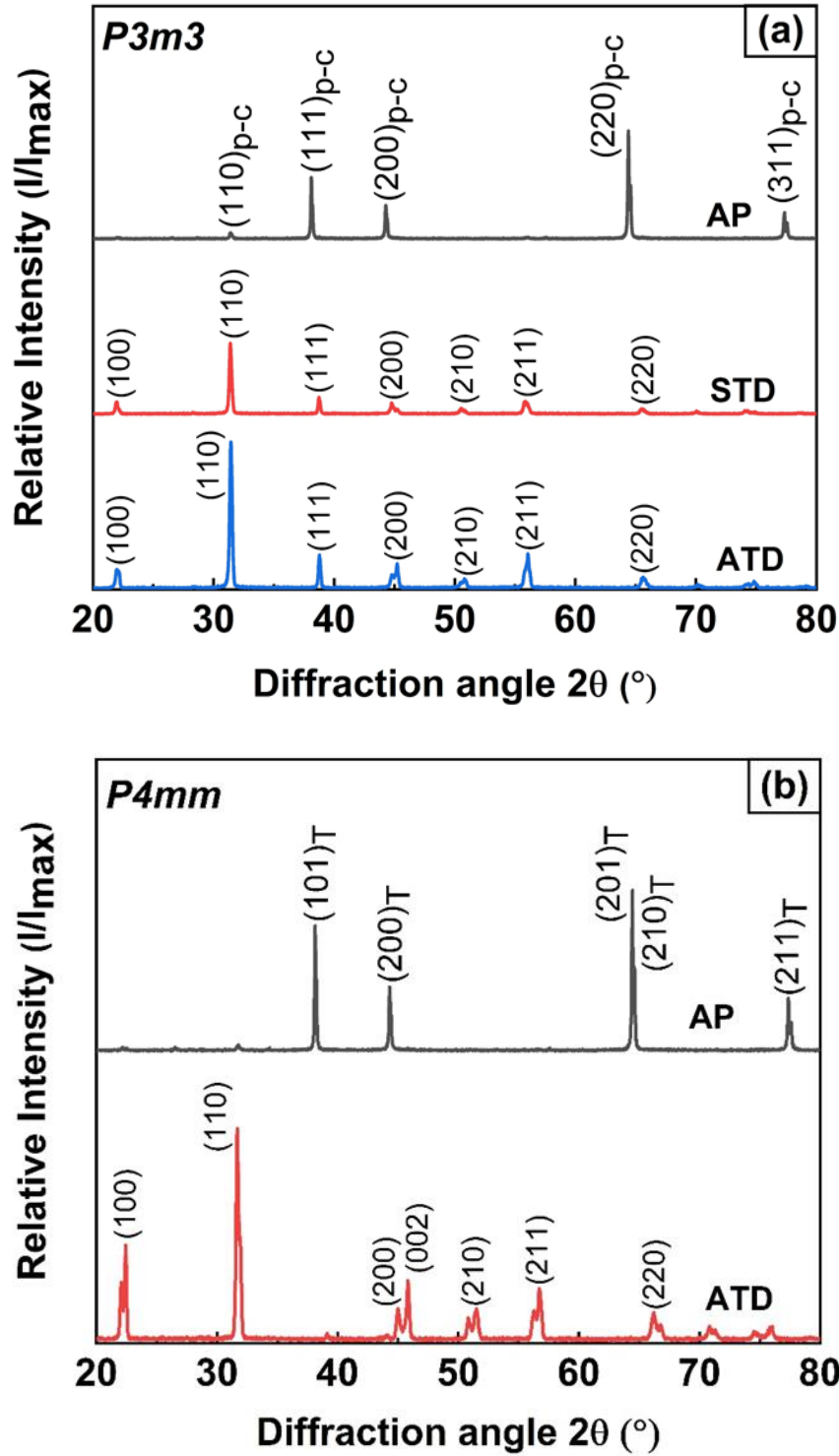


Fig. 2.1 XRD patterns of AP, STD and ATD samples of (a) PMN-PT and (b) NKN-NT. The subscript “p-c” and “T” represents the pseudo-cubic and tetragonal phase, respectively.

The lattice constants of the samples are computed from the diffraction data. The lattice parameters for the pseudo-cubic phase of the AP sample in PMN-PT are evaluated to be $a = 3.76 \text{ \AA}$ and $c = 3.78 \text{ \AA}$ with a tetragonality ratio (c/a) 1.005, while the lattice parameters of

the nearly-cubic perovskite phase are found to be $a = 4.04 \text{ \AA}$. On the other hand, the lattice parameter for the tetragonal phase of the AP sample in NKN-NT are determined to be $a = 3.98 \text{ \AA}$, and $c = 4.02 \text{ \AA}$, while the lattice parameter of the nearly-cubic phase is determined to be $a = 3.94 \text{ \AA}$. The results obtained after XRD analysis are summarized in Table 2.1 below, which agree with previous studies [Swartz and Shrout, 1982, Garg et al., 2013, Guo et al., 2004 and Dai et al., 2007, 2009].

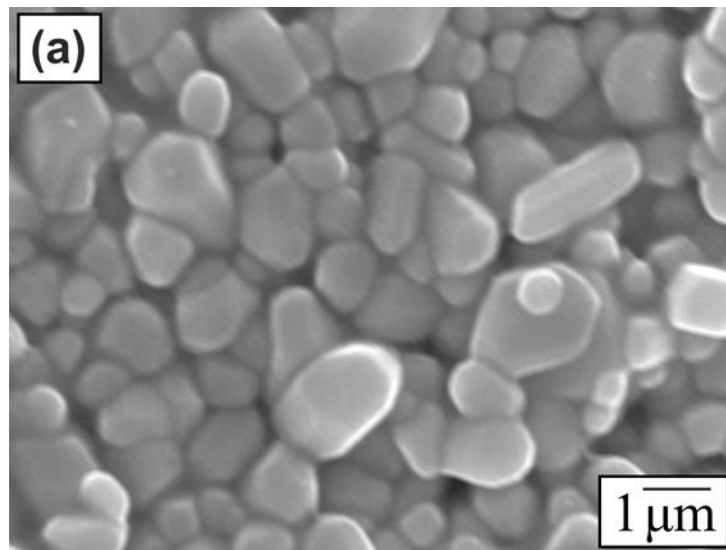
Table 2.1 Summary of XRD results, d_{33} values and d_{avg} values for all the samples of PMN-PT and NKN-NT piezoceramics.

Material	Structural state	Crystal Structure	Lattice parameters, a and c (\AA)	Tetragonality (c/a)	d_{33} (pC/N)	d_{avg} (μm)
PMN-PT	AP	Pseudo-cubic	$a = 3.76,$ $c = 3.78$	1.005	760 ± 5	1.10 ± 0.23
	STD	Near Cubic	$a = 4.04$	--	390 ± 5	1.90 ± 0.38
	ATD	Near Cubic	$a = 4.04$	--	0	1.65 ± 0.23
NKN-NT	AP	Tetragonal	$a = 3.98,$ $c = 4.02$	1.01	210 ± 7	1.28 ± 0.18
	ATD	Near Cubic	$a = 3.94$	--	0	1.72 ± 0.32

The d_{33} values of AP, STD and ATD samples of PMN-PT and NKN-NT piezoceramics are compiled in Table 2.1. Clearly, ATD samples of both the materials exhibit “zero” d_{33} values, indicating that the above- T_c annealing has caused complete randomization of ferroelectric domains, a commonly observed phenomenon in piezoceramics. The d_{33} values of STD samples of PMN-PT annealed at $0.6T_c$ and $0.8T_c$ found to be 390 ± 5 and 230 ± 3 pC/N, respectively. It is interesting to note here that despite having a similar crystal structure to ATD samples, the STD samples of PMN-PT exhibited non-zero d_{33} values suggesting that the ferroelectric domains are not completely randomized in the STD samples. This highlights the relative importance of ferroelectric domains on the piezoelectric properties compared to the crystal structure.

2.3.2. Characterization of microstructures: Composition, grain size, and porosity

Representative SEM images of AP, STD and ATD samples of PMN-PT and NKN-NT piezoceramics are shown in Fig. 2.2 and 2.3, respectively. The average grain size, d_{avg} of the microstructures (Table 2.1) is obtained from the linear intercept method as per ASTM E-112 and 113 standards using Image-J software by maintaining a suitable contrast over a sufficiently large number of grains. It appears that the d_{avg} values of all the samples in both materials are within experimental scatter, suggesting that annealing has not caused an increase in grain size. The AP, STD and ATD samples of PMN-PT exhibited a mixed type of morphology (i.e., cubic and spherical), while in NKN-NT piezoceramics, the cubic morphology of grains is obvious. Furthermore, NKN-NT piezoceramic appears to be softer as the surface contains many scratches and more deformed grain (even with extremely gentle polishing), unlike PMN-PT. Moreover, both AP and ATD samples of PMN-PT showed a large porosity compared to the STD samples. Another interesting feature of the STD and ATD microstructure in PMN-PT and NKN-NT is the cracking along some of the grains, which is not seen either in AP samples. One of the possible reasons for this could be due to the volumetric changes arising from the ferroelectric domain reorientation and domain wall motion, mainly due to the structural transformation from pseudo-cubic to nearly cubic in PMN-PT and tetragonal to near-cubic in NKN-NT piezoceramics which is evident from the XRD patterns (Fig. 2.1).



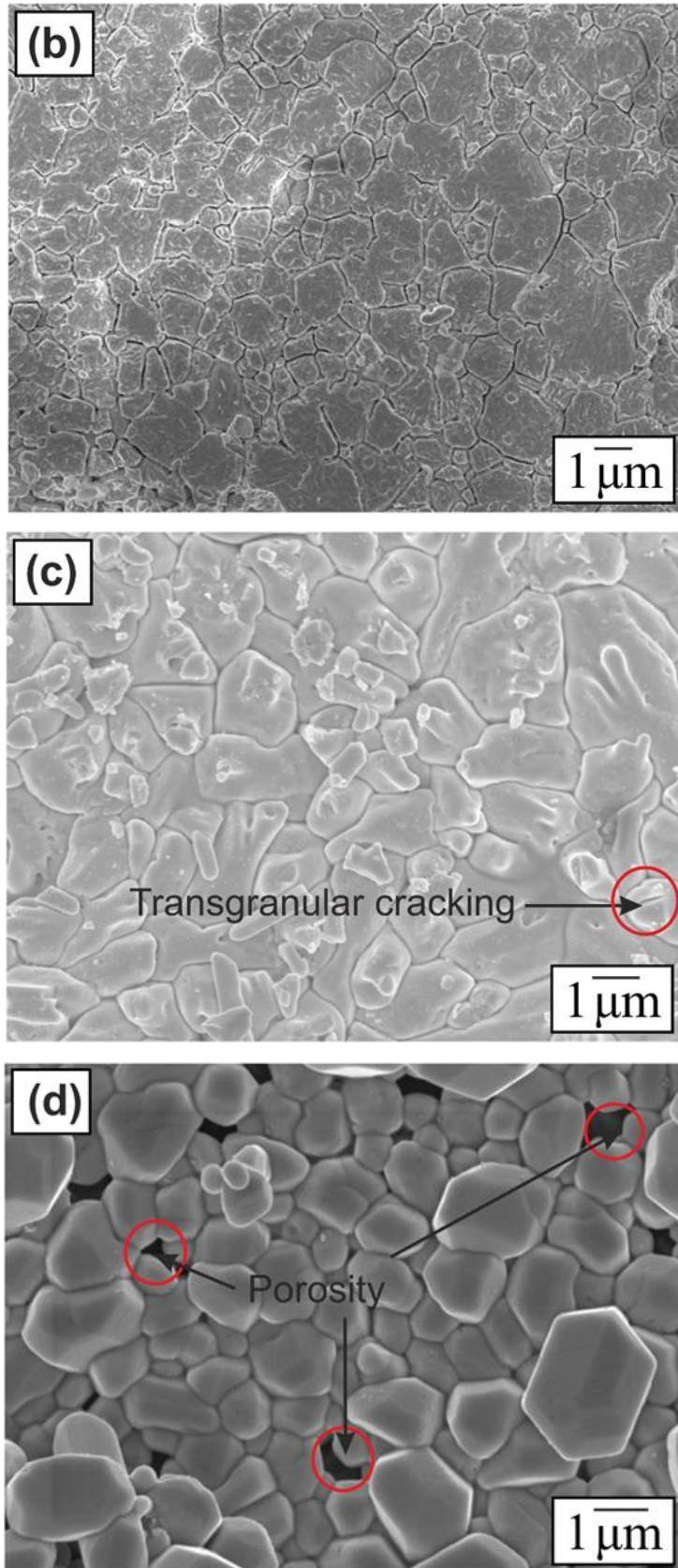


Fig. 2.2 Representative SEM images indicating the microstructures of (a) AP, (b) STD ($0.6T_c$), (c) STD ($0.8T_c$) and (d) ATD samples of PMN-PT piezoceramics.

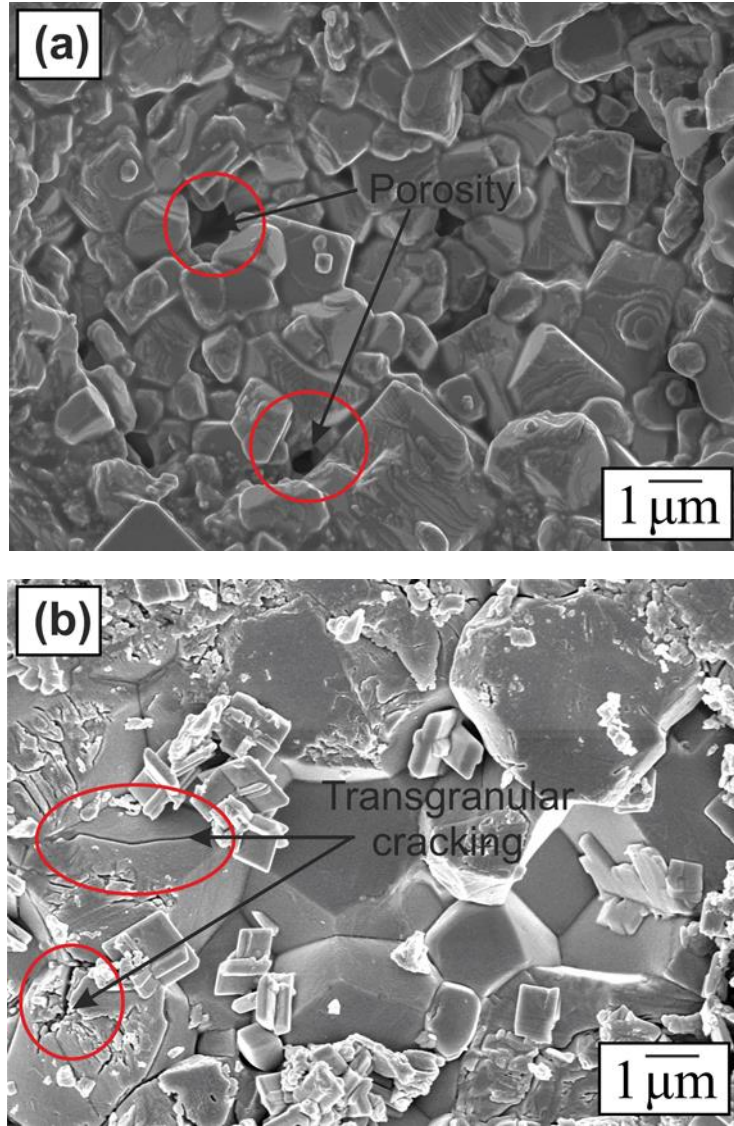


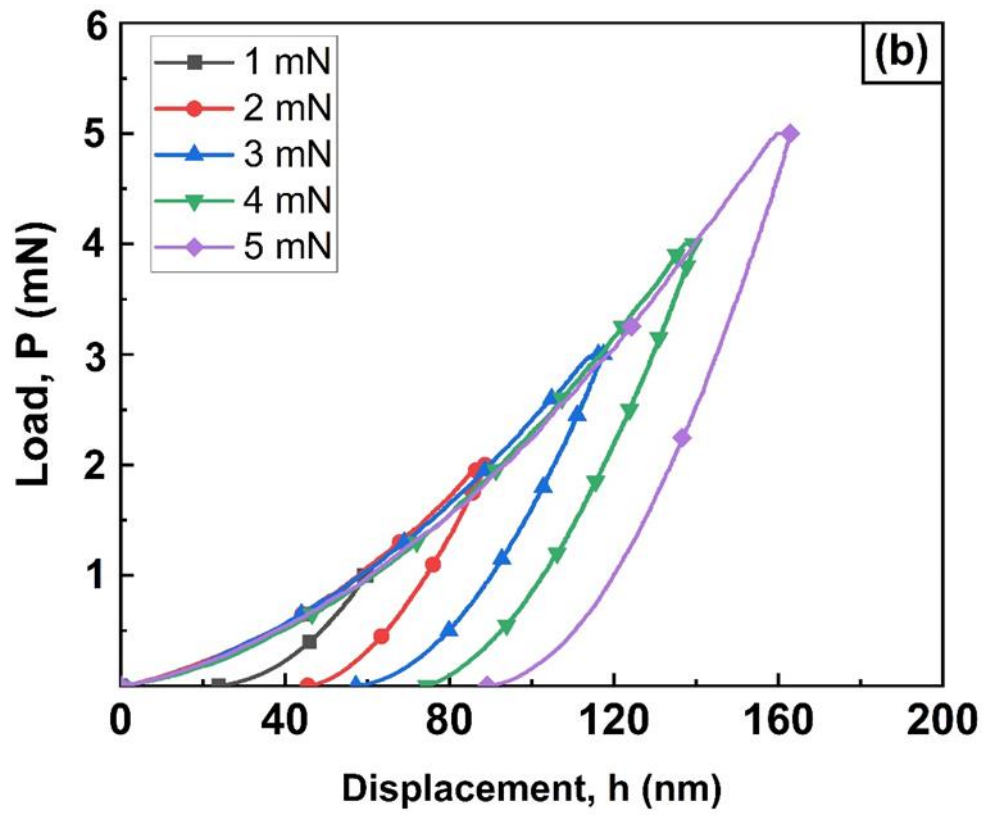
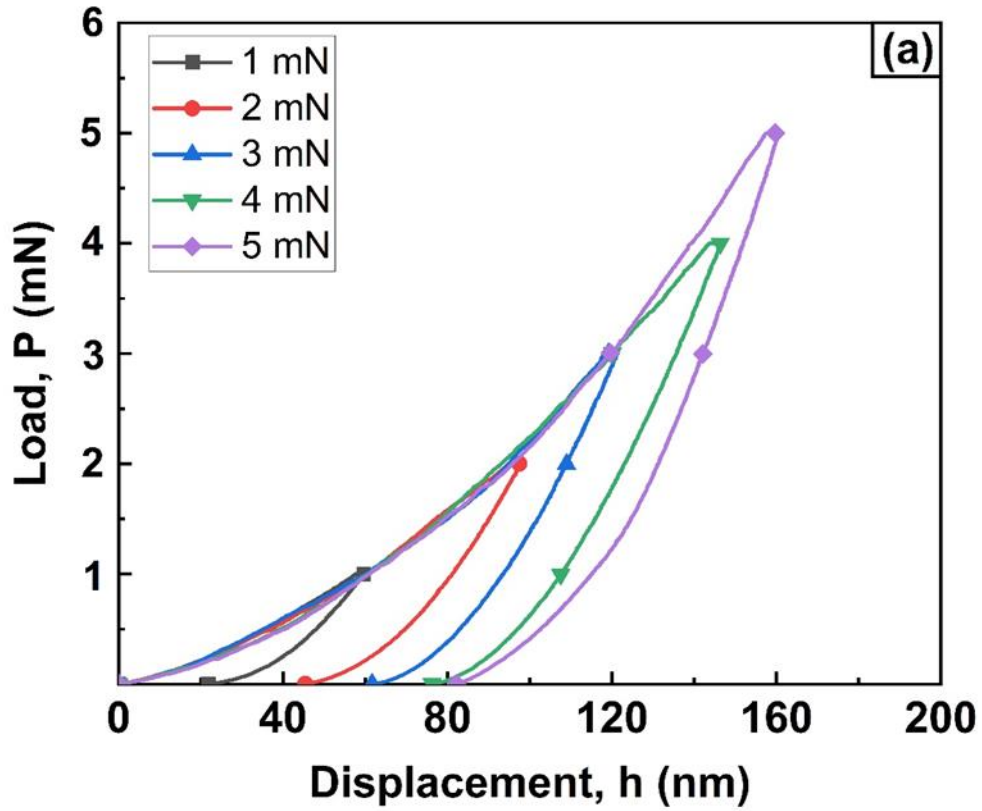
Fig. 2.3 Representative SEM images indicating the microstructures of (a) AP and (b) ATD samples of NKN-NT piezoceramics.

2.3.3. Analysis of indentation load, P vs. displacement, h curves

Representative P vs. h curves obtained from nanoindentation experiments for the AP, STD, and ATD samples of PMN-PT and AP and ATD samples of NKN-NT are shown in Fig. 2.4 and 2.5, respectively. The AFM images of the imprints do not show any evidence of pile up or crack at the imprint corners suggesting that Oliver and Pharr (O&P) analysis [Oliver and Pharr, 1992] can be employed to interpret the indentation data and obtain mechanical properties (Eq. 1). According to O&P analysis, the loading and unloading curves follow the power-law relation, as described in equations 2 and 3;

$$P = \alpha h^m \quad (2)$$

$$P = \alpha(h - h_f)^n \quad (3)$$



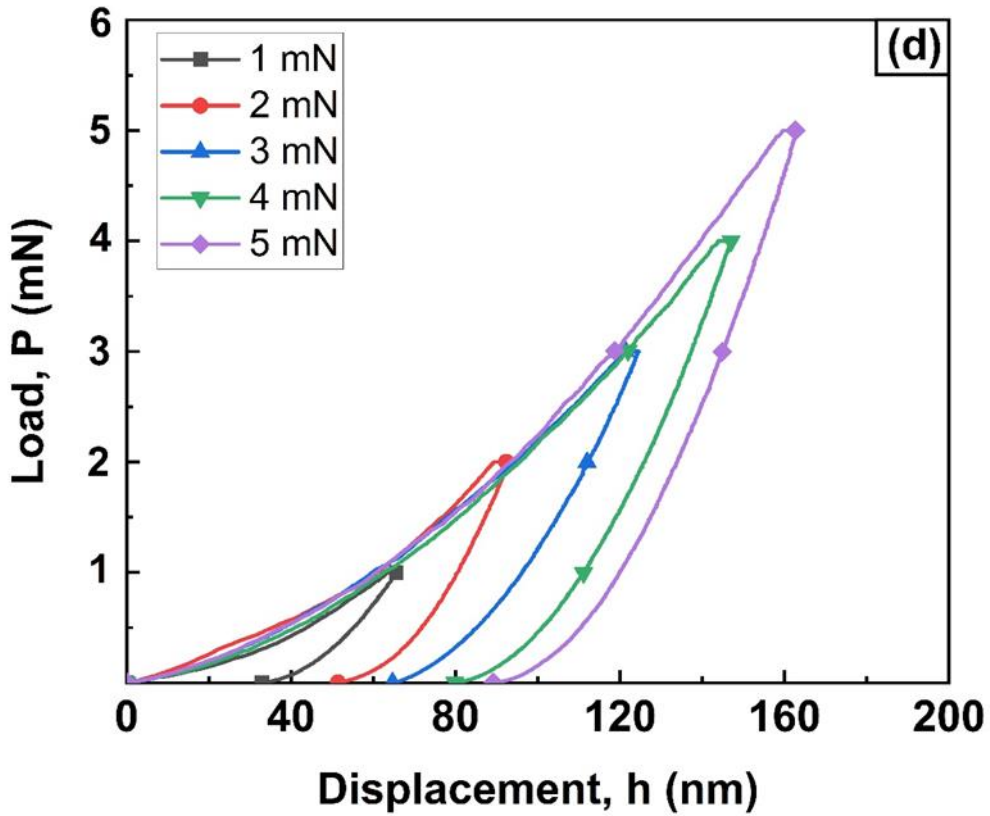
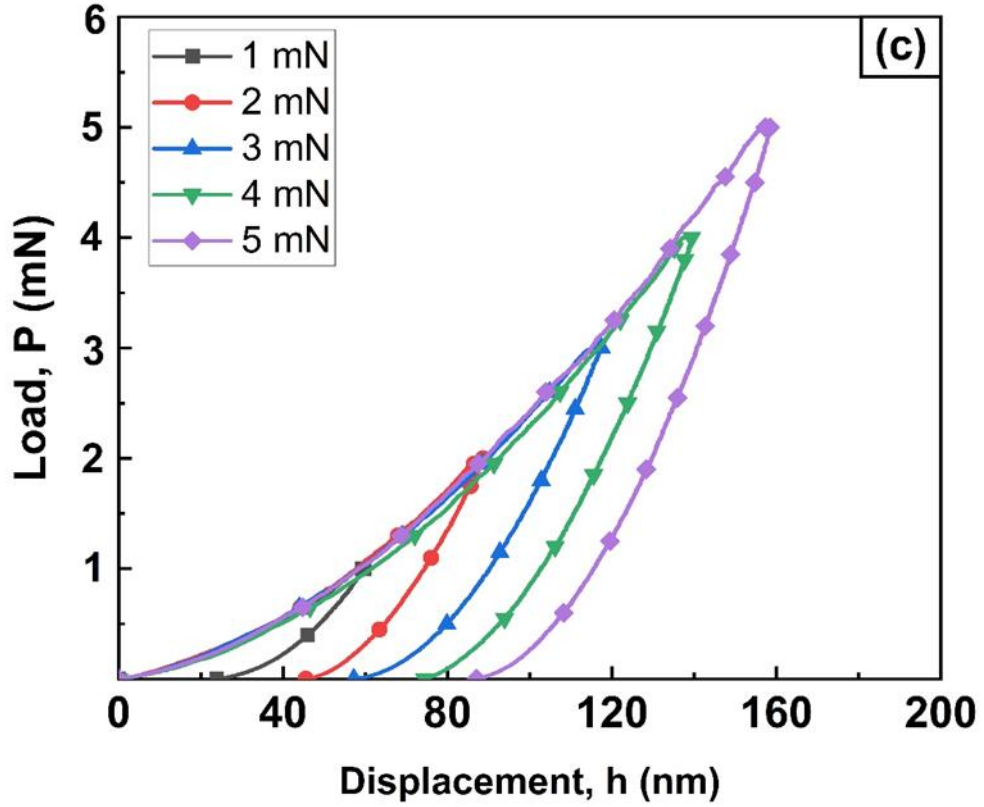


Fig. 2.4 Representative P vs. h curves for (a) AP, (b) STD ($0.6T_c$), (c) STD ($0.8T_c$) and (d) ATD samples of PMN-PT piezoceramics.

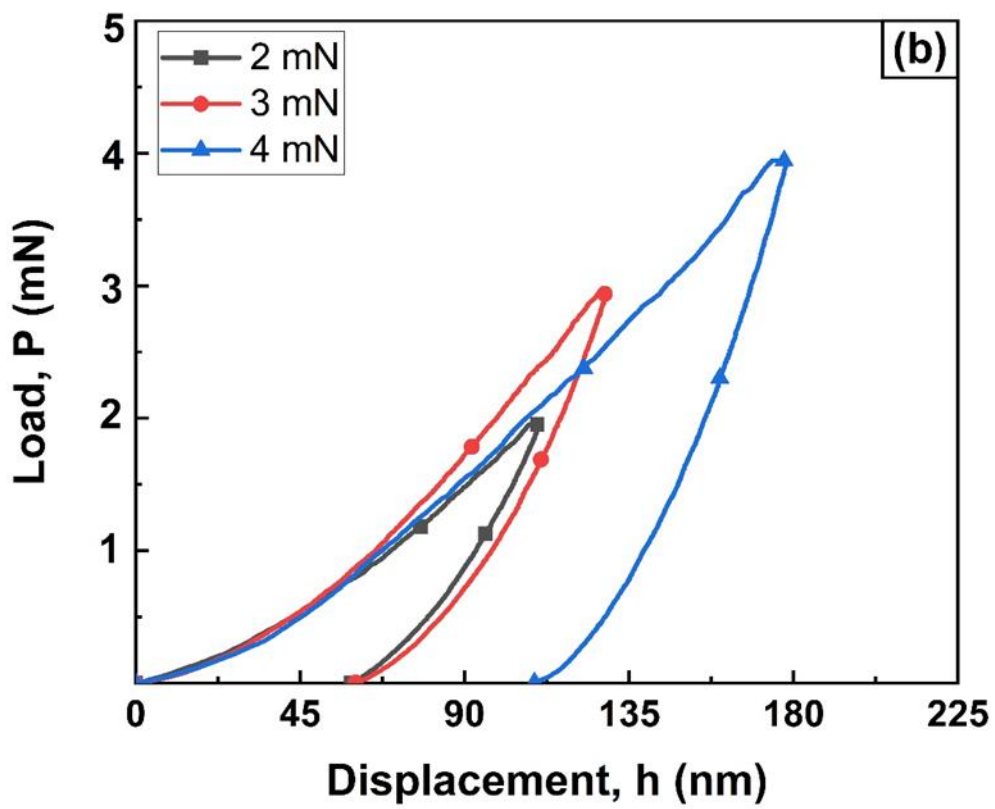
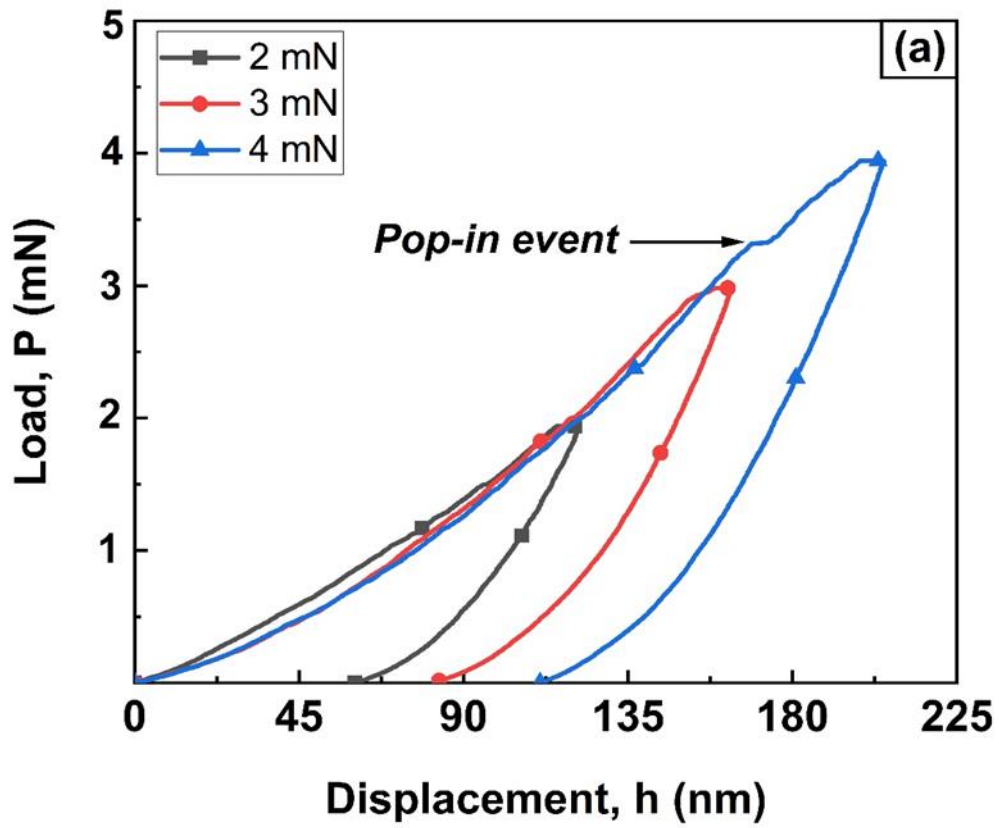


Fig. 2.5 Representative P vs. h curves for (a) AP and (b) ATD samples of NKN-NT piezoceramics.

The loading and unloading part of all the P - h curves are in good agreement with equations 3 and 4 (with a regression coefficient, $R^2 \sim 0.9999$). In addition to this, all the curves (at various P_{max}) yield a similar power-law exponent confirming a high level of repeatability and reproducibility of the results with minimum scatter in the nanoindentation data. Further, the loading part of P - h curves in PMN-PT do not show any noticeable *pop-in* events (i.e., displacement bursts) even at P_{max} of 5 mN, negating the formation of cracks during indentation. However, a caveat here is that the absence of *pop-ins* on the loading curves does not always mean that the cracks have not formed during indentation, as noticed by a recent study [Prasad and Ramesh, 2019]. For instance, *pop-in events* can be seen on the loading curves in AP samples of NKN-NT at P_{max} beyond 3 mN (Fig. 2.4a). The existence of displacement bursts in AP samples of NKN-NT is likely because of the formation of cracks beneath the indenter during relaxation of indentation stresses.

2.3.4. Variation of H with respect to P_{max} : Indentation Size Effects (ISE)

The variation in H values with respect to P_{max} for AP, STD and ATD samples of PMN-PT and NKN-NT is plotted in Fig. 2.6a and 2.6b, respectively. It is evident from Fig. 2.6 that in PMN-PT, the H for all the samples increases with P_{max} initially and decreases thereafter. On the other hand, for any given domain configuration, H decreases with P_{max} in NKN-NT piezoceramics. The increasing trend of H is referred to as a reverse indentation size effect (RISE), while the decreasing trend is referred to as normal ISE. The normal ISE is quite extensively observed in crystalline materials [Li and Bradt, 1993, Nix and Gao, 1998, Gong et al., 1999, Kathavate et al., 2018, Prasad and Ramesh, 2019], including some studies on piezoelectric materials [Zubko et al., 2007, Scholz et al., 2007, Hurtado-Macias et al., 2008 and Gharbi et al., 2009], while RISE is reported in few literature studies [Sangwal, 1989, 2000 and Li and Bradt, 1996]. The possible reasons for normal ISE in metals are the presence high density of geometrically necessary dislocations (GNDs) due to steep strain gradients beneath the indentation. On the other hand, the few limited studies conducted on different piezoelectric materials indicate that the ISE could be due to domain switching events occurring under the indentation, high GND density, and the flexoelectric phenomenon. Despite these studies, a detailed understanding of the role of ferroelectric domains on the ISE in piezoelectric materials still far from complete. Unlike ISE, the RISE in ceramics is explained by the indentation induced cracking (IIC) model proposed by Li and Bradt [Li and Bradt, 1996]. However, none of the indentation imprints show any evidence of the cracking, suggesting that the IIC model is not suitable for explaining the RISE observed in the current

study. Therefore, the observed RISE could be due to the surface irregularities generated during the sample preparation. A detailed analysis of RISE and ISE is presented in chapter 4.

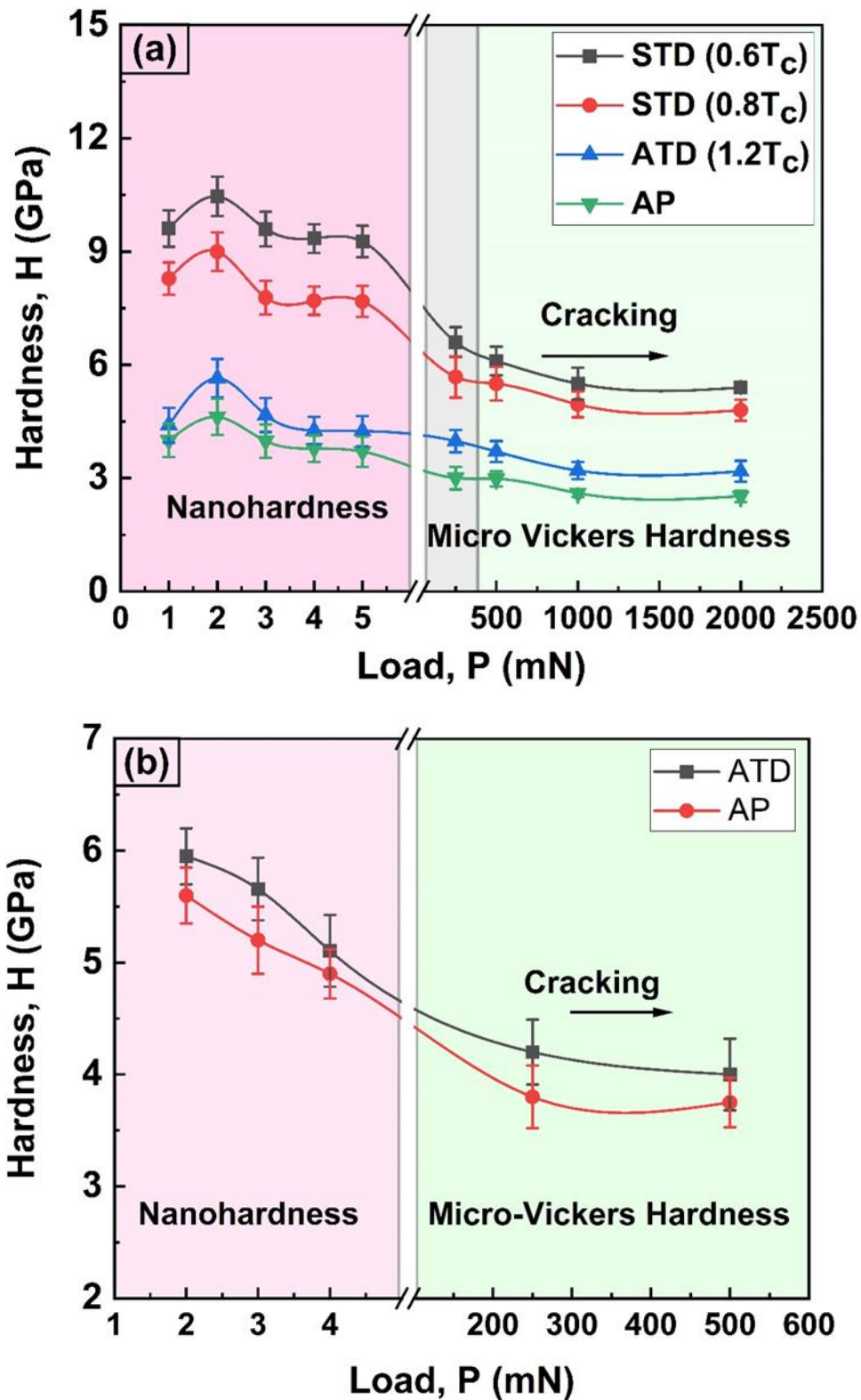


Fig. 2.6 Variation of micro and nanoindentation H with respect to P_{max} for all the samples of (a) PMN-PT and (b) NKN-NT piezoceramics.

Table 2.2 Summary of H and elastic recovery (H/E), χ values obtained from micro and nanoindentation experiments for all the samples of PMN-PT and NKN-NT piezoceramics.

Material	Structural state	Nano H (GPa) at $P_{max} = 5$ mN	Micro H (GPa) at $P_{max} = 2$ N	E (GPa)	χ (H/E)
PMN-PT	AP	4.10±0.50	2.52±0.15	101±1.54	0.040
	STD (0.6T _c)	9.80±0.75	5.40±0.15	118±2.00	0.083
	STD (0.8T _c)	7.90±1.10	4.80±0.28	110±2.20	0.071
	ATD	5.10±0.80	3.18±0.28	106±1.65	0.055
NKN-NT	AP	5.40 ± 0.12	4±0.32	68±7.37	0.078
	ATD	5.77 ± 0.37	3.75±0.22	66±4.54	0.086

The H values determined from the micro and nanoindentation experiments for all the samples of PMN-PT and NKN-NT are summarized in Table 2.2. Clearly, in both materials, annealed samples exhibit higher H values than all other samples. Interestingly, in PMN-PT, the STD samples show relatively higher H than the AP and ATD samples. These differences in H among the various samples can be attributed to the differences in (i) microstructural features such as grain size and porosity, (ii) crystal structure, (iii) ferroelectric domain configurations as a result of DE, and (iv) electro-elastic activity associated with ferroelectric domains (e.g., domain switching and/or reorientation) beneath the indenter. The difference in the d_{avg} between the AP (lowest H) and STD (highest H) samples of PMN-PT is only ~ 30%, while it is ~ 34% between the AP (lowest H) and ATD (highest H) samples of NKN-NT (within standard deviation), indicating that high H of annealed samples cannot be directly related to the differences in d_{avg} . This is obvious as the annealing at such low temperatures (i.e., ~ 1/4th or 1/5th of the sintering temperature) is not the substantial cause for the change in d_{avg} , which further indicates that the effect of d_{avg} is negligible on H . Further, the maximum penetration depth, h_{max} at P_{max} of 5 mN, is in the range 140 to 160 nm for PMN-PT, while it is 180 to 200 nm (at P_{max} of 4 mN) for NKN-NT, which is approximately 1/10th of the d_{avg} , suggesting that the indentation response is most likely comes from an individual grain and strengthening effects due to grain boundaries are negligible. Another important difference between the AP, STD and ATD samples is the amount of porosity. If the porosity is to be the reason for the observed differences in H , then P - h curves should exhibit a large scatter in H values or noticeable *pop-in events* whenever the indentations are made in the proximity of the

pores. However, such behaviour is not observed, suggesting that the variation in H must be related to the intrinsic microstructural features. On the contrary, the relatively high porosity of AP and ATD samples in PMN-PT could be due to their low H , which may have caused easy removal of material, particularly during metallographic sample preparation.

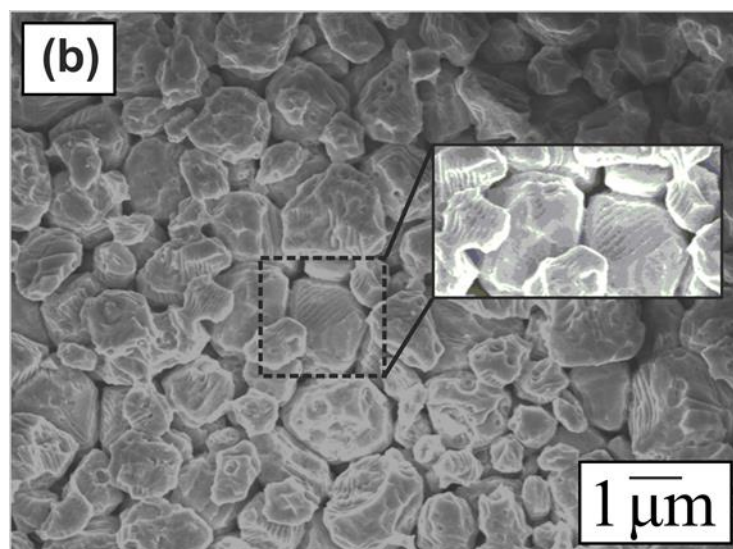
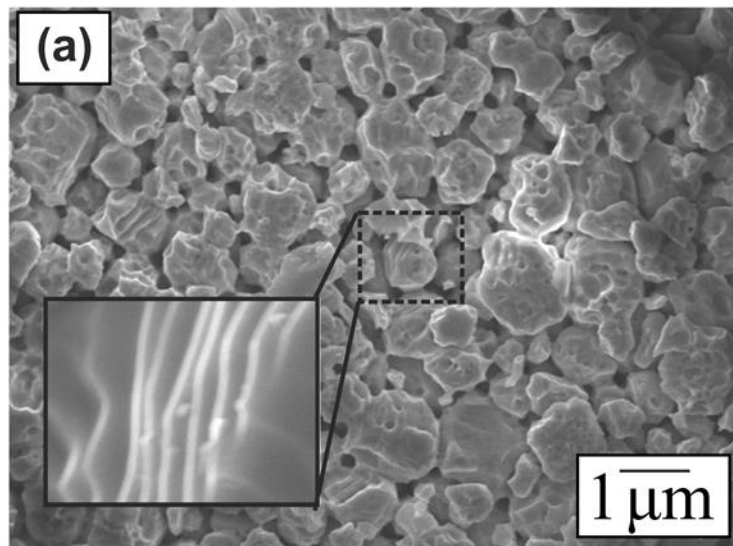
2.3.5. Role of crystal structure and crystal orientation on the mechanical properties

Wada et al. (2004), in the case of BT single crystals, have observed that dielectric and piezoelectric properties are influenced by crystal structure, crystallographic orientation, and ferroelectric domain configurations. However, in the current experiments, if the crystal structure is to be the primary reason for the observed differences in H , both the STD and ATD samples should show a similar value, which is not the case. It is well established that, in polycrystalline materials, the processing route and sintering parameters have considerable influence on the crystallographic texture. Since the annealing temperatures used in the current experiments are well below the sintering temperatures (i.e., $1/6^{\text{th}}$ for PMN-PT and $1/5^{\text{th}}$ for NKN-NT), it is reasonable to assume a similar texture for the STD and ATD samples. This further implies that the orientation of the grains also has a marginal effect on the observed differences in nanomechanical properties.

2.3.6. Role of ferroelectric domain configuration on mechanical properties

The above observations imply that the enhancement in mechanical properties must be related to the differences in ferroelectric domain configurations introduced during the annealing process. The electro-elastic nature of dipoles and domains is most likely to affect the nanomechanical properties. Fig. 2.7 (a-c) demonstrates the ferroelectric domain features of AP, STD and ATD samples of PMN-PT obtained after wet etching. The interesting feature of the observed ferroelectric domains in STD and ATD samples is that DW gets reordered into the needle-like structures, mostly having two-fold symmetry. The high contrast regions in Fig. 2.8 (a-c) of PFM images indicate the piezoactive regions, which further highlights the qualitative differences among the arrangement of ferroelectric domains in AP, STD, and ATD samples. The quantification of these regions and visualization of ferroelectric domain structure in NKN-NT Pb-free piezoceramics requires high-resolution PFM, which requires a higher voltage (~ 80 to 100 V) than the one employed in the current study (~ 5 to 10 V). Further, the d_{33} values in both the materials can indirectly give information about the amount of ordered ferroelectric domains in different samples. The d_{33} and H values for all the

samples of PMN-PT and NKN-NT are plotted against the material state and shown in Fig 2.9a and b, respectively. Unlike H , the d_{33} values follow a specific trend (AP > STD > ATD), which indicates that the degree of randomness in ferroelectric domains increases with increasing annealing temperature, as shown in the schematic Fig. 2.10. The ferroelectric domains are well aligned in AP samples, partially ordered in STD samples, and fully disordered in ATD samples. Based on these observations, it can be construed that the effect of ferroelectric domains on H is much more complex than the d_{33} values and also depends on the elastic recovery of the ferroelectric domains, domain switching mechanisms [Park et al., 2013], DW motion [Promsawat et al., 2017], dislocation mediated plasticity, and plastic strain gradients prevalent underneath the indentation.



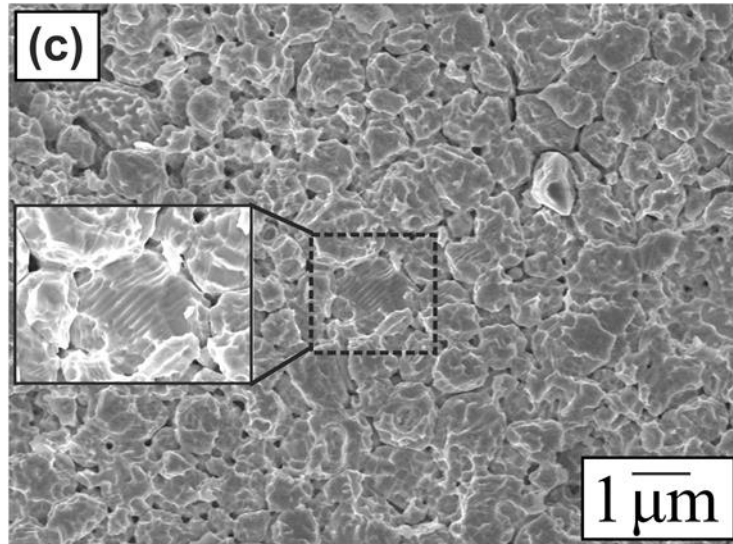


Fig. 2.7 Representative SEM images demonstrating the self-assembled ferroelectric domains after wet etching of (a) AP, (b) STD ($0.8T_c$) and (c) ATD samples of PMN-PT (magnified view of the ferroelectric domains is shown in inset).

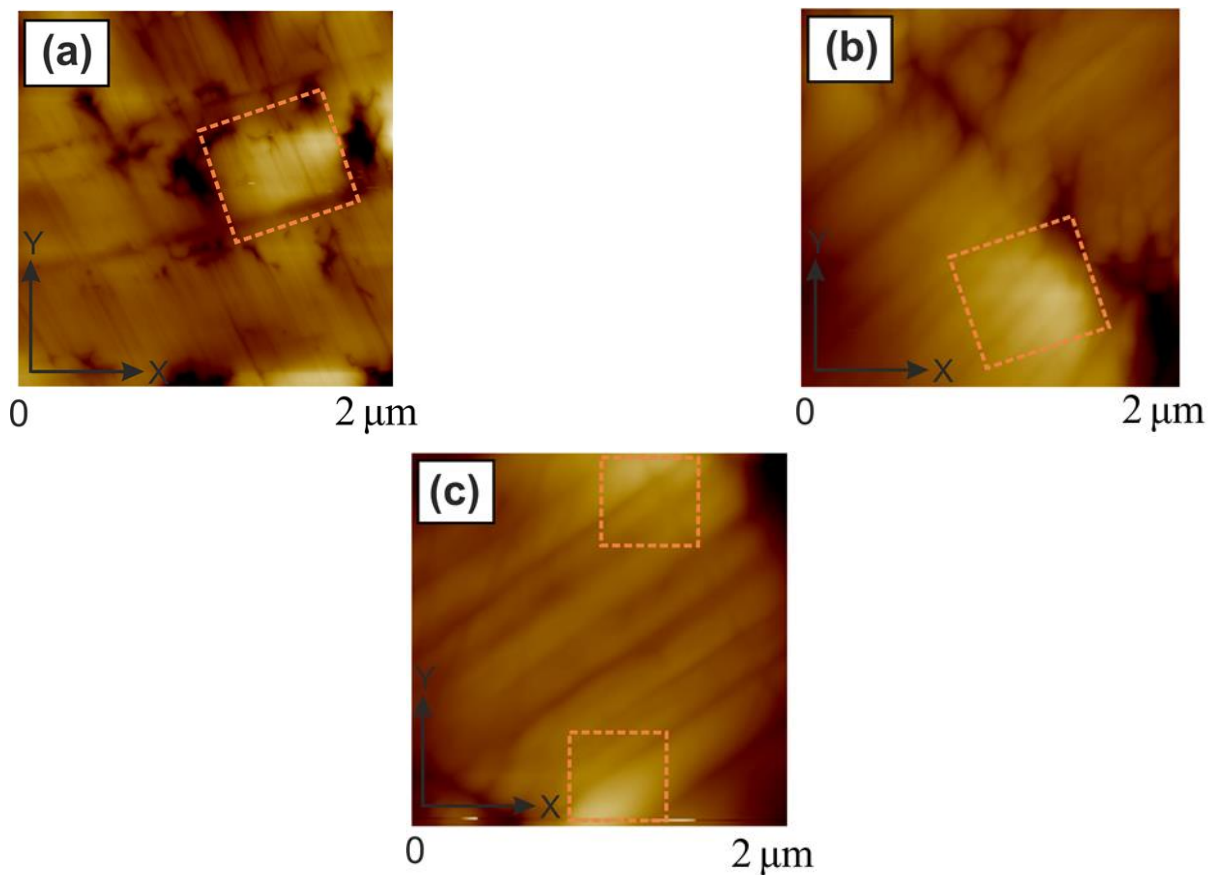


Fig 2.8 Representative PFM (PR signal) topographic images of self-assembled nanodomains in (a) AP, (b) STD ($0.8T_c$) and (d) ATD samples of PMN-PT piezoceramics. Piezoelectrically active region (high contrast region) is shown in dotted rectangle.

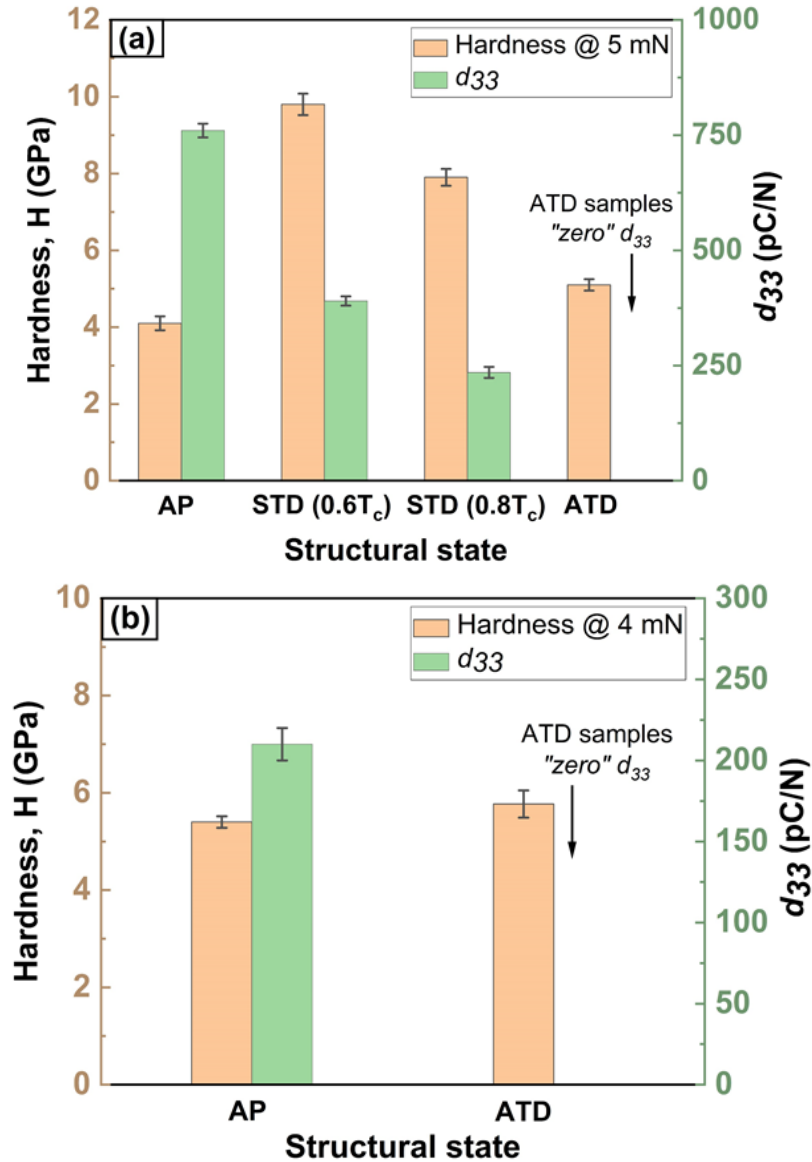


Fig. 2.9 Summary of variation in H and d_{33} values with respect to the different structural states for (a) PMN-PT and (b) NKN-NT piezoceramics.

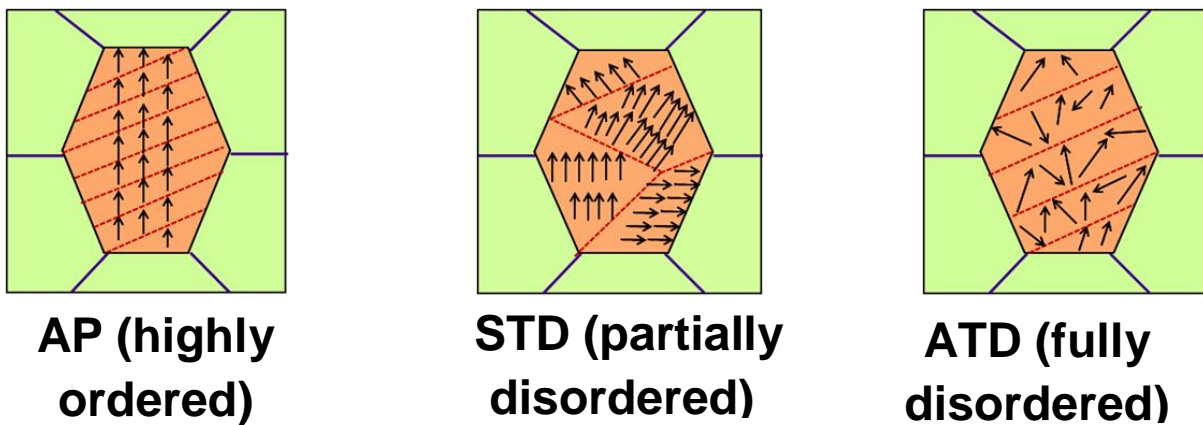


Fig. 2.10 Schematic representing the ferroelectric domain configurations in AP, STD and ATD samples of piezoceramics as a result of thermal treatment.

The electro-elastic nature of different ferroelectric domain configured samples can be estimated by the elastic recovery parameter, χ (defined as the ratio of H and E). The values of χ for all the samples of PMN-PT and NKN-NT are in the range of 0.03 to 0.08, and consistent with the literature reported values for ceramics [Peng et al., 2012]. The χ values indicate that the STD (both $0.6T_c$ and $0.8T_c$) samples of PMN-PT exhibit greater elastic recovery (more than 50%) than the AP and ATD samples, while in NKN-NT, ATD samples reflected the higher χ values than AP samples. The large elastic recovery in annealed samples of both the material could be one reason for the observed high H values in annealed samples. Further, during the elastic-plastic indentation of piezoelectric materials, besides the dislocation mediated plasticity, the ferroelectric domain structure, nature of domain switching and DW motion offers resistance to the indentation and controls H and other mechanical properties in piezoceramics. Ramamurty and co-workers (1999) have also reported higher indentation stiffness in unpoled samples (where the ferroelectric domains are completely disordered). This implies that besides the dielectric properties, orientation and alignment of DW, have a marked effect on the mechanical properties. Further, Park and Dicken [Park et al., 2007] revealed the change in the nanomechanical properties of individual ferroelectric domains (a , c^+ and c^-) due to 90° domain switching have an appreciable influence on E and H . Muñoz-Saldaña et al. (2001) and Schneider and co-workers (2005) have also observed switching of ferroelectric domains within the indented region whose rearrangement is influenced by the multiaxial stress state. Besides the ferroelectric domain switching, the DW motion may also have a considerable influence on the mechanical properties, which is largely unexplored in the literature. It appears from the H values that the partially ordered domain structure and DW boundaries offer increased resistance to the indentation compared to the AP and ATD samples in PMN-PT. Sub- T_c annealing appears to have imposed high residual stresses on the DW due to the local changes in the ferroelectric domain structure, which can also be one of the possible reasons for high H . However, a comprehensive understanding of the role of annealing temperature on ferroelectric domain configurations needs to be investigated in details. Although the SEM and PFM images indicate the qualitative differences between the nature of the ferroelectric domains in the different samples, the domain interaction underneath the indenter and role of strain gradients is needed further investigation. However, the current study demonstrates the possibility of enhancing the H via ferroelectric DE technique, making PMN-PT and NKN-NT piezoceramics suitable for improved wear resistance applications.

2.4. Summary

In summary, the micro and nanoindentation experiments are performed on the PMN-PT and NKN-NT piezoceramics with different ferroelectric domain configurations obtained *via* thermal annealing. The experimental observations from the present chapter can be summarized as follows;

- Sub- T_c annealing of the PMN-PT piezoceramics leads to a pronounced increase in H (~ 2 – 2.5 times that of the AP samples), while above- T_c annealing in NKN-NT marginally tailors the H values with a concomitant decrease in d_{33} values in both the materials.
- The DE *via* annealing treatment causes significant changes in the ferroelectric domain configurations, thereby enhancing mechanical properties. The sub and above- T_c annealing cause a change in the crystal structure of both the materials, and it appears to have less influence on the mechanical properties.
- In the STD and ATD samples, the reorientation of ferroelectric domains induces significant incompatibility in stresses at the DW boundaries, sometimes leading to cracking in some of the grains.
- A higher elastic recovery is observed in the STD samples than the AP and ATD samples of PMN-PT, while in NKN-NT, ATD samples exhibit a higher elastic recovery, which corroborates with the observed H values.

CHAPTER 3

Mechanisms of enhanced mechanical response of polycrystalline hard and soft-doped PZT *via* domain engineering technique

Abstract: The effect of different ferroelectric domain configurations on the strengthening mechanisms in polycrystalline aliovalent cation doped hard and soft PZT is explored in this chapter. Different ferroelectric domain configurations in as-poled samples of both the PZTs are obtained by employing a domain engineering technique *via* thermal annealing at selective temperatures (i.e., below and above Curie temperature, T_c), which are subsequently characterized by piezoresponse force microscopy. A series of nano and microindentation experiments are performed on all the different domain configured samples of hard and soft PZT over a range of indentation loads. The viable strengthening and toughening mechanisms in both the PZTs are explored. Further, a detailed discussion is provided highlighting the role of ferroelectric distortion and defect vacancies on the indentation response of polycrystalline piezoceramics¹.

3.1. Introduction

The solid solution of PbZrO_3 and PbTiO_3 , lead zirconate titanate (abbreviated as PZT) represents the class of perovskite-oxide system (ABO_3) are the potential candidates in many electronics applications such as transducers, piezo generators and piezo actuators due to their excellent electrical-mechanical properties [Jaffe et al., 1971, Takahashi 1982, Pisarenko et al., 1985, Mock et al., 2009]. During service, the self-heating of piezo actuators is a common issue, and these devices experience high mechanical stresses at high cycle frequencies leading to large strain incompatibilities and significant hysteresis in the material which mainly arises due to the reorientation of ferroelectric domains and depolarization. Therefore, practical applications of PZT as an actuator in military impact fuzes and fuel injection systems demand the reliability of these devices at high temperatures [Mock et al., 2009].

¹ The work presented in this chapter is based on the following publications:

[1] V.S. Kathavate, H. Sonagara, B. Praveen Kumar, I. Singh, K. Eswar Prasad, Tailoring nanomechanical properties of hard and soft PZT *via* domain engineering by selective annealing, Mater. Today Comm., 28 (2021) 102495.

[2] V.S. Kathavate, H. Sonagara, B. Praveen Kumar, I. Singh, K. Eswar Prasad, Direct observations of changes in ferroelectric domain configurations around the indentation and ahead of the crack in soft-doped PZT, Materialia, 19 (2021) 101191.

Over the years, considerable efforts have been put to improve the electrical and mechanical performance of PZT by controlling the microstructural features such as grain size and ferroelectric domain configurations [Kugel and Cross, 1998, Galassi et al., 1999, Morozov and Damjanovic, 2010, Li et al., 2015, Horchidan et al., 2016, Promsawat et al., 2017, Limpichaipanit et al., 2018, Huang et al., 2019]. Further, the high-temperature performance of PZT can also be tailored by the addition of aliovalent donor/acceptor cations in PbZrO_3 - PbTiO_3 lattice which differentiates the “hard” and “soft” characteristics in PZT [Kugel and Cross, 1998, Morozov and Damjanovic, 2010, Horchidan et al., 2016, Promsawat et al., 2017].

The addition of aliovalent dopants control the ferroelectric domain configurations and defect vacancies thereby effect the polarization and depolarization behaviour of hard PZT (abbreviated as PZT-H) and soft PZT (abbreviated as PZT-S) [Morozov and Damjanovic, 2010, Horchidan et al., 2016, Promsawat et al., 2017]. The acceptor aliovalent cations such as K^+ , Na^+ replace “A” site cations and Al^{3+} , Mn^{3+} , Fe^{3+} replace “B” site cations when doped in PbZrO_3 - PbTiO_3 , and tends to form PZT-H, while PZT-S are obtained when “A” and “B” sites respectively are replaced with aliovalent dopants such as La^{3+} , W^{6+} and Nb^{5+} , Sb^{5+} cations [Morozov and Damjanovic, 2010, Horchidan et al., 2016, Promsawat et al., 2017]. PZT-H retain their structural stability under high electrical and mechanical stresses thereby making them suitable for high power applications, while PZT-S are mainly used in the high-precision actuator applications due to their superior ferroelectric behaviour such as high electro-mechanical coupling coefficient, k_{33} and piezoelectric charge coefficient, d_{33} [Kugel and Cross, 1998].

In piezoceramic perovskites, the formation of ferroelectric domains is attributed to the alignment of dipoles along distinct polarization directions. Several studies [Zhang et al., 1994, Zhang et al., 2001, Wada et al., 2004, Shur, 2006, Njiwa et al., 2006, Pramanick et al., 2011, Wang et al., 2013, Chang et al., 2018, Pramanik et al., 2019], in the past, have focused on understanding the effects of ferroelectric domain size, domain walls (DW), and interdomain spacing on the electrical properties of piezoceramics. Domain engineering (DE) methods have been adopted by modifying the crystal structure [Wada et al., 2004], controlling the grain size [Shur, 2006, Pramanick et al., 2011, Wang et al., 2013, Pramanik et al., 2019], nano-patterning [Chang et al., 2018], altering remnant polarization, and imposing mechanical stresses during poling [Njiwa et al., 2006]. For instance, Wada et al. (2004), in the case of single-crystal BaTiO_3 , demonstrated a 200% increase in d_{33} by modifying the

crystal structure with different engineered ferroelectric domain configurations. [Shur \(2006\)](#) suggested that merging of neighbouring DW within an individual grain might accelerate the depolarization in the material, which influences the piezoelectric performance of Pb-free piezoceramics. [Pramanick et al. \(2011\)](#) have observed that a decrease in grain size (~50 %) due to the addition of dopants causes a respective increase in the polarization and d_{33} values by ~ 166% and ~ 4 times, respectively, which is attributed to the increased contributions of non-180° DW motions (at nanoscale) and lattice strain incompatibilities. Recently, [Chang and co-workers \(2018\)](#) have shown an increase of ~ 36% and ~ 38% in d_{33} and dielectric constant, ϵ_d respectively, by texturing with MnO_x semiconductor nano-patterns on single-crystal PMN-PT. Among all the DE methods, thermal annealing is cost-effective and less tedious as it requires a simple non-oxidative furnace set up. [Kathavate and co-workers \(2018\) \(2020\)](#) have selectively annealed the NKN-NT (Pb-free) and PMN-PT piezoceramics below and above their Curie temperatures, T_c , and observed a change in d_{33} and nanomechanical properties which is attributed to the annealing induced ferroelectric domain randomization (indirectly determined from the d_{33} values) although it was not fully characterized.

Recent developments in instrumented indentation techniques (IITs) such as nanoindentation and piezoresponse force microscopy (PFM) offer the *in-situ* characterization of the structural properties of the bulk ceramics at small length scales. Previous nanoindentation experiments, particularly on conventional single-crystal BT and PZT have witnessed the ferroelectric domain rearrangement and domain switching underneath the indenter [[Schneider et al., 2005](#), [Scholz et al., 2007](#), [Park et al., 2007](#), [Wong and Zeng, 2008, 2010](#)], existence of the flexoelectric effect [[Gharbi et al., 2009](#)], and dislocation mediated slip [[Wong and Zeng, 2008, 2010](#) and [Mathews et al., 2020](#)] as the primary modes of deformation. Though there are no direct/clear microstructural evidence, the possible reasons for the observed anisotropy is attributed to the ferroelectric domain switching at the crack tip and reversible pressure-induced phase transformation in the material. For instance, a few studies [[Glazounov et al., 2001](#), [Jones and co-workers, 2005, 2006, 2006](#) and [Daniels et al., 2006](#)] have been focused in understanding the changes taking place in the ferroelectric domain configuration as a result of deformation and fracture using indirect methods such as X-ray and neutron diffraction. [Glazounov et al. \(2001\)](#) and [Jones and Hoffman \(2006\)](#) have observed a significant reorientations of ferroelectric domains on the fracture surface and argued that this could be one of the toughening mechanism in piezoceramics. Jones and co-workers [[Jones and co-workers, 2005, 2006](#), [Daniels et al., 2006](#) and [Tutuncu et al., 2014](#)]

have reported that ferroelectric distortion and domain wall (DW) motion (both 90° and 180°) are the primary mechanisms responsible for the dynamic piezoresponse and giant electro-mechanical strain (~ 0.1%) in PZT and BZT-BCT piezoceramics. Further, the above studies [Jones and co-workers, 2005, 2006, Daniels et al., 2006 and Tutuncu et al., 2014] also indicated that the grain size, d_{avg} and relative density, ρ_r of the samples have negligible influence on the DW density and ferroelectric domain mobility. All the studies (except for the works of Schneider et al., 2005) conducted hitherto do not characterize the local ferroelectric domain activities around the indentation zone and hence the conclusions are mostly based on indirect arguments. It is interesting to see the changes in ferroelectric domain configurations taking place around the indentation zone with the help of indentation and PFM experiments.

In earlier work on undoped PZT [Kathavate et al., 2018], it was observed that the randomization of ferroelectric domains favours the increase in nanohardness, H . The doped PZTs (doping with aliovalent acceptor/donor cations) offers superior piezoelectric properties compared to the undoped PZTs and hence are an ideal choice for the high-temperature applications. The role of ferroelectric domain configurations on the electro-mechanical properties of aliovalent cation doped PZTs is not studied in detail, and it would be interesting to examine the effect of changes in the ferroelectric domain configurations on the mechanical behaviour of these materials.

In view of this, the ferroelectric domain configurations of polycrystalline PZT-H and PZT-S are systematically varied by selectively annealing the as-poled (AP) samples below and above the T_c , respectively. A detailed characterization of the ferroelectric domain configurations of the poled and depoled samples is conducted using PFM. Nanoindentation experiments are then performed on the poled and depoled samples with an objective to understand the effect of differences in ferroelectric domain configuration on the mechanical behaviour of doped PZTs. Furthermore, we have characterized the ferroelectric domain configurations in the plastically deformed zone (PDZ), around and ahead of the crack tip of Vickers indentation imprint to understand the effect of deformation on the ferroelectric domain configurations.

3.2. Materials and Experiments

3.2.1. Materials and sample preparation

The test materials used in this study are undoped PZT (abbreviated as PZT-U), K^{1+} acceptor-doped PZT-H and La^{3+} donor-doped PZT-S piezoceramics fabricated *via* solid-state reaction

route. High-quality precursors of PbO (Qualigens, 98% pure), ZrO₂ (99% pure), and TiO₂ (TTK products, 98.5% pure) are uniformly mixed in the stoichiometric ratio (PbZr_{0.52}Ti_{0.48}O₃) for PZT-U, Pb_{0.98}K_{0.02}(Zr_{0.47}Ti_{0.51}Al_{0.02})O₃ for PZT-H and Pb_{0.98}La_{0.02}(Zr_{0.47}Ti_{0.51}Nb_{0.02})O₃ for PZT-S followed by ball milling for 48 h. The ball-milled powders are subjected to calcination at 900 °C for 4 h to remove the impurities, if any. Further, the calcinated powders are ball-milled again using ethanol as a medium for 24 h to ensure homogenous mixing and avoid the agglomeration of particles, if any. The mixture is then granulated in 10% (vol.) polyethylene glycol solution to improve the flowability and cold consolidation behaviour. Subsequently, the calcinated powders are hot-pressed into disc shape pellets having a diameter of 25 mm and thickness of 2 mm followed by sintering in ZrO₂ crucibles at 1200 °C for 2 h. The discs are then coated with conductive silver paste followed by electrode firing along thickness in a silicon oil bath (at 60 °C with an applied electric field 20 kV/cm for PZT-U, 10 kV/cm for PZT-H and 40 kV/cm for PZT-S).

The mechanical quality factor, Q_m of as poled (AP) samples of PZT-H and PZT-S is determined to be 450 and 85, respectively via electrical power method with high frequency (12 Hz to 120 MHz) impedance analyser. The obtained Q_m values are in agreement with the reported values in the literature [Mazheritsky, 2002]. The Q_m values in PZT are reported to decrease with an increase in temperature near the T_c [Mazheritsky, 2002]. However, this requires high frequency equivalent electric circuit set up, which is beyond the scope of the present study (since the present study is centred on probing the mechanical properties and strengthening behaviour of the PZT). The T_c of PZT-U, PZT-H and PZT-S is determined to be 250, 300 and 350 °C, respectively [Promsawat et al., 2017]. Previous studies have shown that annealing of piezoceramic materials near T_c causes randomization of ferroelectric domains [Zhang et al., 1994, Wada et al., 2004, Limpichaipanit et al., 2018, Huang et al., 2019]. Therefore, the AP samples of all the PZTs are selectively annealed in an Argon controlled atmosphere (furnace-INDFURR) at 0.8 T_c and 1.2 T_c with a 2h holding time to obtain samples with different ferroelectric domain configurations. The 0.8 T_c and 1.2 T_c annealed samples of both the PZTs are hereafter referred to as sub- T_c depoled (STD) and above- T_c depoled (ATD), respectively. Different steps involved in sample fabrication, specimen preparation, and DE technique along with a schematic describing the different ferroelectric domain configurations of AP, STD and ATD samples are presented in Fig. 3.1. The d_{33} of all the samples is determined at room temperature at vibratory shake force 250 mN and frequency 110 Hz using piezo d_{33} meter (SINOCERA Model- YE2730A).

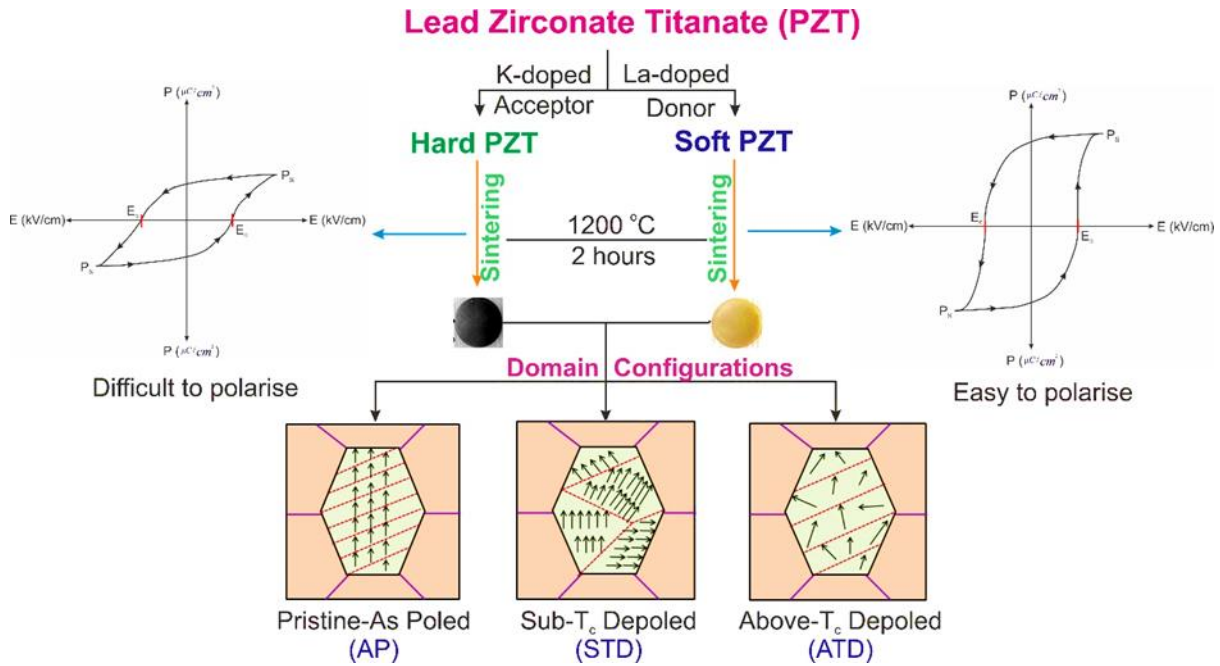


Fig. 3.1 Schematic showing the doping, sintering, and annealing procedure for obtaining different domain configurations in PZT-H and PZT-S.

3.2.2. X-ray Diffraction (XRD) and Microstructural Characterization

The presence of phases and crystal structures of AP, STD, and ATD samples of PZT-U, PZT-H and PZT-S is determined using X-ray diffractometer (Rigaku Smart Lab). Diffraction data is collected at 2θ position in the range of $20-80^\circ$ ($Cu/K\alpha$ radiation, $\lambda=1.54\text{\AA}$) at room temperature with slow scan speed in the step size of 0.02° . The XRD data is then analyzed using standard powder diffraction database (JCPDS) to identify the crystal structure and phases present. The grain size of the samples is determined using field emission-scanning electron microscope (FE-SEM, JEOL JSM-7610FPlus) following standard metallographic sample preparation methods with polishing the samples to a surface finish of $0.25\ \mu\text{m}$ and subsequently etching in 48% (vol.) HF for 2 min followed by 37% (vol.) HNO_3 for 1 min in deionized water. The d_{avg} is calculated using Image J software by maintaining suitable contrast over a sufficiently large number of grains. To confirm the stoichiometric amounts of the constituents, energy dispersive spectroscopy (EDS) (Quantt program) is performed in conjunction with FE-SEM.

3.2.3. Mechanical characterization: Nano and microindentation experiments

Quasistatic nanoindentation experiments are performed on AP, STD and ATD samples of PZT-U, PZT-H and PZT-S in load controlled mode using Bruker Hysitron TI nanoindenter.

All the experiments are conducted with three-sided pyramidal Berkovich indenter at room temperature in the load range of 1 to 5 mN with an interval of 1 mN, constant loading/unloading rate of 0.1 mN/s, and a dwell time of 2 s at P_{max} . The area function, $A(h_c)$ of the indenter is calibrated using a standard quartz sample in the depth range of 50-200 nm. A maximum of 20 indentations are performed at each P_{max} to obtain a statistically representative data. The spacing between successive indentations is taken as 10 times the maximum penetration depth, h_{max} to avoid the strain field interactions of indents. The hardness, H of all the samples is determined using Oliver and Pharr (O&P) method [Oliver and Pharr, 1992] and details of which are mentioned in equation 1;

$$\text{Hardness, } H = \frac{P_{max}}{A(h_c)} \quad (1)$$

Here, P_{max} and h_c specify the maximum indentation load and contact depth, respectively and area function $A(h_c)$ computed from the experiment. After nanoindentation experiments, the micro-Vickers indentation experiments on the AP, STD and ATD samples of PZT-H and PZT-S are performed using a microhardness tester (Micro-Mach Technologies Ltd., Pune) equipped with the Vickers tip in the load range of 0.25 to 2 N with a nominal velocity of Vickers indenter 60 $\mu\text{m/s}$ and a dwell time 10 s at P_{max} . The Meyer's hardness (HV) values from the micro-Vickers indentation experiments are obtained dividing the P_{max} by projected area [Meyer, 1908]. Further, the indentation fracture toughness, K_{IC}^i from the micro-Vickers indentation experiments is determined using the below equation 2 and the details of which are mentioned elsewhere in the ref. [Lawn and Brown, 1977];

$$K_{IC}^i = 0.0016 \left(\frac{E}{H} \right)^{1/2} P_{max} c^{-3/2} \quad (2)$$

Here, c represents the crack length from the centre of the indentation impression. The respective E values for PZT-H and PZT-S are determined to be in the range of 125 GPa to 152 GPa.

3.2.4. Domain visualization - Piezoresponse Force Microscopy (PFM)

The ferroelectric domain configurations (which comprises of "c" and "a" domains) of AP, STD and ATD samples of PZT-H and PZT-S are characterized using piezoresponse force microscope (PFM) (Park-NX Wafer, model-NX20) over an area of 4 μm^2 using Ti/Ir coated conductive cantilever tip (curvature ~ 20 nm). The PFM signals are obtained in contact mode at the DC drive voltage range of 3 to 5 V and a scan frequency of 0.5 Hz. The cantilever is

held at a spring constant and resonant frequency of ~ 2 N/m and 17 kHz, respectively. To probe the local ferroelectric domain switching characteristics, piezoresponse force spectroscopy (SS-PFM) is employed at ramped AC voltage ± 10 V to capture the amplitude, A_m vs. bias, V_B (butterfly loop) and phase shift, θ vs. bias, V_B (hysteresis loop) response.

3.3. Results and Discussion

3.3.1. Effect of DE on crystal structure and microstructures of PZT-U, PZT-H and PZT-S

Room temperature XRD spectra of AP, STD, and ATD samples of PZT-U, PZT-H and PZT-S are shown in Figs. 3.2(a-c), respectively which shows the presence of single perovskite phase (JCPDS card no. 73-2022 for PZT-U, and 33-0784 for PZT-H and PZT-S). No secondary phase formation has been observed within the error limit of diffractometer sensitivity. The absence of small peaks in the XRD patterns of PZT-H and PZT-S demonstrate that the aliovalent cations are completely diffused in the PbZrO_3 - PbTiO_3 lattice, confirming the phase purity and good quality of ceramics. PZT ceramics in AP condition are reported to exhibit the rhombohedral and tetragonal symmetry composition below and above the morphotropic phase boundary (MPB), respectively with a small fraction of cubic phase [Noheda and co-workers, 2000] which is indicated by the (111) peak around 37.5° . The presence of pure rhombohedral phase in AP samples of PZT-U indicates that the stoichiometric proportions of oxides are well below the MPB, while presence of pure tetragonal phase ($\sim 88\%$) in AP samples of PZT-H and PZT-S reflects the composition above MPB. One of the possible reasons for this is the addition of aliovalent acceptor/donor dopants which significantly shifts the crystal structure in PZT. Further, the texture and fraction of highly oriented ferroelectric domains are expected to change with annealing, affecting the d_{33} values (as presented in Table 3.1) and consistent with the phase diagram of PZT [Noheda et al., 2000]. It also appears that the STD and ATD samples of PZT-H exhibit symmetric peak splitting of (001) // (100) planes (Fig. 3.2a), while the PZT-S exhibit asymmetric peak splitting of (002) // (200) planes (Fig. 3.2b). These peak splitting (resolved view) are shown in Fig. A2 of Appendix 1. A priori, one would expect this peak splitting probably due to the size mismatch between aliovalent cations in the PbZrO_3 - PbTiO_3 lattice because of the selective annealing treatment. However, the grain rotations are not expected as the annealing temperature is well below ($< 1/4^{\text{th}}$ of sintering temperature) the sintering temperatures and can only lead to changes in ferroelectric domain configurations.

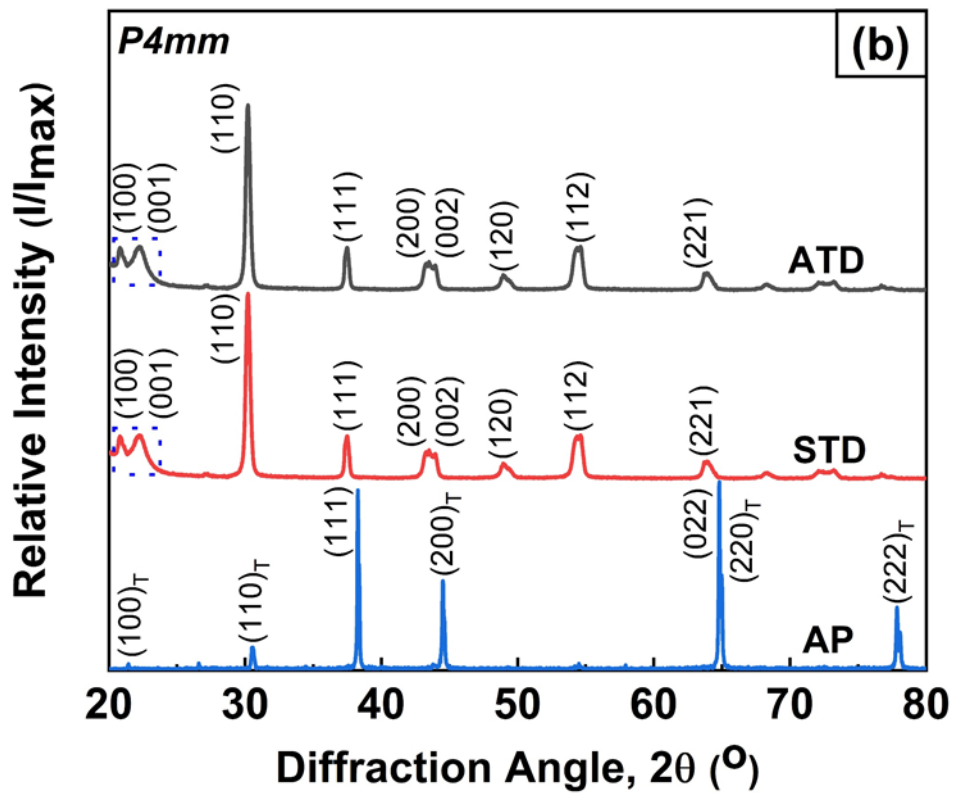
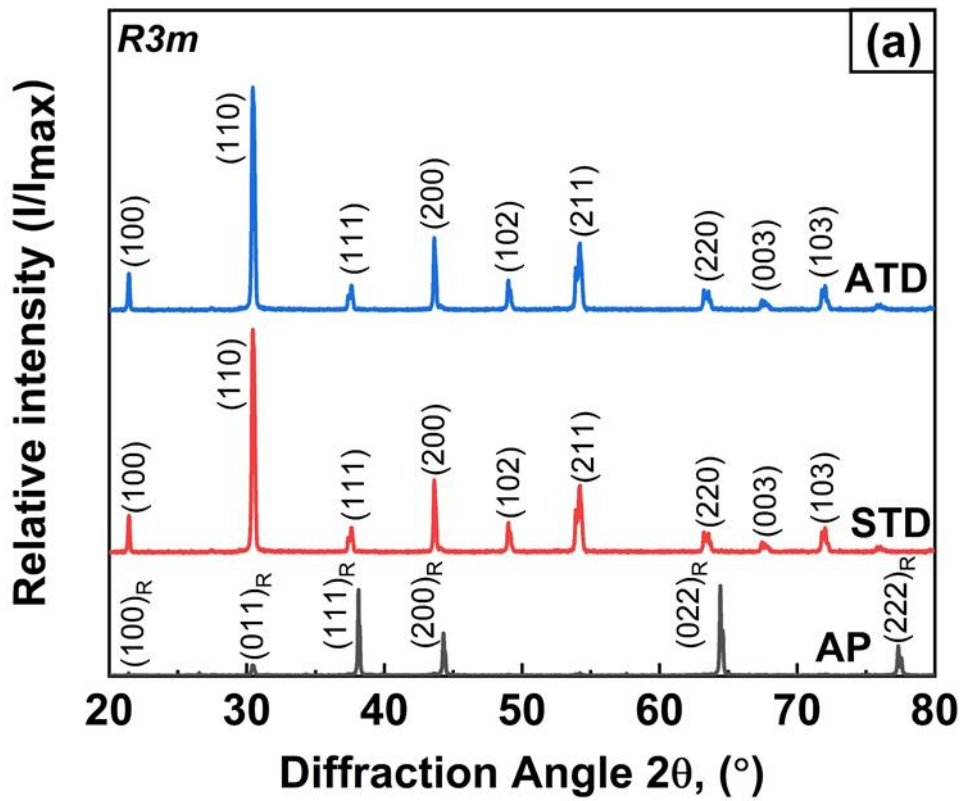
PZT and other piezoceramics are reported to exhibit the distinct peak splitting due to the size misfit between the A-site and B-site ions which further leads to the variation in tetragonality, measured as the lattice parameter ratio between the crystallographic c and a direction [Li et al., 2020, Jin 2011, Hoffmann et al., 2008]. In present work, it is found that the tetragonality of AP samples decreases from 1.025 for PZT-H to 1.018 for PZT-S (Table 3.1), and the amount of cubic phase increases marginally from $\sim 12\%$ for PZT-H to $\sim 13\%$ for PZT-S which is also evident from the peak splitting of (001) // (100) planes (for PZT-H) and (002) // (200) planes (for PZT-S). The decrease in tetragonality also indicates the transition of PZT, albeit slightly, from tetragonal to rhombohedral symmetry [Bijalwan et al., 2018]. Further, the peak splitting in both the PZTs due to size misfit of A-site and B-site cations is analysed using Goldschmidt tolerance (GT) factor (as described Eq. 3) and details of which can be found in ref. [Goldschmidt, 1926]

$$GT = \frac{(R_A + R_O)}{\sqrt{2}(R_B + R_O)} \quad (3)$$

Here, R_A , R_B , and R_O represents the ionic radii of A-site, B-site and O atoms, respectively in ABO_3 perovskite. The GT values represent the structural changes such as lattice distortions, octahedra tilting, and displacement of cations from ideal packing positions [Goldschmidt, 1926]. The marginal decrease in GT values 0.2% for PZT-H and 0.3% for PZT-S manifests the structural disorder in the crystal arising mostly due to the increased contributions from multiple cations which replace the A-site and B-site ions. This could be further attributed to the relative change in the ionic radii of A-site and B-site cations due to the substitution of Pb^{2+} (1.49 Å) with K^+ (1.38 Å) and Ti^{4+} (0.605 Å) with Al^{3+} (0.538 Å) in PZT-H and Pb^{2+} (1.49 Å) with La^{3+} (1.34 Å) and Ti^{4+} (0.605 Å) with Nb^{5+} (0.505 Å) in PZT-S which further likely to increase the localized distortion in the crystal. This highlights the relative importance of the addition of aliovalent dopants on the lattice distortion, which affects the domain configurations of the $PbZrO_3$ - $PbTiO_3$ perovskites.

The representative microstructures of AP, STD and ATD samples of PZT-U, PZT-H and PZT-S are shown in Figs. 3.3, 3.4 and 3.5, respectively. The d_{avg} of all the samples determined using linear intercept method (following ASTM E112-113) is presented in Table 3.2. A similar d_{avg} is observed for all the samples indicating the annealing temperatures used in the experiments does not influence the grain growth [Kathavate et al., 2018, 2020]. Further, the stoichiometric ratios are calculated from EDS mapping of PZT-H and PZT-S,

and shown in Figs. A3 and A4 (in Appendix 1) are in agreement with those used in the actual synthesis.



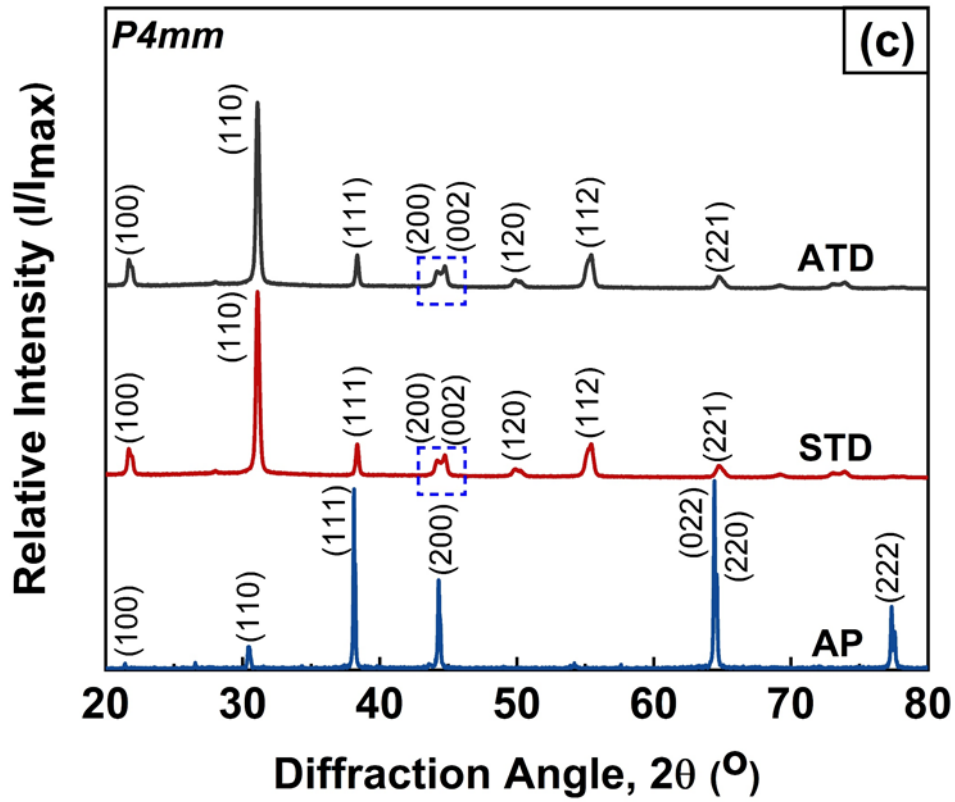


Fig. 3.2 Representative XRD patterns of AP, STD and ATD samples of (a) PZT-U, (b) PZT-H and (c) PZT-S. The subscript “R” and “T” represents the rhombohedral and tetragonal phase, respectively.

Table 3.1 Summary of the XRD results, d_{33} and d_{33}^* values obtained for AP, STD and ATD samples of PZT-U, PZT-H and PZT-S.

Material	Domain configuration	Crystal Structure	Lattice parameters, a and c (Å)	Tetragonality ratio (c/a)	d_{33} (pC/N)	$d_{33}^* \times 10^3$ (pm/V)
PZT-H	AP	Tetragonal	$a = 4.72,$ $c = 4.83$	1.025	315±5	18.63±2
	STD	Near-cubic	$a = 4.08,$ $c = 4.08$	--	148±3	5.10±1
	ATD	Near-cubic	$a = 4.08,$ $c = 4.08$	--	0	0
PZT-S	AP	Tetragonal	$a = 4.68,$ $c = 4.76$	1.018	465±7	195.2±15
	STD	Near-cubic	$a = 4.03,$ $c = 4.03$	--	220±5	112.78±7
	ATD	Near-cubic	$a = 4.03,$ $c = 4.03$	--	0	0
PZT-U	AP	Rhombohedral	--	--	90±3	--
	STD	Near-cubic	--	--	38±2	--
	ATD	Near-cubic	--	--	0	--

Table 3.2 Summary of d_{avg} and H values obtained for AP, STD and ATD samples of PZT-U, PZT-H and PZT-S.

Material	Domain configuration	d_{avg} (μm)	Nano H (GPa) at $P_{max} = 5 \text{ mN}$	Micro H (GPa) at $P_{max} = 2 \text{ N}$
PZT-U	AP	1.52±0.19	5.80±0.70	---
	STD	1.40±0.12	6.50±0.80	---
	ATD	1.88±0.23	7±0.80	---
PZT-H	AP	1.10±0.15	6.57±0.75	4.15±0.30
	STD	1.68±0.38	7.50±0.60	4.70±0.38
	ATD	2.20±0.40	8.70±0.80	5.10±0.30
PZT-S	AP	1.50±0.20	6.57±0.75	4.60±0.28
	STD	1.98±0.35	7.50±0.60	5.40±0.30
	ATD	2.60±0.40	8.70±0.80	5.70±0.32

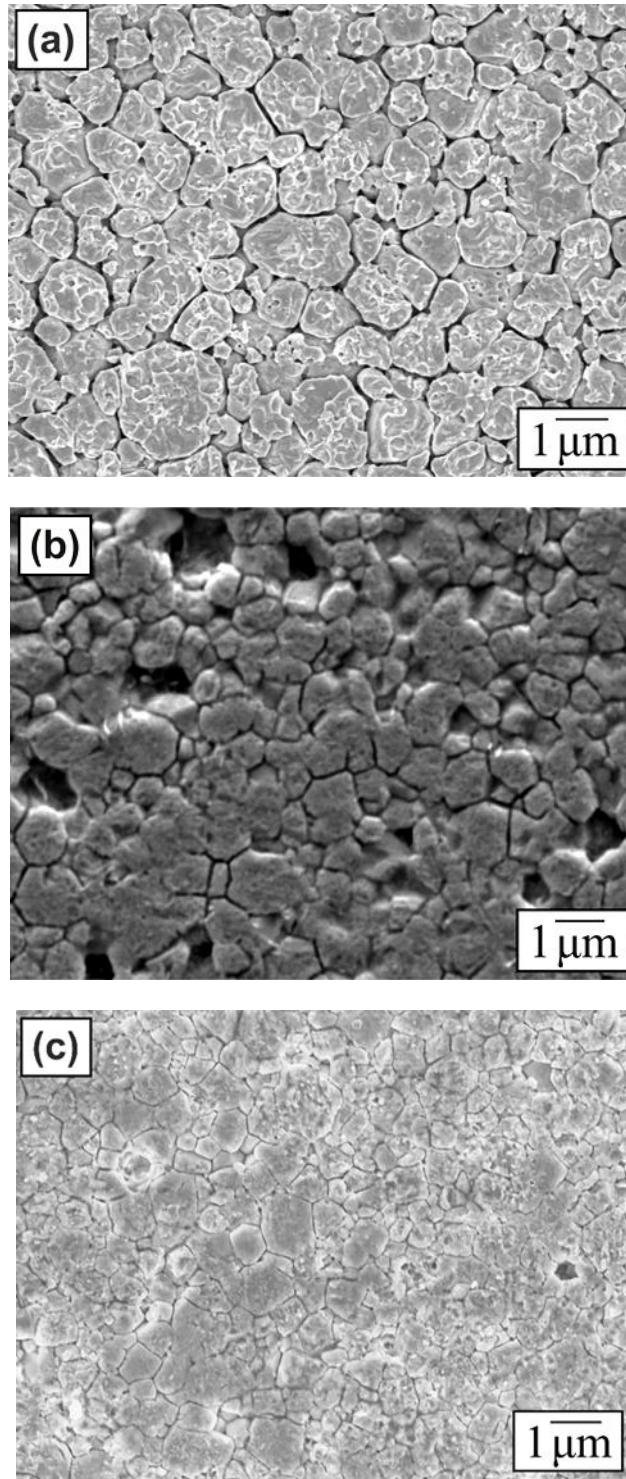


Fig. 3.3 Representative SEM images indicating the microstructures of (a) AP, (b) STD and (c) ATD samples of PZT-U.

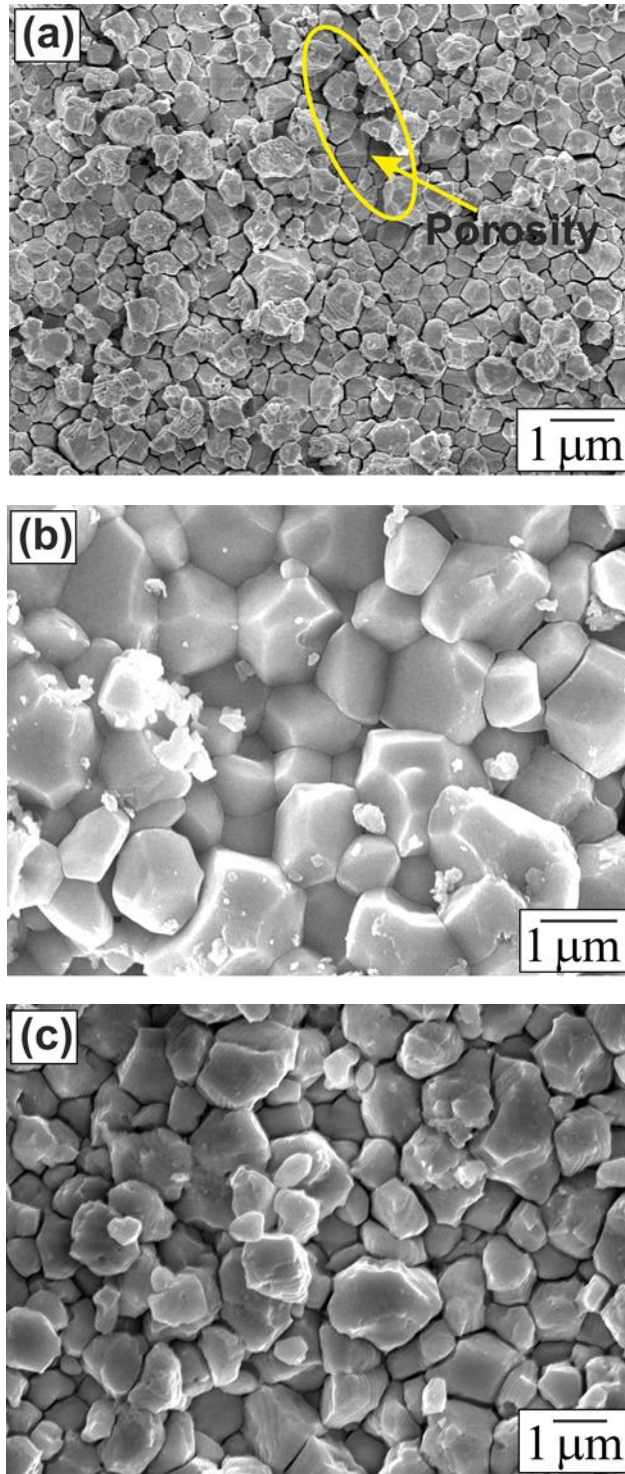


Fig. 3.4 Representative SEM images indicating the microstructures of (a) AP, (b) STD and (c) ATD samples of PZT-H.

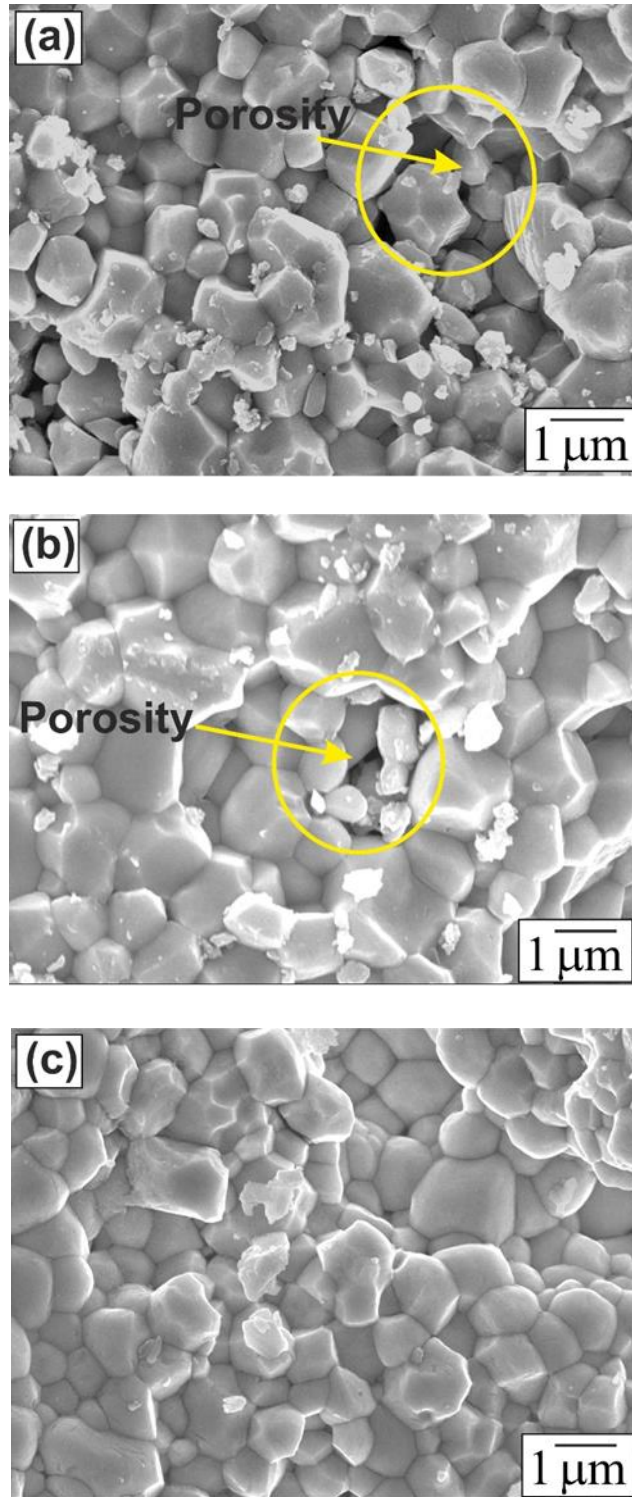


Fig. 3.5 Representative SEM images indicating the microstructures of (a) AP, (b) STD and (c) ATD samples of PZT-S.

3.3.2. Effect of annealing on the ferroelectric domain configurations

Representative PFM phase images of AP, STD and ATD samples of PZT-H and PZT-S are displayed in Figs. 3.6 (a, d and g) and Figs. 3.7 (a, d and g), respectively, which indicate the presence of switchable ferroelectric domains. Results are interpreted keeping in view of the extensive knowledge available in the literature on domain visualization considering the following key points: (i) various ferroelectric domains (i.e., “ c^+ ”, “ c^- ” and “ a ” domains) present in the samples are identified from the differences in colour contrast in PFM phase images [Miriya and Ramadurai, 2016, 2018], (ii) two adjacent polarization vectors (i.e. the collective response of domains having similar character) in poled samples are vertically opposite to each other and show 180° phase difference (i.e., “ c^+ ” and “ c^- ” domains), while “ a ” domains are normal to the “ c ” domains [Zeng et al., 2004, Kholkin et al., 2007, Sharma et al., 2011, Wang and Zeng, 2020] (iii) local domain switching obtained from the SS-PFM manifests the changes in piezoelectric amplitude, A_m vs. bias, V_B (butterfly loop) and phase, θ vs. bias, V_B (hysteresis loop) curves. Figs. 3.6a and 3.7a show that the AP samples in both the PZTs exhibit highly ordered 90° and 180° DW, which is further evident from the increased contribution of “ c^+ ”, “ c^- ”, and “ a ” domains as shown in Figs. 3.6b and 3.7b. Unlike AP samples, the STD and ATD samples exhibit partially and fully disturbed ferroelectric domain structure, respectively, and comprise of high density of mobile ferroelectric domains (i.e., non- 90° and non- 180° DW) as shown in Figs. 3.6(e, h) and 3.7(e, h), respectively. It also appears from Figs. 3.6(b, e and h) and 3.7(b, e and h) that the fraction of mobile ferroelectric domains in PZT-S are higher than PZT-H which may be attributed to the nature of dopants in both the PZTs. The butterfly and hysteresis loops for AP, STD, and ATD samples of PZT-H and PZT-S obtained after SS-PFM are shown in Figs. 3.6(c, f and i) and 3.7(c, f and i), respectively. The symmetric butterfly loops in AP samples indicate highly ordered ferroelectric domain structure, and hence exhibit highest converse piezoelectric charge coefficient, d_{33}^* , while asymmetry in butterfly loops of STD and ATD samples is due to the perturbed ferroelectric domain structure (owing to the formation of non- 90° and non- 180° DW) leading to a decrease in d_{33}^* values (Table 3.1).

The hysteresis loops further confirm the switching nature of ferroelectric domains through non- 90° and non- 180° DW during ramp voltage from -10V to +10V. The decrease in the size of hysteresis loops in STD and ATD samples also indicate that the perturbed ferroelectric domain structure causes transition from piezoelectric (i.e., AP) to paraelectric (i.e., ATD) behaviour. All the above observations reveal that randomization of ferroelectric

domains increases with an increase in annealing temperature in both the PZTs. Note that, the PFM scans are performed over an area of $4 \mu\text{m}^2$, covering a large number of ferroelectric domains, and therefore it can be reasoned that STD samples in both the PZTs still exhibit ordered domain structure in some of the grains.

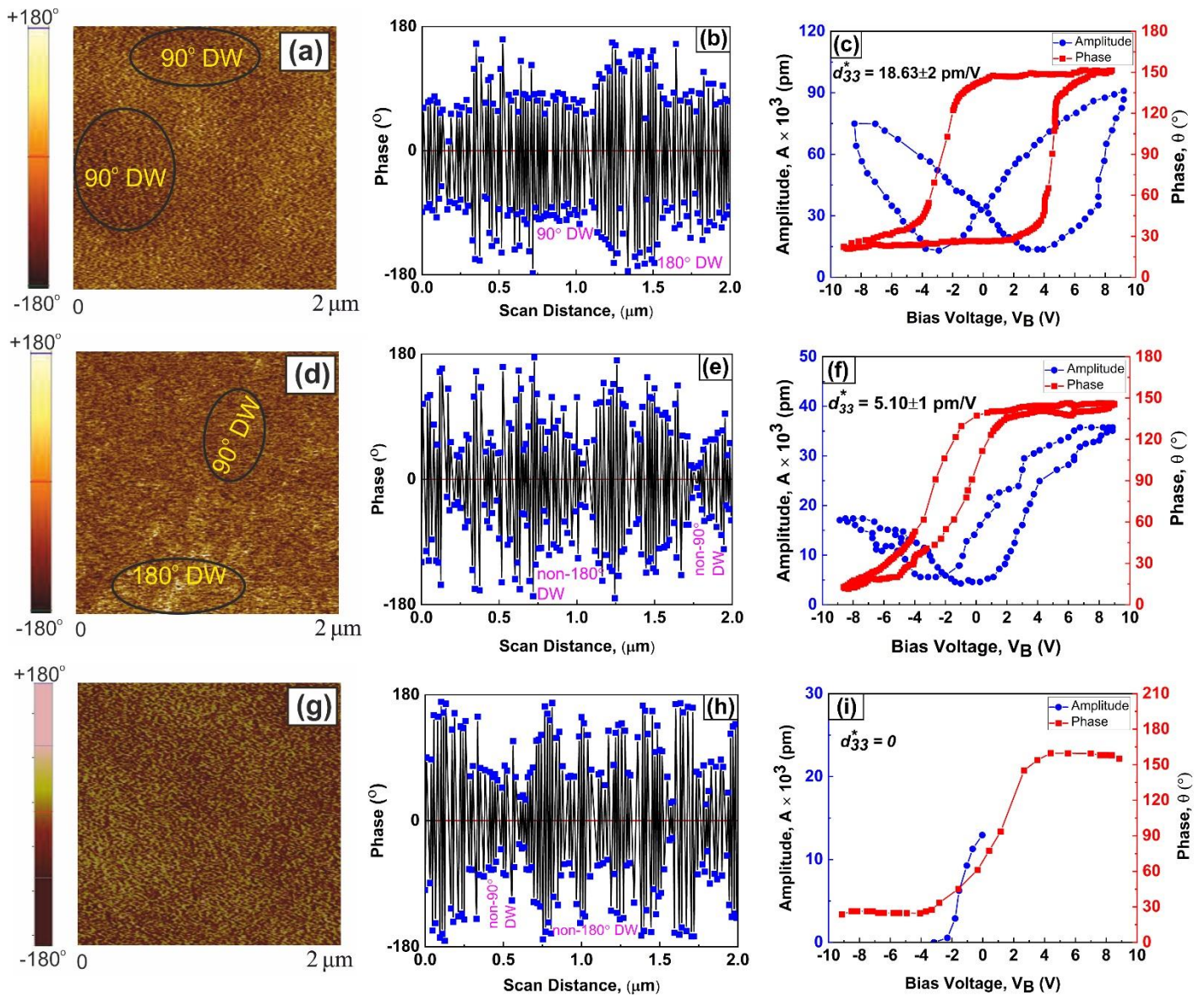


Fig. 3.6 Representative PFM phase images, domain quantification plots, and butterfly and hysteresis curves of (a-c) AP, (d-f) STD and (g-i) ATD samples of PZT-H, respectively.

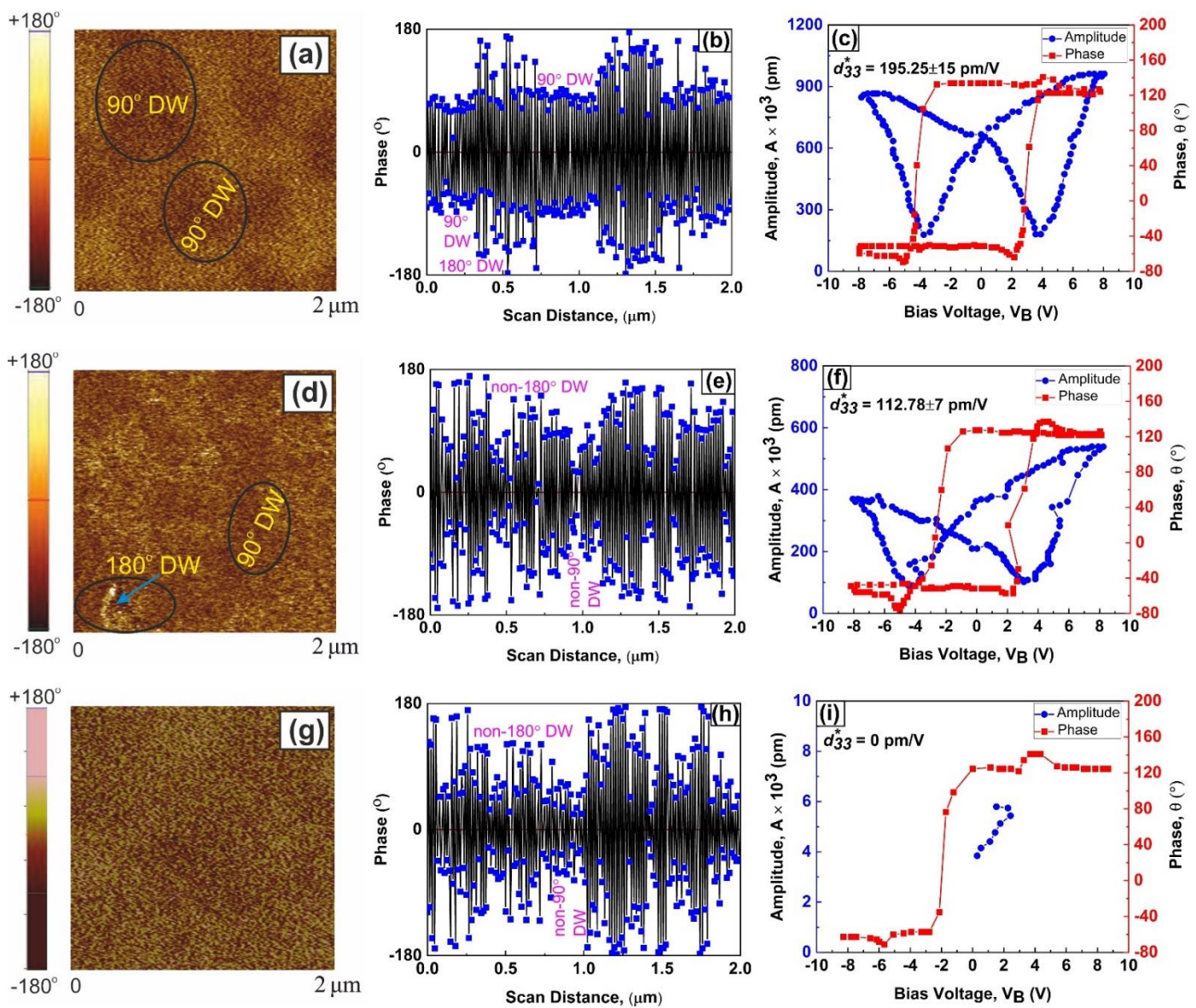
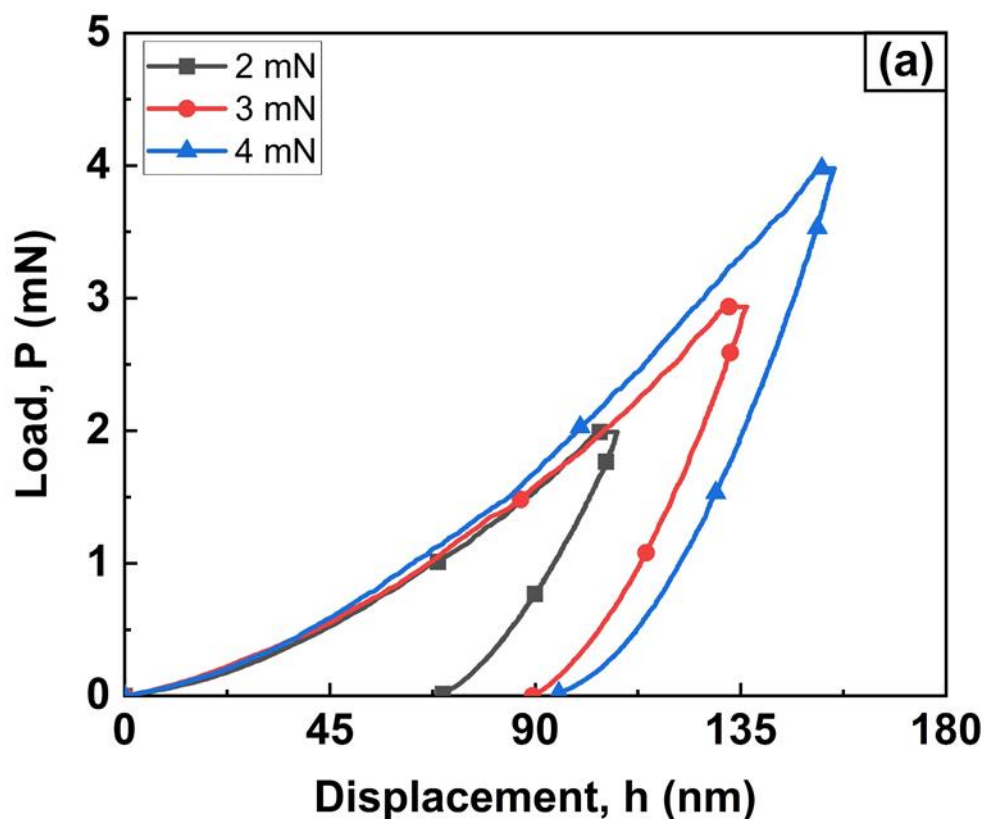


Fig. 3.7 Representative PFM phase images, domain quantification plots, and butterfly and hysteresis curves of (a-c) AP, (d-f) STD and (g-i) ATD samples of PZT-S, respectively.

3.3.3. Analysis of indentation load, P vs. displacement, h curves

Representative P vs. h curves of PZT-U, PZT-H and PZT-S obtained from nanoindentation experiments are shown in Figs. 3.8, 3.9 and 3.10, respectively. The loading curves of all the samples are continuous (without any noticeable displacement bursts) indicating that the indentation response is from the porosity free regions and the P_{max} employed are not high enough to cause cracking in the material. The H values are computed using O&P method [Oliver and Pharr, 1992] from the unloading part of P vs. h curves. The power-law exponent, n of the unloading curves (at all indentation loads) is in the range of 1.60 to 1.85 for PZT-U and 1.55 to 1.70 for PZT-H and PZT-S, which is in agreement with the literature reports [Oliver and Pharr, 1992, 2004, Guillonneau et al., 2012, Prasad and Ramesh, 2019]. Further, the unloading curves do not show any *pop-outs* negating the possibility of pressure-induced phase transformation. However, the absence of *pop-ins* does not always warrant the absence of cracks as the recent studies have shown that cracking at the imprint corners is also a consequence of relaxation of residual stresses underneath indentation during unloading [Schuh, 2006, and Prasad and Ramesh, 2019].



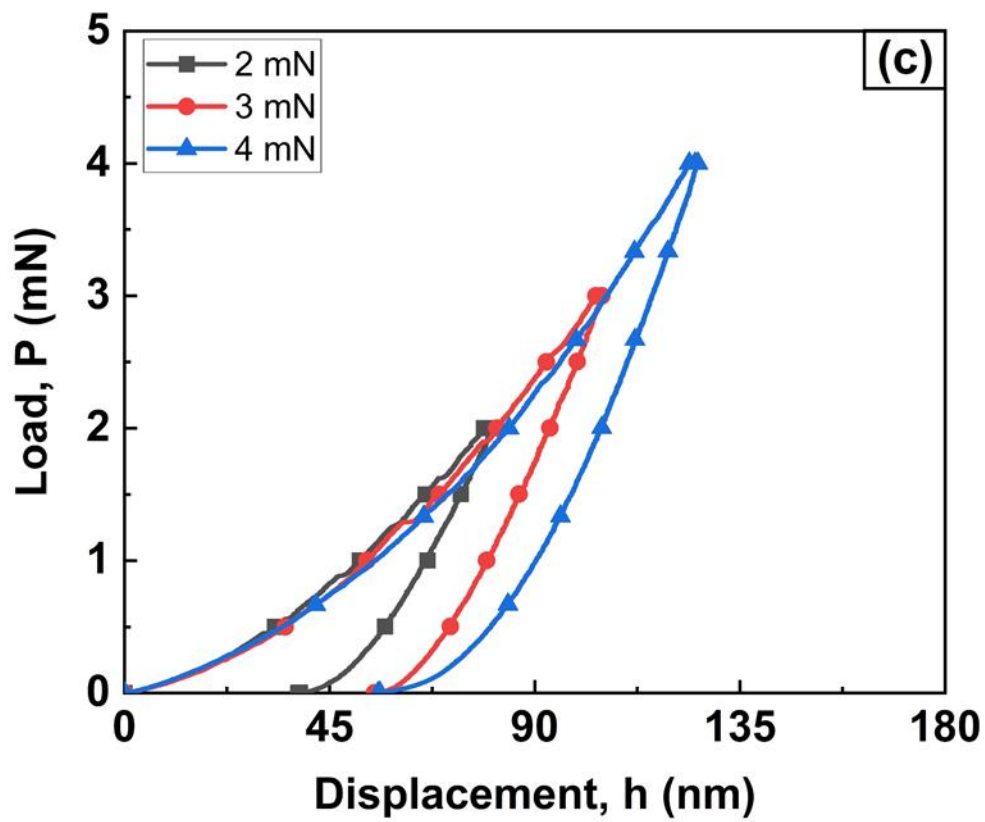
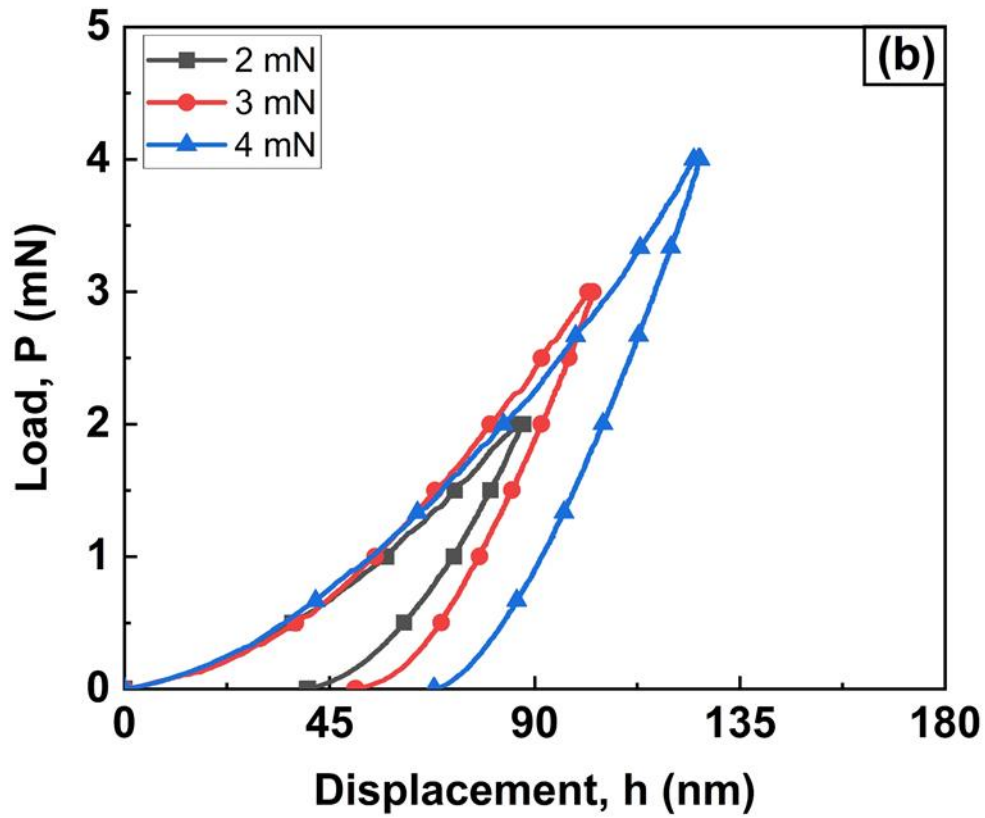
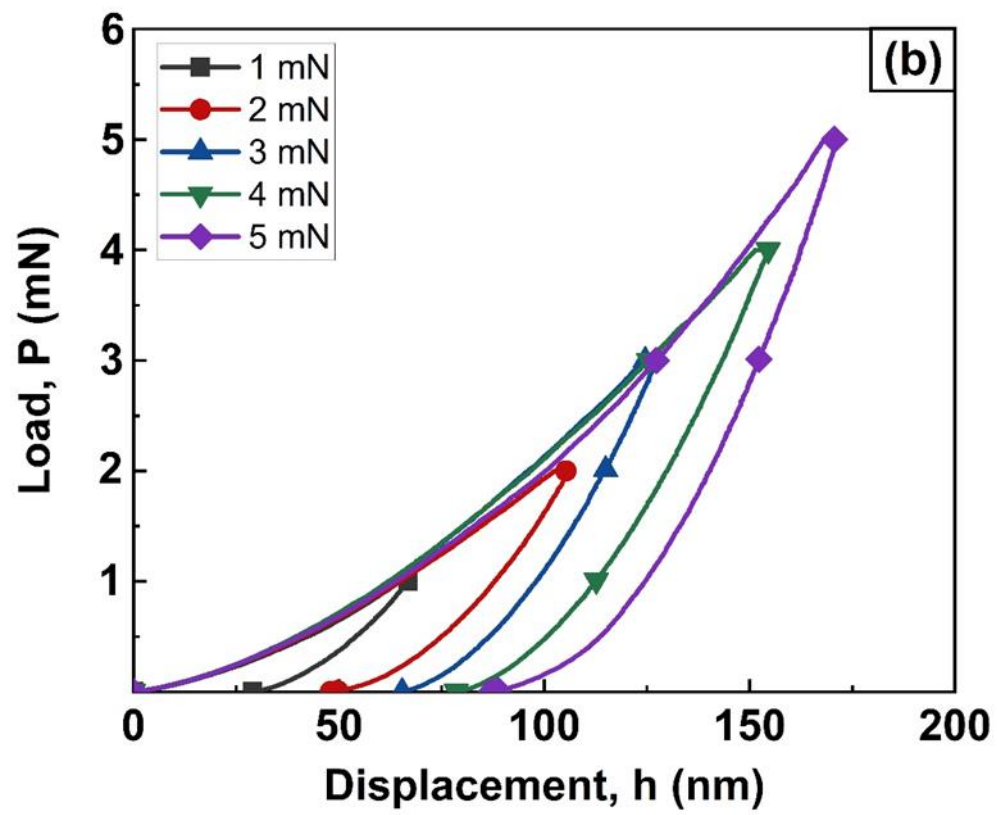
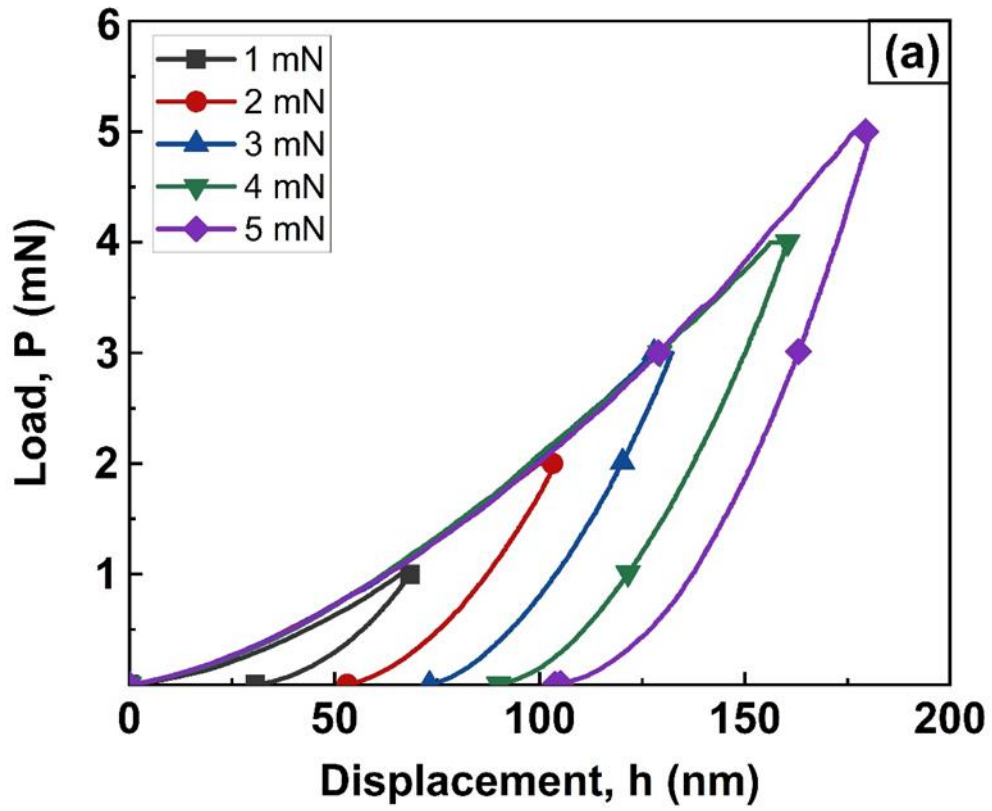


Fig. 3.8 Representative P vs. h curves for (a) AP, (b) STD and (c) ATD samples of PZT-U.



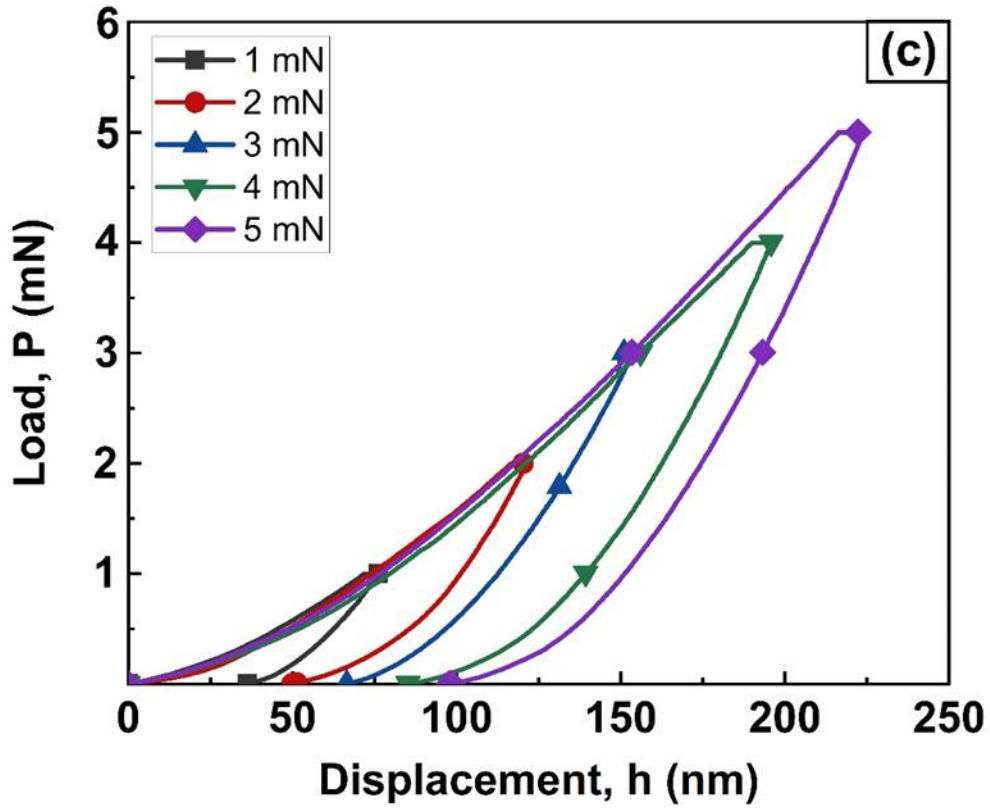
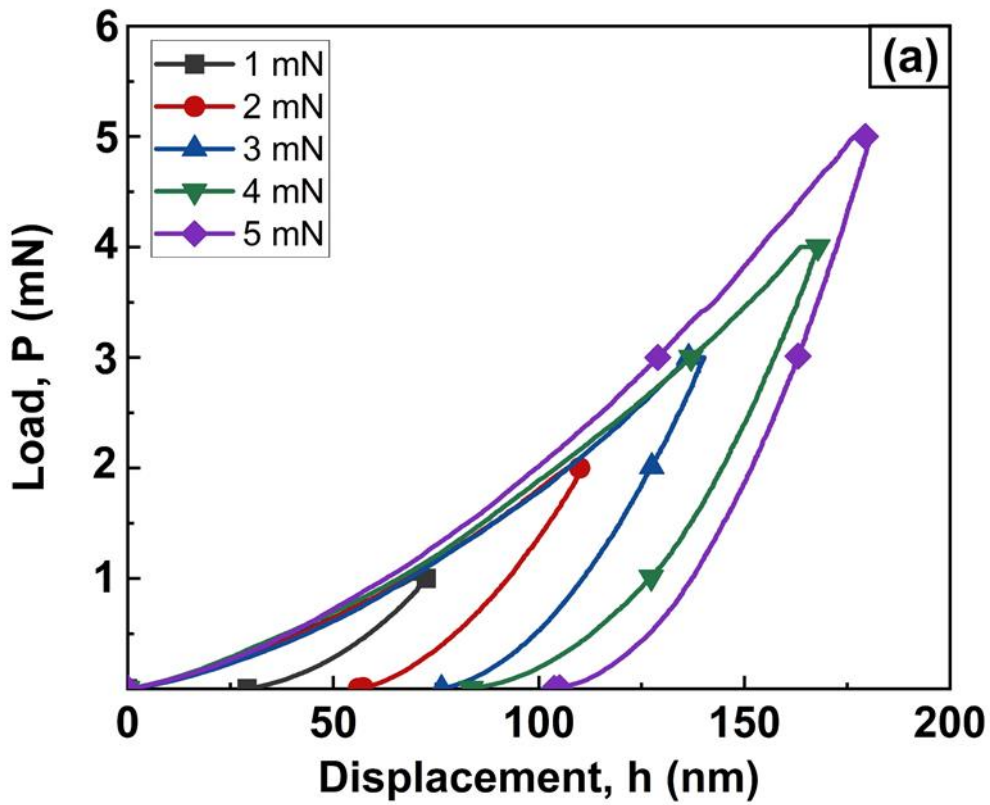


Fig. 3.9 Representative P vs. h curves for (a) AP, (b) STD and (c) ATD samples of PZT-H.



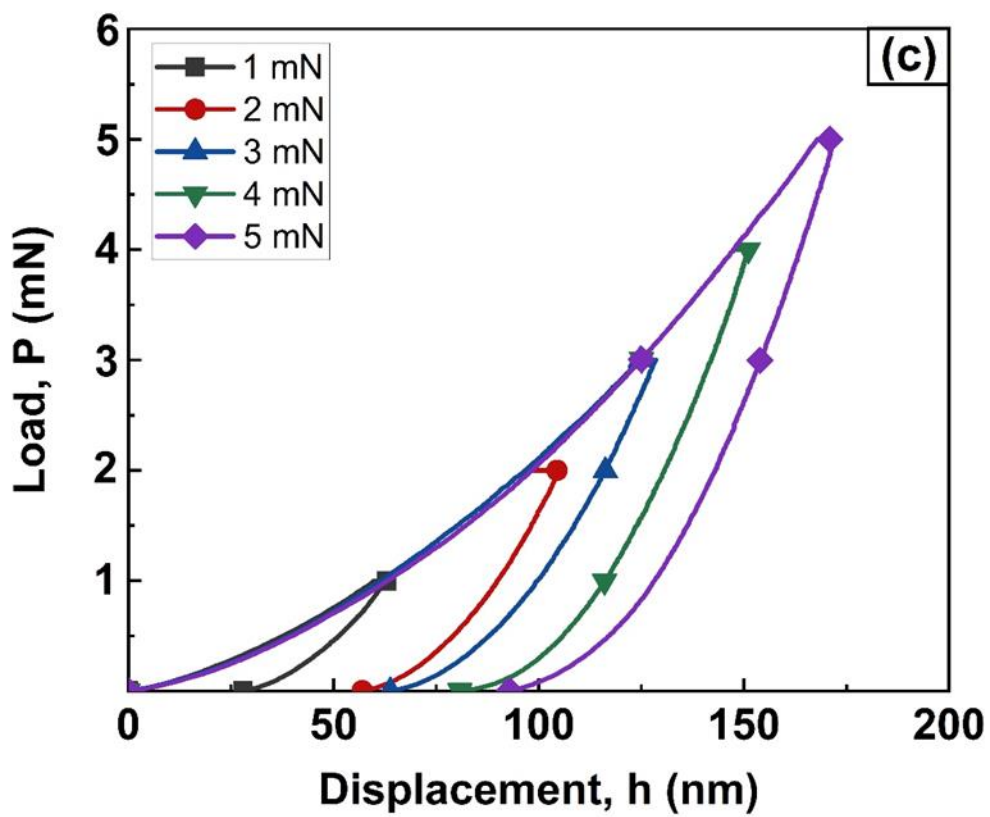
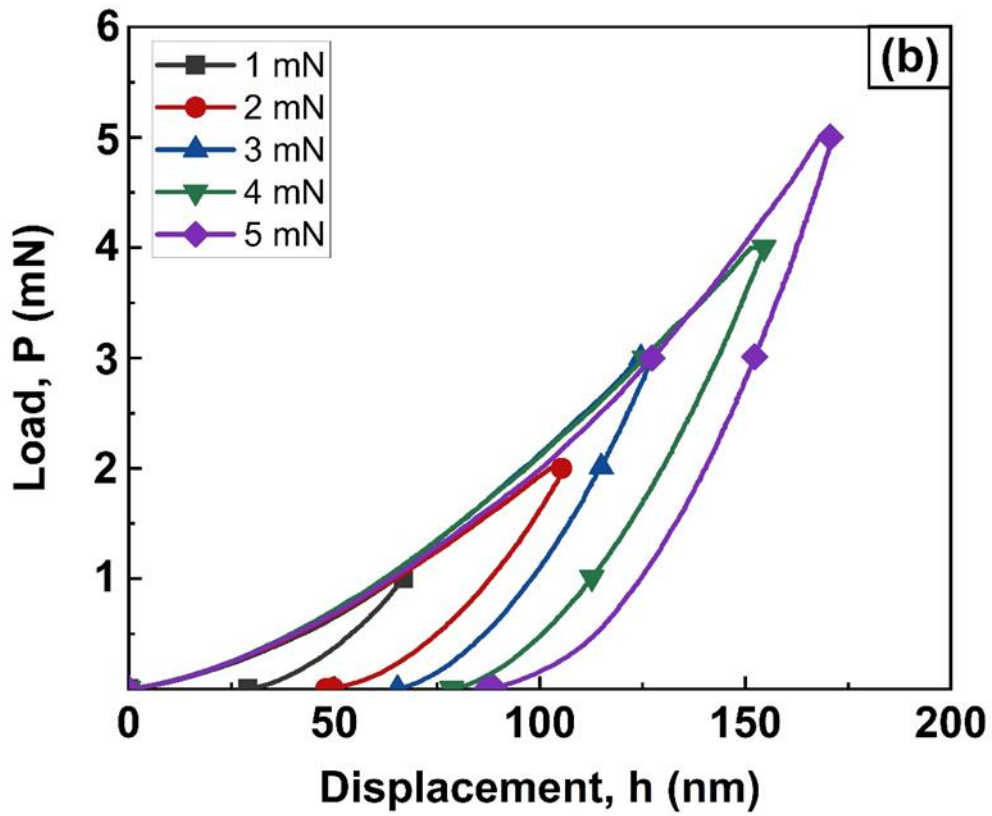
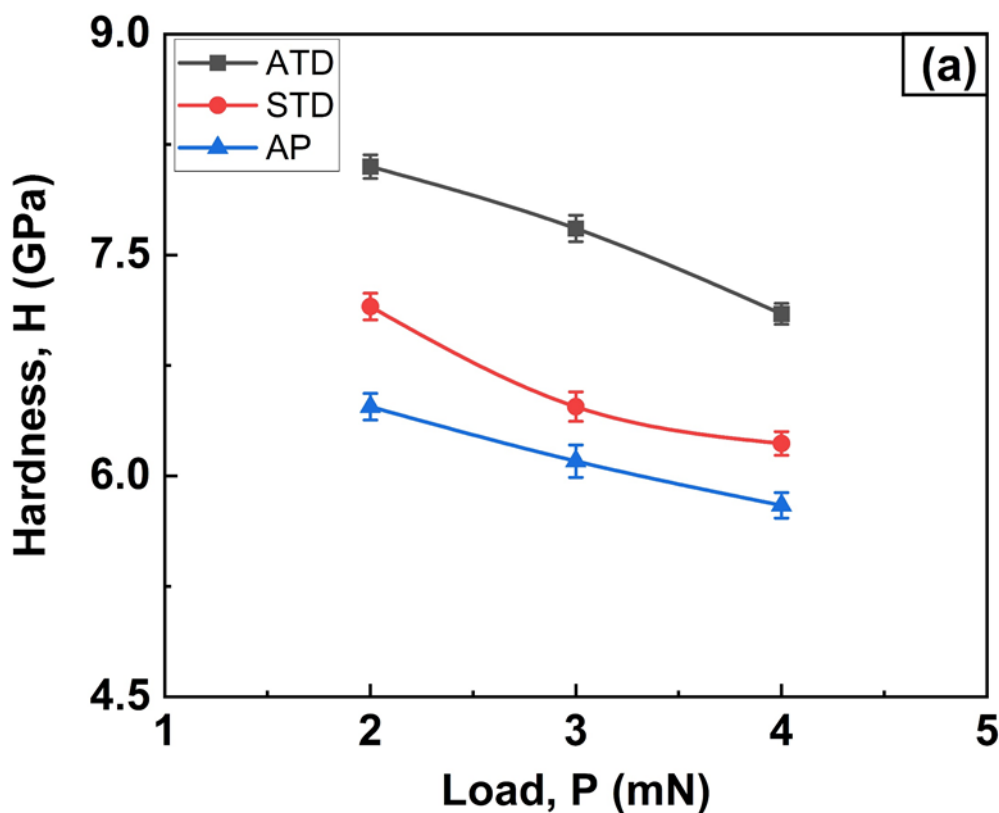


Fig. 3.10 Representative P vs. h curves for (a) AP, (b) STD and (c) ATD samples of PZT-S.

3.3.4. Indentation size effect (ISE) in H

The average nano and micro-Vickers indentation H values for AP, STD and ATD samples of PZT-U, PZT-H and PZT-S are presented in Table 3.2. Clearly, for all the PZTs, H values increase with increase in annealing temperature. Further, the H values of PZT-S are higher than the PZT-H and PZT-U. The variation of H with respect to P_{max} in AP, STD, and ATD samples of PZT-U, PZT-H and PZT-S is presented in Figs. 3.11(a-c), respectively, which clearly shows that H decreases with increasing P_{max} illustrating indentation size effect (ISE). The ISE in H in crystalline metals is attributed to the presence of geometrically necessary dislocations (GNDs) whose density increases with an increase in plastic strain gradients beneath the indenter (which is more pronounced at low P) [Ma and Clarke, 1995, Nix and Gao, 1998]. Quinn and Quinn (1997) have attributed the ISE in ceramics to the fracture events taking place during indentation. Recently, Prasad and Ramesh (2019) observed that high H at low P in ceramics is mainly due to the onsets of incipient plasticity beneath the indenter while low H at high P is because of fracture events occurring underneath the indenter.



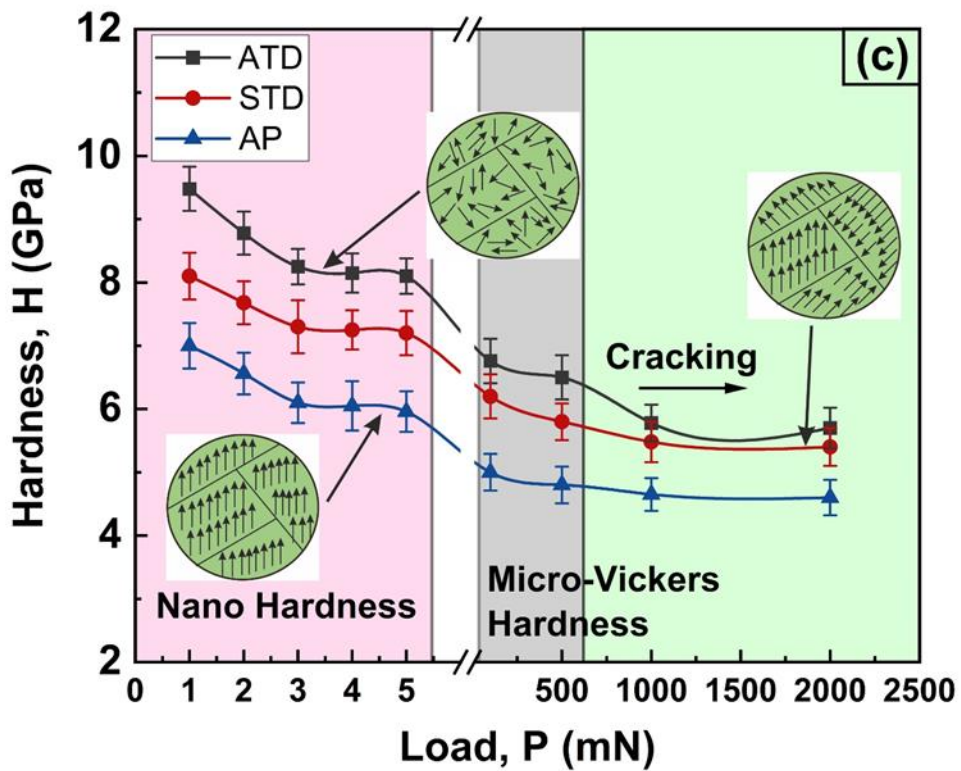
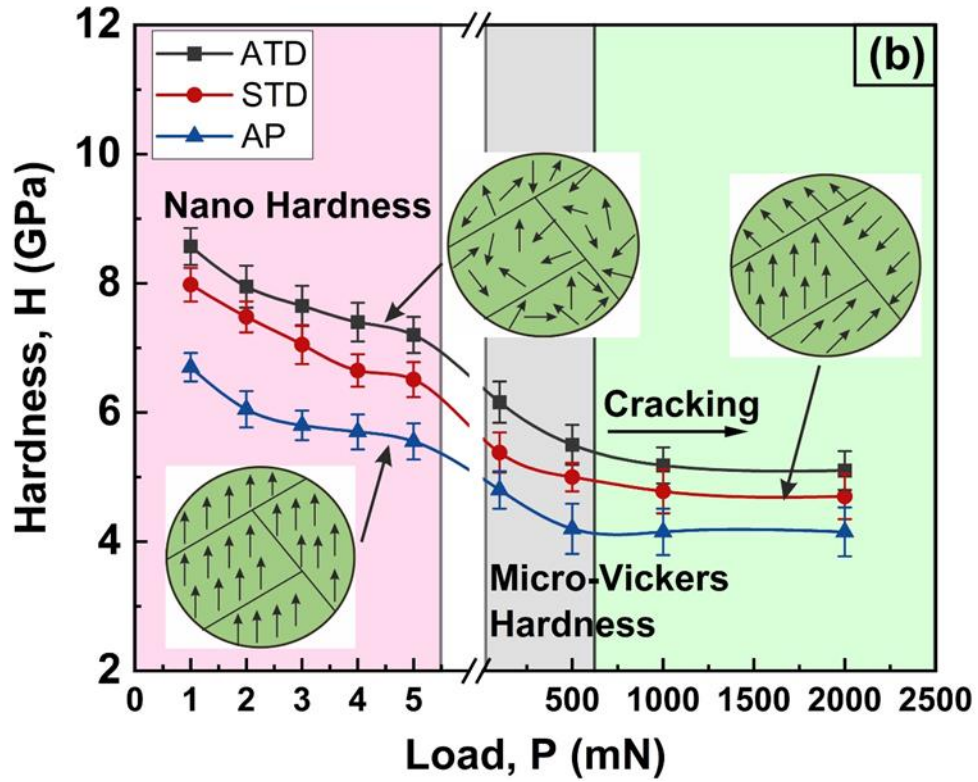


Fig. 3.11 Variation of H with respect to P_{max} in AP, STD and ATD samples of (a) PZT-U, (b) PZT-H and (b) PZT-S indicating the indentation size effect (ISE). The schematics shown in the circles represent the differences in domain density, interdomain spacing, and domain mobility of AP, STD and ATD samples of PZT-H and PZT-S.

Besides this, limited number of indentation studies on piezoceramic materials, particularly on single-crystals have reported that the presence of ISE in contact stiffness is mainly due to the existence of strain gradient polarization (flexoelectric effect) [Gharbi et al., 2009]. Recently, Kathavate and co-workers (2021) (2021) observed that differences in ferroelectric domain configurations also have a pronounced effect on the ISE in H of the polycrystalline piezoceramics.

3.3.5. Effect of microstructural features on H of PZT-H and PZT-S

The maximum penetration indentation depth, h_{max} at $P_{max} = 5$ mN for AP, STD, and ATD samples of PZT-H and PZT-S is in the range of 160-180 nm (Figs. 3.9 and 3.10), which is $\sim 1/10^{\text{th}}$ of the d_{avg} of all the samples. This shows that the nanoindentation response is likely to come from the individual grains. Further, the location of the indentation regions is scanned with AFM to ensure that indentations are made in clean regions, on the individual grains. At each P_{max} , 20 indentations are performed and the average H is obtained, which shows the following trend: $H_{ATD} > H_{STD} > H_{AP}$ (Table 3.2). Further the H values are within the standard deviation $\pm 8\%$ suggesting that the measurements are within the experimental error. Moreover, the highest annealing temperatures (~ 400 °C) used in the experiments are well below the sintering temperatures (1200 °C), which also negates the possibility of grain growth and grain rotation as a result of annealing as shown in Figs. 3.4 and 3.5.

Further, the relative densities, ρ_r of all the samples of PZT-H and PZT-S are calculated from the experimental and theoretical densities measured by Archimedes principle and unit cell volume-weight method, respectively. The ρ_r of AP samples of PZT-H and PZT-S is estimated to be in the range of 84-88%, while ρ_r for annealed samples of both the PZTs is found in the range of 86-91%. This marginal difference in ρ_r between AP and ATD samples is mostly due to the difference in the volume of unit cell (calculated from the lattice parameters in Table 3.1). As mentioned above that nanoindentation in this work is likely to probe the mechanical response of the individual grains. The H values obtained after making the 20 indentations on each sample at different P_{max} (our observation shows that the observed indentation size/depth, h is well below the d_{avg}) falls within the standard deviation of $\pm 8\%$, which indicates that the indentations are made in porosity free regions. Therefore, the effect of ρ_r on the mechanical properties is negligible in this work. However, ρ_r could play a significant role in case of bulk un-axial tension or compression testing (macro scale) and microindentation (as the indentation response comprises of several grains and within

porosities). Contrary to this, the PFM analysis shows substantial changes in the ferroelectric domain configurations as evidenced from the phase images, amplitude, A_m vs. bias voltage, V_B (butterfly loop), and phase, θ vs. bias voltage, V_B (hysteresis) curves presented in Fig. 3.6 and 3.7. These changes in ferroelectric domain configurations are also reflected in the values of direct and converse piezocharge coefficients, d_{33} and d_{33}^* , respectively. Based on this, it is appropriate to correlate the the observed differences in H values to the differences in ferroelectric domain configurations and characteristics behaviour (i.e., “hard” and “soft” vs. *undoped PZT*) rather than to the microstructural features such as d_{avg} , porosity and ρ_r .

3.3.6. Effect of ferroelectric domain configurations on H and indentation fracture toughness, K_{IC}^i

The ferroelectric domain configurations have a considerable influence on the mechanical behaviour of PZT as they offer resistance to deformation under mechanical loading. [Cao and Evans \(1993\)](#) attributed the differences in compressive strength between polycrystalline PZT-H and PZT-S to the differences in ferroelastic domain switching taking place during the deformation. [Park et al. \(2007\)](#), in case of poled single-crystal BT, observed that the “ a ” domains are harder (the difference in H is about 7%) and stiffer than the “ c ” domains and a 90° domain switching (i.e., “ c^- ” and/or “ c^+ ” domains become “ a ” domains and vice-versa) takes place during nanoindentation. During loading and unloading cycles of indentation, state of stresses continuously changes around and underneath the indentation zone which is expected to influence the texture of ferroelectric domains. The elastic strain energy associated with the highly ordered ferroelectric domains in AP samples is likely to be accommodated by 90° switching of ferroelectric domains in the elastic-plastic zone of the indentation which is in agreement with the literature studies on poled PZT [[Mehta and Virkar, 1990](#), [Webber et al., 2009](#), [Seo et al., 2013](#)] (determined indirectly from the concomitant changes in remanent strain, ε_r values). This implies that majority of the switched ferroelectric domains cannot reorient themselves upon unloading thereby leading to irreversible depolarization [[Wong and Zeng, 2008, 2010](#)]. [Landis, \(2003\)](#) proposed that the ε_r and coercive stress, σ_c has a marked influence on the mechanical behaviour of ferroelectric materials. [Marsilius et al. \(2010\)](#) have carried out compression experiments on poled PZT-H and PZT-S samples (in the temperature range of 25 to 300 °C) and reported that both ε_r and σ_c decreases with increasing temperature primarily due to the increase in back-switching of ferroelastic domains. In present work, the STD and ATD samples of PZT-H and PZT-S show respective decrease in ε_r by ~ 60% and ~

76% (for PZT-H), and ~ 43% and ~ 66% (for PZT-S) as compared to AP samples, which is also evident from the butterfly loops shown in Figs. 3.6 (f, i) and 3.7 (f, i). Therefore, it can be reasoned that the back-switching in STD and ATD samples of PZT-H and PZT-S has some obvious effects on the elastic recovery of ferroelastic domains which is expected to increase the resistance to the indentation, and hence H in both the PZTs increases upon annealing. Similar observations have also been found in various piezoceramics which correlates the switching during indentation to the elastic recovery of ferroelastic domains [Algueró et al., 2001, and Wong and Zeng, 2008, 2010].

The indentation and fracture studies on PZT and Pb-free piezoceramics also show that a decrease in ε_r leads to an increase in H and decrease in K_{IC}^i [Mehta and Virkar, 1990, Webber et al., 2009, Seo et al., 2013, Vögler et al., 2015, Wang et al., 2021]. In present work, similar trend is observed, as the obtained K_{IC}^i values (at $P_{max} = 20\text{ N}$) for PZT-H and PZT-S shown in Figs. 3.12a and b follows the trend; $(K_{IC}^i)_{AP} > (K_{IC}^i)_{STD} > (K_{IC}^i)_{ATD}$ within the $\pm 5\%$ error limit. This implies ferroelectric domain configurations and ferroelastic activities during indentation (i.e., ferroelectric domain switching and back-switching) influences toughening mechanisms in piezoceramics. For any given ferroelectric domain configurations, PZT-H exhibited slightly higher K_{IC}^i values than the PZT-S (within $\pm 5\%$ error limit), which is associated the ratio of H and E values (Table 3.3).

Table 3.3 Summary of c , E , H and K_{IC}^i values for AP, STD and ATD samples of PZT-H and PZT-S (All the reported values are within $\pm 5\%$ error limit).

Material	Domain configuration	c (μm)	E (GPa)	H (GPa) at $P_{max} = 20\text{ N}$	K_{IC}^i (MPam ^{1/2})
PZT-H	AP	56.4 \pm 2.8	138	3.92 \pm 0.20	0.51 \pm 0.02
	STD	59.8 \pm 4.5	145	4.44 \pm 0.22	0.44 \pm 0.02
	ATD	60 \pm 2.5	148	4.45 \pm 0.24	0.41 \pm 0.02
PZT-S	AP	63.7 \pm 6.2	145	4.38 \pm 0.15	0.44 \pm 0.02
	STD	72.40 \pm 8.3	152	4.45 \pm 0.30	0.39 \pm 0.19
	ATD	76 \pm 5.3	158	4.50 \pm 0.20	0.37 \pm 0.19

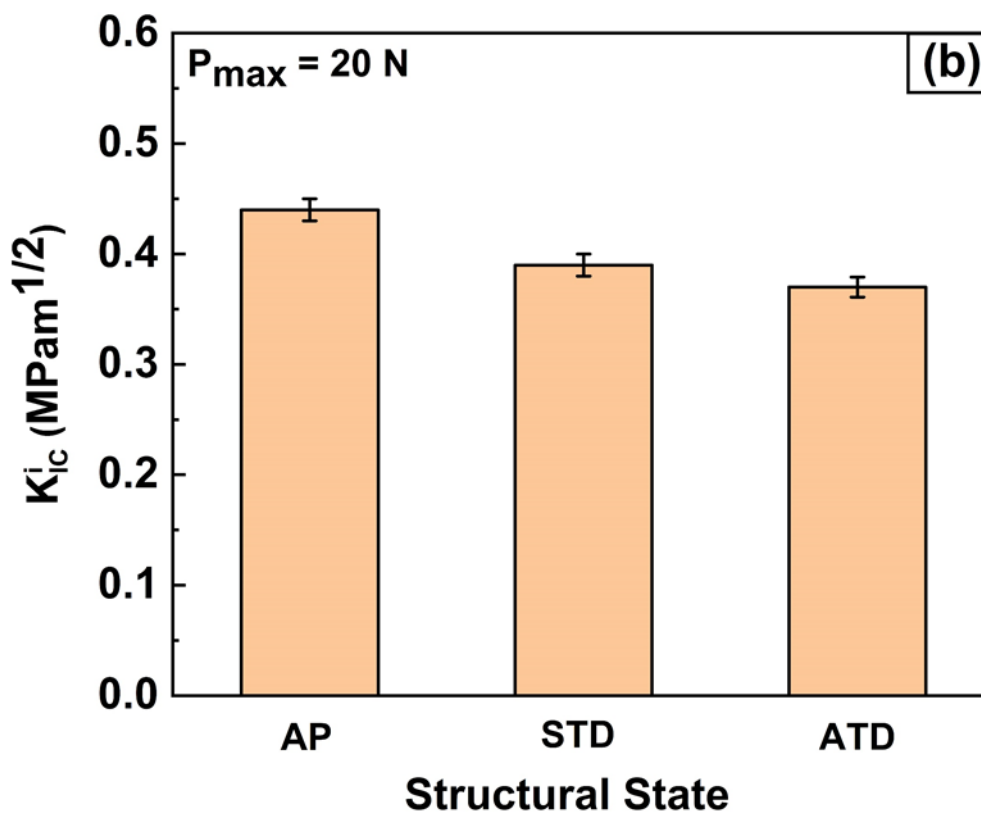
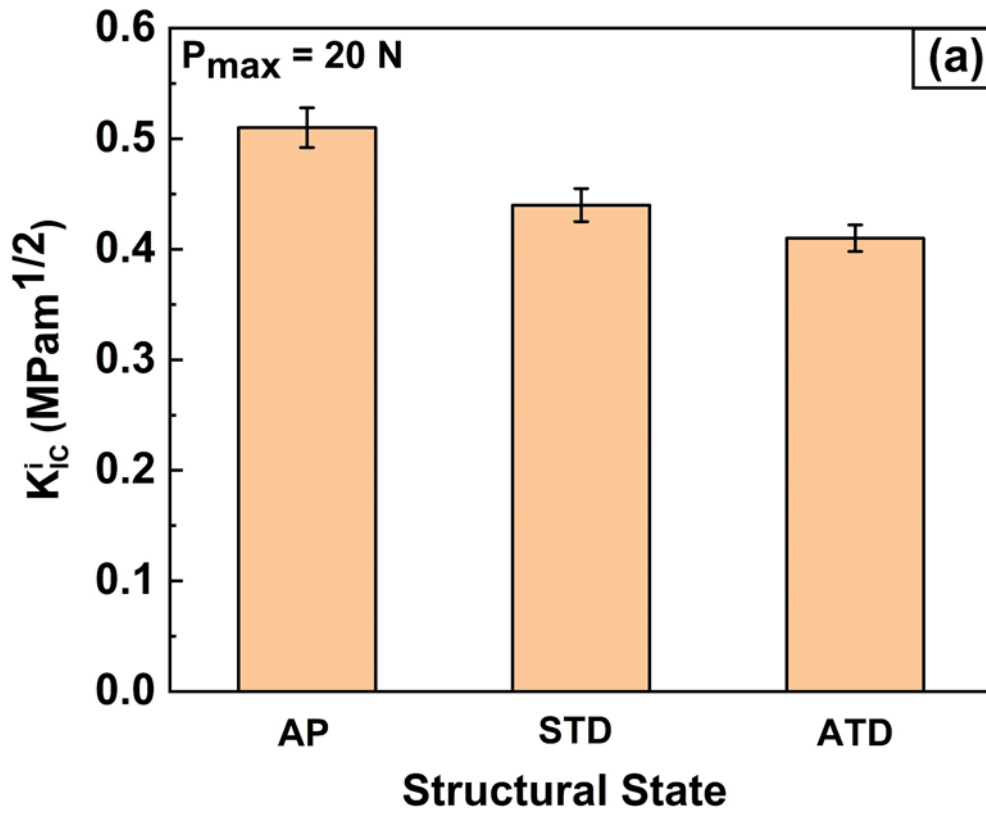


Fig. 3.12 Variation of K_{Ic}^I with respect to different structural states in (a) PZT-H and (b) PZT-S (values within $\pm 5\%$ error limit).

Mehta and Virkar (1990) and Webber and co-workers (2009) (2013) (2015) have reported that the decrease in remanent strain, ε_r and increase in H leads to a decrease in K_{IC}^i values. In present work, annealing is expected to randomize the ferroelectric domains resulting in lower ε_r values (as smaller number of highly ordered ferroelectric domains participate in the domain switching process) which leads to a decrease in K_{IC}^i . Another possible reason which could be partially responsible for the difference in K_{IC}^i values of as-poled and depoled samples in present work is the difference in crack size. The respective typical crack lengths, “ c ” for AP, STD and ATD samples are 56.4 ± 2.8 , 59.8 ± 4.5 and 60 ± 2.5 (for PZT-H), and 63.7 ± 8 , 72.4 ± 8.2 and 76 ± 5.3 μm (for PZT-S), which further indicates that ferroelectric domain structure have a pronounced influence on the crack growth in PZT. Similar observations are also reported by Mehta and Virkar (1990) though they did not characterize the changes in ferroelectric domain configurations.

Table 3.4 Comparison of the K_{IC} values (with ± 5 % error) of PZT-H and PZT-S and other Pb-based and Pb-free piezoceramics (from the literature) to those obtained in the present work. (PZT-S: Soft-PZT, PZT-H: Hard-PZT (doping element))

Materials	Type (single/ poly crystal)	Technique/ Experiment	K_{IC} (MPam ^{1/2})	Reference
PZT-S (Nb)	Polycrystal	4-point bending	0.70	Glazounov et al. (2001)
PZT-H (Sr)	Polycrystal	4-point bending	0.78	Glazounov et al. (2001)
NBT	Polycrystal	4-point bending	1.27	Glazounov et al. (2001)
PbNbO ₃	Polycrystal	4-point bending	0.97	Glazounov et al. (2001)
PbTiO ₃	Polycrystal	4-point bending	1.13	Glazounov et al. (2001)
PMN-PZT	Polycrystal	4-point bending	0.85	Glazounov et al. (2001)
PZT	Polycrystal	Indentation	0.82	Wang et al. (2021)
KNN-2BLT-6BZ	Polycrystal	Indentation	0.72	Wang et al. (2021)
NBT-6BT	Polycrystal	Indentation	1.36	Wang et al. (2021)
PZT (AP)	Polycrystal	SENB	1.85	Mehta and Virkar (1990)
PZT (Annealed)	Polycrystal	SENB	1	Mehta and Virkar (1990)
BZT-BCT (AP)	Polycrystal	Tension	0.67	Vögler et al. (2015)
BZT-BCT (Annealed)	Polycrystal	Tension	0.54	Vögler et al. (2015)
PZT-H (K) (AP)	Polycrystal	Indentation	0.51	Present work
PZT-H (K) (AP)	Polycrystal	Indentation	0.41	Present work
PZT-S (La) (AP)	Polycrystal	Indentation	0.44	Present work
PZT-S (La) (Anne)	Polycrystal	Indentation	0.37	Present work

The fracture toughness, K_{IC} values obtained *via* different techniques for various Pb and Pb-free piezoceramics are summarized in Table 3.4 and compared with those obtained for the PZT-H and PZT-S in present study. The K_{IC} values reported for AP and annealed samples of soft-doped PZTs using single edge notched beam (SENB) tests are 1.85 and 1 MPam^{1/2}, respectively [Mehta and Virkar, 1990], indicating the AP samples offer higher resistance to crack propagation than the annealed samples which may be associated with differences in domain configurations between the two samples. Similar observations are also reported by Seo et al. (2013) for compact-tension soft-PZT specimen at room temperature ($K_{IC} = 1.10$ MPam^{1/2}) and above the T_c ($K_{IC} = 0.7$ MPam^{1/2}).

3.3.7. Direct observations of ferroelastic activities in indentation vicinity

To further explore the nature of ferroelectric domain switching and domain rearrangement, PFM is performed in the vicinity of the indentation imprint and also ahead of the crack tip in AP sample of PZT-S. Fig. 3.13 presents the Vickers imprint indicating the cracks emanating from the corners having crack length, $l \sim 63.7 \pm 8$ μm . The zig-zag path of the crack is an indicative of resistance offered to the crack by the polycrystalline aggregates. PFM measurements along and ahead of the crack tip are presented by A to D and E to H at an equal spacing of 4 μm (Fig. 3.14a) and normal to one of the edges of imprint at locations I to K. All the locations from A to D and E to H shown in Fig. 3.14a are in-plane orientations normal to the poling direction. Owing to the polycrystalline nature of the samples, a particular crystallographic direction cannot be ascribed to either of these directions. The ferroelectric domain orientation maps corresponding to various locations of Fig. 3.14a are shown in Fig. 3.14b, which clearly illustrate the ferroelectric domain switching process. Further, remanent strain, ϵ_r vs. electric field, E_p response (butterfly curves) at the specified locations (shown in Fig. 3.14a) obtained using PFM are shown in Figs. 3.15(a-c). The important observations from these are as follows: (i) The plastic deformation in the severely deformed regions around the indentation and near the crack front is accommodated by ferroelastic domain switching through non-90° and non-180° DW motion (Fig. 3.14b), (ii) Upon the relaxation of indentation stresses, some of the ferroelectric domains ahead of the crack tip are likely to reorient (i.e., switch-back effect) due to overcoming of electrical and mechanical fields on indentation stresses, and (iii) the d_{33}^* values obtained from the slope of amplitude, A_m vs. bias, V_B (butterfly loop) curve (Figs. A5(a-c) in Appendix 1) and ϵ_r are found to be maximum near the crack tip (Table 3.5).

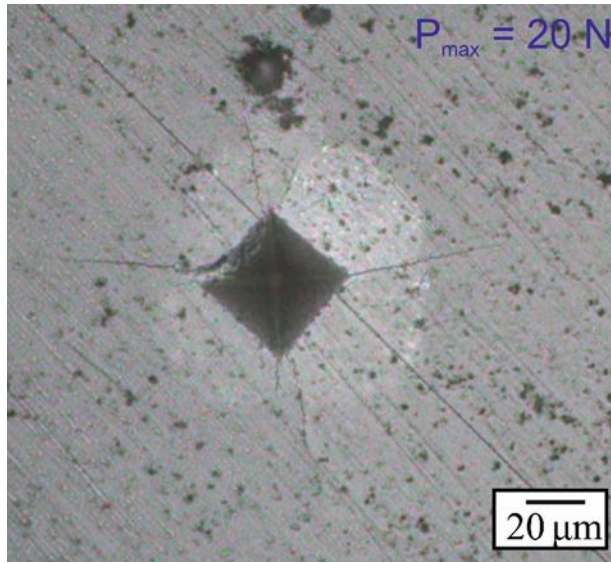
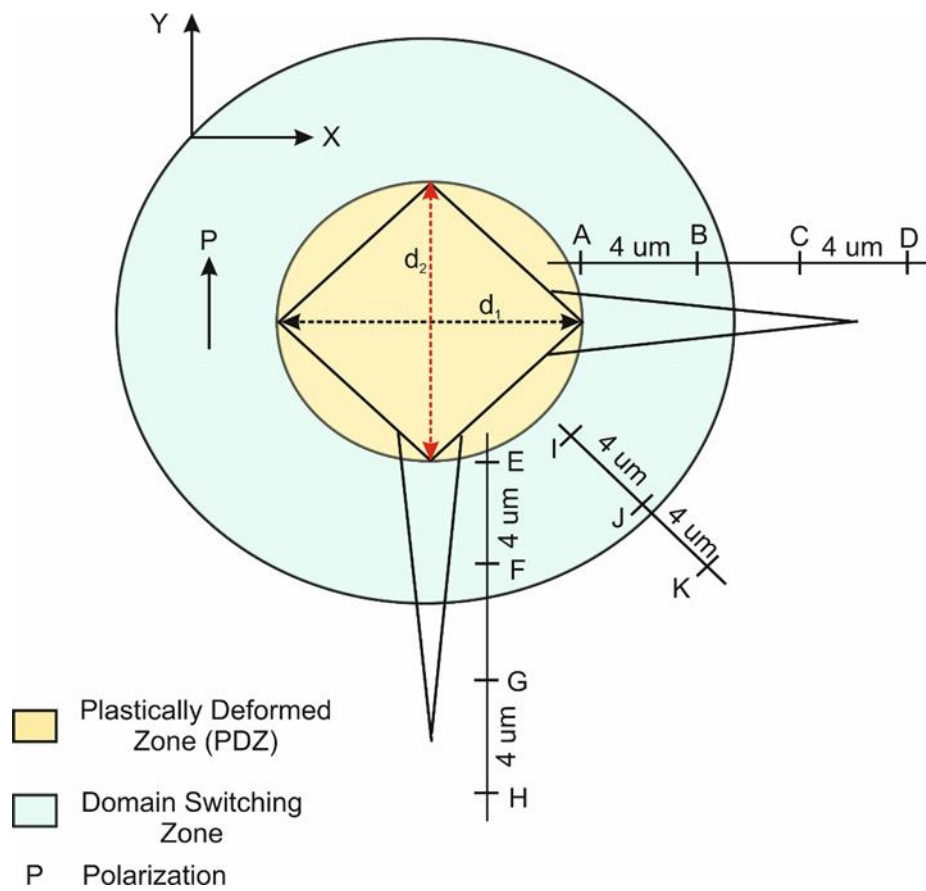


Fig. 3.13 Representative optical microscope image of Vickers indentation imprint (at $P_{max} = 20$ N) on AP sample of PZT-S.

(a)



(b)

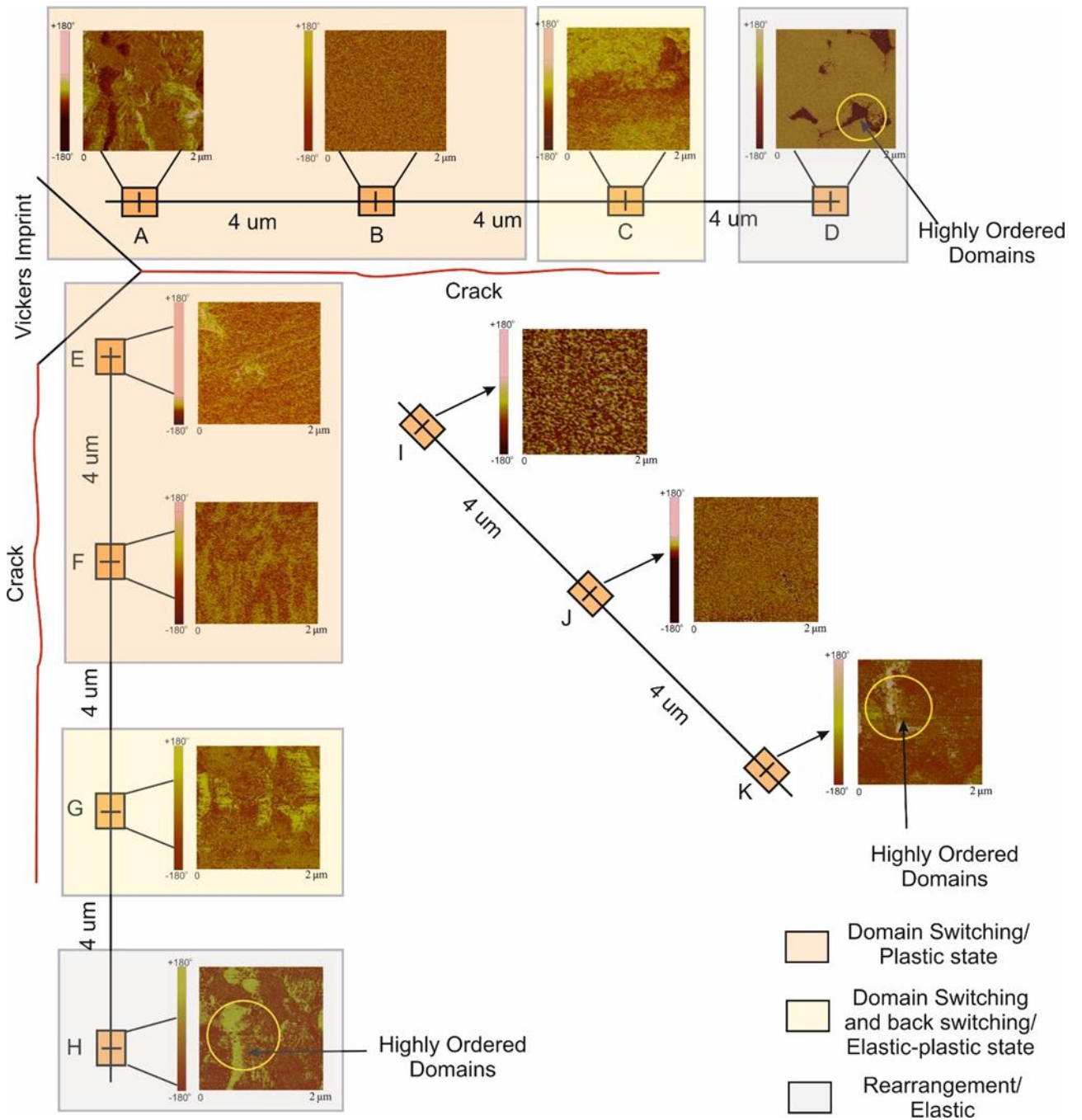
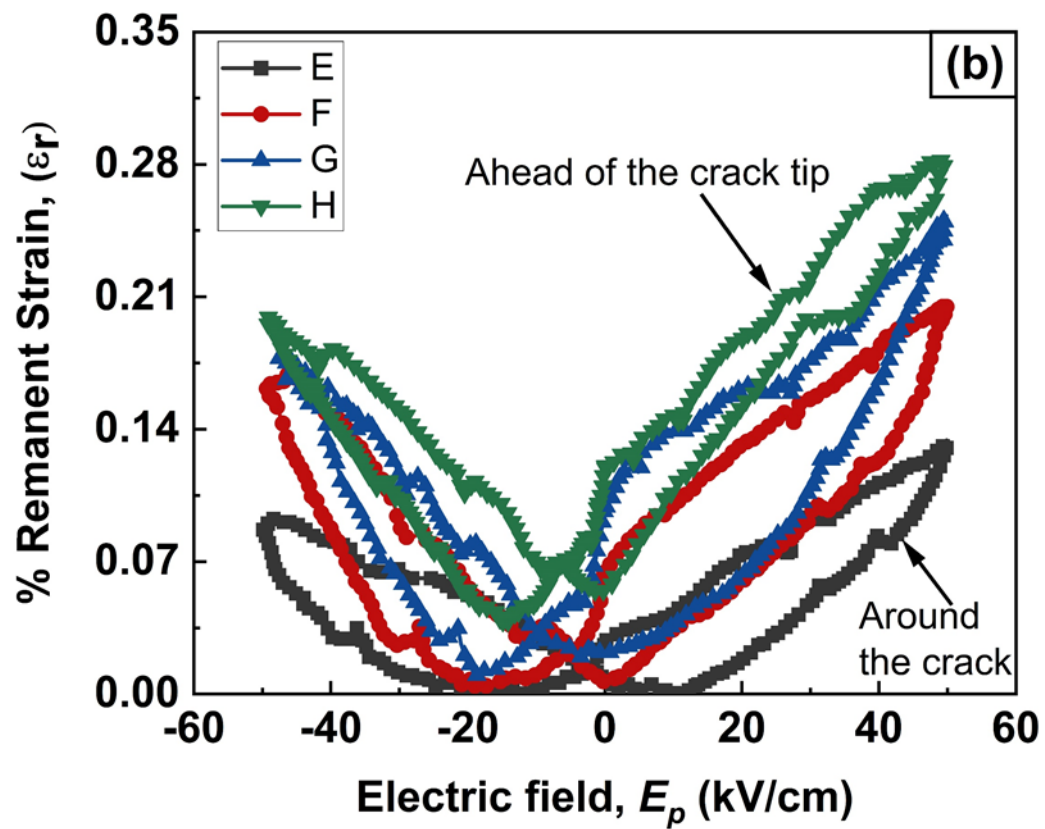
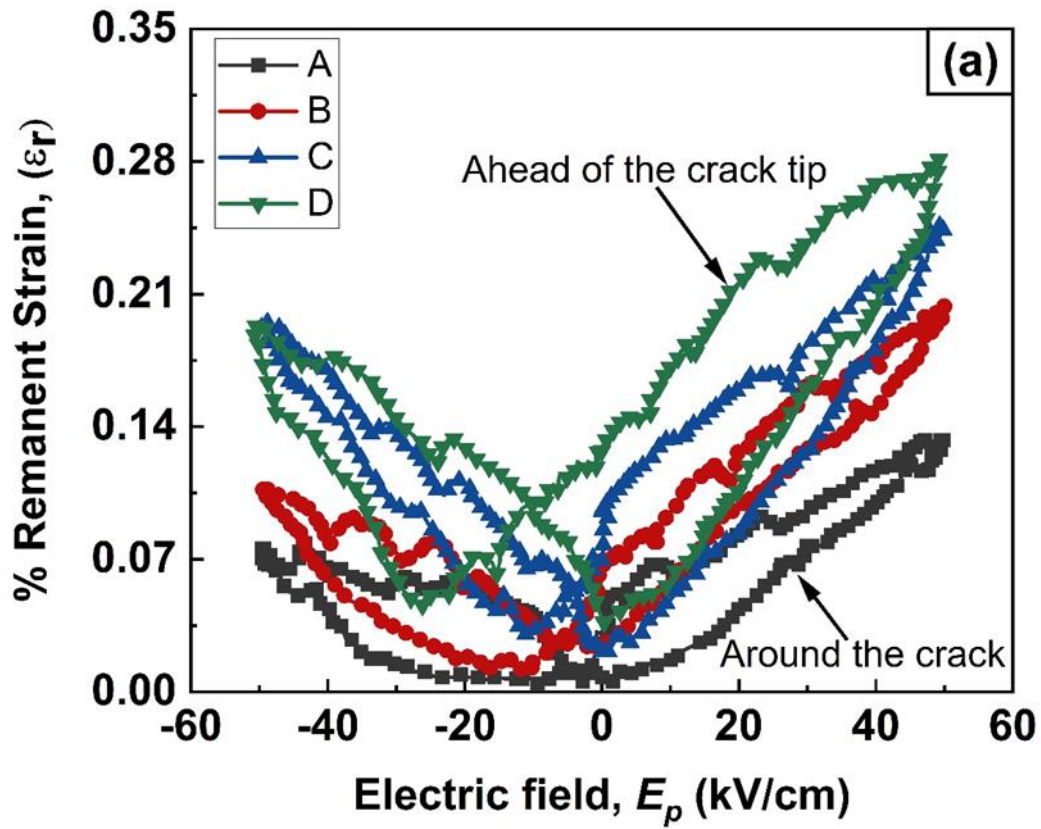


Fig. 3.14 (a) Schematic representing the plan of domain imaging around and ahead of the indentation crack, (b) representative PFM phase images at various locations as per the scheme shown in (a).



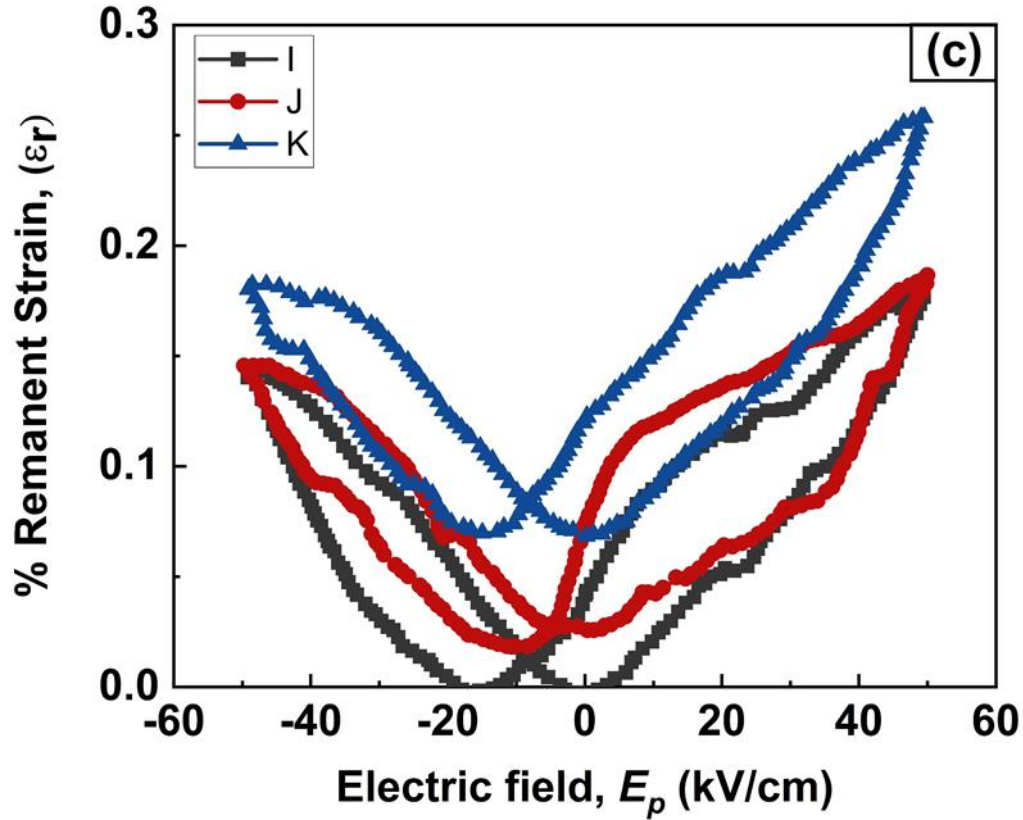


Fig. 3.15 Variation in ϵ_r with respect to E_p at various locations around and ahead of the indentation crack (a) A to D, (b) E-H and (c) I to K as per the plan shown in Fig. 3.14(a).

Table 3.5 Summary of the d_{33}^* and ϵ_r values around and ahead of the indentation crack for AP samples of PZT-S as per the scheme shown in Fig. 3.14a.

Locations	$d_{33}^* \times 10^3$ (pm/V) (± 2 % error)	ϵ_r (%) (± 2 % error)
A	4.28	0.13
B	8.16	0.20
C	20.13	0.24
D	22.84	0.28
E	3.34	0.13
F	7.74	0.20
G	16.8	0.25
H	22.6	0.28
I	4.42	0.17
J	8.14	0.18
K	12.18	0.25

Piezoresponse Force Microscopy (PFM) probes the local changes in ferroelectric domain configurations in piezoceramics unlike bulk characterization techniques such as piezometer. The d_{33} measured from the piezometer (d_{33} meter) is an average response of the piezoceramic specimens (along the thickness), while d_{33}^* obtained from the PFM is the local response of ferroelectric domain configurations and hence differs from one region to the other of the samples based on the ferroelectric domain arrangement. Recently, [Kathavate and co-workers \(2021\)](#) reported the d_{33}^* values in the undamaged regions of PZT-5H and found to be 195.25 ± 15 pm/V (for AP), 112.78 ± 7 pm/V (for STD) and “zero” (for ATD) samples, which are comparatively higher than those measured in the vicinity of indentation/damaged location in this work. The d_{33}^* values also depend on the magnitude of the applied voltage in PFM.

In a poled soft-doped PZT, [Mehta et al. \(1990\)](#) and [Webber and co-workers \(2009\) \(2013\)](#) have shown that the applied stress, $\sigma_a > 1.5$ times the σ_c causes 90° domain switching resulting in ϵ_r upto 0.33%. The typical σ_c observed for PZT-5H during compression experiments is ~ 50 -80 MPa [[Webber et al., 2009](#)] (beyond which stress, σ vs. strain, ϵ curve progressed nonlinearly). This nonlinearity was primarily attributed to the mechanical field induced depolarization in the soft-doped PZT due to ferroelastic domain switching of non- 90° and non- 180° DW. Similar observations have been also made by [Cao and Evans \(1993\)](#) in case of soft-doped PZT. Further, [Ahart et al. \(2012\)](#), in case of PMN-PT, demonstrated the pressure-induced phase transformation using high-pressure XRD and high-pressure Raman scattering (pressure values ranging from 0.3 to 6 GPa). Their observations revealed the shift in Raman spectra with an increase in pressure (upto 5 GPa), indicating the phase change from monoclinic symmetry (Cm) to rhombohedral symmetry ($R3c$), while ferroelectric domains and DW disappears at the pressure beyond 5 GPa. Recently, [Wang et al. \(2021\)](#) also observed the similar phenomenon during the microindentation experiments on some Pb-free piezoceramics, stating that the indentation-induced phase transformation occurs in the piezoceramics due to ferroelectric domain switching during loading, while reversal of the phase transformation takes place upon the relaxation of indentation stresses (and ferroelectric domains) at the crack tip. However, no microstructural evidence is proposed in relation to their hypothesis.

It is also worth mentioning here that the mean indentation pressure in this work (~ 6 GPa at $P_{max} = 20$ N), which encompasses both deviatoric and hydrostatic stresses can be

related to the uniaxial strength of the material by Tabor's approximation [Atkins and Tabor, 1965]. Although the stress field underneath the indenter during indentation is multiaxial in nature (which significantly differs from uniaxial compression), the deviatoric component of the indentation stresses are high enough to cause the cracking and depolarization, while the hydrostatic pressure can lead to phase transformations in the material [Johnson, 1970 and Jang et al., 2005]. Therefore, it can be reasoned that a high degree ferroelastic domain switching occurs in the vicinity of PDZ during the crack propagation, which is evident from the Fig. 3.14b. Further, we note that the difference in H among the different samples is significant particularly at low indentation loads ($\sim P_{max} = 9$ mN) (Figs. 3.11a-c). The maximum penetration depth at $P_{max} = 9$ mN is about 200 nm which is much smaller ($1/10^{\text{th}}$ of) than the d_{avg} . So, the response can be completely attributed to the ferroelectric domain configurations from a single grain, while the crack length observed in Fig. 3.13 at P_{max} of 20 N is $\sim 70 \pm 10$ μm encompasses large number grains (~ 50 grains). Therefore, the resistance offered by the grain boundaries to the crack propagation could be one of the reasons for less significant difference in K_{IC}^I values. This is in agreement with the observations of Reece and Guiu (2002), where they demonstrated that the crack-tip activated domain switching contributes less than 10% in the toughening of single-crystal PZT. However, other factors such as shear strain transformation and creation of new surface (or volume) during indentation may predominantly affect the toughening in poled PZT.

The ferroelastic domain switching is more predominant when the poling of the material is parallel to the loading direction compared to the poling normal to the loading direction [Wang et al., 2021, Webber and co-workers, (2009), (2013), (2015)]. In present work, the indentation direction is parallel to the poling direction of the material, therefore, it is imperative to conclude that the ferroelectric domain switching did occur in PDZ. This can be further evidenced from the ϵ_r values are obtained after domain switching at the locations A ($\sim 0.13\%$), B ($\sim 0.20\%$), C ($\sim 0.24\%$) and D ($\sim 0.28\%$), which are consistent with the literature reported value of $\sim 0.33\%$ (obtained during compression test) [Webber and co-workers, (2009), (2013), (2015)]. Similar trend is also observed at locations E to H and I to K (Table 3.5). The d_{33}^* and ϵ_r values adjacent to crack face and ahead of the crack front (in the crack wake zone) leads to the following observations: (i) The ferroelectric domains cannot switch back completely to the original state in the regions where crack has passed through and (ii) The back switching of ferroelectric domains in the crack wake zone depends on the intensity of the stress ahead of the crack tip. Partial switching occurs just ahead of the crack

tip, while complete switching occurs farther from the crack tip where the stress intensity could be less than σ_c . This shows that ferroelectric domain switching is a viable deformation mechanisms in poled piezoceramics.

3.3.8. Role of characteristics behaviour (*hard and soft vs. undoped*) on H

The H values of AP, STD and ATD samples of PZT-H and PZT-S are plotted and compared with the polycrystalline PZT-U (undoped) are shown in Fig. 3.16. In all the piezoceramics, annealed samples exhibit a higher H than the AP samples, suggesting that the randomization of ferroelectric domains increases the H . For any given ferroelectric domain configuration, H follows the following sequence: $H_{PZT-S} > H_{PZT-H} > H_{AP}$ suggesting that the addition of aliovalent dopants leads to an increase in H as they alter the ferroelectric domain configurations (as manifested by the increase in d_{33} around $\sim 200\%$ for PZT-H and $\sim 265\%$ for PZT-S as compared to the PZT-U shown on Table 3.1) and defect structure.

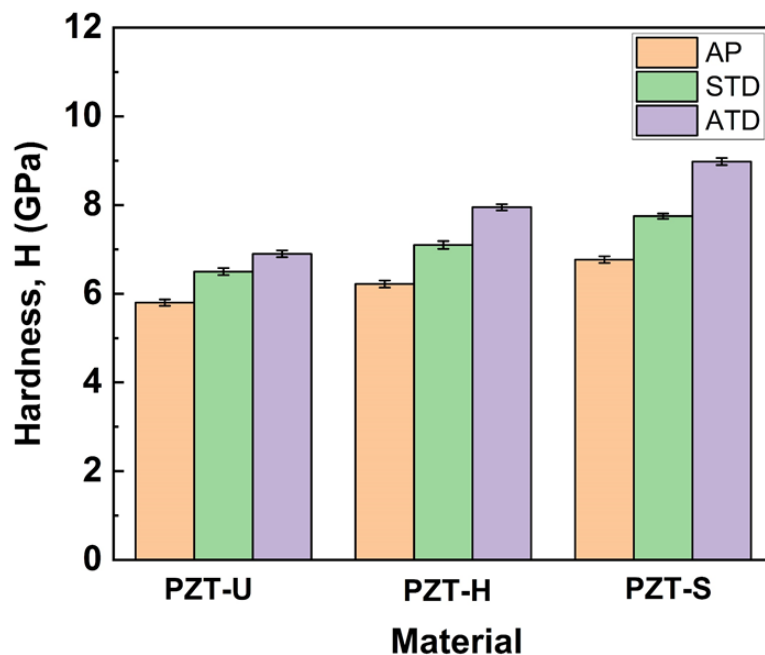


Fig. 3.16 Variation of H (from nanoindentation) with different structural states in PZT-U, PZT-H and PZT-S.

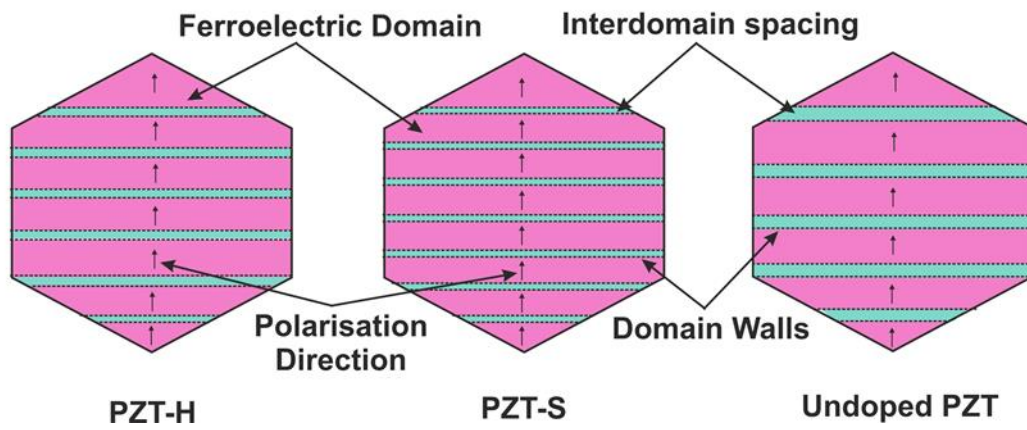
It is reported that PZT piezoceramics exhibit oxygen vacancies when doped with aliovalent cations, thereby creating defect dipoles in the material [Damjanovic, 1998 and Haertling, 1999]. During annealing, oxygen vacancies tend to diffuse to the DW and influence the local electric and elastic energies of ferroelectric domains [Erhart et al., 2013]. The orientation of defect dipoles and arrangement of oxygen vacancies in AP, STD, and ATD

samples of PZT-H, PZT-S and PZT-U are schematically illustrated in Fig. 3.17a-c, respectively. Defect dipoles are presented by , while  represents the oxygen vacancies.

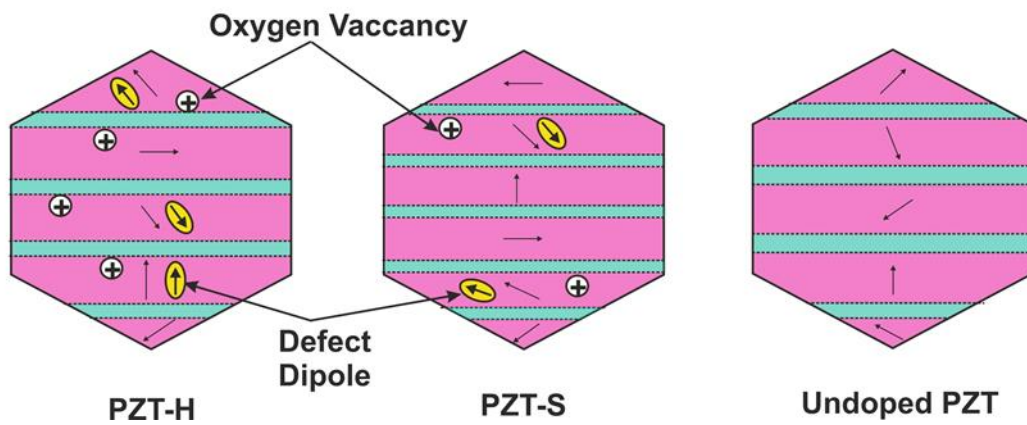
The defects present at the DW impede their motion during indentation effecting the switching phenomenon. The local electro-elastic fields act as a high energy barrier and prevent the back switching of ferroelectric domains during unloading. Ren (2004), in case of single-crystal BT has shown that defect dipoles and oxygen vacancies particularly influences the switching of non-180° ferroelectric domains. Sub and above T_c annealing alters the ferroelectric domain orientations through non-90° and non-180° DW (as seen in Figs. 3.6 and 3.7), and activates the defect dipoles and facilitates oxygen vacancies to diffuse towards DW (Fig. 3.17b and c). The pinned DW in STD and ATD samples offer increased resistance to indentation loads and also back switching is easier in these samples due to the random ferroelectric domain configuration and thus effecting H . Further, the nature of defects present in PZT-H and PZT-S samples, also influences the H .

The main objective of the present study is to examine the strengthening behaviour in PZT-H and PZT-S in light of different ferroelectric domain configurations though the role of grain orientation cannot be ruled out. Being transversely isotropic in nature, the crystallographic orientation might influence the electro-mechanical properties of piezoelectric materials. However, it appears from the H values that the mechanical properties are less influenced by the grain orientations as the standard deviation in H obtained at different locations of the samples is only $\pm 8\%$ (Table 3.2). In case the H is strongly influenced by the orientation of the grains, the differences observed should have been much higher than the observations reported in the current study. So, the results presented in this study clearly shows that the changes in ferroelectric domain configurations have much more influence on the nanomechanical properties than the crystallographic orientations of the grains.

a) As Poled (AP)



b) Sub- T_c Depoled (STD)



c) Above- T_c Depoled (ATD)

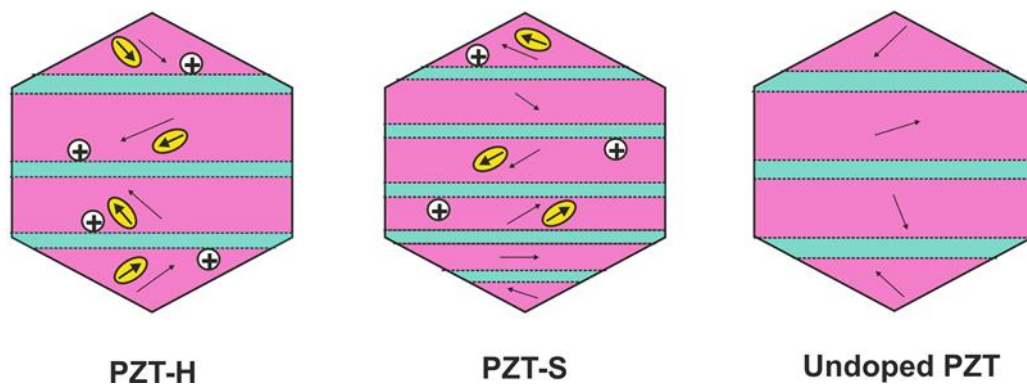


Fig. 3.17 Schematic representing the orientation and arrangement of defect dipoles and oxygen vacancies in (a) AP, (b) STD and (c) ATD samples of PZT-H, PZT-S and undoped PZT. The size, interdomain spacing, defect dipoles and oxygen vacancies increases with increase in annealing temperature.

3.4. Summary

In summary, the role of ferroelectric domain configurations on the strengthening and toughening behaviour of polycrystalline PZT piezoceramics is investigated. The different ferroelectric domain configurations are systematically varied by selectively depoling the poled samples below ($0.8 T_c$) and above ($1.2 T_c$), the Curie temperature, T_c . Further, the ferroelastic activities during the indentation are explored *via* domain orientation maps in the vicinity of the indentation. The important conclusions from the present work can be summarized as follows;

- The degree of ferroelectric domain disorderness increases with increasing annealing temperature as the samples annealed at $1.2 T_c$ exhibits the highest disorder compared to the $0.8 T_c$ depoled and AP samples.
- The H values of PZT-U, PZT-H and PZT-S increases with increasing degree of ferroelectric domain randomization, as in all the PZTs the ATD samples show significant improvement in H ($\sim 20\%$ for PZT-U, $\sim 36\%$ for PZT-H and $\sim 41\%$ for PZT-S) over the AP samples. The reorientation of the ferroelectric domains underneath the indenter through non- 90° and non- 180° DW appears to be an important reason for increased resistance to indentation.
- In all the samples, the H decreases with increasing P showing strong ISE and complex interplay of ferroelectric domain reorientations, and DW interactions appear to be an important reason for the observed ISE in polycrystalline PZT piezoceramics.
- Besides strengthening behaviour, ferroelectric domain configurations also have a pronounced influence on toughening in PZT piezoceramics.
- The ferroelectric domain orientation maps obtained in the vicinity of the indentation reveals the indentation induced domain switching and rearrangement (back-switching) are the viable toughening mechanisms in polycrystalline PZT piezoceramics. This is further rationalized using d_{33}^* and ϵ_r values obtained aside and ahead of the crack front.
- Doping of aliovalent cations alters the ferroelectric domain configuration and defect structures, which appears to be an important reason for improving the H of PZT.

CHAPTER 4

Analysis of indentation size effects (ISE) in nanoindentation hardness of polycrystalline piezoceramics with different ferroelectric domain configurations

Abstract: This chapter presents the role of different ferroelectric domain configurations on the mechanistic modelling of indentation size effect (ISE) in nanoindentation hardness, H of the polycrystalline piezoceramics. Hardness values are obtained at various indentation loads on PMN-PT, PZT-H, and PZT-S piezoceramics having different ferroelectric domain configurations. It has been observed the hardness of all the samples decreases with increasing indentation load (vis-à-vis indentation size) which is known as ISE. The observed ISE is then analyzed using classical Meyer's law, proportion specimen resistance (PSR) model and modified PSR model. The origins of ISE are discussed in detail in light of the differences in ferroelectric domain configurations¹.

4.1. Introduction

The microstructural features at different length scales (i.e., grain size from μm scale to nano assembled domains at nm scale) control the structural properties of piezoceramics. Therefore, a thorough investigation of mechanical, electrical, microstructural properties and the reliability of the components produced by these materials are essential before deploying them for specific applications. In the past, deformation behaviour of the piezoceramics from the microstructural point of view had been a subject of frequent studies [Cao and Evans, 1993, Wong and Zeng, 2010], though some distinctive mechanical properties such as hardness, fracture toughness, and ductility of these piezoceramics are not very well understood. Of all these mechanical properties, indirect estimation of materials strength through indentation hardness, H is perhaps easier one due to the following; (i) it gives fast estimation to the material's resistance to plastic deformation, (ii) require a small volume of test material, and (iii) hardness measurement through indentation is non-destructive because the impressions

¹ The work presented in this chapter is based on the following publications:

[1] V.S. Kathavate, B. Praveen Kumar, I. Singh, K. Eswar Prasad (2021), Analysis of indentation size effect (ISE) in nanoindentation hardness in polycrystalline PMN-PT piezoceramics with different domain configurations, *Ceram. Int.*, 47(09) 11870-11877.

[2] V.S. Kathavate, H. Sonagara, B. Praveen Kumar, I. Singh, K. Eswar Prasad (2021), Role of domain configurations on the mechanistic modelling of indentation size effects (ISE) nanohardness of hard and soft PZT piezoceramics, *Int. J. Adv. Engg. Sci. Appl. Math.*, 13(1) 63-78.

(particularly at lower indentation loads) are limited to a very small area of the material. However, one of the downsides of the hardness testing method is estimating true hardness because H varies with the indentation size or load. This size dependence of H is often referred to as the indentation size effect (ISE). The ISE in crystalline materials is commonly attributed to the geometrically necessary dislocations (whose density increases at high plastic strain gradients, particularly at lower indentation loads) [Nix and Gao, 1998, Lim and Chaudhri, 2007, Swadener et al., 2002], shape and geometry of indenter tip, high dislocation nucleation stresses, [Gane and Cox, 1970, Tarkanian et al., 1973], elastic-plastic nature of the material [Spary et al., 2006], and work hardening characteristics of the material [O'Neill, 1934]. Apart from the above mechanisms, ISE in piezoceramics can also be influenced by the nature of ferroelectric domains, their orientation, dipole movement, and flexoelectric effect arising due to the strain gradient polarization.

Several studies have been conducted in the past to understand the origins of ISE in ceramics using mechanistic models, which typically includes classical Meyer's approach [Li and Bradt, 1993, Quinn and Quinn, 1997], Hays-Kendall (H-K) model [Hays and Kendall, 1973], elastic recovery (ER) model [Tarkanian et al., 1973], energy-balance approach (EBA) [Li and Bradt, 1993, Fröhlich et al., 1977], proportion specimen resistance (PSR) model, and modified proportion specimen resistance (mPSR) model [Li and Bradt, 1993, Quinn and Quinn, 1997]. All these models use simple mathematical equations to describe the experimental data and explain the physics of deformation using the fitting parameters. However, there are limited studies discussing the ISE in nanohardness in piezoelectric materials [Schneider et al., 2005, Scholz et al., 2007, Park et al., 2007, Gharbi et al., 2009] [Gharbi et al., 2009]. For instance, Schneider, Park and co-workers (2005) (2007) studied the role of ferroelectric domain switching and domain rearrangements beneath the indenter on the H and elastic modulus, E of single-crystal BT during the nanoindentation experiments. Further, Gharbi et al. (2009), in the case of BT single-crystal piezoceramics, observed the ISE in contact stiffness which is attributed to the flexoelectric component that arises mainly due to coupling between strain gradient and polarization. Recent nanoindentation experiments on piezoceramics show that all the piezoceramics exhibit ISE, and further, the H shows a strong dependence on ferroelectric domain configurations [Kathavate et al., 2020, Kathavate et al., 2018]. Though the difference in H is attributed to the nature of ferroelectric domain configurations and their interactions, the dependence of ISE on ferroelectric domain configurations is still needed to be investigated in detail. Therefore, it would be interesting to

examine the validity of the analytical models to explain the origins of ISE in piezoceramics having different ferroelectric domain configurations or structural states.

In view of the above, the objective of the current study is to examine the origins of ISE in polycrystalline PMN-PT, PZT-H and PZT-S piezoceramics having different ferroelectric domain configurations using various mechanistic models.

4.2. Experimental Procedure

4.2.1. Materials and Ferroelectric Domain Configurations

The test materials preferred for the present work are the polycrystalline solid solutions of lead magnesium niobate-lead titanate (PMN-PT), hard-doped lead zirconate titanate (PZT-H), and soft-doped lead zirconate titanate (PZT-S) synthesized *via* a conventional solid-state reaction route. The details about synthesis, fabrication, poling process and technique for obtaining the different ferroelectric domain configurations in PMN-PT, PZT-H and PZT-S piezoceramics are mentioned in detail in previous chapter 2 and 3, respectively.

4.2.2. Nanoindentation experiments

The nanomechanical properties of AP, STD and ATD samples of PMN-PT, PZT-H and PZT-S are determined by performing quasi-static nanoindentation experiments with three-sided pyramidal Berkovich diamond indenter using Bruker Hysitron TI nanoindenter. The tip area function, A_c is calibrated using a standard fused silica sample by making about 100 indentations at different loads. All the experiments are performed under load control mode in the load range of 1 to 5 mN at constant loading and unloading rates (0.1 mN/s). In order to obtain statistically significant data, 20 indentations are made at each indentation load. The distance between successive indents is maintained at least ten times the maximum penetration depth to minimize the strain field interactions. The H values are determined using Oliver and Pharr (O&P) method [Oliver and Pharr, 1992] according to equation 1;

$$\text{Hardness, } H = \frac{P_{max}}{24.5h_c^2} \quad (1)$$

Here, P_{max} specifies the maximum indentation load and h_c represents the vertical distance along which the contact is made between Berkovich tip and specimen (Fig. 1.15a and b in Chapter 1), also known as indentation size. Fig. 1.15a (in Chapter 1) presents a graphical representation of the quantities used in nanoindentation data analysis on load, P vs.

displacement, h scale. The O&P method considers the sink-in effects in the materials during nanoindentation and estimates the corrected h_c according to eq. 2;

$$h_c = h_{max} - \beta \frac{P_{max}}{S} \quad (2)$$

where, h_{max} specifies the maximum penetration depth, β is the constant which depends on indenter geometry (has an empirical value of 0.75 for Berkovich indenter), and S is the stiffness obtained from the slope of the unloading curve (eq. 3) which obeys a power-law relation (eq. 4)

$$S = \frac{dP}{dh} = \frac{2}{\sqrt{\pi}} E_{red} \sqrt{A_p} \quad (3)$$

$$P = C (h - h_f)^m \quad (4)$$

where, A_p and E_{red} specifies the projected area of elastic contact and reduced elastic modulus, respectively, while C and m specify the empirically determined power-law coefficient and index, respectively, h_f represents the final penetration depth after complete removal of P_{max} and h is the penetration depth. It is worth mentioning here that only A , m and h_f are evaluated by curve fitting.

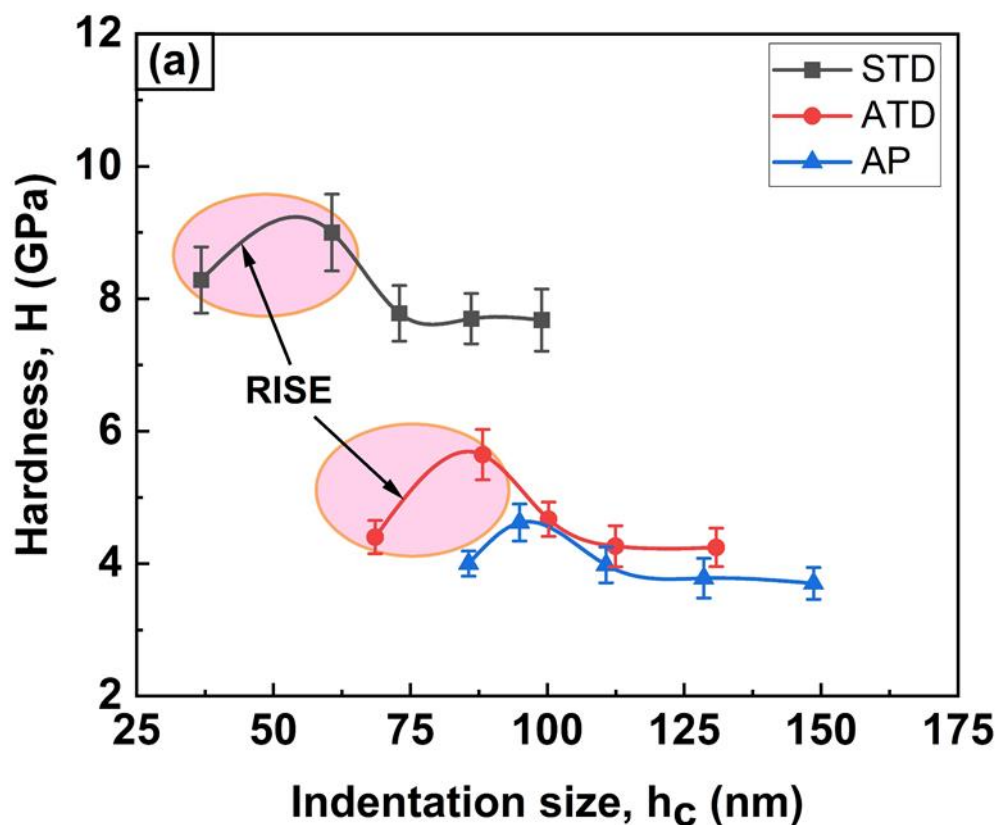
4.3. Results and Discussion

4.3.1. Analysis of P vs. h curves and H of different ferroelectric domain configurations

Representative P vs. h responses of AP, STD and ATD samples are presented in Fig. 2.4 (in chapter 2 for PMN-PT) and Figs. 3.9 and 3.10 (in chapter 3 for PZT-H and PZT-S, respectively). The loading part of P vs. h curves overlap with each other for all the samples, indicating a high level of reproducibility. Further, the loading and unloading curves do not show any noticeable *pop-in* and *pop-out* events even at $P_{max} = 5$ mN ruling out the possibility of crack formation and pressure-induced phase transformation during the indentation, if any. The area function, $A(h_c)$ calibration curve is presented in Fig. A6 in Appendix 1, indicating the best polynomial fit with a high correlation coefficient ($R^2 \sim 1$) and negating the uncertainties related to tip blunting and deviation from the ideal geometry of the indenter, if any. The variation in H as a function of h_c for AP, STD and ATD samples of PMN-PT, PZT-H and PZT-S is shown in Figs. 4.1 a, b and c, respectively, which clearly shows ISE in H , where H decreases with increase in h_c in all the materials. Interestingly, in

PMN-PT, H increases with an increase in h_c (particularly at lower h_c) irrespective of the domain configurations, indicating the reverse indentation size effects (RISE).

The possible reasons for the RISE in PMN-PT below a certain critical indentation size, h_{crit} is attributed to the deformation confined only to particular slip systems due to the plastic anisotropy and indentation induced cracking (IIC) [Li and Bradt, 1996 and Sangwal, 1989, 2000]. However, the indentation imprints do not show any evidence of cracking in the vicinity of indentation, indicating that the IIC is not suitable for explaining RISE. Therefore, it can be reasoned that the observed RISE could be due to the surface irregularities generated during the sample preparation. It also appears from the Fig. 4.1a that critical indentation size, h_{crit} at which the transition from RISE to ISE occurs is almost similar for AP, STD and ATD samples of PMN-PT. The possible mechanisms of ISE in H in crystalline metals are attributed to the presence of strain gradient beneath the indenter [Nix and Gao, 1998, Lim and Chaudhri, 2007, Swadener et al., 2002, Prasad and Ramesh, 2019], grain boundary strengthening effects [Nix and Gao, 1998], the surface free energy of the material [Jäger, 2004], while ISE in polycrystalline ceramics, in addition to the above, is also attributed to the fracture taking place underneath indentation [Quinn and Quinn, 1997].



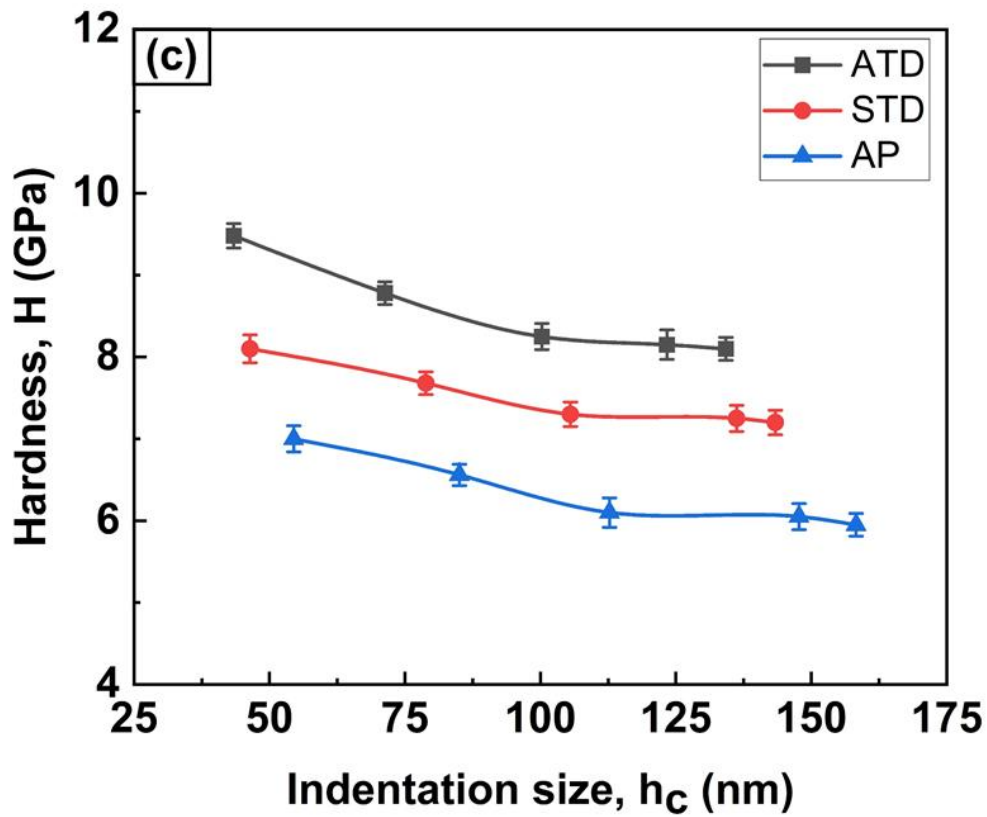
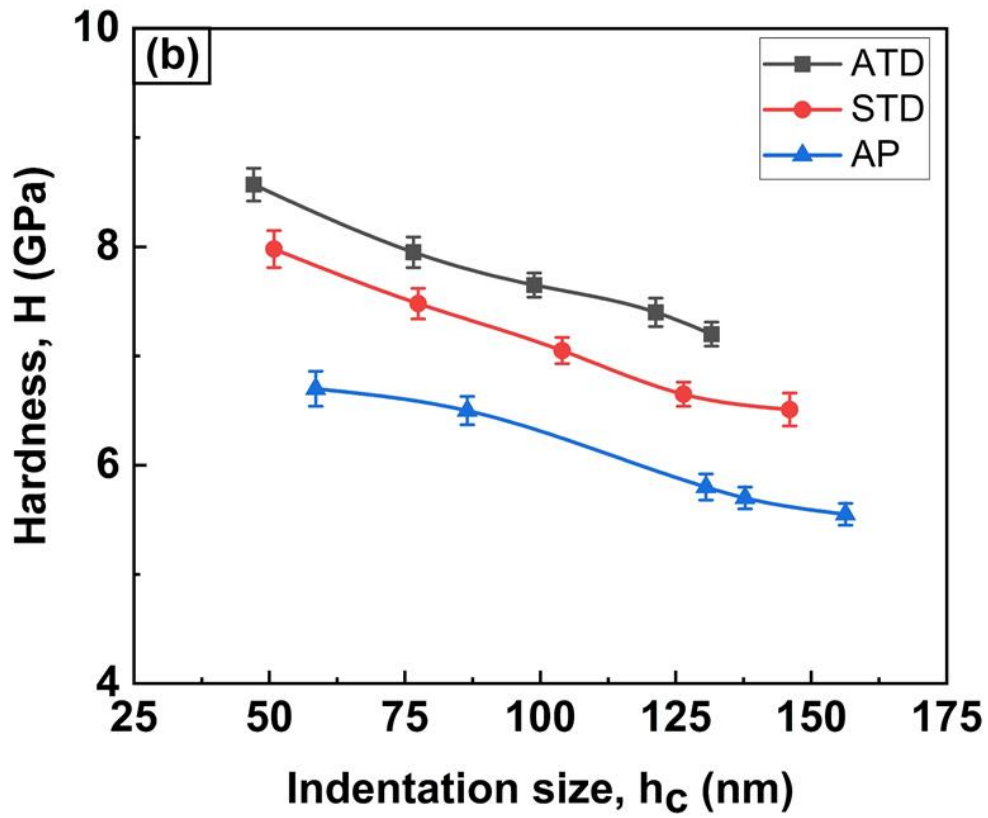


Fig. 4.1 Variation of nanoindentation H with respect to h_c for AP, STD and ATD samples of (a) PMN-PT, (b) PZT-H, and (c) PZT-S piezoceramics. All the materials exhibit typical ISE in H .

However, the limited number of studies, particularly on single-crystal PZT and BT, suggest that the ISE in piezoceramics can be related to the distinct *pop-in* events occurring mainly due to ferroelectric DW motion beneath the indenter [Hurtado-Macias et al., 2008] and strain gradient polarization (flexoelectric effect) underneath the indentation [Gharbi et al., 2009]. Besides this, Schneider and co-workers (2005) have demonstrated the role of local ferroelectric domain rearrangements (e.g., domain switching mechanisms) taking place in the indentation zone on the indentation behaviour of single-crystal BT. Further, Kathavate and co-workers (2018) (2020) highlighted the role of differences in ferroelectric domain configurations on the ISE in H of some polycrystalline Pb-based and Pb-free piezoceramics. All the above observations construed the fact that dislocation activities and ferroelectric domain rearrangements beneath the indenter are the primary sources of ISE in piezoceramic materials. Note that the h_{max} at P_{max} in all the samples is in the range of ~ 150 - 200 nm, which is nearly an order of magnitude smaller than d_{avg} indicating that the hardness response most probably comes from an individual grain. Based on this, it can be construed that RISE and ISE in H are mostly from an individual grain which further suggests that H is dependent on the indentation size rather than the grain size.

It is also evident from Fig. 4.1 that for PMN-PT, the H follows the following trend: $H_{STD} > H_{ATD} > H_{AP}$, while for both the PZT, H follows the trend: $H_{ATD} > H_{STD} > H_{AP}$, which is attributed to the differences in ferroelectric domain configurations and also the domain switching mechanisms taking place in respective materials underneath the indentation. The ferroelectric domains in AP samples are perfectly aligned (i.e., highest piezoelectric effect) by forming 90° and 180° DW, while ferroelectric domains in STD and ATD samples show significant disorderness by reorienting through non- 90° and non- 180° DW (i.e., lowest piezoelectric effect) as shown in Figs. 3.6 and 3.7 in previous chapter 3. Upon indentation, the ferroelectric domains in AP samples are likely to exhibit switching through 90° DW, which further minimizes the elastic strain energy associated with them. This minimization of elastic strain energy can be intimately related to the reduction in the driving force for the elastic recovery of ferroelectric domains, which eventually offers less resistance to the indentation. In fact, Park and Dicken (2007) demonstrated the formation of 90° DW during the nanoindentation of single-crystal BaTiO₃. However, non- 90° and non- 180° DW formation during indentation in STD and ATD samples cause irreversible depolarization in the material [Wong and Zeng, 2010], which further increases the domain mobility and offers more restrictions on switching of ferroelectric domains at grain

boundaries. Furthermore, the onset of fracture in piezoceramic materials is attributed to the intergranular residual stresses [Sun et al., 2012], which may arise due to the lattice strain incompatibilities during ferroelectric domain switching. Upon annealing, ferroelectric domain relaxation is expected to occur due to the relaxation of intergranular residual stresses, which eventually delays the onsets of plastic deformation. Therefore, disturbed domain structure in STD and ATD samples shows increased resistance to the indentation, which further appears to increase H .

Among both the PZTs, PZT-S exhibits slightly higher H compared to the PZT-H due to the closely spaced ferroelectric domain structure (Figs. 3.6 and 3.7 in chapter 3), which is corroborated by the observations of Cao and Evans (1993), who have attributed the high strength in the case of PZT-S samples to the differences in ferroelastic domain configurations and domain switching during compression experiments. In the subsequent sections, ISE in H of PMN-PT, PZT-H and PZT-S are examined in detail using various mechanistic models for the improved understanding of the role of various ferroelectric domain configurations.

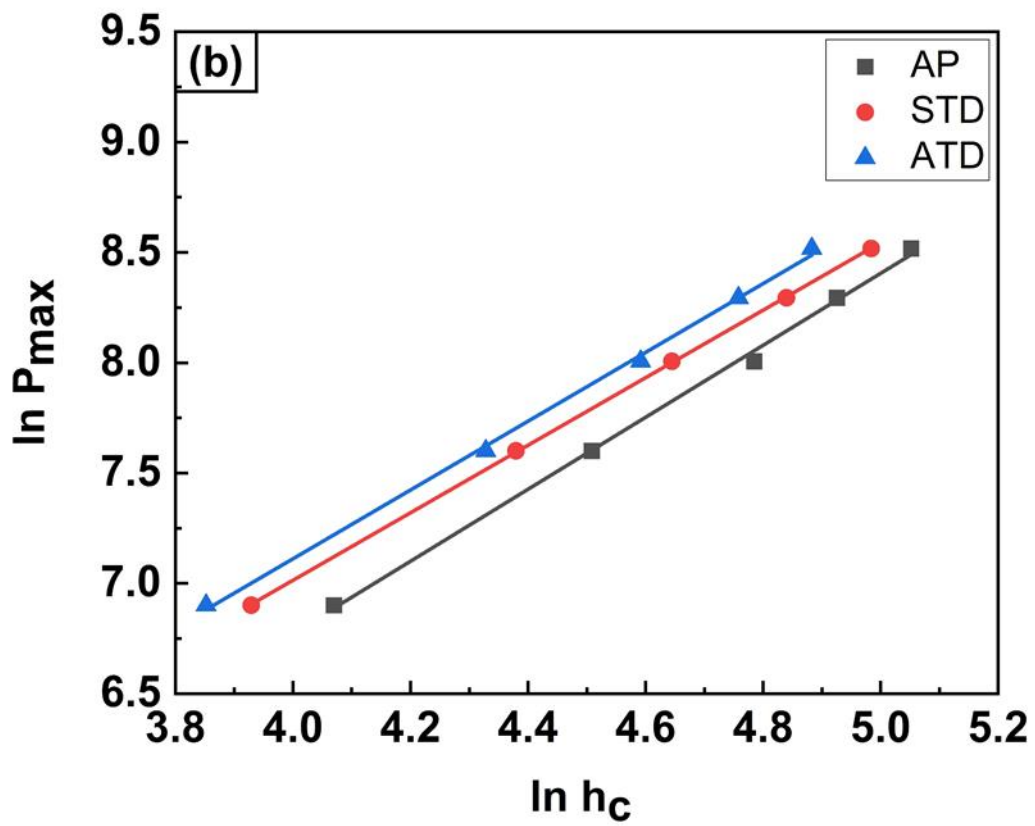
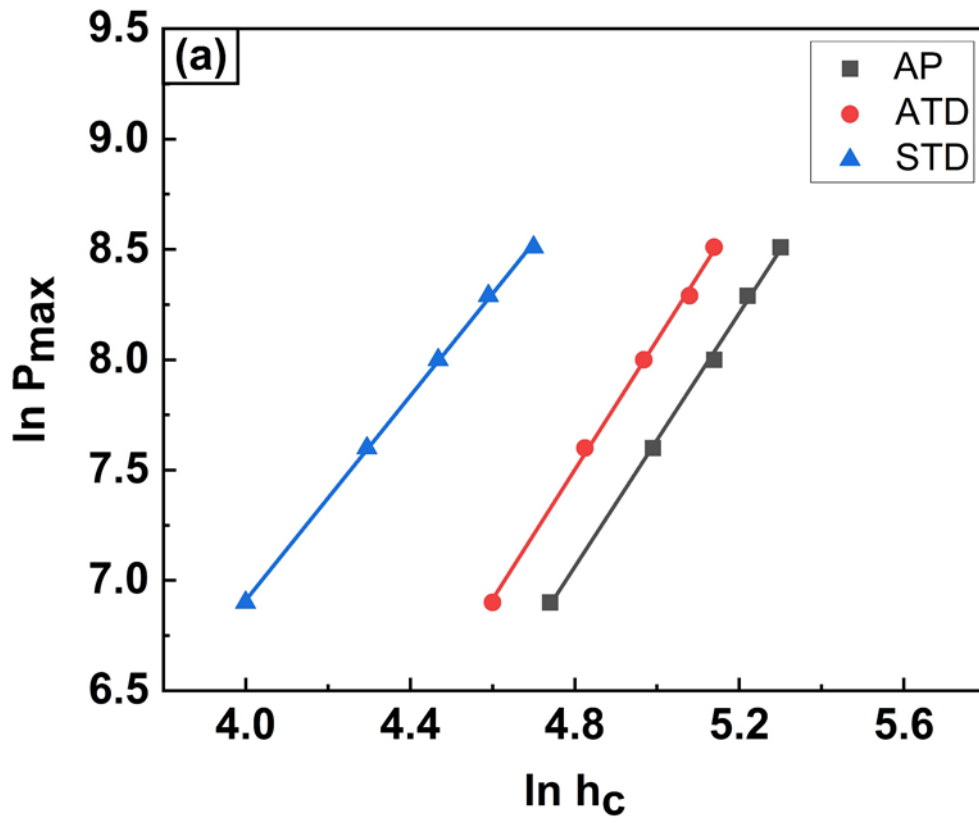
4.3.2. Assessment of nanoindentation data: Mechanistic modelling of ISE

4.3.2.1. Meyer's Law and Hays-Kendall (H-K) model

The ISE has been conventionally described by the relation between P and h_c given below, and sometimes referred to as Meyer's law [Lysaght, 1949, McColm, 1990];

$$P = \alpha h_c^n \quad (5)$$

where " n " refers to Meyer's index and/or exponent, which quantifies the degree of ISE, while the proportionality constant, α with a unit mN/nm^n , represents the material's resistance to the initial plastic deformation. The nanoindentation data for all the samples of PMN-PT, PZT-H and PZT-S is plotted on $\ln P_{max}$ vs. $\ln h_c$ scale in Figs. 4.2(a-c), respectively indicating the linear relationship with good regression values ($R^2 \sim 0.9999$), which also suggests that the conventional Meyer's law very well captures the ISE in PMN-PT, PZT-H and PZT-S. The best fit values of " n " and α are summarized in Table 4.1. The " n " values are in the range of 1.2 to 1.9 for PMN-PT and 1.40 to 1.63 for PZT-H and PZT-S, which is in concurrence with the reported literature values ~ 1 -2 [Li and Bradt, 1993, Quinn and Quinn, 1997, Lysaght, 1949, McColm, 1990].



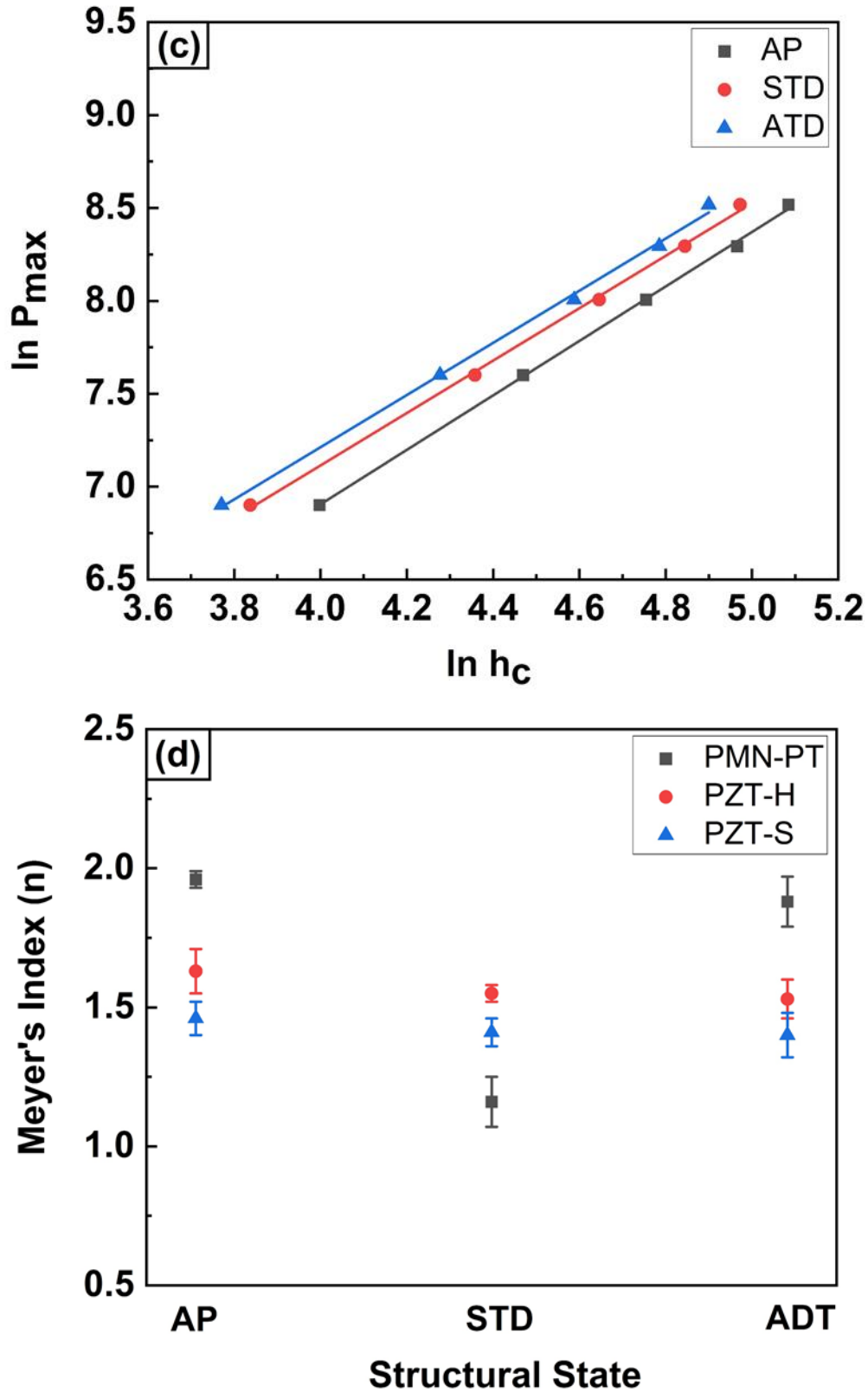


Fig. 4.2 Representative plots of $\ln P_{max}$ vs. $\ln h_c$ data according to Meyer's model for AP, STD and ATD domain configurations of (a) PMN-PT, (b) PZT-H, and (c) PZT-S, and (d) variation in Meyer's index, "n" with respect to different structural states of PMN-PT, PZT-H and PZT-S.

The previous studies indicated that the curvature of the size effects curve (i.e., H vs. h_c curve) has a marked dependency on " n " values, as at $n = 2$, H vs. h_c curve exhibits a flat line indicating that the H is size-independent, while for $n < 2$, H decreases with an increase in h_c (representing ISE), as shown schematically in Fig. A7 in Appendix 1 [Tate, 1945, Sargent, 1978, 1984, Babini et al., 1978, Sangwal, 1989, 2000, Li and Bradt, 1993, Kim and Kim, 2002]. Further, the presence of RISE (i.e., increase in H with an increase in h_c) can be seen when $n > 2$ [Sangwal, 1989, 2000]. The relationship between " n " and α has been a subject of frequent studies in Meyer's law. For instance, Sargent and Babini and co-workers (1978) (1984) have studied the role of d_{avg} (in the range of 10 μm to 100 μm) on " n " and α using micro-indentation experiment on polycrystalline ceramics and observed that " n " decreases with an increase in d_{avg} , while α values also increase. However, in the current study, the dependence of " n " values on d_{avg} is minimal as the h_{max} is much smaller than the d_{avg} . Further, due to the similar d_{avg} in all the samples within the standard deviation, the difference in " n " values among different samples are intimately connected to the differences in ferroelectric domain configurations. Fig. 4.2d represents the variation of " n " with different ferroelectric domain configurations in PMN-PT, PZT-H and PZT-S, which further indicates the following trend: $n_{AP} > n_{ATD} > n_{STD}$ for PMN-PT and $n_{AP} > n_{STD} > n_{ATD}$ for PZT-H and PZT-S. The possible reasons for this are attributed to the changes taking place in the ferroelectric domain configurations during the annealing, and the high H values in annealed samples can also be further related to the lower " n " values, which is in agreement with the previous studies [Sargent, 1978, 1984, Babini et al., 1978, Li and Bradt, 1993, Kim and Kim, 2002].

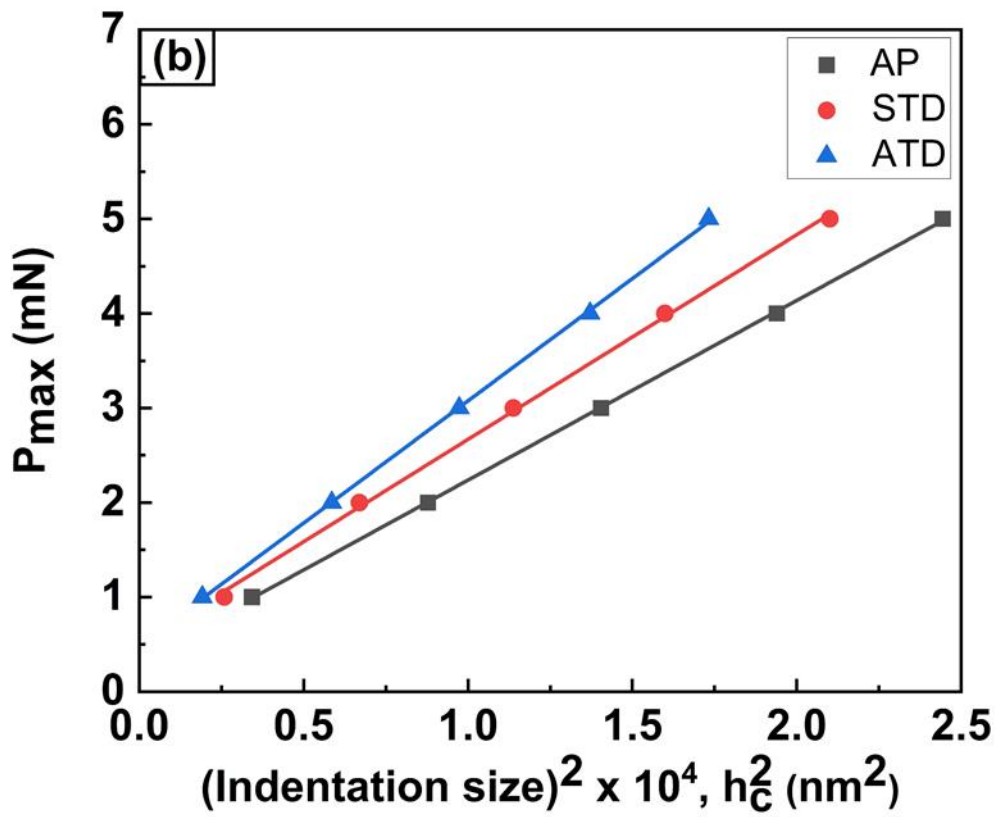
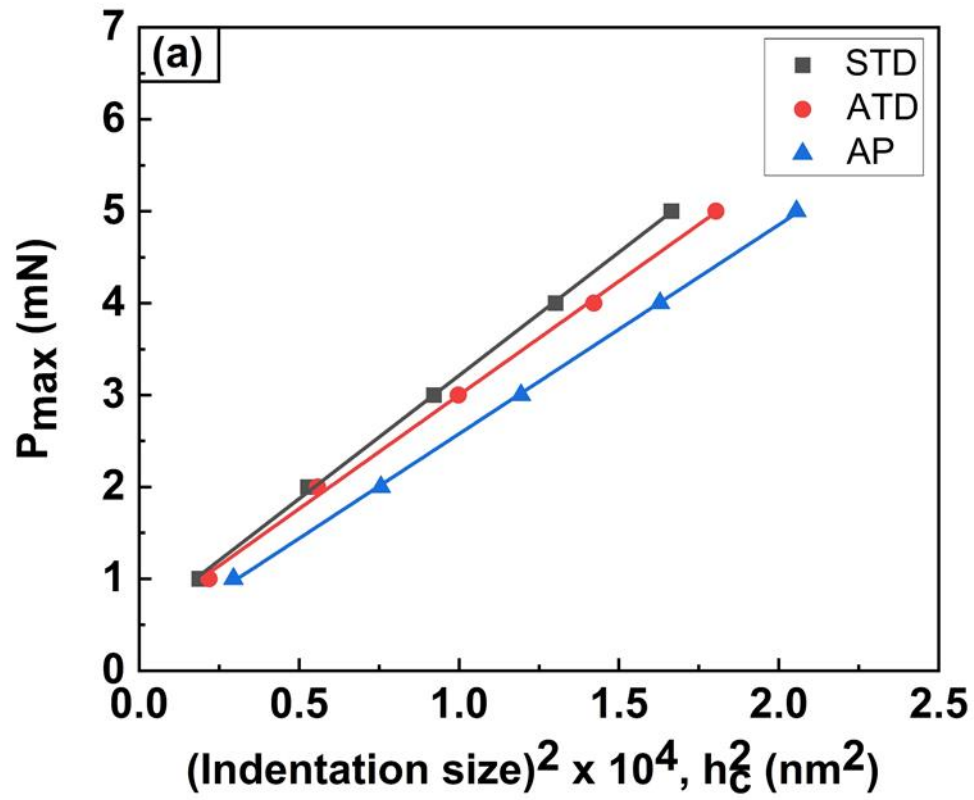
Unlike Meyer's law which uses the P_{max} to describe the ISE, Hays and Kendall (1973) developed a model known as Hays-Kendall (H-K) model which considers the effective indentation load, P_{eff} to describe the ISE. The P_{eff} is obtained by subtracting the minimum test load, P_{min} from P_{max} , where P_{min} is the minimum test load below which the material does not undergo permanent deformation. The P_{min} in H-K model can be intimately related to the microfriction between the indenter and contact surface Gane and Bowden (1968). According to the H-K model, the P_{eff} is related to the h_c as;

$$P_{eff} = (P_{max} - P_{min}) = Bh_c^2 \quad (6)$$

Table 4.1 Summary of the descriptive parameters obtained from Meyer’s law and H-K model for all the samples of PMN-PT, PZT-H and PZT-S piezoceramics.

Materials	Structural state	Meyer’s law			Hays-Kendall model		
		n	$\alpha \times 10^{-3}$ (mN/nm ⁿ)	R ²	P_{min} (mN)	$B \times 10^{-3}$ (mN/nm ²)	R ²
PMN-PT	AP	1.96 ± 0.04	0.35	0.9999	0.30 ± 0.02	2.27	0.9993
	STD	1.16 ± 0.12	0.53	0.9999	0.53 ± 0.01	2.68	0.9999
	ATD	1.88 ± 0.08	0.37	0.9998	0.45 ± 0.01	2.47	0.9999
PZT-H	AP	1.63 ± 0.07	1.27	0.9997	0.33 ± 0.01	1.90	0.9998
	STD	1.55 ± 0.04	2.38	0.9999	0.48 ± 0.02	2.16	0.9999
	ATD	1.53 ± 0.03	2.43	0.9998	0.50 ± 0.05	2.56	0.9999
PZT-S	AP	1.46 ± 0.02	4.34	0.9989	0.34 ± 0.03	1.81	0.9996
	STD	1.41 ± 0.02	4.82	0.9993	0.50 ± 0.02	2.27	0.9998
	ATD	1.40 ± 0.03	4.90	0.9997	0.57 ± 0.04	2.44	0.9999

The plots of P_{max} vs. h_c^2 for AP, STD and ATD samples of PMN-PT, PZT-H and PZT-S showed in Figs. 4.3(a-c), respectively reflect the best fitting of the nanoindentation data with high correlation coefficients ($R^2 \sim 0.9999$). The values of P_{min} and B are obtained from the linear fitting of P_{max} vs. h_c^2 data are summarized in Table 4.1, which further indicate that the P_{min} values are much lower than the minimum indentation load (i.e., 1 mN) used in the current experiments. This also suggests that all the samples of PMN-PT, PZT-H and PZT-S piezoceramics exhibit P_{min} values where the behaviour of the material is elastic. Also, the P_{min} values are found to be higher in STD samples in PMN-PT, while in PZT-H and PZT-S, ATD samples exhibit higher P_{min} suggesting a higher resistance to the plastic flow offered by them. We further note that Meyer’s index, “ n ” and exponent, B of h_c in the H-K model (i.e., “2”) are two different quantities. The first one characterizes the size effects curve, while the later one is the empirical constant in the power-law series [Fröhlich et al., 1977]. Therefore, any attempt to correlate the “ n ” values with the exponent, B of h_c in the H-K model is inappropriate. Both Meyer’s law and H-K model do not distinguish the difference between load-dependent and independent H , although they quantify the ISE by means of fitting parameters.



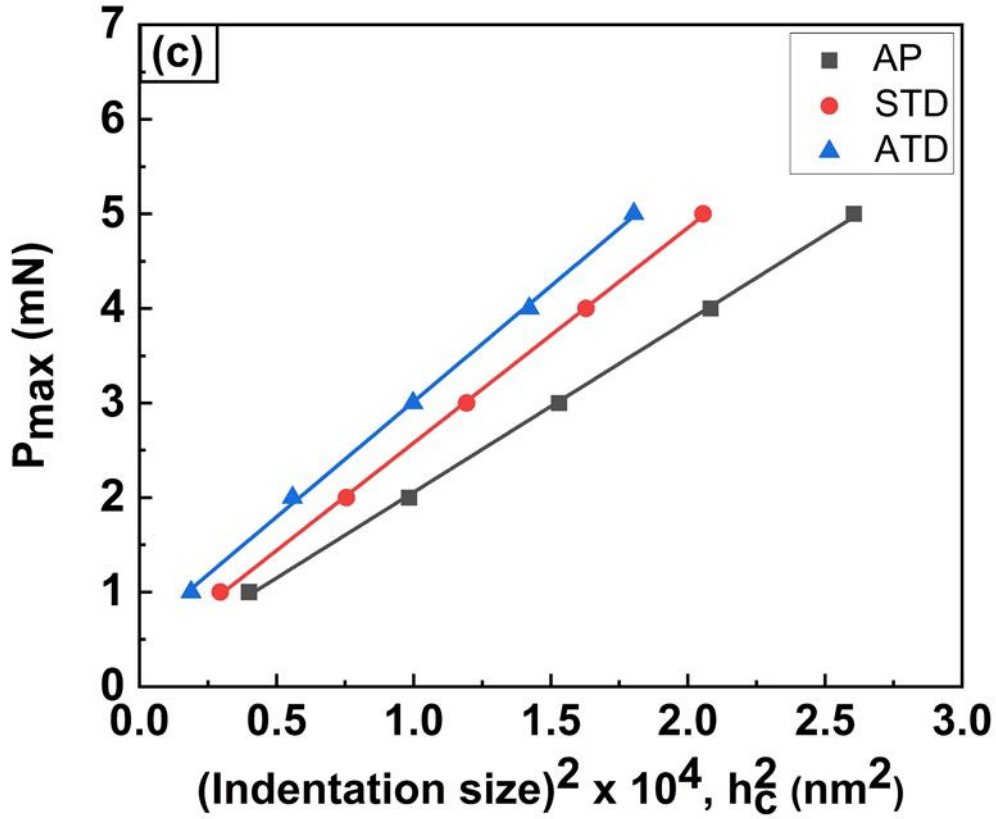


Fig. 4.3 Representation of the Hays-Kendall model on the plots of P_{max} vs. h_c^2 for AP, STD and ATD samples of (a) PMN-PT, (b) PZT-H, and (c) PZT-S.

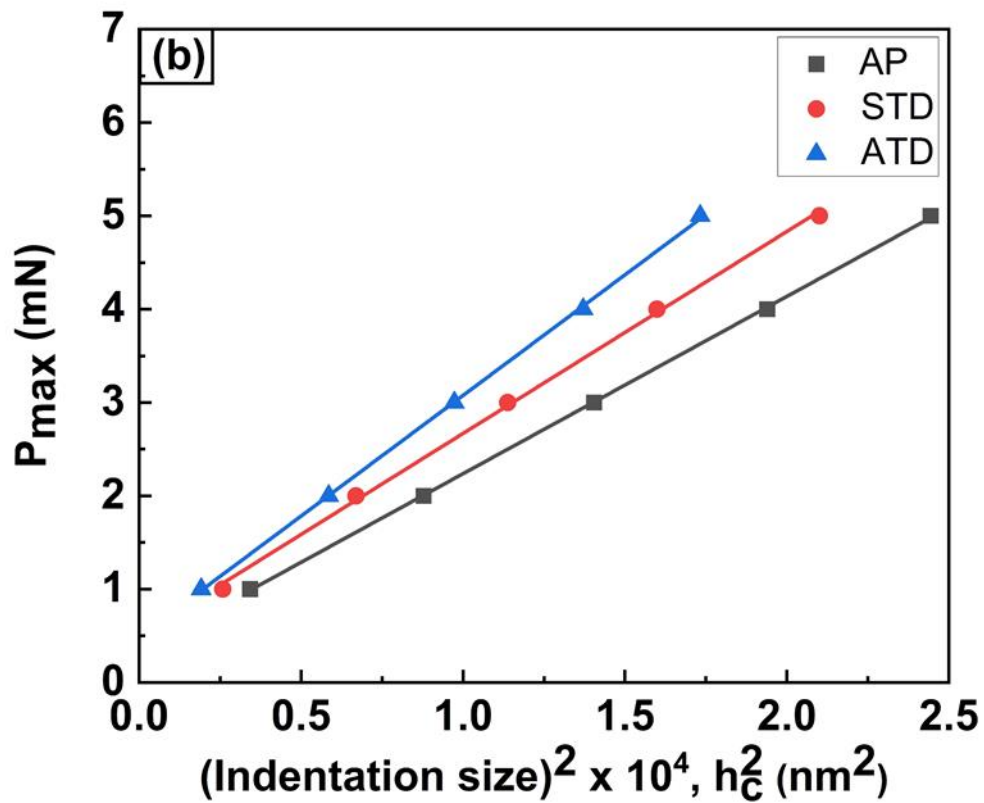
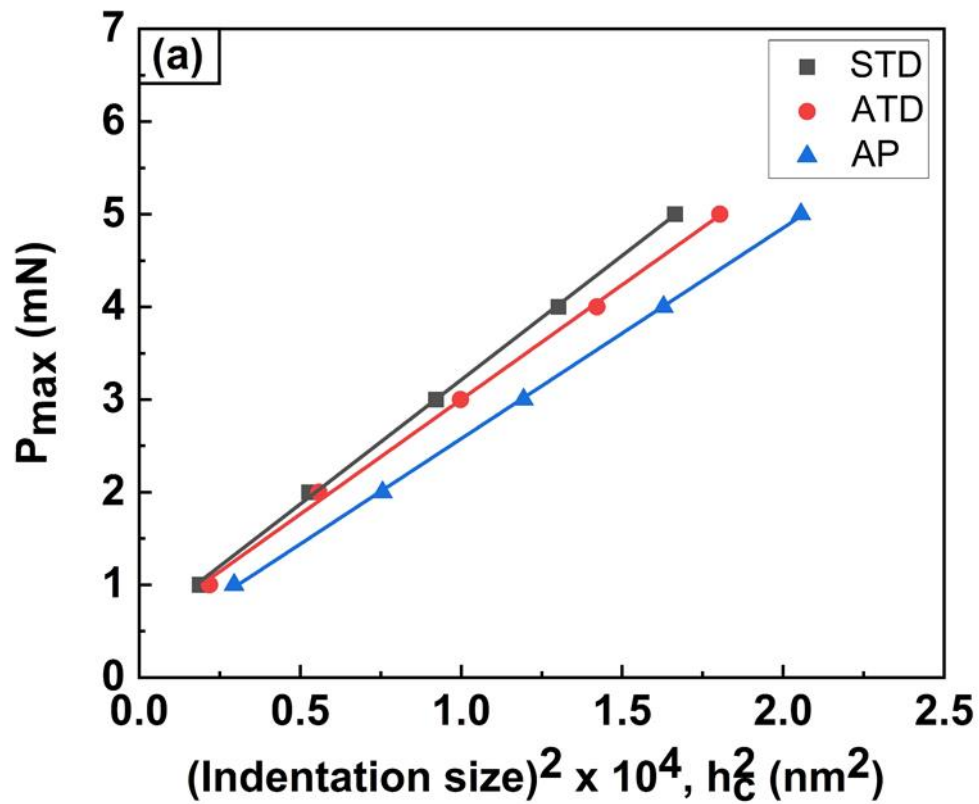
4.3.2.2. Elastic Recovery (ER) model

The elastic recovery (ER) model considers that the h_c decreases upon the removal of P_{max} due to the elastic recovery (or shortening) in the vicinity of the indentation impression. These changes in the h_c due to the elastic recovery, if not taken into consideration, overestimate the H values. Therefore, the corrections in h_c can decouple the true hardness of the material from apparent or machine hardness. The ER model connects the P_{max} to h_c and corrections in indentation size, h_c^* as;

$$P_{max}^{1/2} = \gamma^{1/2} h_c + \gamma^{1/2} h_c^* \quad (7)$$

The linear fitting of $P_{max}^{1/2}$ vs. h_c data for AP, STD and ATD samples of PMN-PT, PZT-H and PZT-S (Figs. 4.4a-c) reflects the high regression coefficient ($R^2 \sim 0.9999$) and the best fit values of descriptive constant, γ and h_c^* are compiled in Table 4.2. The h_c^* (as shown in Table 4.2) is much lower than the actual h_c for all the samples of PMN-PT, PZT-H and PZT-S. For ex., the h_c^* of AP sample of PZT-H is 0.19 nm which is approximately 400 times lower

than the experimentally recorded h_c (74.14 nm), and therefore rules out the possibility of tip blunting effect and confirms the validity of nanoindentation experiments.



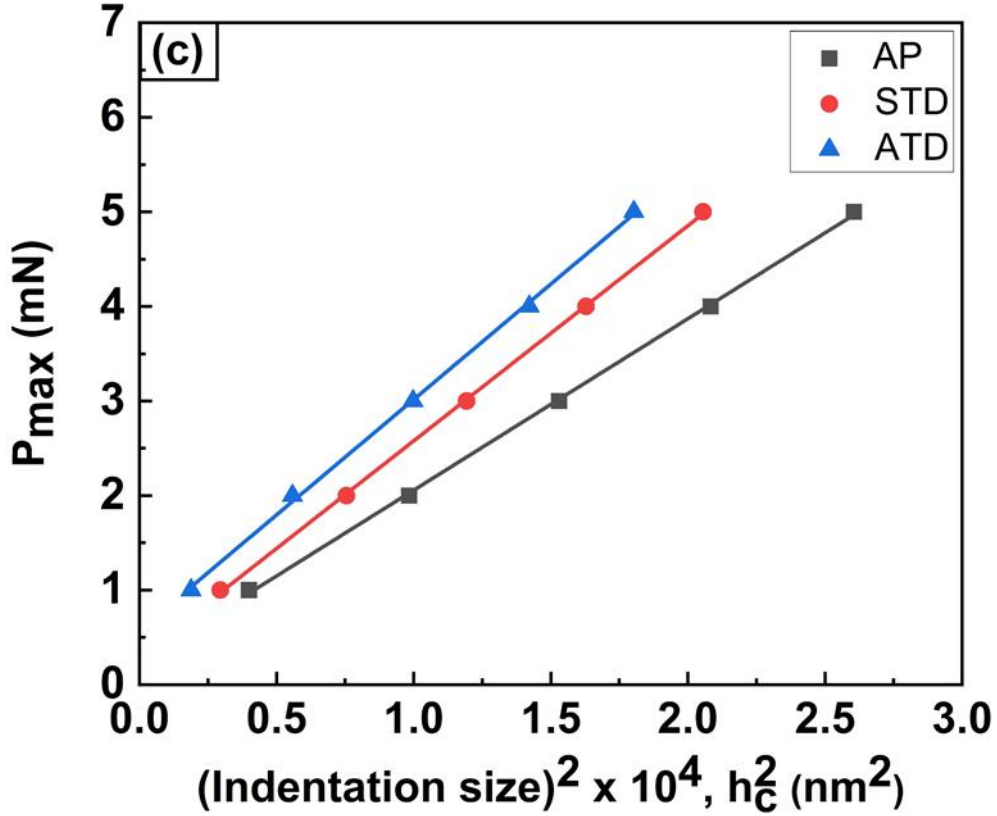


Fig. 4.4 Dependency of h_c on $P_{max}^{1/2}$ according to the ER model for AP, STD and ATD samples of (a) PMN-PT, (b) PZT-H and (c) PZT-S piezoceramics.

The STD samples in PMN-PT exhibit the higher h_c^* values, while ATD samples in both the PZTs show a higher h_c^* values compared to AP configurations, suggesting higher elastic recovery of the material. The ferroelectric domains in annealed samples tend to split by forming non-180° and non-90° DW because of high domain mobility. The reduced energy barrier due to thermal annealing likely to impede the ferroelectric domain switching process in annealed samples during indentation. Therefore, the formation of such DW offers more resistance to the plastic deformation due to reorientation during indentation, which can be intimately connected to their elastic recovery. The load-dependent true hardness, (H_1) from the ER model can be calculated as;

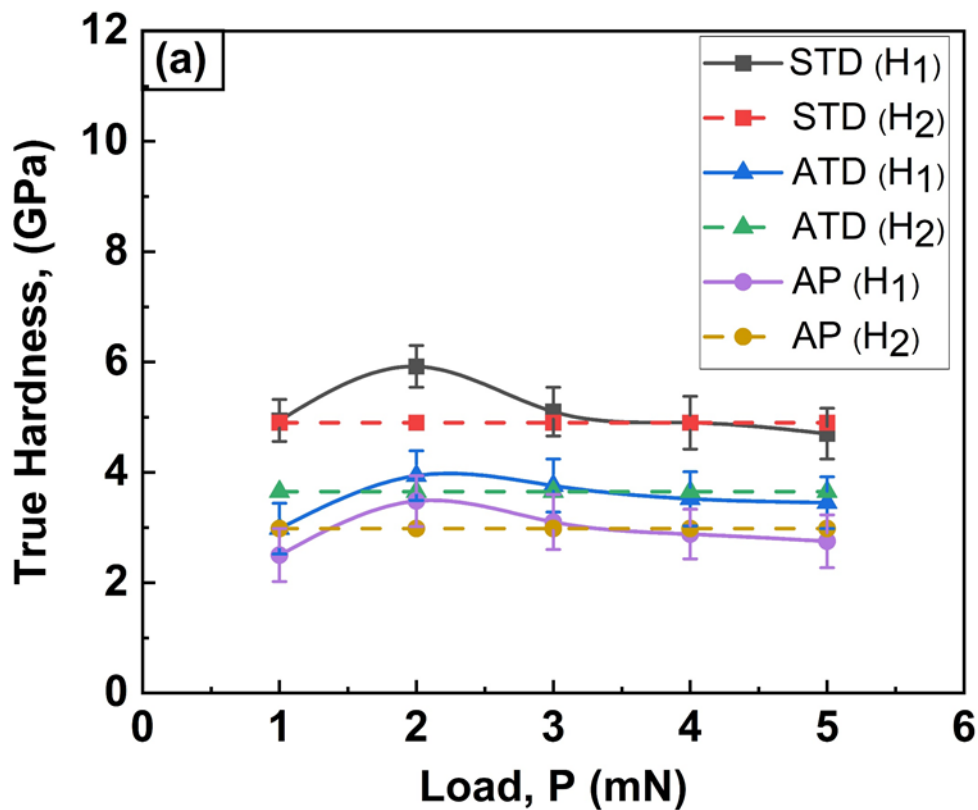
$$(H_1) = \frac{\varepsilon P_{max}}{(h_c + h_c^*)^2} \quad (8)$$

where “ ε ” represents the constant related to the geometry of the indenter and has an empirical value of 0.04 for the Berkovich tip. Further, the descriptive constant γ from eq. 7 is related to the plastic deformation in the material and often associated with load-independent true hardness (H_2);

$$(H_2) = \beta \varepsilon \quad (9)$$

Table 4.2 Summary of the descriptive parameters and true hardness values obtained from the ER model for all the samples of PMN-PT, PZT-H and PZT-S piezoceramics. (H_1)- Load-dependent hardness, (H_2)- Load-independent hardness).

Materials	Structural state	Elastic recovery model				
		h_c^* (nm)	$\gamma \times 10^{-4}$ (mN/nm ²)	R ²	H_1 (GPa)	H_2 (GPa)
PMN-PT	AP	0.19 ± 0.01	1.49	0.9998	3.10 ± 0.50	2.98
	STD	0.29 ± 0.03	1.77	0.9999	4.94 ± 0.38	4.90
	ATD	0.21 ± 0.02	1.69	0.9998	3.94 ± 0.45	3.65
PZT-H	AP	0.19 ± 0.03	1.57	0.9993	6.36 ± 0.70	6.44
	STD	0.33 ± 0.08	1.89	0.9998	7.37 ± 0.62	7.50
	ATD	0.34 ± 0.02	1.94	0.9998	7.84 ± 0.58	7.99
PZT-S	AP	0.35 ± 0.01	1.71	0.9999	6.84 ± 0.78	6.97
	STD	0.38 ± 0.02	1.82	0.9998	7.42 ± 0.60	7.46
	ATD	0.44 ± 0.01	1.99	0.9999	8 ± 0.80	8.14



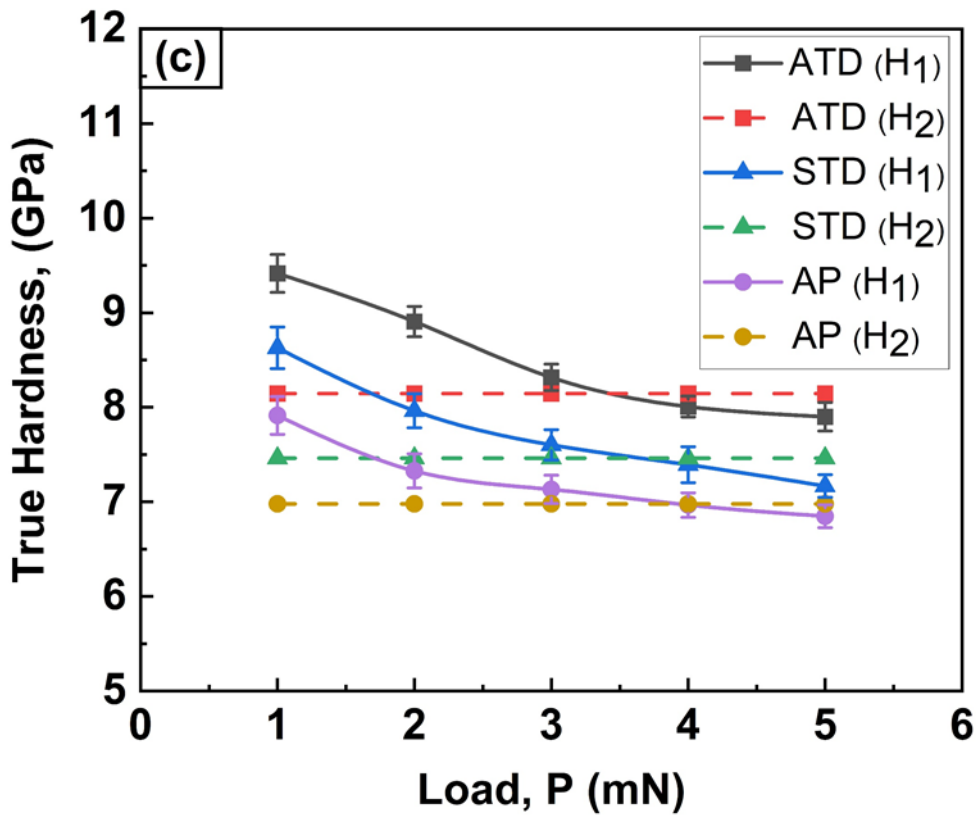
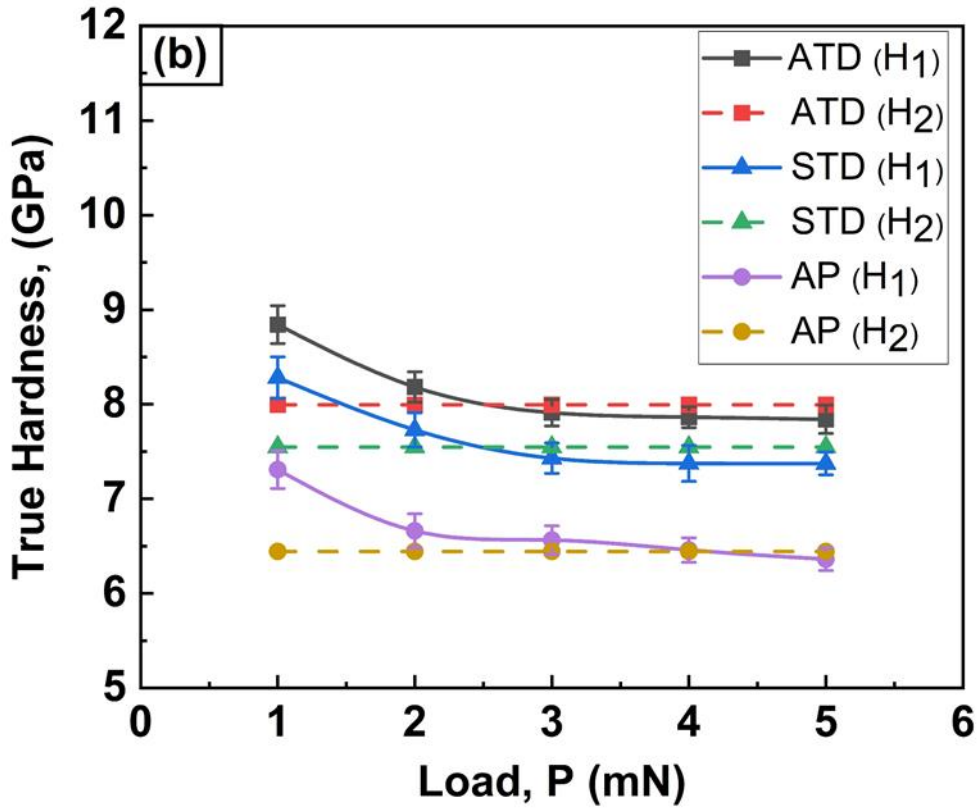


Fig. 4.5 Representation of typical ISE in true hardness values for AP, STD and ATD samples of (a) PMN-PT, (b) PZT-H and (c) PZT-S piezoceramics according to the ER model. ((H_1) - Load-dependent hardness, (H_2) - Load-independent hardness).

The H_1 and H_2 values for AP, STD and ATD samples of PMN-PT and both the PZTs are summarized in Table 4.2. It appears that the H_1 values of all the samples of PMN-PT, PZT-H and PZT-S are comparable to the H values (Figs. 4.2a-c) and also exhibit the RISE and ISE shown in Figs. 4.5a-c. Interestingly, [Maiti et al. \(2018\)](#) have observed a higher H_1 values than the H indicating the overestimation of h_c^* values at higher P (from 100 to 1000 mN), and therefore limiting the applicability of the ER model. Further, the errors introduced due to the tip roundness and blunting effect are not the only sources of ISE.

4.3.2.3. Proportion specimen resistance (PSR) model

The Proportion specimen resistance (PSR) model, proposed by [Li and Bradt \(1993\)](#), is an alternative approach to describe the ISE in crystalline materials according to which the P_{min} from the H-K model [[Hays and Kendall, 1973](#)] is not constant but depends on h_c according to the eq. 10 [[Li and Bradt, 1993](#)];

$$P_{min} = \alpha_1 h_c \quad (10)$$

Further, the relation between P_{eff} and h_c in a PSR model is expressed as;

$$P_{eff} = (P_{max} - P_{min}) = \alpha_2 h_c^2 \quad (11)$$

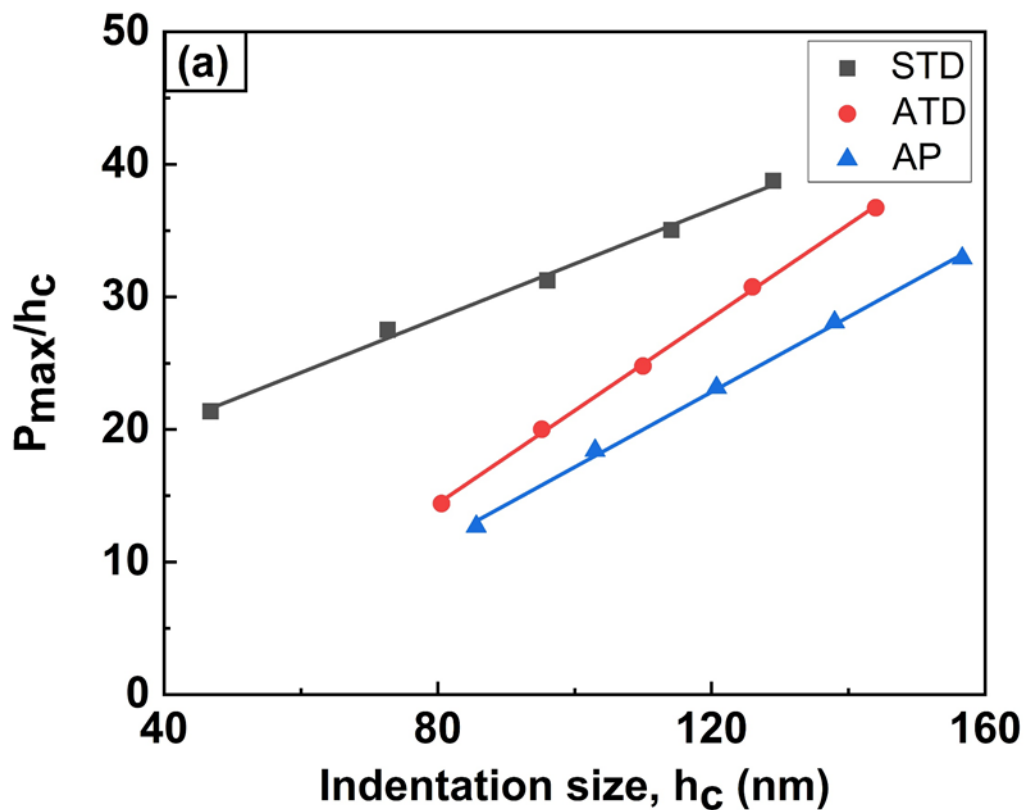
where the descriptive parameters α_1 (mN/nm) and α_2 (mN/nm²) are related to the elastic stiffness and plastic deformation of the material, respectively [[Li and Bradt, 1993](#)]. Equation 11 can be further simplified as;

$$\frac{P_{max}}{h_c} = \alpha_1 + \alpha_2 h_c \quad (12)$$

which yields a straight line fit when P_{max}/h_c is plotted against h_c with a high correlation coefficient ($R^2 \sim 0.9999$) as shown in Figs. 4.6a-c. The values of α_1 and α_2 summarized in Table 4.3 suggest that the PSR model is suitable to describe the ISE in all the domain configurations of PMN-PT, PZT-H and PZT-S. The studies of [Fröhlich et al. \(1977\)](#) and [Quinn and Quinn \(1997\)](#) using energy balance approach indicated that α_1 represents the surface energy generated during the indentation (due to the creation of new surfaces), while α_2 is the measure of the plastic deformation produced per unit volume. This further implies that the α_1 and α_2 are the material-dependent parameters rather than the surface properties.

Table 4.3 Summary of the descriptive parameters and true hardness values obtained from the PSR model for all the samples of PMN-PT, PZT-H and PZT-S piezoceramics. (H_1)- Load-dependent hardness, (H_2)- Load-independent hardness).

Materials	Structural state	Proportion specimen resistance (PSR) model				
		$\alpha_1 \times 10^{-3}$ (mN/nm)	$\alpha_2 \times 10^{-3}$ (mN/nm ²)	R ²	H_1 (GPa)	H_2 (GPa)
PMN-PT	AP	1.41 ± 0.22	0.20	0.9997	2.85 ± 0.40	2.85
	STD	11.09 ± 0.38	0.34	0.9999	4.82 ± 0.38	4.82
	ATD	8.04 ± 0.28	0.28	0.9999	3.68 ± 0.40	3.68
PZT-H	AP	8.16 ± 0.10	0.15	0.9998	5.90 ± 0.70	5.94
	STD	11.97 ± 0.18	0.16	0.9999	6.58 ± 0.50	6.53
	ATD	12.11 ± 0.22	0.19	0.9995	7.17 ± 0.60	7.34
PZT-S	AP	12.37 ± 0.13	0.16	0.9999	5.98 ± 0.78	6.03
	STD	15.61 ± 0.24	0.18	0.9999	6.85 ± 0.90	6.46
	ATD	17.39 ± 0.35	0.20	0.9997	7.80 ± 0.80	7.77



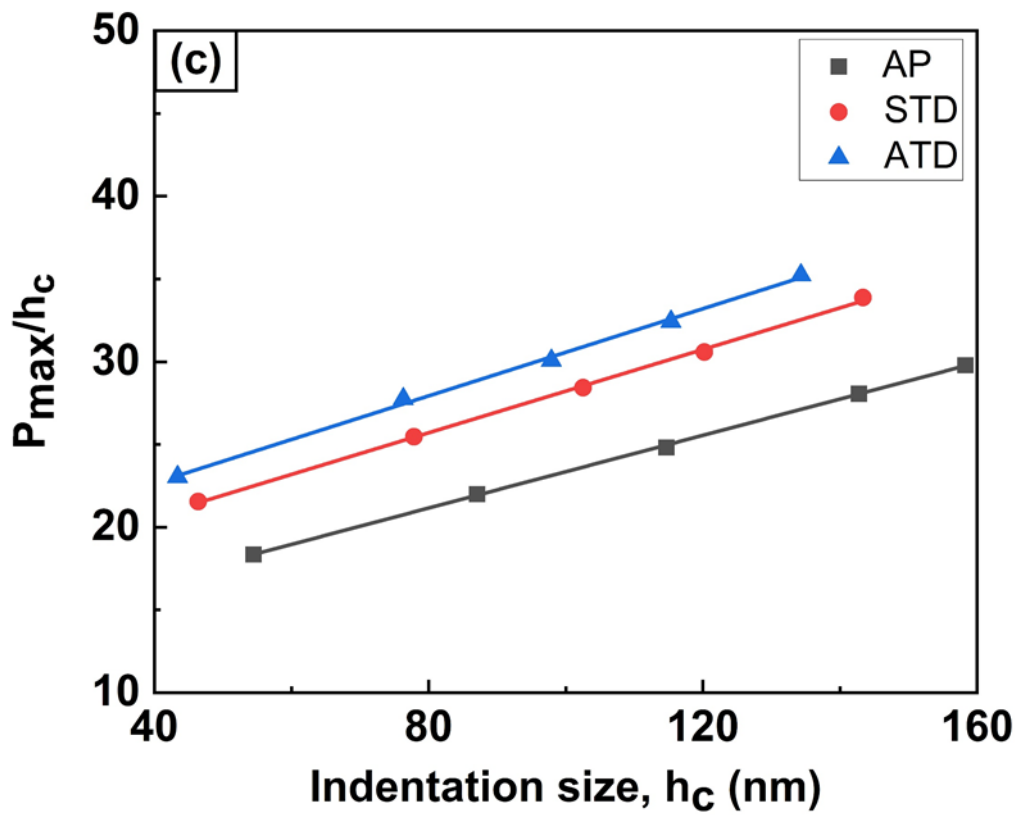
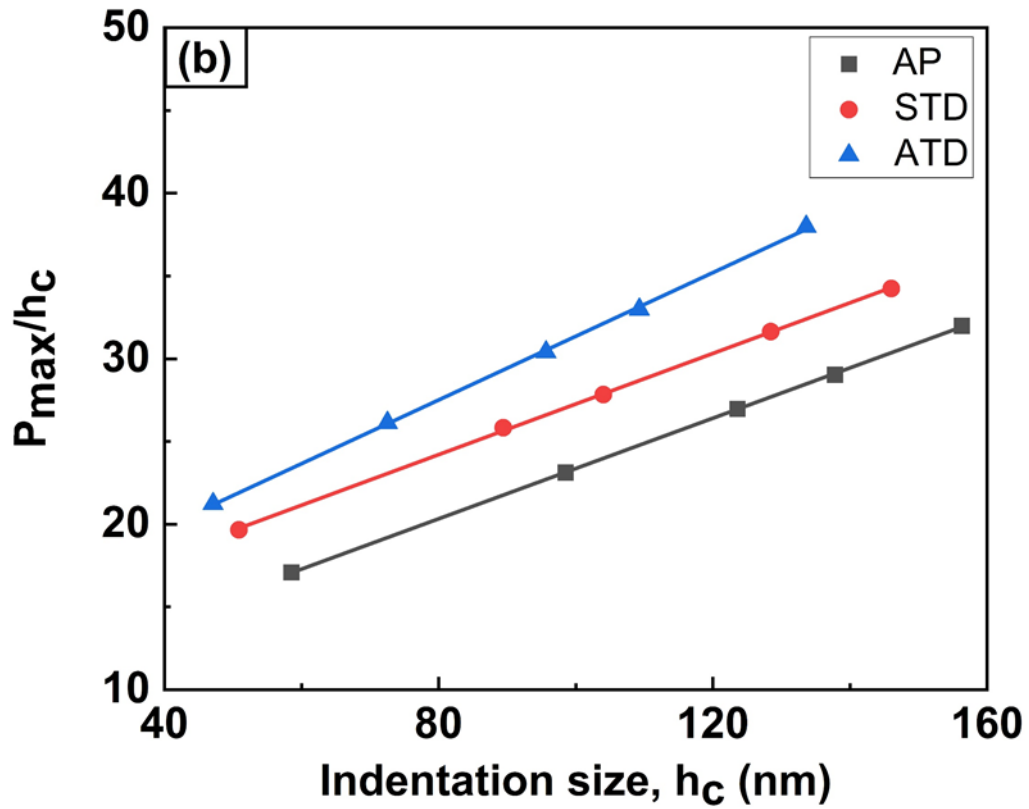


Fig. 4.6 Representation of the nanoindentation data on P_{max}/h_c vs. h_c scale to the PSR model for AP, STD and ATD samples of (a) PMN-PT, (b) PZT-H and (c) PZT-S piezoceramics.

The annealed samples in PMN-PT and both the PZTs exhibit higher α_1 and α_2 values than the AP samples, indicating the higher elastic and plastic resistance to the deformation. This may be attributed to the increased contribution of non-90° and non-180° DW beneath the indenter. The ferroelectric domain structure in AP samples exhibit domain switching by forming 90° DW when subjected to uniaxial compressive loads [Cao and Evans, 1993, Park et al., 2007] to minimize the elastic strain energy associated with them, which can be intimately connected to the lower elastic recovery of ferroelectric domains in the material [Wong and Zeng, 2010]. However, the above phenomenon is unlikely in STD and ATD samples, as the disturbed ferroelectric domain structure shows a rearrangement of domains [Wong and Zeng, 2010, Schneider et al., 2005] by forming non-180° and non-90° DW due to electro-elastic defects such as defect dipoles (due to O and/or Pb vacancies) and micro void or cracks associated with them [Damjanovic and Hysteresis, 2005, Promsawat et al., 2017]. The formation of non-180° and non-90° DW could be advantageous, as they restrict the switching process by extremely weakening the motion of ferroelectric domains at grain boundaries. Consequently, pinning or clamping of ferroelectric domains takes place, which offers the increased resistance to plastic deformation during indentation.

Further, the H_1 and H_2 values computed from the PSR model using Eqs. 13 and 14 are presented in Table 4.3.

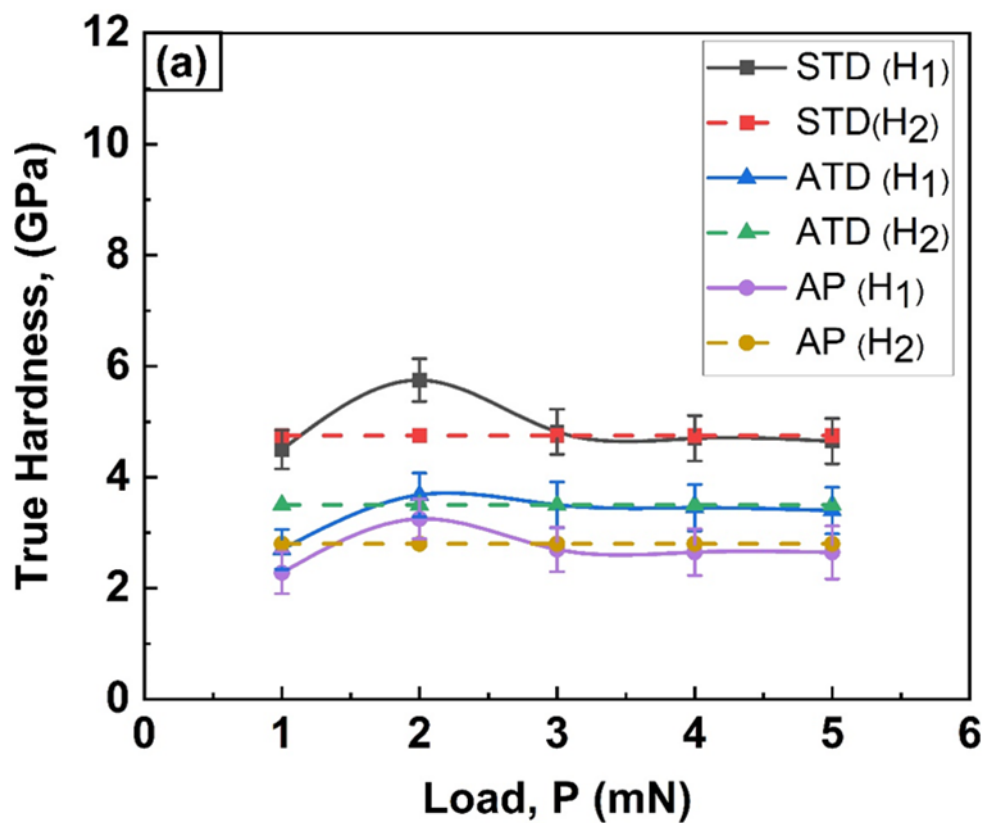
$$H_1 = \frac{(P_{max} - P_{min})}{24.5h_c^2} = \frac{(P_{max} - \alpha_1 h_c)}{24.5h_c^2} \quad (13)$$

$$H_2 = \frac{\alpha_2}{24.5} \quad (14)$$

Clearly, the H_1 values of AP, STD, and ATD samples of PMN-PT, PZT-H and PZT-S are comparable to the H values (Figs. 4.2a-c) and show the size dependence shown in Figs. 4.7(a-c). Further, the H_1 values in PMN-PT follows the trend: $(H_1)_{STD} > (H_1)_{ATD} > (H_1)_{AP}$, while for PZT-H and PZT-S, H_1 values follow the trend: $(H_1)_{ATD} > (H_1)_{STD} > (H_1)_{AP}$, which is also on the expected lines. Figs. 4.8(a-c) demonstrates the variation in H_1 with respect to h_c for AP, STD and ATD samples of PMN-PT, PZT-H and PZT-S indicating the ISE boundary on the basis of h_{crit} above which ISE is less significant and/or inactive. The ISE boundary differs significantly among the AP, STD and ATD samples in all the

materials, which stems from the differences in ferroelectric domain configurations among the samples as schematically illustrated in Fig. 4.8d.

Unlike the ER model, the PSR model can describe the ISE even at higher h_c [Li and Bradt, 1992, 1993, Li et al., 1993, Peng et al., 2004] though few studies showed that it overestimates the H_1 values [Maiti et al., 2018]. Despite its applicability to various ceramics, the PSR model does not consider the effect of residual stresses or surface artefacts induced during machining or polishing of the specimen on the ISE. Therefore, the PSR model (as proposed in equation 12) is slightly modified by Li and Bradt (1993), to satisfactorily describe the hardness variation over a range of loads or indentation sizes which is referred to as the “modified PSR” (MPSR) model.



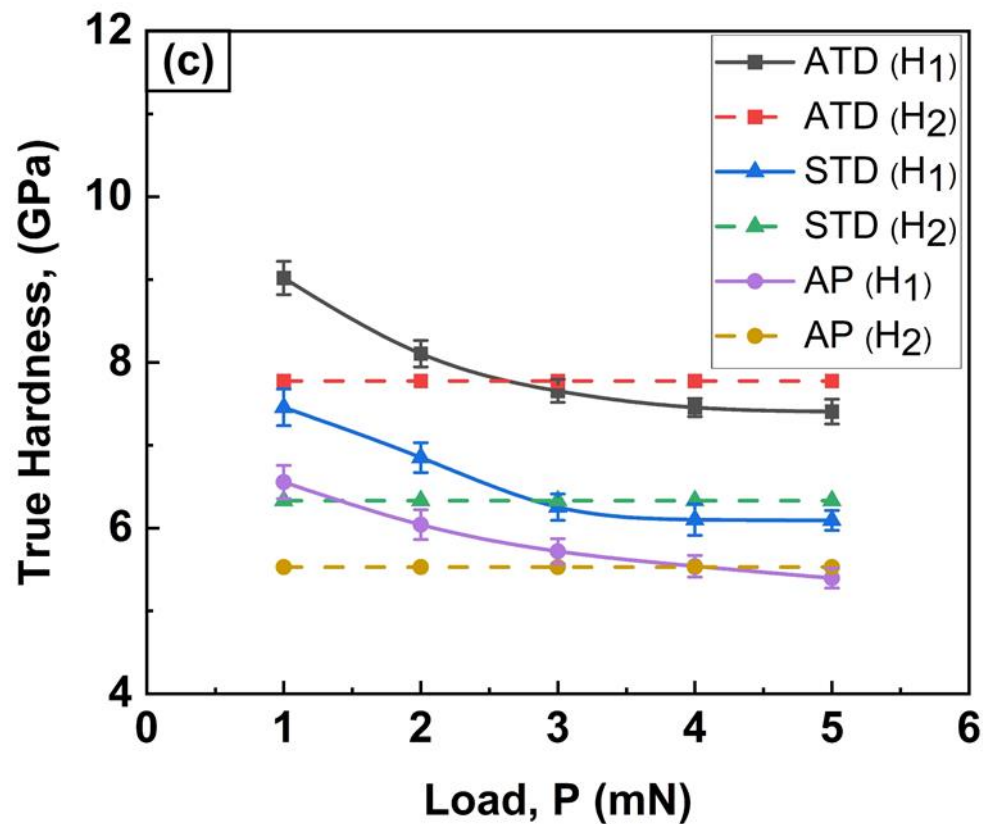
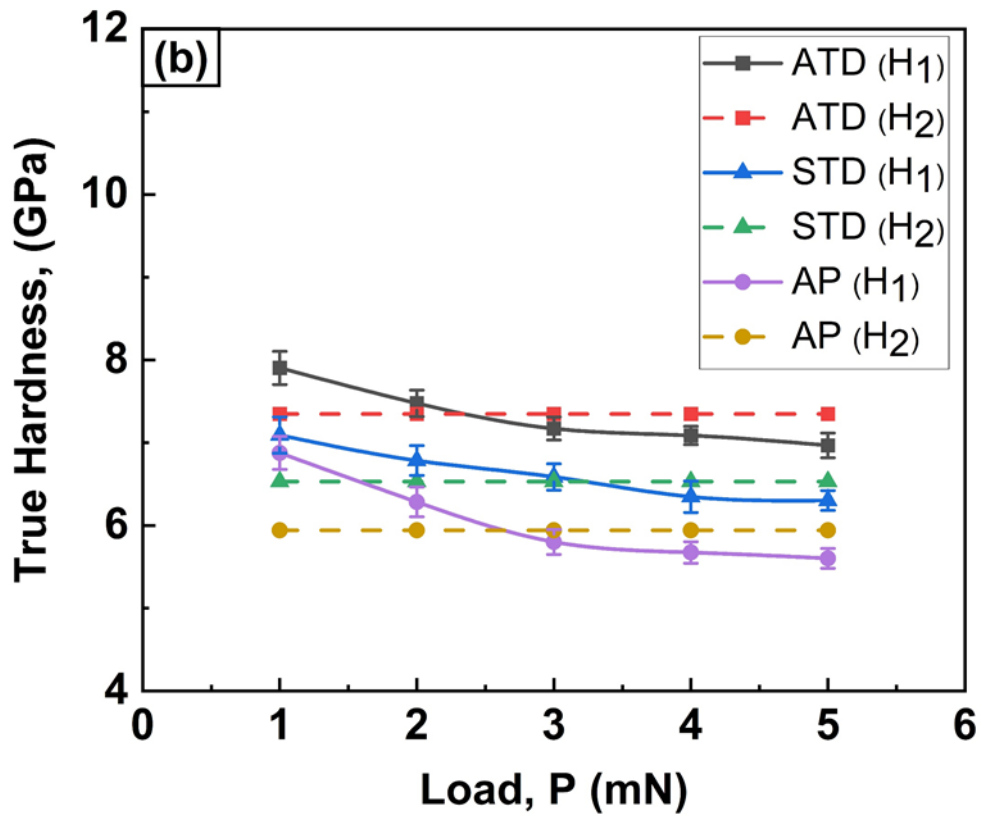
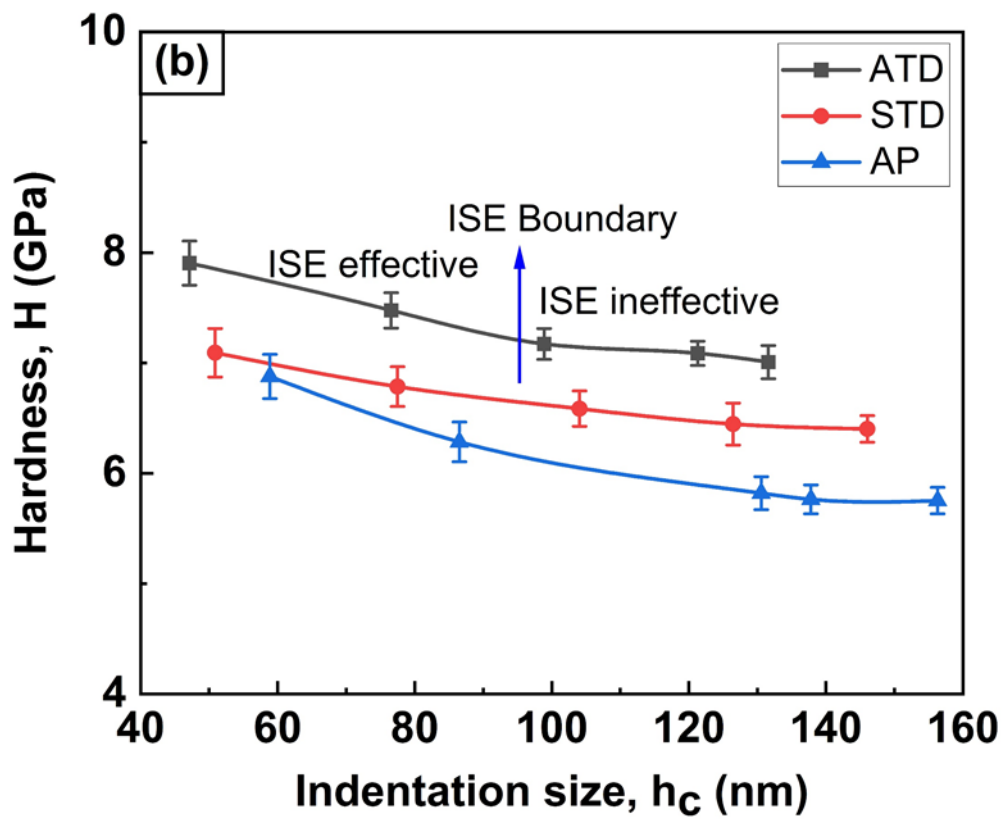
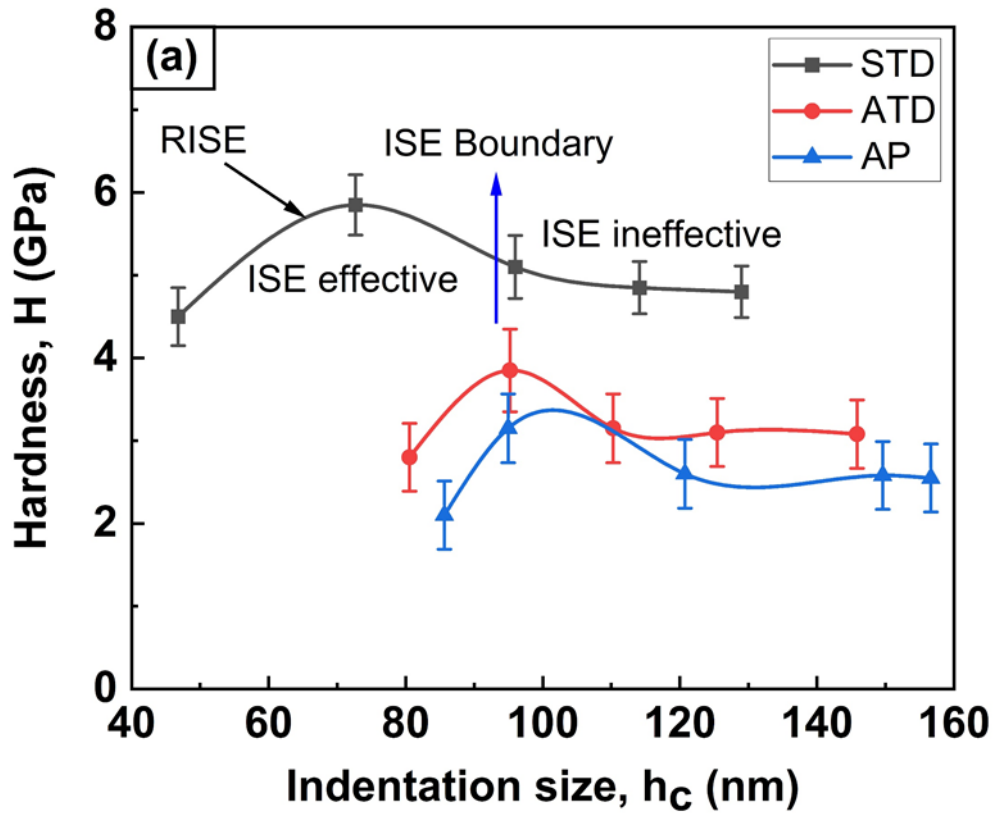


Fig. 4.7 Representation of typical ISE in true hardness values for AP, STD and ATD samples of (a) PMN-PT, (b) PZT-H and (c) PZT-S piezoceramics according to the PSR model. (H_1)- Load-dependent hardness, (H_2)- Load-independent hardness).



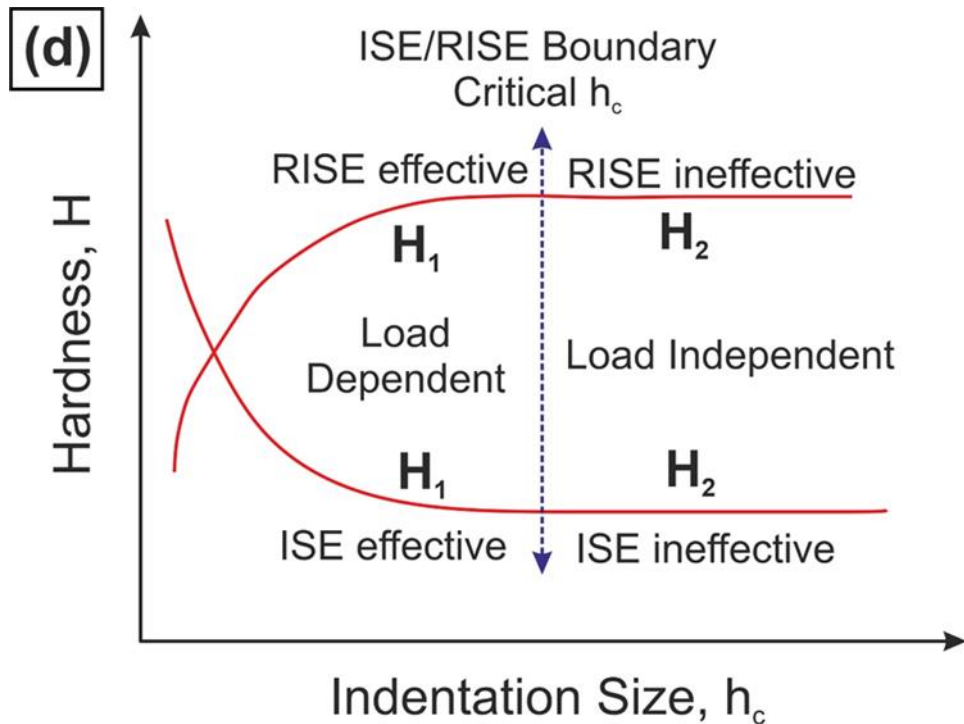
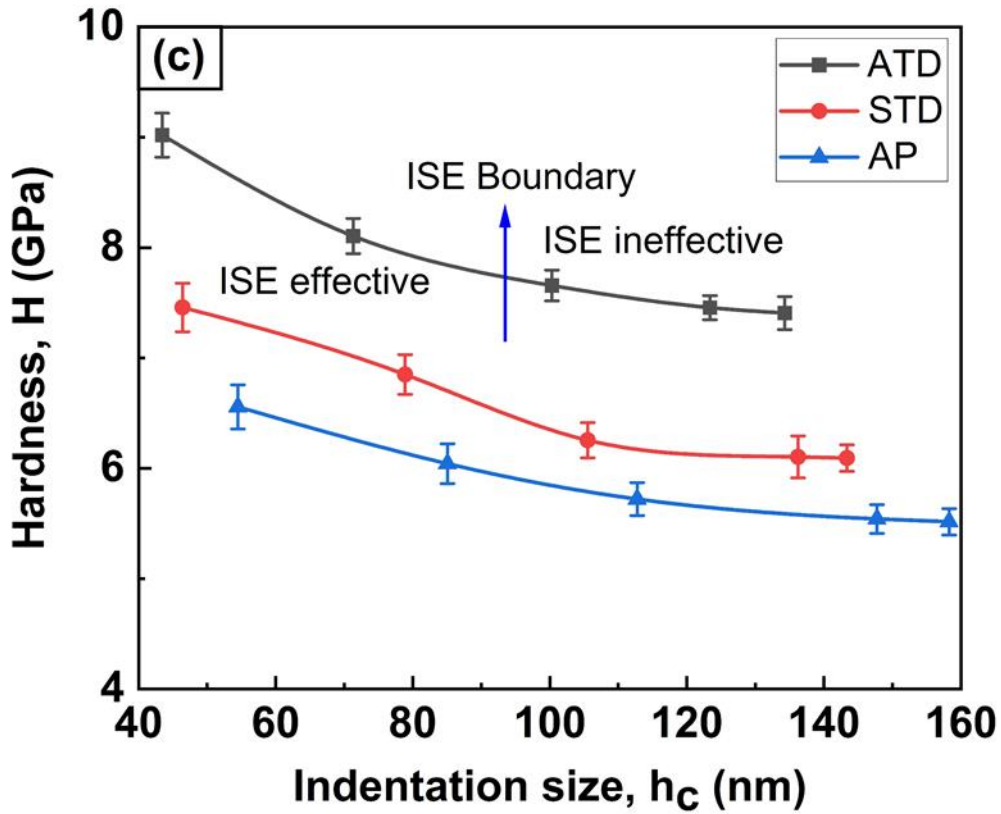


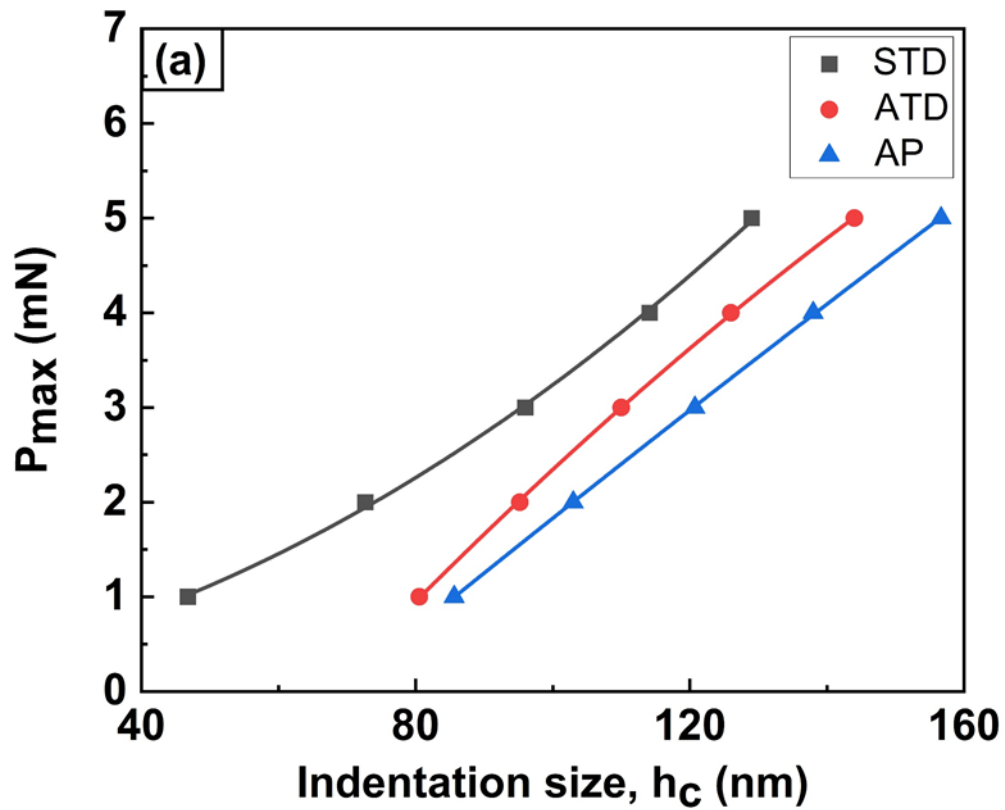
Fig. 4.8 (a-c) Representation of ISE on size effect curve according to the PSR model for AP, STD and ATD samples of PMN-PT, PZT-H and PZT-S, respectively clearly showing the ISE boundary and (d) schematic representation of the PSR effective zone and h_{crit} beyond which these ISE are ineffective.

4.3.2.4. Modified proportion specimen resistance (MPSR) model

The surface artefacts, such as residual stresses induced during specimen preparation, have a marked influence on the ISE [Jäger, 2004, Li and Bradt, 1993, Gong et al., 1998]. Gong et al. (1999) have modified the PSR model by introducing an additional constant, α_0 , which considers the surface artefacts and expressed as Eq. 15.

$$P_{max} = \alpha_0 + \alpha_1 h_c + \alpha_2 h_c^2 \quad (15)$$

The polynomial fitting of P_{max} vs. h_c data for AP, STD and ATD samples in PMN-PT, PZT-H and PZT-S shown in Figs. 4.9(a-c), respectively, enables to determine α_0 , α_1 and α_2 .



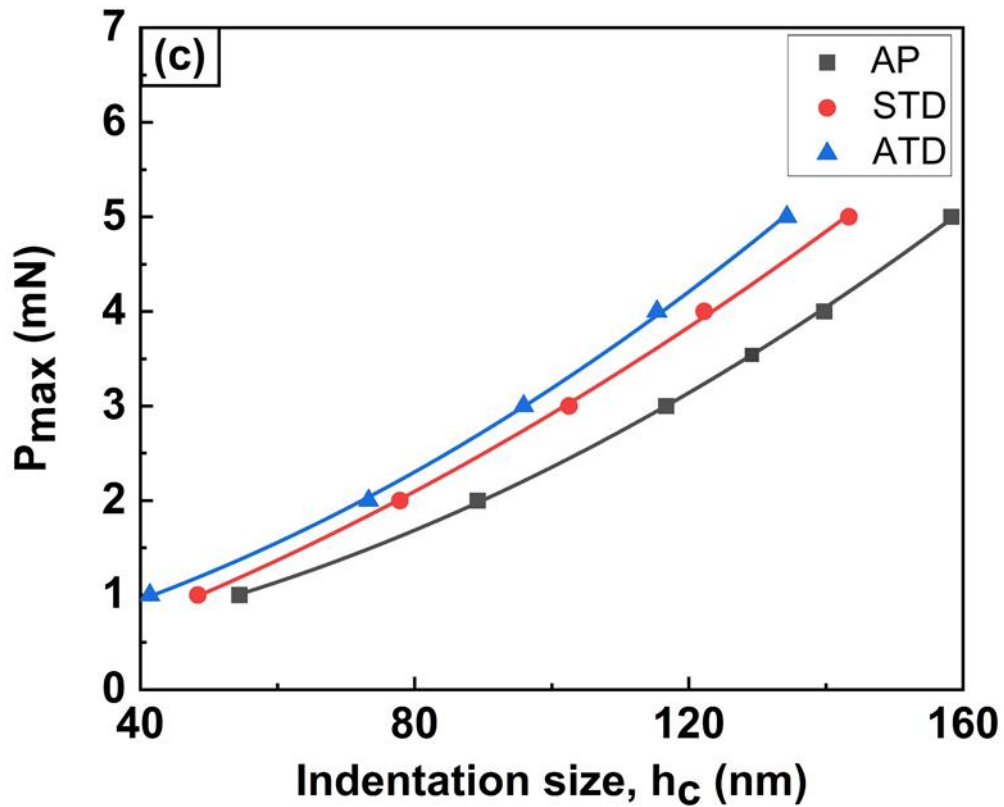
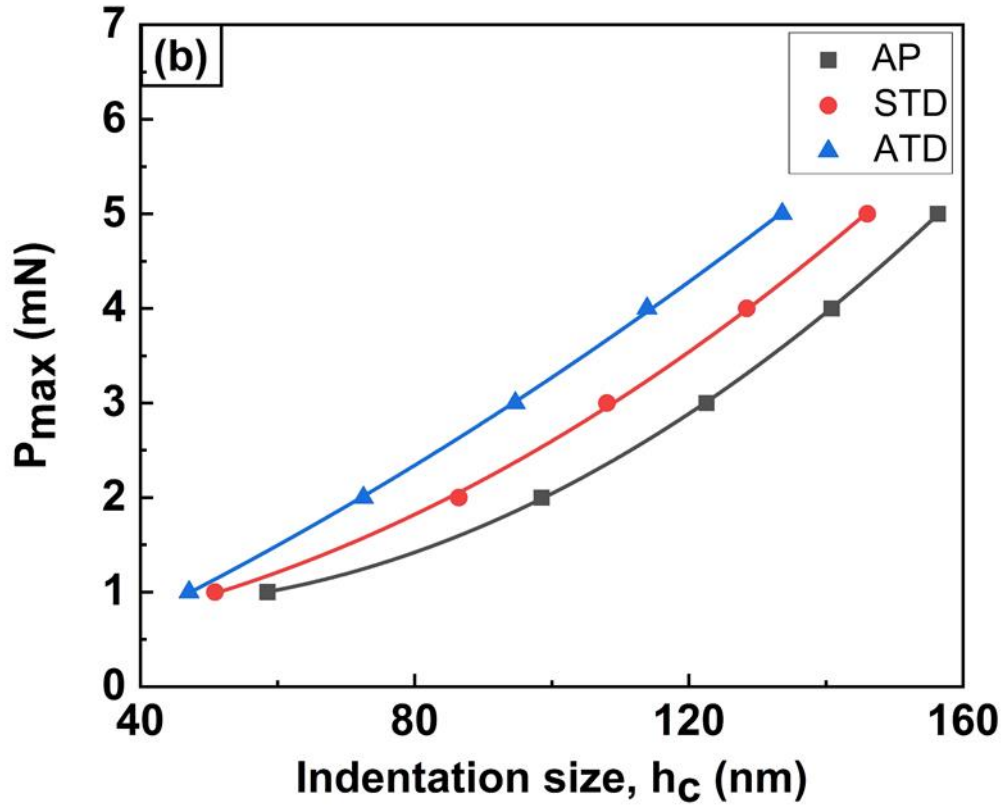


Fig. 4.9 Representation of the nanoindentation data on P_{max} vs. h_c scale to the MPSR model for AP, STD and ATD samples of (a) PMN-PT, (b) PZT-H and (c) PZT-S piezoceramics.

The negative and positive values of α_0 indicate the compressive and tensile nature of the surface residual stresses, respectively. The statistical analysis of the indentation data [Gong et al., 1999 and Gong and Li, 2000] further shows that α_0 can also be related to the experimental inaccuracies arising due to sensitivity of load cell and/or objective lens in the indentation set up. It is evident from the α_0 values (as shown in Table 4.4) that the residual stresses are tensile in nature in AP samples, while become compressive in STD and ATD samples in all the materials. One possible reason for this could be due to the plastic strain incompatibilities arising due to the ferroelectric domain reorientation during annealing treatment [Kathavate et al., 2018]. Further, the α_1 and α_2 values show a similar trend as that of the PSR model.

Table 4.4 Summary of the descriptive parameters and true hardness values obtained from the MPSR model for all the samples of PMN-PT, PZT-H and PZT-S piezoceramics. (H_1)- Load-dependent hardness, (H_2)- Load-independent hardness).

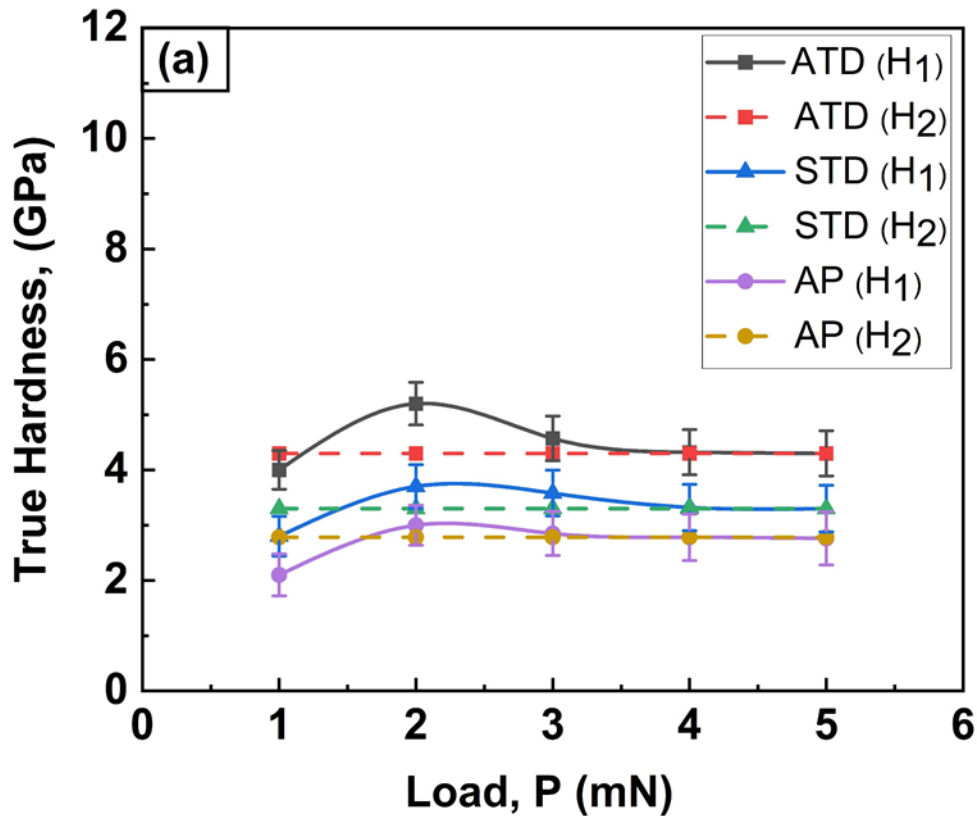
Materials	Structural state	Modified proportion specimen resistance (MPSR) model					
		α_0 (mN)	$\alpha_1 \times 10^{-3}$ (mN/nm)	$\alpha_2 \times 10^{-3}$ (mN/nm ²)	R ²	H_1 (GPa)	H_2 (GPa)
PMN-PT	AP	0.41±0.08	1.48±0.09	-0.026	0.998	2.7±0.53	2.80
	STD	-0.11±0.10	9.38±0.15	0.22	0.999	4.3±0.52	4.35
	ATD	-0.57±0.12	9.87±0.18	-0.14	0.997	3.3±0.48	3.30
PZT-H	AP	1.12±0.12	10±0.14	0.13	0.999	5.9±0.7	6.12
	STD	-0.12±0.04	12.1±0.28	0.15	0.999	6.8±0.58	7
	ATD	-0.55±0.03	14.2±0.25	0.18	0.997	7.52±0.8	7.64
PZT-S	AP	0.24±0.13	6.30±0.18	0.15	0.999	6±0.78	5.74
	STD	-0.14±0.05	10.14±0.3	0.16	0.998	7±0.90	6.66
	ATD	-0.35±0.04	12±0.38	0.19	0.999	7.68±0.7	7.87

Similar to the PSR model the H_1 and H_2 values of the MPSR model are expressed as;

$$(H_1) = \frac{(P_{max} - P_{min})}{24.5h_c^2} = \frac{(P_{max} - \alpha_0 - \alpha_1 h_c)}{24.5h_c^2} \quad (16)$$

$$(H_2) = \frac{\alpha_2}{24.5} \quad (17)$$

The H_1 and H_2 values deduced from the MPSR model for AP, STD, and ATD samples (as presented in Table 4.4) are also similar to those obtained from the PSR model. Further, the H_1 values of PMN-PT, PZT-H and PZT-S, as shown in Figs. 4.10(a-c), follows the trend; $(H_1)_{STD} > (H_1)_{ATD} > (H_1)_{AP}$ (for PMN-PT) and $(H_1)_{ATD} > (H_1)_{STD} > (H_1)_{AP}$ (for PZT-H and PZT-S). Although the H_1 and H_2 values from the MPSR model are identical to the ones obtained from the PSR model, the origins of ISE in AP and ATD samples of PMN-PT cannot be satisfactorily explained on the basis of the MPSR model due to non-acceptable negative values of the descriptive parameter, α_2 . On the other hand, the MPSR model captures the ISE in both PZTs and indicates the reasons for high H values observed in STD and ATD samples.



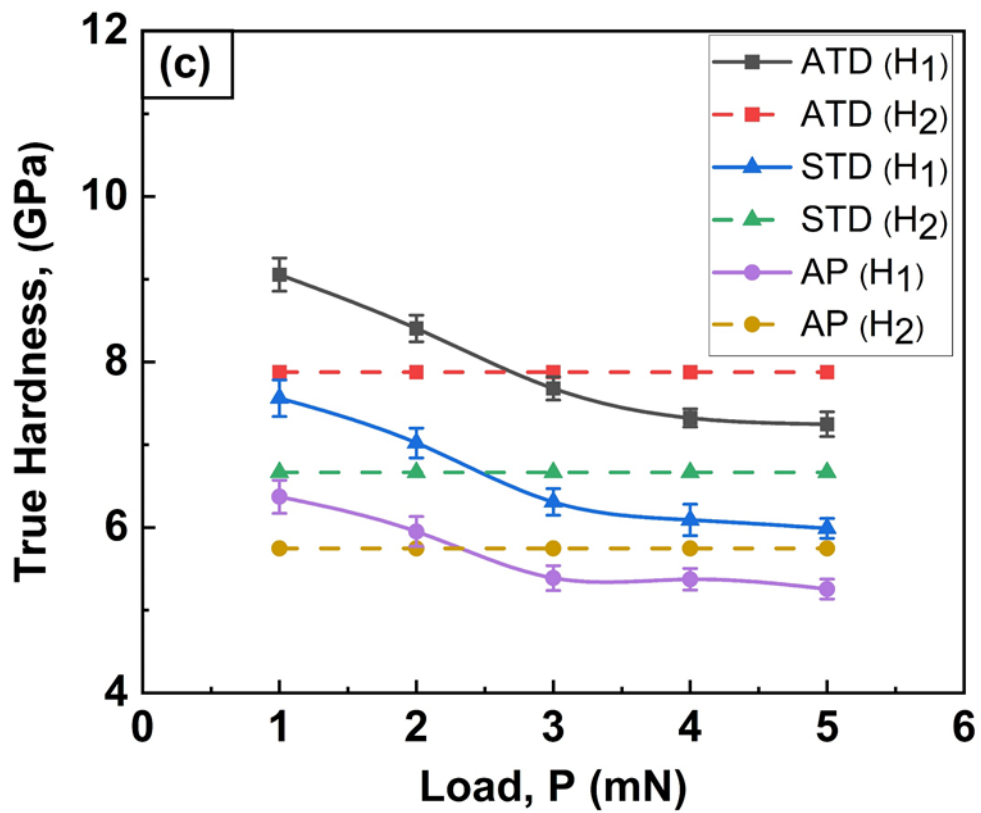
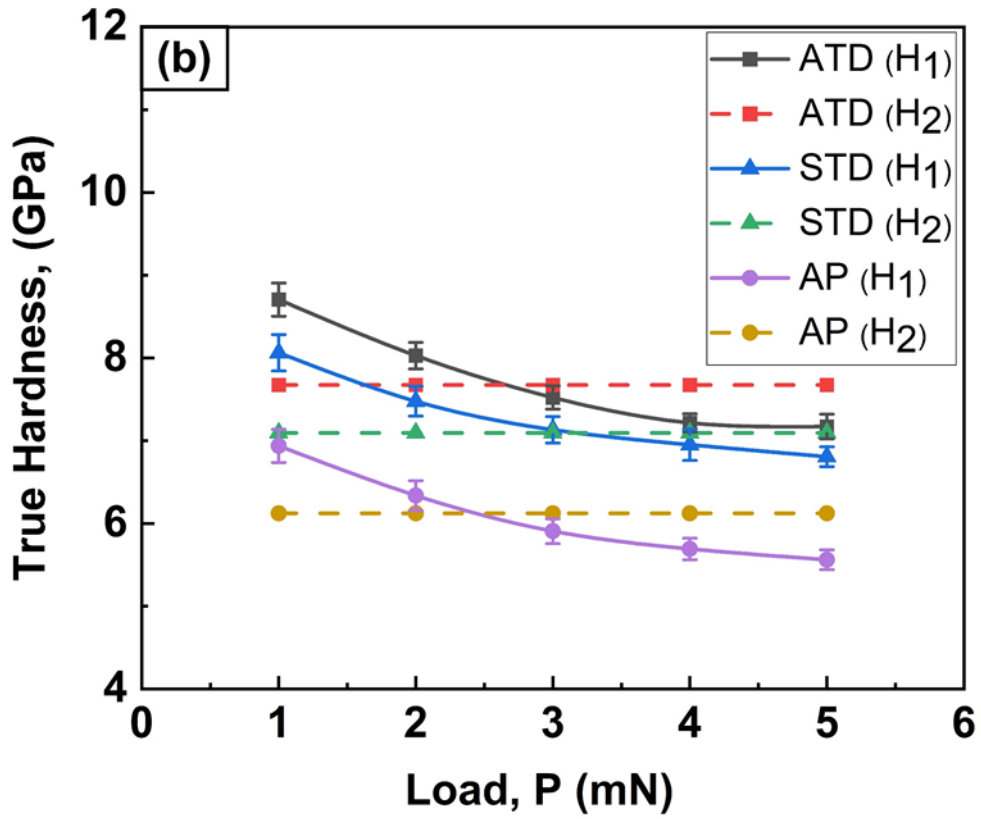


Fig. 4.10 Representation of typical ISE in true hardness values for AP, STD and ATD samples of (a) PMN-PT, (b) PZT-H and (c) PZT-S piezoceramics according to the MPSR model. (H_1)- Load-dependent hardness, (H_2)- Load-independent hardness).

The main objective of explaining the ISE on the basis of the ER, PSR and MPSR model is to evaluate true hardness numbers. The H_1 and H_2 values obtained from the different models summarized in Tables 4.2, 4.3 and 4.4 are in reasonable agreement with each other despite the differences in fitting constants. These fitting constants and hence the ISE appears to be sensitive to underlying microstructural parameters of the materials such as grain size, grain orientation and ferroelectric domain configurations etc., in addition to the other errors associated with the specimen preparation and machine uncertainties. The current study clearly reveals that the H and ISE in piezoelectric materials are independent of the grain size but depends on the ferroelectric domain configurations. Being transversely isotropic in nature, the crystallographic orientation might have an influence on the mechanical properties of piezoelectric materials. Therefore, the role of crystallographic orientation on the H cannot be conclusively ruled out from the current experiments, although the indentations are confined to an individual grain. However, the micro-indentation experiments are helpful in determining the role of grain orientations on the H of polycrystalline ceramics (as it comprises the average response from several grains). Further, indentation experiments on the single-crystal samples will be able to provide a profound understanding of the role of individual ferroelectric domains (i.e., c^+ , c^- and a) on the nanomechanical properties, and ISE.

4.4. Summary

The present work describes the origins of ISE in nanoindentation hardness of polycrystalline PMN-PT, PZT-H and PZT-S with different ferroelectric domain configurations. The P vs. H data is fitted with the different mechanistic models that are available in the literature for the improved understanding of ISE and true hardness in polycrystalline piezoceramics. The key outcomes from the present chapter after a critical analysis of nanoindentation data can be summarized as follows:

- The variation of H with respect to h_c indicates that PMN-PT, PZT-H and PZT-S piezoceramics, independent of their ferroelectric domain configurations, exhibit RISE (particularly in PMN-PT) and ISE in H .
- All the mechanistic models satisfactorily describe the ISE to various levels. Further, the ISE and descriptive parameters from each model are sensitive to the differences in ferroelectric domain configurations.
- The classical Meyer's law and H-K model are suitable to describe the ISE at lower indentation loads; however, they cannot explain the origins of RISE or ISE. The lower

values of Meyer's exponent " n " and higher P_{min} values (from the H-K model) for annealed samples indicate the increased resistance to the indentation (i.e., higher H values) compared to AP samples.

- The ER model very well captures the ISE in all the samples of PMN-PT, PZT-H and PZT-S by eliminating the errors in the measurement of indentation dimensions.
- The PSR model can describe the RISE or ISE in all the piezoceramics in the current study and estimate the load-dependent and independent true hardness values. However, the MPSR model failed to explain the origins of RISE and ISE in AP and ATD samples of PMN-PT due to non-acceptable negative values of fitting parameters. However, it satisfactorily describes the origins of ISE in all the domain configurations of PZT-H and PZT-S.
- Further, the constant in the MPSR model suggests that the surface residual stresses are compressive in nature in the case of STD and ATD samples, mostly due to the reorientation of ferroelectric domains during annealing, and hence the possibility of showing an increased H . This also suggests that the ferroelectric domain configurations have a marked influence on the H values and RISE or ISE in H .
- The true hardness values obtained from the ER, PSR and MPSR model in all the samples of PMN-PT, PZT-H and PZT-S are more or less similar to each other due to similar attributes in fitting the nanoindentation data.

CHAPTER 5

Conclusions and Future Scope

Abstract: This chapter summarizes the important results and key conclusions from the present thesis. The scope for future work based on the experiments performed and proposed mechanisms is mentioned in the last part of the chapter.

5.1. Summary and Conclusions

This thesis presents a systematic investigation of the role of intrinsic microstructural length scales (e.g., ferroelectric domain configurations) on the deformation response of polycrystalline piezoceramics. Although the role of ferroelectric domain configurations on piezoelectric behaviour is reasonably well understood, limited studies are available to ascertain their influence on mechanical behaviour. The ferroelectric domain configurations are systematically varied by employing a cost-effective domain engineering (DE) technique *via* thermal annealing at temperatures below and above the curie temperature, T_c . Subsequently, the ferroelectric domain configurations (e.g., orientation and nature of domains) are characterized using piezoresponse force microscopy (PFM). The role of different domain configurations on the nano and micromechanical properties are investigated using instrumented nano- and micro-indentation. Following conclusions can be drawn from the current results and detailed analysis:

- The DE *via* annealing treatment causes significant changes in the ferroelectric domain configurations. In all the piezoceramics investigated in this work, the degree of disorderness in ferroelectric domain configurations increases with annealing temperatures. The direct and converse piezocharge coefficient, d_{33} and d_{33}^* , respectively decreases with increasing randomness in ferroelectric domain configurations and approaches to a value of zero in the samples annealed above the curie temperature, T_c . These ferroelectric domain re-orientations often cause cracking in some of the grains, possibly due to the incompatibility in strains at the domain wall (DW) boundaries.
- The results from the nano- and micro-indentation experiments reveal that the ferroelectric domain configurations have a marked influence on the hardness, H , elastic modulus, E , and indentation fracture toughness, K_{IC}^i . The H values of undoped PZT (PZT-U), hard-doped PZT (PZT-H), soft-doped PZT (PZT-S), and NKN-NT

increases with increasing degree of ferroelectric domain randomization. ATD samples show the highest H (~ 20 to 40% for PZTs and $\sim 10\%$ for NKN-NT) compared to AP samples. The reorientation of ferroelectric domains through non- 90° and non- 180° DW in response to mechanical stresses appears to offer an increased resistance to the deformation during indentation (and hence a higher elastic recovery of ferroelectric domains in ATD samples), thereby leading to enhanced H .

- Owing to relaxor ferroelectric nature, the H values of PMN-PT follows a different trend: STD samples exhibit the highest H (~ 2.5 times) values compared to ATD and AP samples. The transition of PMN-PT from piezoelectric to relaxor ferroelectric near the T_c delays randomization of ferroelectric domains, thereby leading to the formation of the small island (polar nano regions, NPR). These NPR thought to hinder the ferroelectric domain switching process during indentation in STD samples, and therefore the increase in H . On the contrary, NPR disappears (above the T_c) in ATD samples, and the ferroelectric distortion becomes much easier, thereby leading to low H values.
- The PFM studies revealed that the DE *via* doping of aliovalent cations (i.e., controlling the crystal structure) significantly alters the ferroelectric domain configurations, leading to enhanced d_{33} ($\sim 200\%$ for PZT-H and $\sim 265\%$ for PZT-S) and H values ($\sim 36\%$ for PZT-H and $\sim 41\%$ for PZT-S) compared to PZT-U. The differences in electro-mechanical response (i.e., higher d_{33} and H values) in PZT-S compared to PZT-H could be attributed to the differences in ferroelectric behaviour of both the PZTs such as highly mobile ferroelectric domain structure, close interdomain spacing and higher density of ferroelectric domains in PZT-S compared to PZT-H.
- The indentation induced domain switching (IIDS) during loading, back-switching (completely or partially) during unloading have a pronounced influence on the toughening behaviour of PZT piezoceramics. The variation of d_{33}^* and ϵ_r values obtained ahead and around of the indentation crack front clearly show the ferroelectric domain switching mechanisms prevalent at these locations.
- All the piezoceramics irrespective of their initial ferroelectric domain configuration, exhibit both reverse indentation size effect (RISE) and normal indentation size effect (ISE) in H .

- The critical analysis of RISE and ISE in PMN-PT, PZT-H and PZT-S using classical Meyer's law, Hays-Kendall (H-K) model, Elastic recovery (E-R) model, Proportion specimen resistance (PSR), and Modified proportion specimen resistance (MPSR) model revealed the following: (i) The differences in ferroelectric domain configurations has a marked influence on the descriptive parameters and exponents of all the models, (ii) The classical Meyer's law and H-K model quantitatively very well capture the ISE in all the piezoceramics, but failed to explain the origins of ISE, (iii) The ER model very well describes the origins of ISE in all the piezoceramics by eliminating the errors in the measurement indentation size, h_c during indentation and estimate the critical indentation size, h_{crit} beyond which ISE are ineffective, (iv) The PSR and MPSR models explain the origins of ISE on the basis of (a) material-dependent constants and (b) surface artefacts (due to surface residual stresses and experimental inaccuracies). However, differences in ferroelectric domain configurations appear to have a pronounced influence on both material-dependent constants and surface artefacts, (v) Initially, the surface residual stresses are tensile in AP samples and become compressive in STD and ATD samples of all the piezoceramics, possibly due to the reorientation of ferroelectric domains during thermal annealing, (vi) The true H values obtained from the ER, PSR and MPSR models in all the piezoceramics are lower than the machine H values (which is generally correct) and confirm the validity of the nanoindentation experiments and (vii) The MPSR model does not hold good for explaining the ISE in AP and ATD samples of PMN-PT due to non-acceptable negative values of descriptive (or fitting) parameters.

5.2. Directions for Future Work

The present study attempts to ascertain the role of ferroelectric domain configurations on the strengthening and toughening behaviour of polycrystalline piezoceramics. On this front, the possible underlying mechanisms such as IIDS and rearrangement of ferroelectric domains during the indentation of polycrystalline piezoceramics are explored in details. However, this study is not exhaustive by any means, and still, there are some possibilities for future work.

- Most of the studies in the open literature are centred on investigating the toughening behaviour in single-crystal piezoceramics. Therefore, the toughening behaviour in polycrystalline piezoceramics, particularly in Pb-free ceramics in light of different ferroelectric domain configurations, is highly a debatable aspect in this area.
- Although the present work provides the direct observation of ferroelastic activities such as IIDS and ferroelectric domain rearrangement around the vicinity of the indentation, not much attention has been given to ferroelastic activities beneath the indentation (except the work by [Schneider et al., 2005](#)). Therefore, it would be interesting in future to examine these ferroelastic activities beneath the indentation in polycrystalline piezoceramics.
- Only a few studies have reported the influence of high strain rate and dynamic failure on the electro-mechanical characteristics of piezoceramics [[Lamberson and Ramesh, 2017](#) and [Wang et al., 2020](#)]. This is one of the important open problems and can be addressed in future by performing high strain rate experiments using Split-Hopkinson pressure bar (SHPB) to suit these piezoceramics for variable high-frequency loading environment.
- The cyclic nanoindentation experiments would be helpful to investigate the pressure induced phase transformation, particularly at lower length scales.
- The role of plastic strain gradient beneath the indentation on DW motion in polycrystalline piezoceramics cannot be conclusively ruled out. The sub-surface indentation experiments and domain orientation maps in the sub-surface deformation zone may provide deeper insights.
- There is ample room for the predictive capabilities of PFM to characterize the ferroelectric domain configurations and their polarization directions (crystallographic) in polycrystalline piezoceramics, particularly *via* V-PFM tool and at high bias voltage.

APPENDIX 1

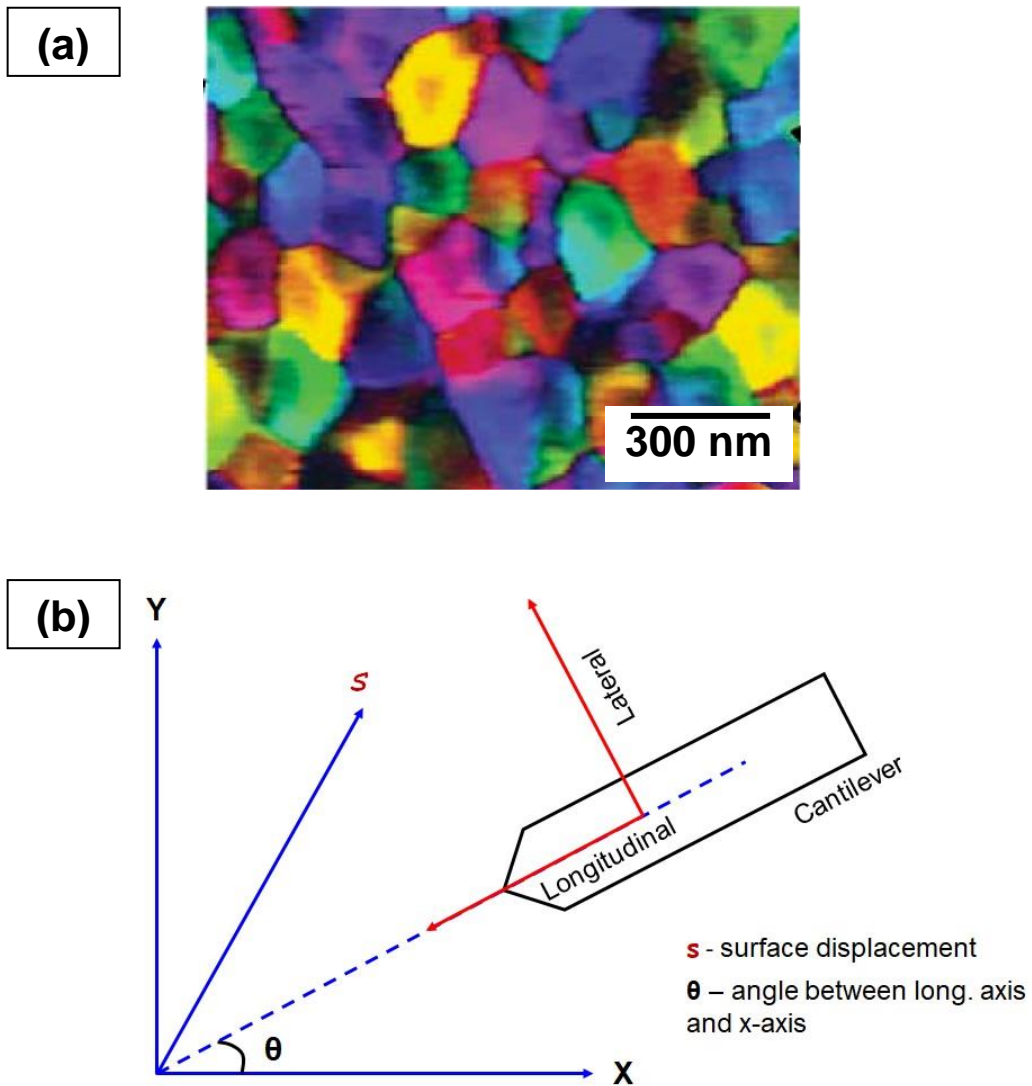


Fig. A1 (a) Vector representation of ferroelectric domains in PbTiO_3 thin film visualized using PFM phase images [Adpoted from Kalinin et al., 2006] (b) schematic representing the contributions of cantilever deflection.

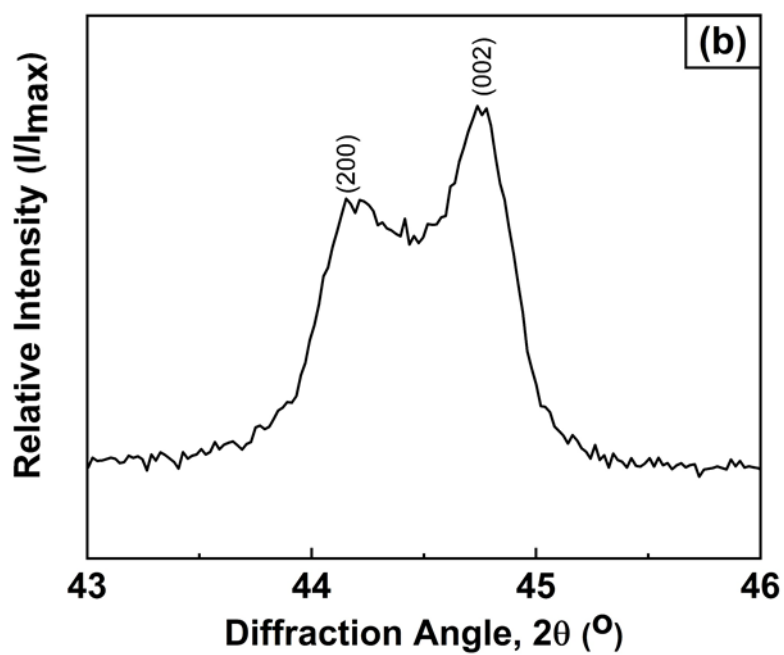
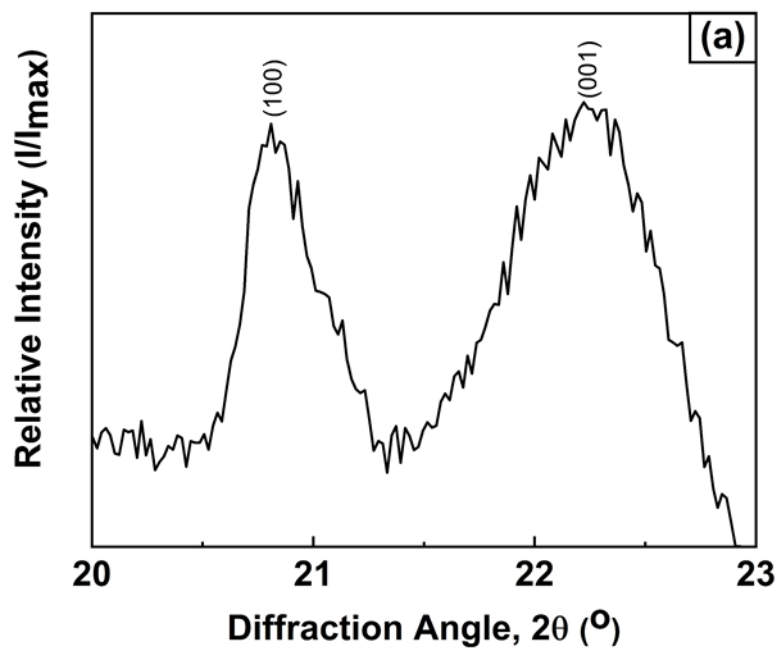


Fig. A2 Representative XRD pattern showing the peak splitting in (a) PZT-H and (b) PZT-S.

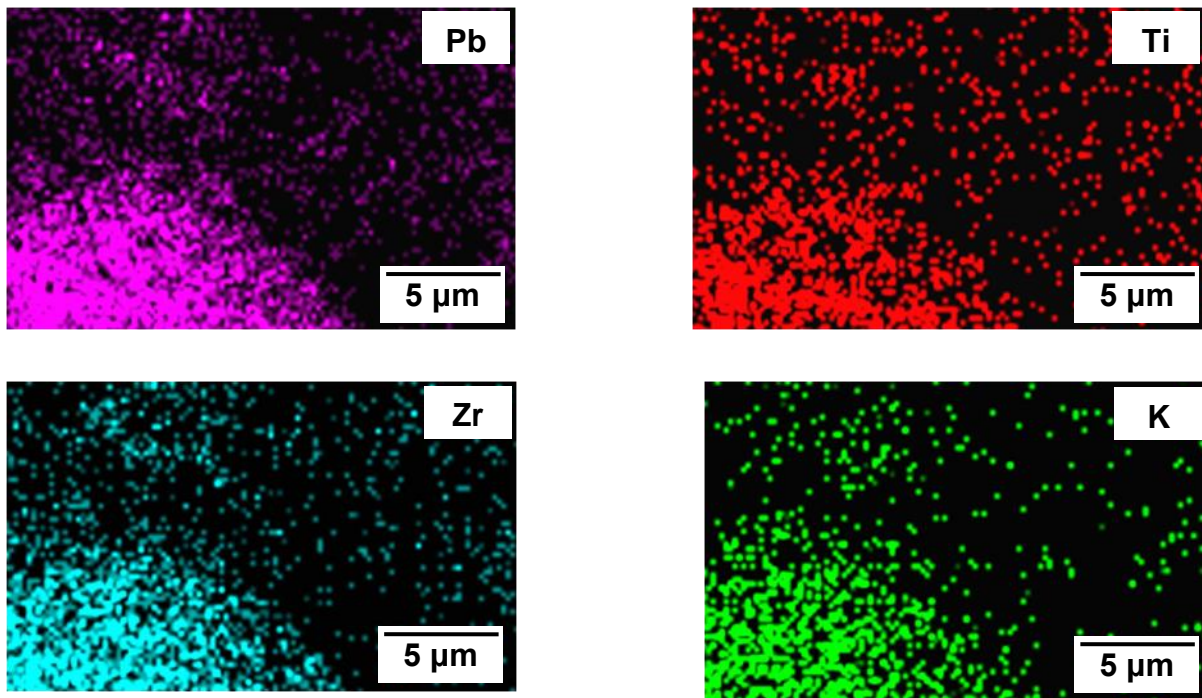
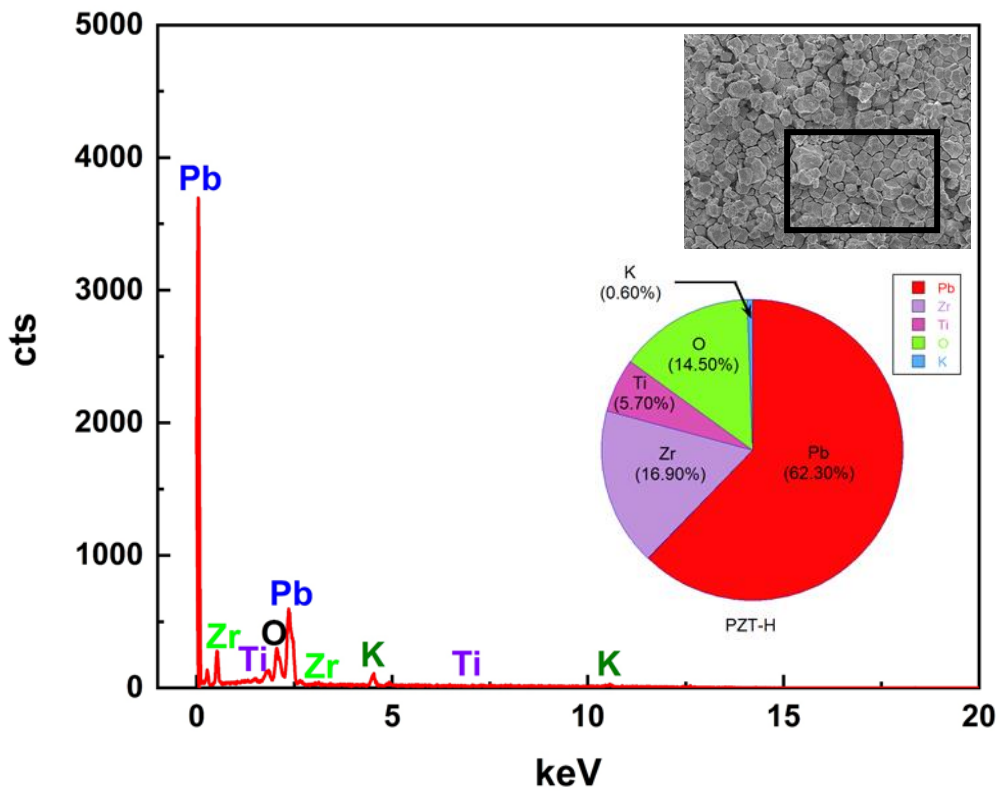


Fig. A3 Representative mapping of the elemental constituents present in PZT-H obtained through EDS (scanned area is shown in inset) as well as stoichiometric %wt proportions are presented in the pie chart.

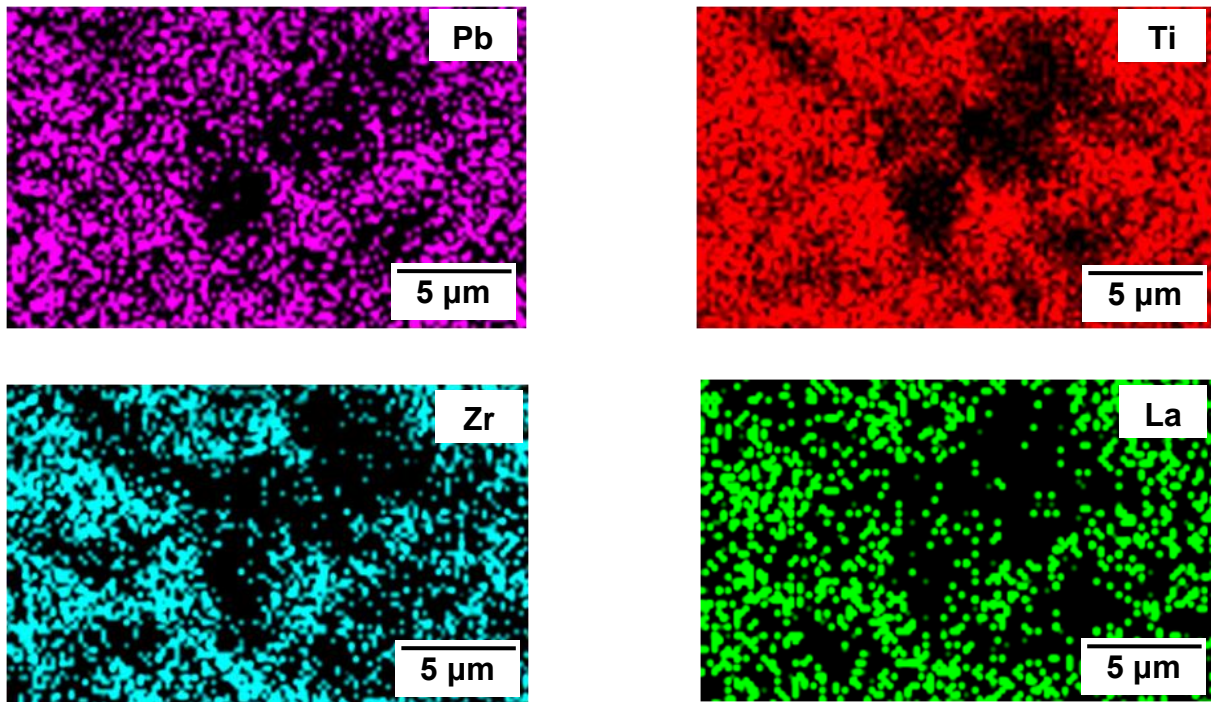
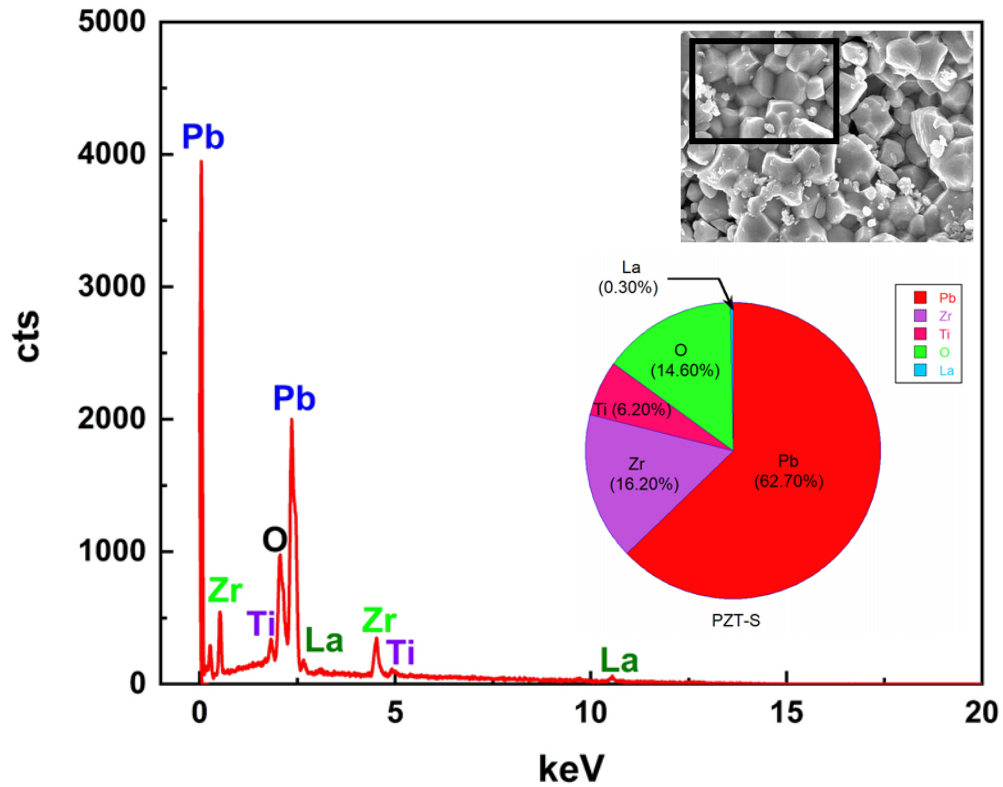
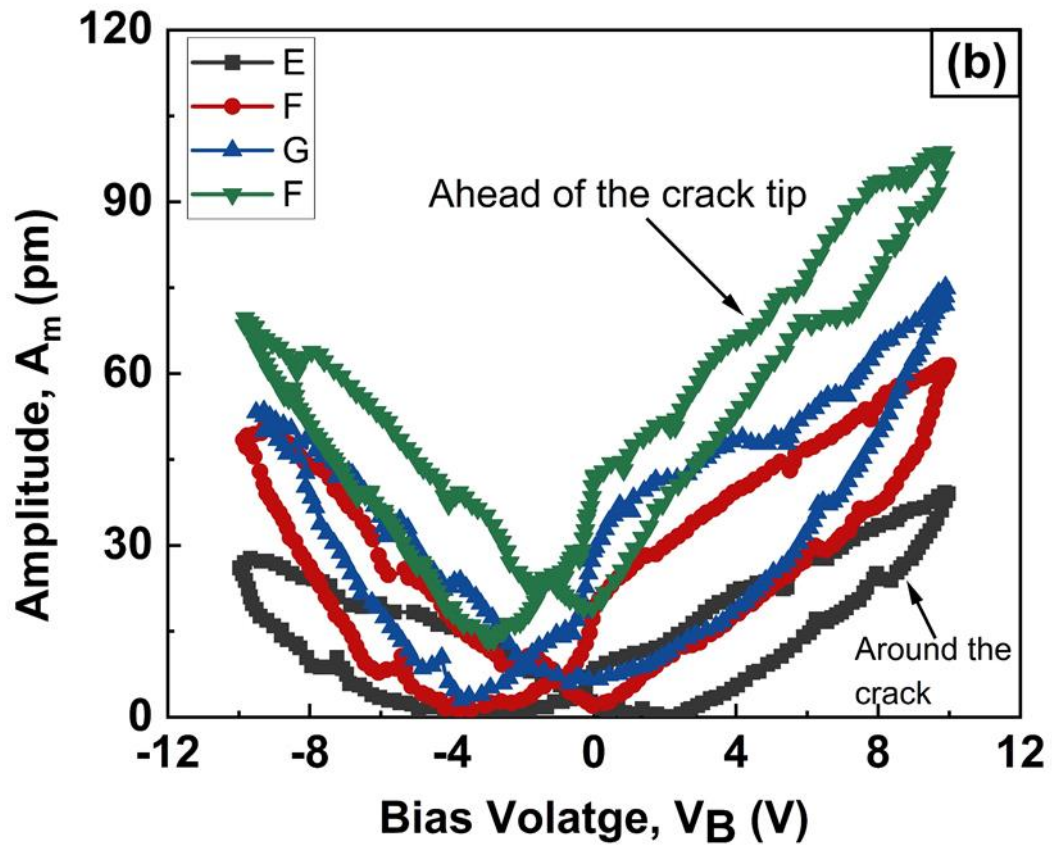
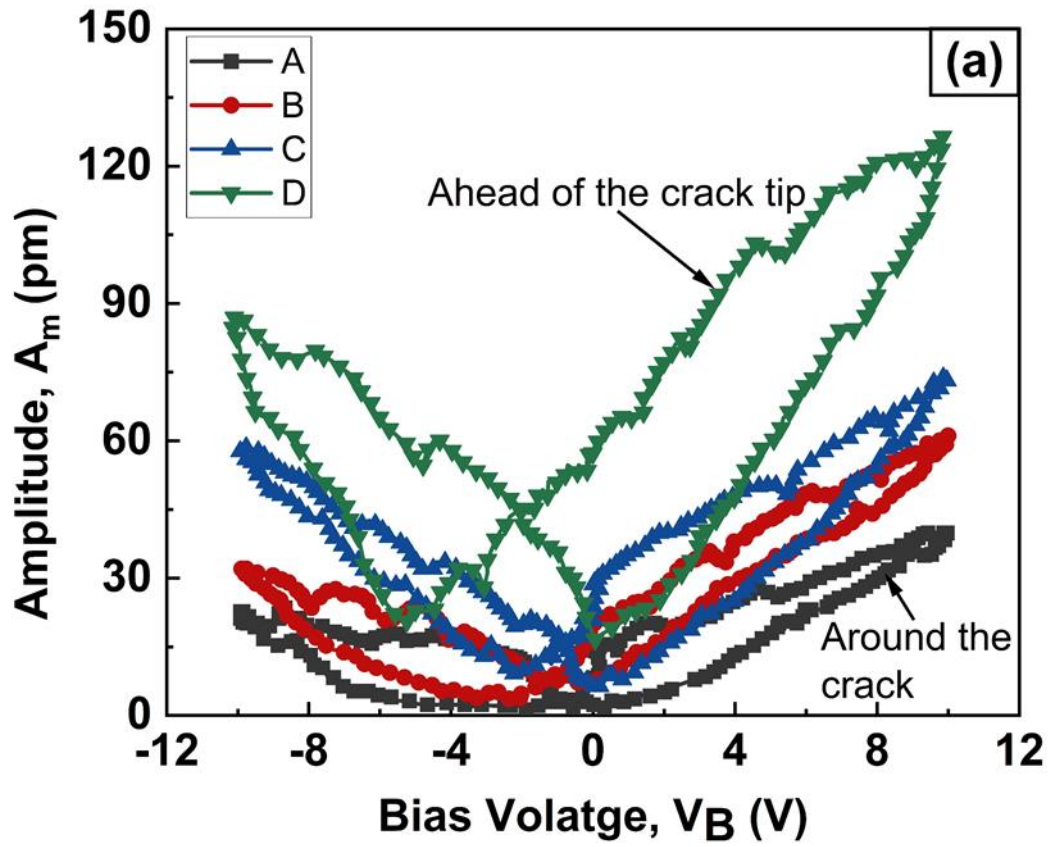


Fig. A4 Representative mapping of the elemental constituents present in PZT-S obtained through EDS (scanned area is shown in inset) as well as stoichiometric %wt proportions are presented in the pie chart.



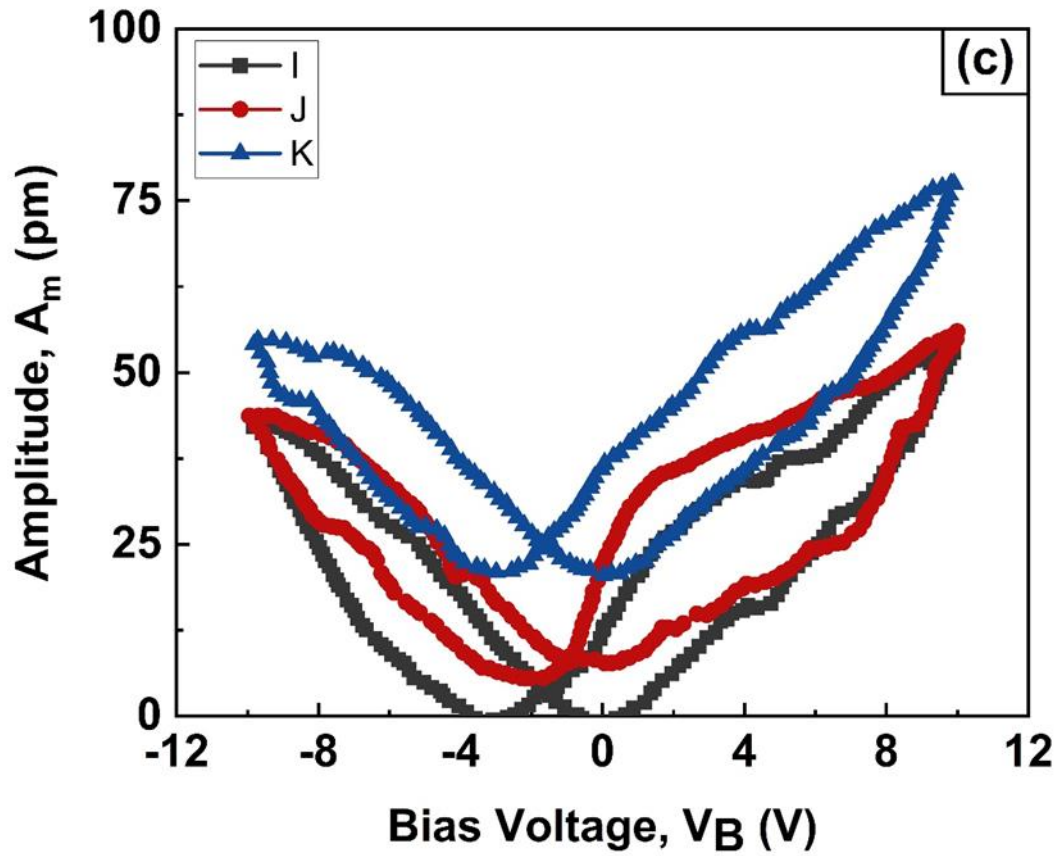


Fig. A5 Variation in A_m with respect to V_B at various locations around and ahead of the indentation crack (a) A to D, (b) E-H and (c) I to K as per the plan shown in Fig. 3.14(a).

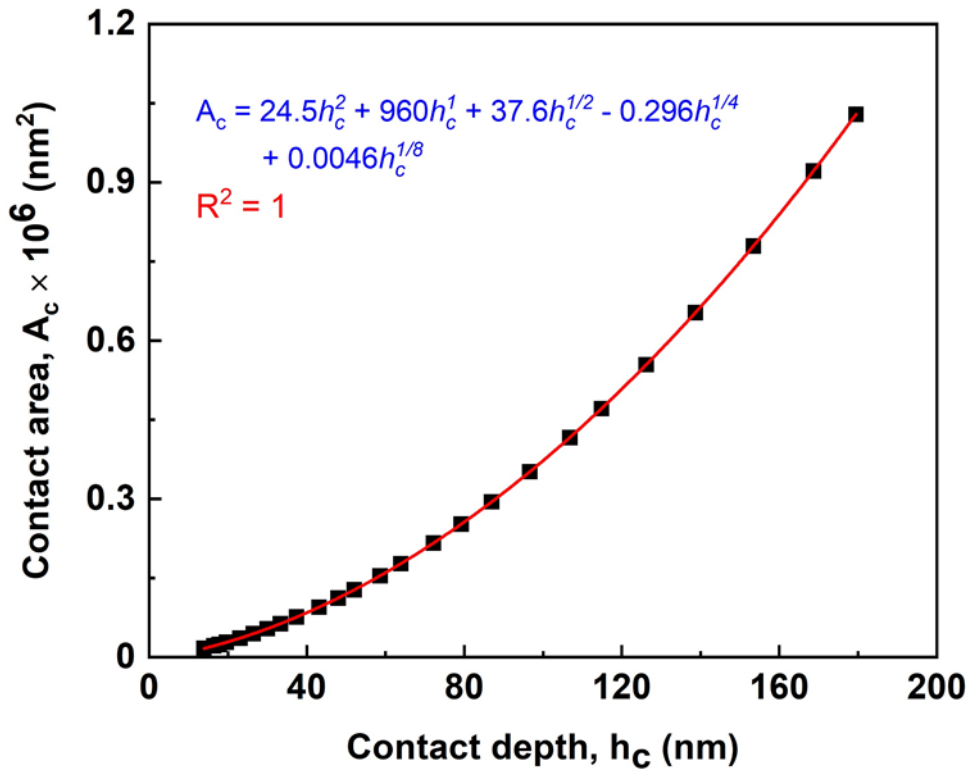


Fig. A6 Representative area function calibration curve obtained before performing nanoindentation experiments on piezoceramics. The polynomial fit ($R^2 \sim 1$) indicates the zero deviation from of the ideal geometry of the Berkovich indenter.

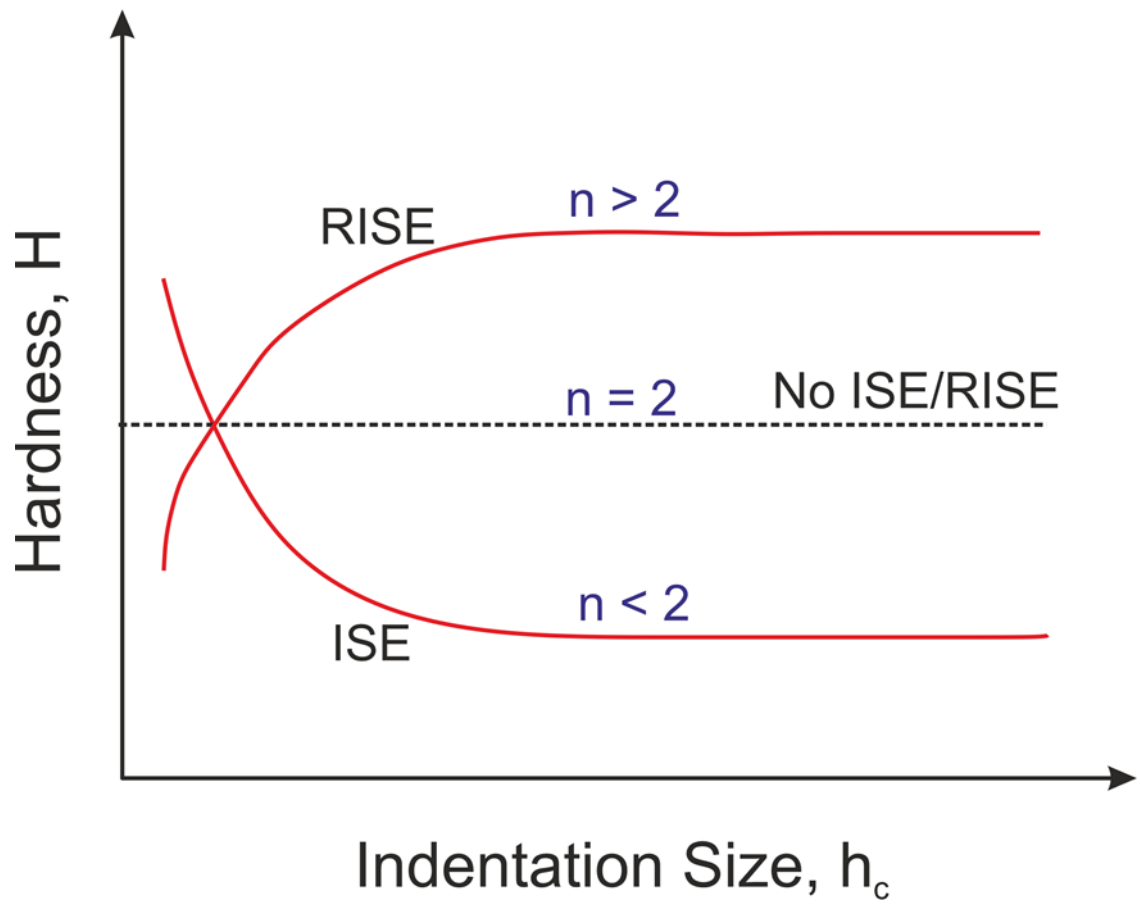


Fig. A7 Representation of Meyer's index, " n " values on size effect curve.

BIBLIOGRAPHY

Ahart M., Sinogeikin S., Shebanova O., Ikuta D., Ye Z.G., Mao H.K., Cohen R.E., Hemley R.J. (2012), Pressure dependence of the monoclinic phase in $(1 - x)\text{Pb}(\text{Mg}_{1/3}\text{Nb}_{2/3})\text{O}_3$ - $x\text{PbTiO}_3$ solid solutions, *Phys. Rev. B*, 86 224111.

Ahluwalia R., Cao W. (2001), Size dependence of domain patterns in a constrained ferroelectric system, 89(12) 8105-8109.

Ahluwalia R., Lookman T., Saxena A., Cao W. (2004), Piezoelectric response of engineered domains in ferroelectrics, 84(18) 3450-3452.

Atkins A.G., Tabor D. (1965), Plastic indentation in the metals with cones, *J. Mech. Phys. Solids*, 13 149-164.

Bai W., Chen D., Zheng P., Zhang J., Shen B., Zhai J., Ji Z. (2017), Grain-orientated lead-free BNT-based piezoceramics with giant electrostrictive effect. *Ceram. Int.*, 43(3) 3339–3345.

Bai W., Wang L., Zheng P., Wen F., Zhai J., Ji Z. (2018), Pairing high piezoelectric properties and enhanced thermal stability in grain-oriented BNT-based lead-free piezoceramics. *Ceram. Int.*, 44(10) 11402–11409.

Banno H., Tsunooka T., Shimano I. (1975), Phase diagram and piezoelectric properties of $\text{Pb}(\text{Ni}_{1/3}\text{Nb}_{2/3})\text{O}_3$ - PbTiO_3 - PbZrO_3 and an application to ceramic wave filter. In: *Proc. 1st meeting on Ferroelectric materials and their applications*, no. F-14.

Bellaiche L., García A., Vanderbilt D. (2001), Electric-field induced polarization paths in $\text{Pb}_x\text{Zr}_{1-x}\text{Ti}_x\text{O}_3$ alloys, *Phys. Rev. B*, 64 060103.

Bechmann R. (1956), Elastic, piezoelectric, and dielectric constants of polarized barium titanate ceramics and some applications of the piezoelectric equations, *J. Acoust. Soc. Am.* 28(3) 347–350.

Bechmann R. (1958), Elastic and piezoelectric constants of alpha-quartz, *Phys. Rev.*, 10(5) 1060–1071.

Bell A.J. (2001), Phenomenologically derived electric field-temperature phase diagrams and piezoelectric coefficients for single crystal barium titanate under fields along different axes, *J. Appl. Phys.*, 89(07) 3907-3914.

Bharat Bhushan, Nosonovsky M. (2005), Scale effects in mechanical properties and tribology in *Nanotribology and Nanomechanics*, Springer, Berlin, Heidelberg, 1st Edition 773-824.
https://doi.org/10.1007/3-540-28248-3_16

Bharat Bhushan (2017), Depth sensing nanoindentation measurement techniques and applications, *Microsynt. Tech.*, 23 1595-1649.

Bijalwan V., Tofel P., Holcman V. (2018), Grain size dependence of the microstructures and functional properties of $(\text{Ba}_{0.85}\text{Ca}_{0.15-x}\text{Ce}_x)(\text{Zr}_{0.1}\text{Ti}_{0.9})\text{O}_3$ lead-free piezoelectric ceramics, *J. Asian Ceram. Soc.*, 06(04) 384-393.

Birol H., Damjanovic D., Setter N. (2006), Preparation and characterization of $(\text{K}_{0.5}\text{Na}_{0.5})\text{NbO}_3$ ceramics, *J. Euro. Ceram. Soc.*, 26 861–866.

Bo H., Zhang Z., Hu H., Wang R. (2012), Ferroelectric domain engineering in stoichiometric LiNbO_3 by scanning probe microscopy, *Adv. Mater. Res.*, 485 5100-513.

Bouزيد A., Bourim E.M., Gabbay M., Fantozzi G. (2005), PZT phase diagram determination by measurement of elastic moduli, *Acta Mater.*, 25 3213-3221.

Bulychev S.I., Alekhin V.P., Shorshorov M.K., Ternovskii A.P., Shnyrev G.D. (1975), Determination of Young's modulus according to indentation diagram, *Zavod. Lab.*, 41 1137–1140.

Byer R.L. (1997), Quasi-phases-matched nonlinear interactions and devices, *J. Nonlinear Opt. Phys. Mater.*, 6(4), 549-592.

Cady W.G. (1946), *Piezoelectricity*, Mc-Graw-Hill, New York.

Cao H., Evans A.G. (1993), Nonlinear deformation of ferroelectric ceramics, *J. Am. Ceram. Soc.*, 76(4) 890-896.

Chang W.Y., Chung C.C., Yuan Z., Chang C.H., Tian J., Viehland D., Li J.F., Jones J.L., Jiang X. (2018), Patterned nanodomains in PMN-PT single crystal, *Acta Mater.* 143 166-173.

- Chen X., Karpinski P., Shvedov V., Koynov K., Wang B., Trull J., Cojocar C., Krolikowski W., Sheng Y. (2015), Ferroelectric domain engineering by focused infrared femtosecond pulses, *Appl. Phys. Lett.*, 107 141102.
- Cheng G., Venkatesh T.A. (2012), Nanoindentation response of anisotropic piezoelectric materials, *Philos. Mag. Lett.*, 92(06) 278-287.
- Cheng G., Venkatesh T.A. (2013), Effect of electric fields on the nanoindentation response of piezoelectric materials, *Scripta Mater.*, 69 682-685.
- Cheng G., Sriram S., Bhaskaran M., Venkatesh T.A. (2014), Nanoindentation response of piezoelectric nano-islands, *Appl. Phys. Lett.*, 105 122902.
- Cheng X., Wu J., Zheng T., Wang X., Zhang B., Xiao D., Zhu J., Wang X., Lou X. (2014), Rhombohedral–tetragonal phase coexistence and piezoelectric properties based on potassium–sodium niobate ternary system, *J. Alloys Compd.*, 610 86–91.
- Chou C.C., Chen C.S., Heryeh T. (2009), Domain and microstructural characterization of ferroelectric materials using transmission electron microscopy, *Ferroelectrics* 380 141-149.
- Choudhury S., Li Y.L., Krill III C., Chen L.Q. (2007), Effect of grain orientation and grain size on ferroelectric domain switching and evolution: Phase-field simulations. *Acta Mater.*, 55(4) 1415–1426.
- Curie J., Curie P. (1881), Contractions and expansions produced by voltages in hemihedral crystals with inclined faces, *Compt. Rend.*, 93, 1137-1140.
- Dahiya R.S., Valle M. (2013), Fundamentals of piezoelectricity, *Robotic Tactile Sensing*, Springer Science, New York, 195-230.
- Dai Y., Zhang X., Zhou G. (2007), Phase Transitional Behavior in $K_{0.5}Na_{0.5}NbO_3$ - $LiTaO_3$ Ceramics, *App. Phys. Lett.* 90 2602903.
- Dai Y., Zhang X., Chen K. (2009), Morphotropic Phase Boundary and Electrical Properties of $K_{1-x}Na_xNbO_3$ Lead-Free Ceramics, *App. Phys. Lett.*, 94 042905.
- Damjanovic D. (1998), Ferroelectric, dielectric and piezoelectric properties of ferroelectric thin films and ceramics, *Rep. Prog. Phys.*, 61, 1267-1324.

- Daniels J.E., Jones J.L., Finlayson T.R. (2006), Characterization of domain structures from diffraction profiles in tetragonal ferroelastic ceramics, *J. Phys. D: Appl. Phys.*, 39 5294-5299.
- Denning D., Guyonnet J., Rodriguez B.J. (2016), Applications of piezoresponse force microscopy in materials research: from inorganic ferroelectrics to biopiezoelectrics and beyond, *Int. Mater. Rev.*, 61 46–70.
- Ding S.H., Song T.X., Liu G.B. (2013), The dielectric dispersion properties of BaTiO₃ based ferroelectric ceramics doped with Nb/Mn, *Ferroelectrics* 445 (1) 26–31.
- Du H.L., Li Z.M., Tang F.S., Qu S.B., Pei Z.B., Zhou W.C. (2006), Preparation and piezoelectric properties of (K_{0.5}Na_{0.5})NbO₃ lead-free piezoelectric ceramics with pressure-less sintering, *Mater. Sci. Engg. B* 131 83-87.
- Dogheche E., Remiens D., Shikata S., Hachigo A., Nakahata H. (2005), High-frequency surface acoustic wave devices based on LiNbO₃/diamond multilayered structure, *Appl. Phys. Lett.*, 87(21) 213503.
- Erhart P., Träskelin P., Albe K. (2013), Formation and switching of defect dipoles in acceptor-doped lead titanate: A kinetic model based on first principles calculations, *Phys. Rev. B*, 88 024107.
- Esfahani E.N., Liu X., Li J. (2017), Imaging ferroelectric domains via charge gradient microscopy enhanced by principal component analysis, *J. Materiomics* 3 280-285.
- Fan G., Lu W., Wang X., Liang F. (2007), Morphotropic phase boundary and piezoelectric properties of (Bi_{1/2}Na_{1/2})TiO₃-(Bi_{1/2}K_{1/2})TiO₃-KNbO₃ lead-free piezoelectric ceramics, *Appl. Phys. Lett.*, 90 202908.
- Fancher C.M., Brewer S., Chung C.C., Rohrig S., Rojac T., Esteves G., Deluca M., Bassirri-Gharb N., Jones J.L. (2017), The contribution of 180° domain wall motion to dielectric properties quantified from *in situ* X-ray diffraction. *Acta Mater.*, 126 36-43.
- Feng D., Ming N.B., Hong J.F., Yang Y.S., Zhu J.S., Yang Z., Wang Y.N. (1980), Enhancement of second-harmonic generation in LiNbO₃ crystals with periodic laminar ferroelectric domains, *Appl. Phys. Lett.*, 37(1) 607-609.
- Feng Y., Li W.L., Xu D., Fei W.D. (2015), Enhanced piezoelectric properties of Li⁺ and Al³⁺-modified barium Titanate ceramics, *Ferroelectrics* 489(1) 156–163.

- Freitas V.A., Protzek O.A., Montoro L.A., Gonçalves A.M., Garcia D., Eiras J.A., Guo R., Bhalla A.S., C'oticaad L.F., Santos I.A. (2014), A phenomenological model for ferroelectric domain walls and its implications for BiFeO₃-PbTiO₃ multiferroic compounds, *J. Mater. Chem. C* 2 364-372.
- Fröhlich F., Grau P., Grellmann W. (1977), Performance and analysis of recording microhardness tests, *Phys. Status Solidi.*, 42(1) 79-89.
- Fu R., Zhang T.R. (2000), Effects of an electric field on the fracture toughness of poled lead zirconate titanate ceramics, *J. Am. Ceram. Soc.*, 83 1215-1218.
- Galassi C., Roncari E., Capiani C., Craciun F. (1999), Processing and characterization of high Q_m ferroelectric ceramics, *J. Euro. Ceram. Soc.*, 19 1237-1241.
- Gane N., Cox J.M. (1970), The microhardness of metals at very low loads, *Philos. Mag.*, 22 881-890.
- Gane N., Bowden F.P. (1968), Micro deformation of solids, *J. Appl. Phys.*, 39(3) 1432-1435.
- Gao B., Yao Z., Lai D., Guo Q., Pan W., Hao H., Cao M., Liu H. (2020), Unexpectedly high piezoelectric response in Sm-doped PZT ceramics beyond the morphotropic phase boundary region, *J. Alloys Comp.*, 836 155474.
- Gao Y., Zhang J., Qing Y., Tan Y., Zhang Z., Hao X. (2011), Remarkably Strong Piezoelectricity of Lead-Free (K_{0.45}Na_{0.55})_{0.98}Li_{0.02}(Nb_{0.77}Ta_{0.18}Sb_{0.05})O₃ Ceramic, *J. Am. Ceram. Soc.*, 94 2968-2973.
- García A., Vanderbilt D. (1998), Electromechanical behavior of BaTiO₃ from first-principles, *Appl. Phys. Lett.* 72(23) 2981-2983.
- Garg T., Kulkarni A.R., Venkatramani N. (2013), Influence of PbTiO₃ Addition on Microstructure of (1-x)Pb(Mg_{1/3}Nb_{2/3})O₃-xPbTiO₃ Ceramics. *Proceeding of International Conference on Recent Trends in Applied Physics and Material Science*, AIP Conference Proceedings, 1536 669-670.
- Gharbi M., Sun Z.H., Sharma P., White K. (2009), The origins of electromechanical indentation size effect in ferroelectrics, *Appl. Phys. Lett.* 95(14) 3-5.

Glazounov A.E., Kungl H., Reszat J.T., Hoffmann M.J., Kolleck A., Schneider G.A., Wroblewski T. (2001), Contribution from ferroelastic domain switching detected using x-ray diffraction to R-curves in lead zirconate titanate ceramics, *J. Am. Ceram. Soc.*, 84 2921-2929.

Goldschmidt V.M. (1926), Die gesetze der krystallochemie, *Naturwissenschaften*, 14 477-485.

Gong J.H., Wu J.J., Guan Z.D. (1998), Description of indentation size effects in hot-pressed silicon-nitride-based ceramics, *J. Mater. Sci. Lett.*, 17 473–475.

Gong J.H., Wu J.J., Guan Z.D. (1999), Examination of the indentation size effect in low-load Vickers hardness testing of ceramics, *J. Euro. Ceram. Soc.*, 19 2625-2631.

Gong J.H., Li Y. (2000), An energy balance analysis for the size effect in low-load hardness testing, *J. Mater. Sci.*, 35 209–213.

Gopalan V., Jia Q.X., Mitchel T.E. (1999), In situ video observation of 180° domain kinetics in congruent LiNbO₃ crystals, *Appl. Phys. Lett.*, 75(16) 2482-2484.

Gopalan V., Mitchel T.E. (1999), In situ video observation of 180° domain switching in LiTaO₃ by electro-optic imaging microscopy, *J. Appl. Phys.*, 85(4) 2304-2311.

Grilli S., Ferraro P., Natale P.D., Tiribilli B., Vassalli M. (2005), Surface nanoscale periodic structures in congruent lithium niobate by domain reversal patterning and differential etching, *Appl. Phys. Lett.*, 87 233106.

Gruverman A., Alexe M., Meier D. (2019), Piezoresponse force microscopy and nanoferroic phenomena, *Nature Comm.*, 1-9. <https://doi.org/10.1038/s41467-019-09650-8>

Guillonneau G., Kermouche G., Bec S., Loubet J.L. (2012), Determination of mechanical properties by nanoindentation independently of indentation depth measurement, *J. Mater. Res.*, 27 2551-2560.

Gupta R.K., Venkatesh T.A. (2008), Electromechanical response of piezoelectric composites: effects of geometric connectivity and grain size. *Acta Mater.*, 56(15) 3810–3823.

Guo R.L., Cross E., Park S.E., Noheda B., Cox D.E., Shirane G. (2000), Origin of the high piezoelectric response in PbZr_{1-x}Ti_xO₃, *Phys. Rev. Lett.*, 84 5423-5426.

Guo Y., Kakimoto K., Ohsato H. (2004), Phase Transitional Behavior and Piezoelectric Properties of $(\text{Na}_{0.5}\text{K}_{0.5})\text{NbO}_3\text{--LiNbO}_3$ Ceramics, *App. Phys. Lett.*, 85 4121.

Güthner P., Dransfeld K. (1992), Local poling of ferroelectric polymers by scanning force microscopy, *Appl. Phys. Lett.* **61**(9) 1137–1139.

Habib M., Lee M.L., Kim D.J., Choi H., Kim M.H., Kim W.J., Song T.K., Choi K.S. (2019), Enhanced piezoelectric performance of donor La^{3+} -doped $\text{BiFeO}_3\text{--BaTiO}_3$ lead-free piezoceramics, *Ceram. Int.*, 46(06) 7074-7080.

Haertling G.H. (1999), Ferroelectric ceramics: history and technology, *J. Am. Ceram. Soc.*, 82(4) 797–818.

Hays C., Kendall E.G. (1973), An analysis of Knoop microhardness, *Metall.*, 6 275-282.

Hoffmann M.J., Kungl H., Theissmann R., Wagner S. (2008), Microstructural Analysis Based on Microscopy and X-Ray Diffraction, in the book *Piezoelectricity- Evolution and Future of a Technology* edited by Walter Heywang, Karl Lubitz and Wolfram Wersing, Springer Verlag, Berlin, 403-421.

Horchidan N., Ciomaga C.E., Frunza R.C., Capiiani C., Galassi C., Mitoseriu L. (2016), A comparative study of hard/soft PZT-based ceramic composites, *Ceram. Int.*, 42 9125-9132.

Hu H., Zhu M., Xie F., Lei N., Chen J., Hou Y., Yan H. (2009), Effect of Co_2O_3 Additive on Structure and Electrical Properties of $85(\text{Bi}_{1/2}\text{Na}_{1/2})\text{TiO}_3\text{--}12(\text{Bi}_{1/2}\text{K}_{1/2})\text{TiO}_3\text{--}3\text{BaTiO}_3$ Lead-Free Piezoceramics, *J. Am. Ceram. Soc.* 92 2039–2045.

Huang X., Peng J., Zeng J., Zheng L., Li G., Karaki T. (2019), The high piezoelectric properties and high temperature stability in Mn doped $\text{Pb}(\text{Mg}_{0.5}\text{W}_{0.5})\text{O}_3\text{--Pb}(\text{Zr,Ti})\text{O}_3$ ceramics, *Ceram. Int.*, 45 6523-6527.

Huan Y., Wang X., Fang J., Li L. (2014), Grain size effect on piezoelectric and ferroelectric properties of BaTiO_3 ceramics. *J. Euro. Ceram. Soc.*, 34(5) 1445–1448.

Hurtado-Macias A., Muñoz-Saldña J., Espinoza-Beltrán, T. Scholz, M.V. Swain, Schneider G.A. (2008), Indentation size effect in soft PZT ceramics with tetragonal structure close to the MPB, *J. Phys. D: Appl. Phys.*, 41 035407.

Jaffe B. (1971), in the book *“Piezoelectric Ceramics”* 1st Edition, Academic Press (Elsevier).

- Jaffe B., Cook W.R., Jaffe H. (1971), Piezoelectric ceramics, *J. Sound Vib.*, 20 562–563.
- Jäger I.L. (2004), Surface free energy- a possible source of error in nanohardness? *Surf. Sci.*, 565 173-179.
- Jang J., Lance M.L., Wen S., Tsui T.Y., Pharr G.M. (2005), Indentation induced phase transformation in silicon: influences of load, rate and indenter angle on the transformation behaviour, *Acta Mater.*, 53(6) 1759-1770.
- Jang J., Pharr G.M. (2008), Influence of indenter angle on cracking in Si and Ge during nanoindentation, *Acta Mater.*, 56 4458-4469.
- Jin Y.M., Wang Y.U., Khachatryan A.G., Li J.F., Viehland D. (2003), Adaptive ferroelectric states in systems with low domain wall energy: Tetragonal microdomains, *J. Appl. Phys.*, 94 3629-3640.
- Jo E., Dittmer R., Acosta M., Zang J., Groh C., Sapper E., Wang K., Rödel J. (2012), Giant electric-field-induced strains in lead-free ceramics for actuator applications – status and perspective, *J. Electroceramics*, 29 71-93.
- Johnson K. L. (1970), The correlation of indentation experiments, 18(2) 115-126.
- Jones J.L., Slamovich E.B., Bowman K.J. (2005), Domain texture distributions in tetragonal lead zirconate titanate by x-ray and neutron diffraction, *J. Appl. Phys.*, 97 034113.
- Jones J.L., Hoffman M. (2006), R-curve and stress–strain behavior of ferroelastic ceramics, *J. Am. Ceram. Soc.*, 89 3721-3727.
- Jones J.L., Hoffman M., Daniels J.E., Studer A.J. (2006), Direct measurement of the domain switching contribution to the dynamic piezoelectric response in ferroelectric ceramics, *Appl. Phys. Lett.*, 89 092901.
- K. Eswar Prasad., Ramesh K.T. (2019), Hardness and mechanical anisotropy of hexagonal SiC single crystals polytypes, *J. Alloys Comp.*, 770 158-165.
- Kalinin S.V., Rodriguez B.J., Jesse S., Shin J., Baddorf A.P., Gupta P., Jain H., Williams D.B., Gruverman A. (2006), Vector piezoresponse force microscopy, *Microsc. Microanal.*, 12 206–220.

Kalinin S.V., Eliseev E.A., Morozovska A. N. (2006), Materials contrast in piezoresponse force microscopy, *Appl. Phys. Lett.*, 88 232904.

Kalinin S.V., Morozovska A. N., Chen L.Q., Rodriguez B.J. (2010), Local polarization dynamics in ferroelectric materials. *Rep. Prog. Phys.*, 73 056502. Review article on imaging, manipulation and spectroscopy of ferroelectric switching by PFM with special emphasis on resolution limits.

Kamble S.N., Kubair D.V., Ramamurty U. (2009), Indentation strength of piezoelectric ceramics: experiments and simulations, *J. Mater. Res.*, 24(3) 926-935.

Karaki T., Yan K., Miyamoto T., Adachi M. (2007), Lead-Free Piezoelectric Ceramics with Large Dielectric and Piezoelectric Constants Manufactured from BaTiO₃ Nano-Powder, *Jpn. J. Appl. Phys.* 46 L97–L98.

Kao K.S., Chung C.J., Chen Y.C., Cheng C.C. (2004), Phase tunable SAW device on LiNbO₃ substrate, *Ferroelectrics*, 304 969–972.

Kathavate V.S., Praveen Kumar B., Singh I., Chaudhary Palash Roy, K. Eswar Prasad (2018), Nanoindentation response of PZT and NKN-NT piezoceramics, *J. Coupled. Syst. Multiscale Dyn.*, 6(4) 291-299.

Kathavate V.S., Praveen Kumar B., Singh I., K. Eswar Prasad (2020), Effect of sub and above curie temperature annealing on the nanomechanical properties of PMN-PT piezoceramics, *Ceram. Int.*, 46(08) 12876-12883.

Kathavate V.S., Praveen Kumar B., Singh I., K. Eswar Prasad (2021), Analysis of indentation size effects (ISE) in nanoindentation hardness in polycrystalline PMN-PT with different domain configurations, *Ceram. Int.*, 47(09) 11870-11877

Kathavate V.S., Sonagara H., Praveen Kumar B., Singh I., K. Eswar Prasad (2021), Role of domain configurations on the mechanistic modelling of indentation size effects (ISEs) in nano hardness of hard and soft PZT piezoceramics, *Int. J. Adv. Engg. Sci. Appl. Math.*, 13(01) 63-78.

Kathavate V.S., Sonagara H., Praveen Kumar B., Singh I., K. Eswar Prasad (2021), Tailoring the nanomechanical properties of hard and soft PZT via domain engineering by selective annealing, *Mater. Today Comm.*, 28 102495.

- Kholkin D.A.L., Kalinin D.S.V., Roelofs D.A., Gruverman P.A. (2007), Review of ferroelectric domain imaging by piezoresponse force microscopy, in: S. Kalinin, A. Gruverman (Eds.), *Scanning Probe Microscopy*, Springer, New York, pp. 173–214.
- Kim H., Kim T. (2002), Measurement of hardness on traditional ceramics, *J. Eur. Ceram. Soc.*, 22 1437-1445.
- Kim S.B., Chung T.J., Kim D.Y. (1993). Effect of external compressive stress on the domain configuration of barium titanate ceramics. *J. Euro. Ceram. Soc.*, 12(2) 147-151.
- Kitamura K., Furukawa Y., Takekawa S., Hatanaka T., Ito H., Gopalan V. (2001), Non-stoichiometric control of LiNbO₃, and LiTaO₃ in ferroelectric domain engineering for optical devices, *Ferroelectrics*, 257 235-243.
- Kugel V.D., Cross L.E. (1998), Behavior of soft piezoelectric ceramics under high sinusoidal electric fields, *J. Appl. Phys.*, 84 2815.
- Kuwata J, Uchino K, Nomura S. (1981), Phase transitions in the Pb(Zn_{1/3}Nb_{2/3})O₃–PbTiO₃ system, *Ferroelectrics*, 37(1) 579–582.
- Lamberson L., Ramesh K.T. (2017), Dynamic electromechanical behaviour of single-crystal α -Quartz, *Int. J. Impact Engg.*, 110 338-345.
- Landis C. (2003), On the fracture toughness of ferroelastic materials, *J. Mech. Phys. Sol.*, 51 1347-1369.
- Levassort, F., Grégoire, J.M., Lethiecq, M., et al., (2011), High frequency single element transducer based on pad-printed lead-free piezoelectric thick film. In: *Proceedings of the IEEE International Ultrasonics Symposium*, p. 848.
- Li F., Lin D., Chen Z., Cheng Z., Wang J., Li C.C., Xu Z., Huang Q., Liao X., Chen L.Q. (2018), et al. Ultrahigh piezoelectricity in ferroelectric ceramics by design. *Nature Mater.*, 17(4) 349.
- Li F., Zhang S., Xu Z., Wei X., Shrout T.R. (2011), Critical property in relaxor PbTiO₃ single crystals- shear piezoelectric response, *Adv. Funct. Mater.*, 21 2118-2128.
- Li H., Bradt R.C. (1992), The indentation load/size effect and the measurements of the hardness of vitreous silica, *J. Non-Cryst. Solids*, 146 197–212.

Li H., Bradt R.C. (1993), The microhardness indentation load/size effect in rutile and cassiterite single crystals, *J. Mater. Sci.*, 28 917-926.

Li H., Bradt R.C. (1996), The effect of indentation-induced cracking on the apparent microhardness, *J. Mater. Sci.*, 31 1065-1070.

Li H., Ghosh A., Han Y.H., Bradt R.C. (1993), The frictional component of the indentation size effect in low load microhardness testing, *J. Mater. Res.*, 8 1028–1032.

Li H.L., Zhang Y., Zhou J.J., Zhang X.W., Liu H., Fang J.Z. (2015), Phase structure and electrical properties of xPZN–(1-x)PZT piezoceramics near the tetragonal/rhombohedral phase boundary, *Ceram. Int.*, 41 4822-4828.

Li H.T., Zhang B.P., Shang P.P., Fan Y., Zhang Q. (2011), Phase Transition and High piezoelectric properties of $\text{Li}_{0.058}(\text{Na}_{0.52}\text{K}_{0.48})_{0.942}\text{NbO}_3$ Lead-Free Ceramics, *J. Am. Ceram. Soc.*, 94 628– 632.

Li J. (2011), Broadband Dielectric Response in Hard and Soft PZT: Understanding Softening and Hardening Mechanisms, Ph.D. Thesis at École Polytechnique Fédérale De Lausanne.

Li J.Y., Liu D. (2004), On ferroelectric crystals with engineered domain configurations, *J. Mech. Phys. Sol.*, 52 1719-1742.

Li Y., Zhang L., Yu L., Li D., Meng H., Ai Q., Hu J., Jin Li., Gao J., Liu G. (2020), Study of the structure, electrical properties, and energy storage performance of ZnO-modified $\text{Ba}_{0.65}\text{Sr}_{0.245}\text{Bi}_{0.07}\text{TiO}_3$ Pb-free ceramics, *Ceram. Int.*, 46 8-16.

Lim Y.Y., Chaudhri M.M. (2007), The effect of the indenter load on the nanohardness of ductile metals: An experimental study on polycrystalline work-hardened and annealed oxygen-free copper, *Philos. Mag. A*, 79(12) 2979-3000.

Limpichaipanit A., Somwan S., Ngamjarurojana A. (2018), Dielectric properties of PFN–PZT composites: From relaxor to normal ferroelectric behavior, *Ceram. Int.*, 44 14797-14802.

Lines M.E., Glass A.M. (1979), *Principles and Applications of Ferroelectrics and Related Materials* (Oxford: Clarendon)

Lippman G. (1881), Principal of the conservation of electricity, *Annales de Chemie et de Physique*, 24, 145.

Liu H., Chen J., Huang H., Fan L., Ren Y., Zhao P., Deng J., Chen L.Q., Xing X. (2018), Role of reversible phase transformation for strong piezoelectric performance at the morphotropic phase boundary, *Phys. Rev. Lett.*, 120 055501.

Liu M., Yang F. (2012), Finite element analysis of the spherical indentation of transversely isotropic piezoelectric materials, *Model. Simul. Mater. Sci. Eng.*, 20 045019.

Liu S.F., Park S.E., Shrout T.R., Cross L.E. (1999), Electric field dependence of piezoelectric properties for rhombohedral $0.955\text{Pb}(\text{Zn}_{1/3}\text{Nb}_{2/3})\text{O}_3-0.045\text{PbTiO}_3$ single crystals, *J. Appl. Phys.*, 85(5) 2810–2814

Liu W., Ren X. (2009), Large piezoelectric effect in Pb-free ceramics, *Phys. Rev. Lett.*, 103 257602.

Liu X., Tan X. (2016), Giant Strains in Non-Textured $(\text{Bi}_{1/2}\text{Na}_{1/2})\text{TiO}_3$ -Based Lead-Free Ceramics, *Adv. Mater.*, 28 574-578.

Luo C., Chang W.Y., Gao M., Chang C.H., Li J., Viehland D., Tian J., Jiang X. (2020), Multi-layered domain morphology in relaxor single crystals with nano-patterned composite electrode, *Acta Mater.*, 182 10-17.

Lysaght V.E. (1949), *“Indentation Hardness Testing”*, Reinhold, New York.

Ma Q., Clarke D.R. (1995), Size dependent hardness of silver single crystals, *J. Mater. Res.*, 10 853-863.

Maiti P., Bhattacharya M., Das P.S., Devi P.S., Mukhopadhyay A.K. (2018), Indentation size effect and energy balance issues in nanomechanical behavior of ZTA ceramics, *Ceram. Int.*, 44(8) 9753-9772.

Maranganti R., Sharma P (2007), Length scales at which classical elasticity breaks down for various materials, *Phys. Rev. Lett.*, 98(19) 1-4.

Marshall D.B., Lawn B.R. (1977), An indentation technique for measuring stresses in tempered glass, *J. Am. Ceram. Soc.*, 60(1-2) 86-87.

- Marsilius M., Webber K.G., Aulbach E., Granzow T. (2010), Comparison of the temperature-dependent ferroelastic behavior of Hard and Soft lead zirconate titanate ceramics, *J. Am. Ceram. Soc.*, 91 2850-2856.
- Mathews N.G., Saxena A.K., Kirchiechner C., Dehm G., Jaya B.N. (2020), Effect of size and domain orientation on strength of Barium Titanate, *Scripta Mater.*, 182 68-73.
- Mazheritsky A.V. (2002), Quality factors of piezoceramics, *Ferroelectrics*, 266 277-304.
- McColm I. J. (1990), "*Ceramic Hardness*", Springer, New York.
- Mehta K., Virkar A.V. (1990), Fracture mechanisms in ferroelastic-ferroelectric lead zirconate titanate (Zr:Ti = 0.54:0.46) ceramics, *J. Am. Ceram. Soc.* 73(3) 567-574.
- Meyer E. (1908), Contribution to the knowledge of hardness and hardness testing, *Z. Ver. Dtsch. Ing.* 52 740-835.
- Ming N.B., Hong J.F., Feng D. (1982), The growth striations and ferroelectric domain structures in Czochralski-grown LiNbO_3 single crystals, *J. Mater. Sci.*, 17 1663-1670.
- Minhong J., Manjiao D., Huaxin L., Shi W., Xinyu L. (2011), Piezoelectric and dielectric properties of $\text{K}_{0.5}\text{Na}_{0.5}\text{NbO}_3\text{-LiSbO}_3\text{-BiScO}_3$ lead-free piezoceramics, *Mat. Sci. Engg. B.*, 176 167– 170.
- Miriyala K., Ramadurai R. (2016), Tunable ferroelectric domain orientation in polycrystalline and highly oriented $\text{Na}_{0.5}\text{Bi}_{0.5}\text{TiO}_3$ Thin Films, *Mater. Lett.*, 178 23-26.
- Miriyala K., Ramadurai R. (2018), Microstructural influence on ferroelectric domain pattern and piezoelectric properties of $\text{Na}_{0.5}\text{Bi}_{0.5}\text{TiO}_3$ thin films, *Ceram. Int.*, 44 14556-14562.
- Mock R., Lubitz K., in: Heywang W., Lubitz K., Wersing (Eds.) W. (2009), Piezoelectricity. Evolution and Future of a Technology, Springer Series in Materials Science 114, Berlin, pp. 299–310.
- Morozov M.I., Damjanovic D. (2010), Charge migration in $\text{Pb}(\text{Zr,Ti})\text{O}_3$ ceramics and its relation to ageing, hardening, and softening, *J. Appl. Phys.* 107 034106.
- Muñoz-Saldaña J., Schneider G.A., Eng L.M. (2001), Stress induced movement of ferroelastic domain walls in BaTiO_3 single crystals evaluated by scanning force microscopy. *Surf. Sci.*, 480 1-2.

- Mylnikova I.R., Bokov V.A. (1959), *Kristallografiya*, 4 433-440.
- Nagata H., Shinya T., Hiruma Y., Takenaka T. (2004), *Developments in Dielectric Materials and Electronic Devices*, *Ceram. Trans.*, 167 213–221.
- Nelson C.T., Gao P., Jokisaari J.R., Heikes C., Adamo C., Melville A., Baek S.H., Folkman C.M., Winchester B., Gu Y. et al. (2011), Domain dynamics during ferroelectric switching. *Science*, 334(6058) 968–971.
- Neumann, F. E. (1885), *Vorlesungen über die Theorie der Elastizität der festen Körper und des Lichtäthers* (in German), edited by O. E. Meyer. Leipzig, B. G. Teubner-Verlag.
- Newnham R.E., Miller C.S., Cross L.E., Cline W.T. (1975), Tailored domain patterns in piezoelectric crystals, *Phys. Stat. Sol. (a)*, 32, 69-78.
- Newnham R.E., Ruschau G.R. (1991), Smart electroceramics, *J. Am. Ceram. Soc.*, 74(3) 463–480.
- Nix W.D., Gao H. (1998), Indentation size effects in crystalline materials: a law for strain gradient plasticity, *J. Mech. Phys. Solid.*, 46 411-425.
- Njiwa A.B.K., Fett T., Lupasu D.C., Rödel J. (2006), Effect of geometry and electrical boundary conditions on R curve for lead zirconate titanate ceramics, *Engg. Fract. Mech.* 73 309-317.
- Noheda B., Cox D.E., Shirane G. (2000), Stability of the monoclinic phase in the ferroelectric perovskite $\text{PbZr}_{1-x}\text{Ti}_x\text{O}_3$, *Phys. Rev. B* 63 014103.
- Noheda B., Cox D.E., Shirane G., Ye Z.G., Gao J. (2002), Phase diagram of the ferroelectric relaxor $(1-x)\text{Pb}(\text{Mg}_{1/3}\text{Nb}_{2/3})\text{O}_3-x\text{PbTiO}_3$, *Phys. Rev. B*, 66 054104.
- Noheda B., Cox C.E., Shirane G., Guo R., Jones B., Cross L.E. (2000), Stability of the monoclinic phase in the ferroelectric perovskite $\text{PbZr}_{1-x}\text{Ti}_x\text{O}_3$, *Phys. Rev.*, B 63 014103.
- Noheda B., Gonzalo J.A., Cross L.E., Guo R., Park S.E., Cox D.E., Shirane G. (2000), Tetragonal-to-monoclinic phase transition in a ferroelectric perovskite: The structure of $\text{PbZr}_{0.52}\text{Ti}_{0.48}\text{O}_3$, *Phys. Rev.*, B 61(13) 8687-8695.

Noheda B., Gonzalo J.A., Caballero A.C., Moure C., Cox D.E., Shirane G. (2000), New features of the morphotropic phase boundary in the $\text{Pb}(\text{Zr}_{1-x}\text{Ti}_x)\text{O}_3$ system, *Ferroelectrics*, 237 237-244.

Oliver W.C. Pharr G.M. (1992), An improved technique for determining hardness and elastic modulus using load and displacement sensing indentation experiments, *J. Mater. Res.*, 7 1564-1584.

Oliver W.C., Pharr G.M. (2004), Measurement of hardness and elastic modulus by instrumented indentations: advances in understanding and refinements to the methodology, *J. Mater. Res.*, 19 3-20.

O'Neill H. (1934) ,The hardness of metals and its measurement, Sherwood, Cleveland, OH, 43.

Paik D.S., Park S.E., Wada S., Liu S.F., Shrout T.R. (1999), E-field induced phase transition in $\langle 001 \rangle$ -oriented rhombohedral $0.92\text{Pb}(\text{Zn}_{1/3}\text{Nb}_{2/3})\text{O}_3-0.08\text{PbTiO}_3$ crystals, *J. Appl. Phys.* 85(2) 1080–1083.

Park S.E., Shrout T.R. (1997), Ultrahigh strain and piezoelectric behavior in relaxor based ferroelectric single crystals, *J. Appl. Phys.*, 82 1804-1811.

Park Y.B., Dicken M.J., Xu Z.H., Li X. (2007), Nanoindentation of *a* and *c* domains in tetragonal BaTiO_3 single crystal, *J. Appl. Phys.* 102 083507.

Park M., Yoo J., Park Y. (2013), Piezoelectric and dielectric properties of $(\text{Na}_{0.54}\text{K}_{0.46})_{0.96}\text{Li}_{0.04}(\text{Nb}_{0.80}\text{Ta}_{0.20})\text{O}_3$ ceramics substituted with Co, *J. Electroceram.*, 30 66-71.

Peng Z., Gong J., Miao H. (2004), On the description of indentation size effect in hardness testing for ceramics: Analysis of the nanoindentation data, *J. Euro. Ceram. Soc.*, 24 2193–2201.

Peng Z., Wen T., Gong J., Wang C., Fu Z., Miao H. (2012), Relationship Between the Ratio of Young's Modulus to Hardness and the Elastic Recovery of Nanoindentation, *Key Eng. Mater. In Trans. Tech. Publications, Switzerland* 492 5.

Pisarenko G.G., Chushko V.M., Kovalev S.P. (1985), Anisotropy of fracture toughness of piezoelectric ceramics, *J. Am. Ceram. Soc.*, 68(5) 259-265.

- Pramanick A., Damjanovic D., Daniels J.E., Nino J.C., Jones J.L. (2011), Origins of electro-mechanical coupling in polycrystalline ferroelectrics during subcoercive electrical loading, *J. Am. Ceram. Soc.* 94(2) 293–309.
- Pramanik R., Sahukar M.K, Mohan Y., Praveen Kumar B., Sangwar S.R., Arockiarajan A. (2019), Effect of grain size on piezoelectric, ferroelectric and dielectric properties of PMN-PT ceramics, *Ceram. Int.* 45(5) 5731-5742.
- Promsawat M., Marungsri B., Promsawat N., Janphuang P., Luo Z., Pojprapai S. (2017), Effects of temperature on aging degradation of soft and hard lead zirconate titanate ceramics, *Ceram. Int.*, 43 9709-9714.
- Quinn J.B., Quinn G.D. (1997), Indentation brittleness of ceramics: a fresh approach, *J. Mater. Sci.*, 32 4331-4346.
- Ragini, Mishra S.K., Pandey D., Lemmens H., Tendeloo G.V. (2001), Evidence for another low-temperature phase transition in tetragonal $\text{Pb}(\text{Zr}_x\text{Ti}_{1-x})\text{O}_3$ ($x=0.515, 0.520$), *Phys. Rev. B* 64 054101.
- Ramajo L., Castro M., Fernandez J.F., Rubio-Marcos F. (2017), Mechanical properties enhancement in potassium-sodium niobate lead-free piezoceramics: the impact of chemical modifications, *J. Mater. Sci.: Mater. Electron.*, 28 5128-5134.
- Ramamurty U., Sridhar S., Giannakopoulos A.E., Suresh S. (1999), An experimental study of spherical indentation on piezoelectric materials, *Acta Mater.*, 47(8) 2417-2430.
- Ramamurty U., Jang J. (2014), Nanoindentation for probing mechanical behaviour of molecular crystals- a review of the technique and how to use it, *Cryst. Engg. Comm.*, 16(01) 12-23.
- Ramesh Nath, Hong S., Klug J.A., Imre A., Bedzyk M.J., Katiyar R.S., Auciello O. (2010), Effects of cantilever buckling on vector piezoresponse force microscopy imaging of ferroelectric domains in BiFeO_3 nanostructures, *Appl. Phys. Lett.*, 96 163101.
- Ranjan K.K., Ng Y.S., Zhang J., Lim L.C. (2004), [001] Poled $\text{Pb}(\text{Zn}_{1/3}\text{Nb}_{2/3})\text{O}_3$ - (6, 7)% PbTiO_3 k_{31} actuators: Effects on initial domain structure, length orientation and poling conditions, *Appl. Phys. Lett.*, 85 4136-4138.

Redhu P., Sharma P., Hooda A., Singh A., Sharma G., Punia R. (2021), Role of charge compensation mechanism and defect dipoles on properties of Mn doped BCT ceramics, *Ceram. Int.*, 47(8) 14491-11505.

Reece M.J., Guiu F. (2002), Toughening produced by crack-tip-stress-induced domain reorientation in ferroelectric and/or ferroelastic materials, *Phil. Mag. A*, 82 29-38.

Ren X. (2004), Large electric-field-induced strain in ferroelectric crystals by point-defect-mediated reversible domain switching, *Nature Mater.*, 03 91-94.

Rödel J., Jo W., Siefert K.T.P., Anton E.M., Granzow T. (2009), Perspective on the Development of Lead-free Piezoceramics, *J. Am. Ceram. Soc.*, 92(6) 1153-1177.

Rojac T., Bencan A., Malic B., Tutuncu G., Jones J.L., Daniels J.E., Damjanovic D. (2014), BiFeO₃ Ceramics: Processing, Electrical, and Electromechanical Properties, *J. Am. Ceram. Soc.*, 1-19.

Sai N., Rabe K.M., Vanderbilt D. (2002), Theory of structural response to macroscopic electric fields in ferroelectric systems, *Phys. Rev. B*, 66 104108.

Saito Y., Takao H., Tani T., Nonoyama T., Takatori K., Homma T., Nagaya T., Nakamura M. (2004), Lead free piezo ceramics, *Nature*, 432, 84-87.

Sangwal K. (1989), Microhardness of as-grown and annealed lead sulphide crystals, *J. Mater. Sci.*, 24(3) 1128-1132.

Sangwal K. (2000), On the reverse indentation size effect and microhardness measurement of solids, *Mater. Chem. Phys.*, 63 145-152.

Sargent P.M. (1984), *“Microindentation technique in materials science and engineering”*, ASTM STP 889, Philadelphia, US, 160-174.

Sargent P.M., Page T.F. (1978), The influence on the microhardness of ceramic materials, *Proceedings of the British Ceramics Society* 26 209-224.

Schaab J., Krug I.P., Nickel F., Gottlob D.M., H. Doğanay, Cano A., Hentschel M., Yan Z., Bourret E., Schneider C.M., Ramesh R., Meier D. (2014), Imaging and characterization of conducting ferroelectric domain walls by photoemission electron microscopy, *Appl. Phys. Lett.* 104 232904.

Schneider G.A., Scholz T., Mũoz-Saldãa J., Swain M.V. (2005), Domain rearrangement during nanoindentation in single-crystalline barium titanate measured by atomic force microscopy and piezoresponse force microscopy, *Appl. Phys. Lett.*, 86(19) 1-3.

Schierholz R., Fuess H. (2012), Ferroelectric domains in PZT ceramics at the morphotropic phase boundary. Can the splitting of reflections in SAED patterns be used for the distinction of different pseudo-cubic phases? *J. Appl. Crystallogr.*, 45 766-777.

Schmitt L.A., Schönau K.A., Theissmann R., Fuess H., Kungl H., Hoffman M.J. (2007), Composition dependence of the domain configuration and size in $\text{Pb}(\text{Zr}_{1-x}\text{Ti}_x)\text{O}_3$ ceramics. *J. Appl. Phys.* 101 074107.

Scholz T., McLaughlin K.K, Giuliani F., Clegg W.J., Espinoza-Beltrán F.J., Swain M.V., Schneider G.A. (2007), Nanoindentation initiated dislocations in barium titanate (BaTiO_3), *Appl. Phys. Lett.* 91(6) 2005-2008.

Schönau K.A., Knapp M., Kungl H., Hoffmann M.J., Fuess H. (2007), In situ synchrotron diffraction investigation of morphotropic $\text{Pb}[\text{Zr}_{1-x}\text{Ti}_x]\text{O}_3$ under an applied electric field, *Phys. Rev. B*, 76 144112.

Schönau K.A., Knapp M., Maglione M., Fuess H. (2009), In situ investigation of the stability field and relaxation behavior of nanodomain structures in morphotropic $\text{Pb}[\text{Zr}_{1-x}\text{Ti}_x]\text{O}_3$ under variations in electric field and temperature, *Appl. Phys. Lett.*, 94 122902.

Schuh C.A. (2006), Nanoindentation studies of materials, *Mater. Today*, 9 32-40.

Setter N., Cross L.E. (1980), Flux growth of lead scandium tantalate $\text{Pb}(\text{Sc}_{0.5}\text{Ta}_{0.5})\text{O}_3$ and lead magnesium niobate $\text{Pb}(\text{Mg}_{1/3}\text{Nb}_{2/3})\text{O}_3$ single crystals, *J. Cryst. Growth*, 50 555-556.

Seo Y.H., Vögler M., Isaia D., Aulbach E., Rödel J., Webber K.G. (2013), Temperature-dependent R-curve behaviour of $\text{Pb}(\text{Zr}_{1-x}\text{Ti}_x)\text{O}_3$, *Acta Mater.* 61 6418-6427.

Sharma P., Reece T.J., Ducharme S., Gruverman A. (2011), High-resolution studies of domain switching behavior in nanostructured ferroelectric polymers, *Nano Letters*, 11 1670-1675.

Shibata K., Wang R., Tou T., Koruza J. (2018), Applications of lead-free piezoelectric materials, *MRS Bull.*, 43 612-616.

Shur V. Y. (1996), in “Ferroelectric Thin Films: Synthesis and Basic Properties,” 153 (ed. by C. A. Paz de Araujo, J. F. Scott, and G. W. Taylor, Gordon and Breach, New York).

Shur V.Y. (2006), Kinetics of ferroelectric domains: Application of general approach to LiNbO_3 and LiTaO_3 , *J. Mater. Sci.*, 41, 199-210.

Shur V.Y. (2006), Domain engineering in lithium niobate and lithium tantalate: Domain wall motion, *Ferroelectrics*, 340, 3-16.

Shur V.Y. (2013), Domain nanotechnology in ferroelectric single crystals: Lithium Niobate and Lithium Tantalate Family, *Ferroelectrics*, 443 71-82.

Simmons G., Wang H. (1971), Single crystal elastic constants and calculated aggregate properties: A Handbook, 2nd edition, The M.I.T. Press, Cambridge, MA, USA.

Singh A.K., Ragini, Mishra S.K., Pandey D., Yoon S., Baik S., Shin S. (2008), Origin of high piezoelectric response of $\text{Pb}(\text{Zr}_x\text{Ti}_{1-x})\text{O}_3$ at the morphotropic phase boundary: Role of elastic instability, *Appl. Phys. Lett.*, 92 022910.

Smith R.T., Welsh F.S. (1971), Temperature dependence of the elastic, piezoelectric, and dielectric constants of lithium tantalate and lithium niobate, *J. Appl. Phys.*, 42(6) 2219–2230.

Song R., Zhao Y., Li W., Yu Y., Sheng J., Li Z., Zhang Y., Xia H., Fei W.D. (2019), High temperature stability and mechanical quality factor of donor-acceptor co-doped BaTiO_3 piezoelectrics, *Act Mater.*, 181 200-206.

Spary I.J., Bushby A.J., Jennett N.M. (2006), On the indentation size effect in spherical indentation. *Philos. Mag.*, 86(33–35 SPEC. ISSUE) 5581-5593.

Sridhar S., Giannakopoulos A.E., Suresh S., Ramamurthy U. (1999), Electrical response during indentation of piezoelectric materials: A new method for material characterization, *J. Appl. Phys.*, 85 380-387.

Stemmer S., Streiffer S.K., Ernst F. Rühle M. (1995), Atomistic structure of 90° domain walls in ferroelectric PbTiO_3 thin films, *Phil. Mag. A*, 71, 713-724.

Sun C.T., Park S.B. (2000), Measuring fracture toughness of piezoceramics by Vickers indentation under the influence of electric fields, *Ferroelect.*, 248 79-95.

Sun E., Cao W. (2014), Relaxor-based ferroelectric single crystals: Growth, domain engineering, characterization and applications, *Prog. Mater. Sci.*, 64 124-210.

Sun X., Su Y.J., Gao K.W., Guo L.Q., Qiao L.J. (2012), Charge accumulation in grain boundary promotes intergranular fracture of lead zirconate titanate piezoceramics under mechanical and electric load, *Scripta Mater.*, 66 292-295.

Swadener J.G., George E.P., Pharr G.M. (2002), The correlation of the indentation size effect measured with indenters of various shapes. *J. Mech. Phys. Sol.*, 50(4) 681-694.

Swartz S.L., ShROUT T.R. (1982), Fabrication of perovskite lead magnesium niobate, *Mater. Res. Bull.*, 17(10) 1245-1250.

Tan L., Wang Y., Sun Q., Zeng F. (2020), Effects of $(K_{0.5}Na_{0.5})(Nb_{0.96}Sb_{0.04})O_3$ on microstructure and electrical properties of BNT-based piezoelectric ceramics, *Mat. Sci. Engg. B*, 260 114653.

Tang X., Chen T., Liu Y., Zhang J., Zhang T., Wang G., Zhou J. (2016), Composition dependence of phase structure and electrical properties in $(0.98-x)K_{0.35}Na_{0.65}NbO_3-0.02BaZrO_3-xBi_{0.5}Na_{0.5}ZrO_3$ ternary ceramics, *J. Alloys Comp.*, 672 277-281.

Takahashi S. (1982), Effect of impurity doping in lead zirconate titanate ceramics, *Ferroelectrics*, 41 143–156.

Takeuchi T., Tabuchi M., Kageyama H., Suyama Y. (1999), Preparation of dense $BaTiO_3$ ceramics with submicrometer grains by spark plasma sintering. *J. Am. Ceram. Soc.*, 82(4) 939–943.

Tarkanian M.L., Neumann J.P., Raymond L. (1973), Determination of the temperature dependence of {100} and {112} slip in tungsten from Knoop hardness measurements, in *The Science of Hardness Testing and its Research Applications*, American Society of Metals, 1st edition, 187-198.

Tate D.R. (1945), A comparison of microhardness tests, *Trans. of ASM* 35 374-389.

Theissmann R., Schmitt L.A., King J., Schierholz R., Knapp M., Kungl H., Hoffmann M.J. (2007), Nanodomains in morphotropic lead zirconate titanate ceramics: On the origin of the strong piezoelectric effect, *J. Appl. Phys.* 102, 024111.

Tian H.Y., Kwok K.W., Chan H.L.W., Buckley C.E. (2007), The effects of CuO-doping on dielectric and piezoelectric properties of $\text{Bi}_{0.5}\text{Na}_{0.5}\text{TiO}_3\text{-Ba}(\text{Zr,Ti})\text{O}_3$ lead-free ceramics, *J. Mater. Sci.*, 42 9750–9755.

Tutuncu G., Li B., Bowman K., Jones J.L. (2014), Domain wall motion and electromechanical strain in lead-free piezoelectrics: Insight from the model system $(1-x)\text{Ba}(\text{Zr}_{0.2}\text{Ti}_{0.8})\text{O}_3-x(\text{Ba}_{0.7}\text{Ca}_{0.3})\text{TiO}_3$ using in situ high-energy X-ray diffraction during application of electric fields, *J. Appl. Phys.*, 115 144104.

Veenhuizen K., McAnany S., Vasudevan R., Nolan D., Aitken B., Jesse S., Kalinin S.V., Jain H., Dierolf V., Ferroelectric domain engineering of lithium niobate single crystal confined in glass, *MRS Comm.*, 1-6.

Vögler M., Acosta M., Brandt D.R.J., Molina-Luna L., Webber K.G. (2015), Temperature-dependent R-curve behavior of the lead-free ferroelectric $0.615\text{Ba}(\text{Zr}_{0.2}\text{Ti}_{0.8})\text{O}_3\text{-}0.385(\text{Ba}_{0.7}\text{Ca}_{0.3})\text{TiO}_3$ ceramic, *Eng. Fract. Mech.*, 144 168-177.

Voigt W. (1928), *Lehrbuch der Kristallphysik* (textbook on crystal physics), Teubner, Leipzig.

Wada S., Kakemoto H., Tsurumi T. (2004), Enhanced piezoelectric properties of piezoelectric single crystals by domain engineering, *Mater. Trans.*, 45(2) 178-187.

Wada S. (2006), *Domain Wall Engineering in Lead-free Piezoelectric Materials and Their Enhanced Piezoelectricities*. Springer, New York, 1st Edition.

Wang D., Wang G., Murakami S., Fan Z., Fateira A., Zhou D., Sun S., Zhao Q., Reany I.M. (2018), $\text{BiFeO}_3\text{-BaTiO}_3$: A new generation of lead-free Electroceramics, *J. Adv. Dielectr.*, 8(6) 1830004.

Wang H., Zeng K. (2020), Characterization of domain structure and imprint of $\text{Pb}(\text{Zn}_{1/3}\text{Nb}_{2/3})\text{O}_3\text{-}4.5\%\text{PbTiO}_3$ (PZN-4.5%PT) single crystals by using PFM and SS-PFM techniques, *Ceram. Int.*, 46(4) 4274-4279.

Wang J., Shu W., Shimada T., Kitamura T., Zhang T.Y. (2013), Role of grain orientation distribution in the ferroelectric and ferroelastic domain switching of ferroelectric polycrystals, *Acta Mater.* 61(16) 6037–6049.

- Wang K., Li J.F. (2012), (K,Na)NbO₃-based lead-free piezoceramics: Phase transition, sintering and property enhancement, *J. Adv. Ceram.*, 1(1) 24-37.
- Wang K., Yao F.Z., Jo W., Gobeljic D., Shvartsman V.V., Lupascu D.C., Wang K., Li J.F., Rödel J. (2013), Temperature-Insensitive (K,Na)NbO₃-Based Lead-Free Piezoactuator Ceramics, *Adv. Funct. Mater.*, 1-8.
- Wang R., Wang K, Yao F., Li J.F., Schader F.H., Webber K.G., Jo W., Rödel J. (2015), Temperature stability of lead-free niobate piezoceramics with engineered morphotropic phase boundary, *J. Am. Ceram. Soc.*, 98 2177–2182.
- Wang R., Tang E., Yang G., Han Y., Chen C. (2020), Discharge characteristics of fractured soft piezoelectric ceramic under repeated impact, *Ceram. Int.*, 46 23499-23504.
- Wang X., Venkataraman L.K., Tan C., Li Y. (2021), Fracture behaviour in electrically poled alkaline bismuth- and potassium- based lead free piezoceramics using Vickers indentation, *Scripta Mater.*, 194 113647.
- Wang Y. (2016), Effects of indenter angle and friction on the mechanical properties of thin film, *Results Phys.*, 6 509-514.
- Wang Y.U. (2006), Three intrinsic relationships of lattice parameters between intermediate monoclinic M_C and tetragonal phases in ferroelectric Pb[(Mg_{1/3}Nb_{2/3})_{1-x}Ti_x]O₃ and Pb[(Zn_{1/3}Nb_{2/3})_{1-x}Ti_x]O₃ near morphotropic phase boundaries, *Phys. Rev. B* 73 014113.
- Wang Y.U. (2007), Diffraction theory of nanotwin superlattices with low symmetry phase: Application to rhombohedral nanotwins and monoclinic M_A and M_B phases, *Phys. Rev. B*, 76, 024108.
- Webber K.G., Aulbach E., Key T., Marsilius M., Granzow T., Rödel J. (2009), Temperature-dependent ferroelastic switching of soft lead zirconate titanate, *Acta Mater.*, 57 4614-4623.
- Wu Y., Zhang J., Tan Y., Zheng P. (2016), Notable grain-size dependence of converse piezoelectric effect in BaTiO₃ ceramics. *Ceramics International*, 42(8) 9815–9820.
- Wong M.F., Zeng K. (2008), Deformation behavior of PZN–6%PT single crystal during nanoindentation, *Philos. Mag.*, 88(26) 3105-3128.

- Wong M.F., Zeng K. (2010), Elastic–plastic deformation of $\text{Pb}(\text{Zn}_{1/3}\text{Nb}_{2/3})\text{O}_3$ –(6–7)% PbTiO_3 single crystals during nanoindentation, *Philos. Mag.*, 90(13) 1685-1700.
- Xu D., Li W.L., Wang L.D., Wang W., Cao W.P., Fei W.D. (2014), Large piezoelectric properties induced by doping ionic pairs in BaTiO_3 ceramics, *Acta Mater.* 79 (Supplement C) 84–92.
- Xiang Y., Zhang R., Cao W. (2010), Optimization of piezoelectric properties for $[001]_c$ poled $0.94\text{Pb}(\text{Zn}_{1/3}\text{Nb}_{2/3})\text{O}_3$ - 0.06PbTiO_3 single crystals, *Appl. Phys. Lett.* 96 092902.
- Yamada M., Nada N., Saitoh M., Watanabe K. (1993), First-order quasi-phase matched LiNbO_3 waveguide periodically poled by applying an external field for efficient blue second-harmonic generation, *Appl. Phys. Lett.*, 62(05), 435-436.
- Yang J., Liu P., Bian X., Jing H., Wang Y., Zhang Y., Wu Y., Song W. (2011), Dielectric, ferroelectric and piezoelectric properties of $\text{Bi}_{0.5}\text{Na}_{0.5}\text{TiO}_3$ – $(\text{Ba}_{0.7}\text{Ca}_{0.3})\text{TiO}_3$ ceramics at morphotropic phase boundary composition, *Mat. Sci. Engg. B*, 176 260-265.
- Yang W., Fang F., Fang D.N. (2003), “*Fracture and fatigue of ferroelectrics*”, in the reference book, *Comprehensive structural integrity*, edited by Milne I., Ritchie R., Karihaloo B., vol. 2 645-686.
- Yao J., Yang Y., Ge W., Li J., Viehland D. (2011), Domain evolution in $\text{PbMg}_{1/3}\text{Nb}_{2/3}\text{O}_3$ -60at% PbTiO_3 with temperature and electric field, *J. Am. Ceram. Soc.*, 94(08) 2479-2482.
- Ye Z.G., Dong M. (2000), Morphotropic domain structures and phase transitions in relaxor-based piezo-/ferroelectric $(1-x)\text{Pb}(\text{Mg}_{1/3}\text{Nb}_{2/3})\text{O}_3$ – $x\text{PbTiO}_3$ single crystals. *J. Appl. Phys.*, 87 2312–2319.
- Ye Z.G., Noheda B., Dong M., Cox D., Shirane G. (2001), Monoclinic phase in the relaxor-based piezoelectric/ferroelectric $\text{Pb}(\text{Mg}_{1/3}\text{Nb}_{2/3})\text{O}_3$ – PbTiO_3 system, *Phys. Rev. B.*, 64 184114.
- Yuan R., Xue D., Zhou Y., Ding X., Sun J., Xue D. (2017), Ferroelectric, elastic, piezoelectric, and dielectric properties of $\text{Ba}(\text{Ti}_{0.7}\text{Zr}_{0.3})\text{O}_3$ - $x(\text{Ba}_{0.82}\text{Ca}_{0.18})\text{TiO}_3$ Pb-free ceramics, *J. Appl. Phys.*, 122 044105.

Zeng H.R., Yu H.F., Chu R.Q., Li G.R., Luo H.S., Yin Q.R. (2004), Domain orientation imaging of PMN–PT single crystals by vertical and lateral piezoresponse force microscopy, *J. Cryst. Growth*, 267 194–198.

Zgonik M., Bernasconi P., Duelli M., Schlessner R., Günter P., Garrett M.H., Rytz D., Zhu Y., Wu X. (1994), Dielectric, elastic, piezoelectric, electro-optic, and elasto-optic tensors of BaTiO₃ crystals. *Phys. Rev. B*, 50(9) 5941–5499.

Zhang Q. M., Wang H., Kim N., Cross L. E. (1994), Direct evaluation of domain wall and intrinsic contributions to the dielectric and piezoelectric response and their temperature dependence on lead zirconate titanate ceramics, *J. Appl. Phys.*, 75 454-459.

Zhang R., Jiang B., Cao W.W. (2001), Elastic, piezoelectric, and dielectric properties of multidomain 0.67Pb(Mg_{1/3}Nb_{2/3})O₃–0.33PbTiO₃ single crystals, *J. Appl. Phys.*, 90(7) 3471–3475.

Zhang R., Jiang B., Jiang W.H., Cao W.W. (2002), Anisotropy in domain engineered 0.92Pb(Zn_{1/3}Nb_{2/3})O₃–0.08PbTiO₃ single crystal and analysis of its property fluctuations. *IEEE Trans. Ultrason. Ferroelectr. Freq. Contr.*, 48(12) 1622–1627.

Zhang S., Laurent L., Liu S., Rhee S., Randall C.A., Shrout T.R. (2002), Piezoelectric shear coefficient of Pb(Zn_{1/3}Nb_{2/3})O₃-PbTiO₃ single crystals, *Jap. J. Appl. Phys.*, 41 L1099-L1102.

Zhang S., Eitel R.E., Randall C.A., Shrout T.R., Alberta E.F. (2005), Manganese-modified BiScO₃-PbTiO₃ piezoelectric ceramic for high temperature shear mode sensor, *Appl. Phys. Lett.*, 86 262904.

Zhang Y.R., Li J.F., Zhang B.P. (2008), Enhancing Electrical Properties in NBT–KBT Lead Free Piezoelectric Ceramics by Optimizing Sintering Temperature, *J. Am. Ceram. Soc.*, 91 2716– 2719.

Zheng P., Zhang J.L., Tan Y.Q., Wang C.L. (2012), Grain-size effects on dielectric and piezoelectric properties of poled BaTiO₃ ceramics. *Acta Mater.*, 60(13-14) 5022–5030.

Zheng X.L., Zhou Y.C., Li J.Y. (2003), Nano-indentation fracture test of Pb(Zr_{0.52}Ti_{0.48})O₃ ferroelectric thin films, *Acta Mater.*, 51 3985-3997.

Zhou M., Zhang J.J., Ji L.D., Wang Y.D., Wang J.Y., Yu F.X. (2014), Phase transition and piezoelectric, ferromagnetic response of B-site (Co, Nb) modified BaTiO₃ ceramics, *Ceram. Int.*, 40(1) 853–857.

Zubko P., Catalan G., Buckley A., Welche P.R.L., Scott J.F. (2007), Strain-gradient-induced polarization in SrTiO₃ single crystals, *Phys. Rev. Lett.*, 99(16) 99-102.